

Anion Photoelectron Spectroscopy Of Semiconductor Clusters And Solvated Species

by

Harry Gomez

B.S. (University of Puerto Rico, Rio Piedras) 1997

A thesis submitted in partial fulfillment of the

requirements for the degree of

Doctor of Philosophy

in

Chemistry

in the

GRADUATE DIVISION

of the

UNIVERSITY OF CALIFORNIA, BERKELEY

Committee in charge:

Professor Daniel M Neumark, Chair

Professor Charles B. Harris

Professor Robert Dibble

Fall 2002

UMI Number: 3082202

UMI<sup>®</sup>

---

UMI Microform 3082202

Copyright 2003 by ProQuest Information and Learning Company.

All rights reserved. This microform edition is protected against  
unauthorized copying under Title 17, United States Code.

---

ProQuest Information and Learning Company  
300 North Zeeb Road  
P.O. Box 1346  
Ann Arbor, MI 48106-1346

Anion Photoelectron Spectroscopy Of Semiconductor Clusters And Solvated Species

Copyright 2002

By

Harry Gomez

Abstract

**Anion Photoelectron Spectroscopy Of Semiconductor Clusters And  
Solvated Species**

by

Harry Gomez

Doctor of Philosophy in Chemistry

University of California, Berkeley

Professor Daniel M. Neumark, Chair

Anion photoelectron spectroscopy is employed to study semiconductor clusters and solvated species. The electronic structure of III-V semiconductor clusters have been studied in an effort to understand how their electronic structure changes as a function of size from discrete molecular states to bulk band structure. Several low-lying electronic states and spin orbit splittings have been determined for group III-V diatomics, AlP, GaP, InP, and GaAs. Photoelectron angular distributions allowed us to identify overlapping electronic states.

Vibrationally resolved photoelectron spectra of Aluminum Phosphide ( $\text{Al}_x\text{P}_y$ ) and  $\text{GaX}^-$ ,  $\text{GaX}_2^-$ ,  $\text{Ga}_2\text{X}^-$ , and  $\text{Ga}_2\text{X}_3^-$  ( $\text{X} = \text{P, As}$ ) clusters were measured at various photodetachment wavelengths. Electron affinities, term energies, and vibrational frequencies for the ground and excited electronic states of the neutral clusters have been obtained. The assignments of excited electronic states were aided by *ab initio* calculations, as well as measurements of photoelectron angular distributions.

Other system studied include  $I_2^+ \cdot (CO_2)$  Van der Waals clusters and solvated transition state precursors. The  $I_2^+ \cdot (CO_2)$  experiment yields size-dependent vertical and adiabatic detachment energies for the formation of the ground state and low-lying valence-excited states of the neutral cluster. Vertical detachment energies are successively blue-shifted with increasing cluster size, indicating a stronger stabilization of the anionic cluster relative to the neutral counterpart. Very interesting ion-solvent interactions are observed for  $I_2^+ \cdot (CO_2)$  clusters. Photoelectron spectra of clusters of the type  $XHX^+(M)$  ( $X = Br, I$ ) where  $M = H_2O, HBr$  and  $HI$ , provide information about solvent induced changes to the transition state of a bimolecular reaction.

*To the memory of my grandmother,*  
***Mariana Bauzó García***

## *Table of Contents*

<b>Table of Contents .....</b>	<b>ii</b>
<b>List of Figures.....</b>	<b>v</b>
<b>List of Tables .....</b>	<b>viii</b>
<b>-1- Introduction .....</b>	<b>1</b>
I. Anion Photoelectron Spectroscopy .....	2
II. Electronic Structure Evolution of Clusters.....	5
III. Probing Solute and Solvent Interactions in clusters .....	7
IV. Figures .....	9
V. Reference .....	10
<b>-2- Experimental Improvements.....</b>	<b>12</b>
I. Overview .....	12
II. Ion sources.....	14
III. Magnetic Bottle Electron Analyzer .....	16
IV. Data Acquisition Software.....	18
V. Figures.....	20
<b>-3- Spectroscopy of the low-lying states of the group III-V diatomics, AlP, GaP, InP, and GaAs, via anion photodetachment spectroscopy .....</b>	<b>25</b>
I. Introduction .....	26
II. Experimental .....	28
A. Photoelectron spectrometer.....	28
B. ZEKE Spectrometer .....	30
III. Results.....	31
IV. Analysis .....	33
A. General.....	33
B. Singlet Manifolds .....	35
a. AlP.....	35
b. GaP.....	36
c. InP and GaAs .....	37
C. Triplet Manifolds.....	39
a. AlP.....	39
b. GaP.....	43
c. InP .....	45
d. GaAs .....	47
V. Discussion .....	49
VI. References: .....	53
VII. Tables .....	56
VIII. Figures.....	60
<b>-4- Photoelectron spectroscopy of <math>\text{GaX}_2^-</math>, <math>\text{Ga}_2\text{X}^-</math>, <math>\text{Ga}_2\text{X}_2^-</math>, and <math>\text{Ga}_2\text{X}_3^-</math> (<math>\text{X}=\text{P,As}</math>) .....</b>	<b>67</b>
I. Introduction .....	68
II. Experimental .....	71

III. Results.....	73
IV. Analysis and Discussion.....	77
A. GaX <sub>2</sub> .....	79
B. Ga <sub>2</sub> X.....	82
C. Ga <sub>2</sub> X <sub>2</sub> .....	86
D. Ga <sub>2</sub> X <sub>3</sub> .....	87
V. Conclusions.....	89
VI. References.....	107
<b>-5- Anion Photoelectron Spectroscopy of Aluminum Phosphide Clusters.....</b>	<b>109</b>
I. Introduction.....	110
II. Experimental.....	112
III. Results.....	114
IV. Analysis and Discussion.....	116
V. Tables.....	126
VI. Figures.....	131
VII. References.....	135
<b>-6- Anion Photoelectron Spectroscopy of I<sub>2</sub><sup>-</sup>(CO<sub>2</sub>)<sub>n</sub> (n=1-8) Clusters.....</b>	<b>137</b>
I. Introduction.....	138
II. Experiment.....	139
III. Results.....	141
A. Photoelectron spectra.....	141
B. Electronic structure calculations.....	143
IV. Analysis and Discussion.....	145
A. Franck-Condon analysis.....	145
B. Cluster Energetics.....	147
V. Conclusions.....	151
VI. References.....	158
<b>-7- Anion Photoelectron Spectroscopy of Solvated Transition State Precursors.....</b>	<b>160</b>
I. Introduction.....	161
II. Experiment.....	164
III. Results.....	166
A. Electronic structure calculations.....	168
a. XHX <sup>+</sup> •(H <sub>2</sub> O).....	168
b. IHI <sup>+</sup> •(HI) <sub>n</sub> .....	169
c. BrHI <sup>+</sup> •(HX) <sub>n</sub> .....	170
IV. Analysis and Discussion.....	171
V. Conclusions.....	176
VI. References.....	177
VII. Figures.....	185
<b>Appendix A: Frank-Condon Simulation Program.....</b>	<b>190</b>
I. Introduction.....	190
II. Usage.....	192
III. Advanced usage/Modifications.....	195
IV. To do list.....	197
V. Description of files.....	198
a. init.h.....	198



b. pesn.cpp .....	198
c. reap.cpp .....	198
d. hofcf.cpp .....	198
e. simfcf.cpp .....	198
f. misc.cpp .....	198
g. writep.cpp .....	198
VI. Source code listing .....	198
a. init.h .....	198
b. pesn.cpp .....	199
c. readp.cpp .....	202
d. hofcf.cpp .....	205
e. simfcf.cpp .....	209
f. misc.cpp .....	216
g. writep.cpp .....	219

## *List of Figures*

<b>-1- Introduction .....</b>	<b>1</b>
Figure 1-1. Anion Photoelectron Spectroscopy Principle.....	9
<b>-2- Experimental Improvements.....</b>	<b>12</b>
Figure 2-1. Diagram of the dual time-of-flight anion photoelectron spectrometer. Figure	
2-2. Time of Flight (top) and energy photoelectron (bottom) spectra of I <sup>-</sup> collected	
using 266 nm and ion beam energy of 2500V. ....	20
Figure 2-3. Diagram of the laser ablation disc source coupled with a liquid nitrogen	
cooled clustering channel.....	22
Figure 2-4. Graphical user interface (GUI) of the new data acquisition software PES	
2002. Br(HBr) <sub>n</sub> (n = 0-24) clusters mass spectrum illustrates mass spectra	
capabilities of the program.....	23
Figure 2-5. Graphical user interface (GUI) of the new data acquisition software PES	
2002. AIP <sup>-</sup> photoelectron spectra illustrates Electron Time of Flight (eTOF)	
capabilities of the program.....	24
<b>-3- Spectroscopy of the low-lying states of the group III-V diatomics, AIP, GaP, InP,</b>	
<b>and GaAs, via anion photodetachment spectroscopy .....</b>	<b>25</b>
Figure 3-1. Energy level diagram for XY <sup>-</sup> /XY (X = Al, Ga, In and Y = P, As) as derived	
from <i>ab initio</i> calculations. ....	60
Figure 3-2. Composite plots of the anion photoelectron spectra of XP (X = Al, Ga, In)	
and GaAs taken at the polarization angle of $\theta \approx 54^\circ$ . See text for further	
description.....	61
Figure 3-3. Anion photoelectron spectrum AIP <sup>-</sup> and GaP <sup>-</sup> triplet manifold taken at 498	
nm and laser polarization of $\theta = 90^\circ$ and $\theta = 0^\circ$ . Experimental $\beta$ parameters at the	
same photon energy are plotted in the top panel. FC simulation of the $\theta = 90^\circ$ ( $\theta = 0^\circ$	
for AIP) spectrum is shown in the bottom panel.....	62
Figure 3-4. Anion photoelectron spectrum InP <sup>-</sup> and GaAs <sup>-</sup> triplet manifold taken at 498	
nm and laser polarization of $\theta = 90^\circ$ and $\theta = 0^\circ$ . Experimental $\beta$ parameters at the	
same photon energy are plotted in the top panel. FC simulation of the $\theta = 90^\circ$	
spectrum is shown in the bottom panel.....	63
Figure 3-5. Anion photoelectron spectrum AIP <sup>-</sup> and GaP <sup>-</sup> singlet manifold taken at 498	
nm and laser polarization of $\theta = 90^\circ$ and $\theta = 0^\circ$ . Experimental $\beta$ parameters at the	
same photon energy are plotted in the top panel. FC simulation of the $\theta = 90^\circ$ ( $\theta = 0^\circ$	
for AIP) spectrum is shown in the bottom panel.....	64
Figure 3-6. Anion photoelectron spectrum InP <sup>-</sup> and GaAs <sup>-</sup> singlet manifold taken at 355	
nm (416nm for InP) and laser polarization of $\theta = 90^\circ$ and $\theta = 0^\circ$ . Experimental $\beta$	
parameters at the same photon energy are plotted in the top panel. FC simulation of	
the $\theta = 90^\circ$ spectrum is shown in the bottom panel. ....	65

Figure 3-7. Energy level diagram showing the electronic structure of the anion and neutral states of the isoelectronic species, Si<sub>2</sub>, Ge<sub>2</sub>, AlP, GaP, InP, and GaAs. The energy is referenced with respect to the <sup>3</sup>Σ state for each species. .... 66

#### -4- Photoelectron spectroscopy of GaX<sub>2</sub><sup>-</sup>, Ga<sub>2</sub>X<sup>-</sup>, Ga<sub>2</sub>X<sub>2</sub><sup>-</sup>, and Ga<sub>2</sub>X<sub>3</sub><sup>-</sup> (X=P,As) ..... 67

Figure 4-1. Diagram of the liquid nitrogen cooled clustering channel coupled with the laser ablation disc source. The diagram is labeled as follows: (a) pulsed piezo electric valve, (b) disc ablation target, (c) incident laser beam, (d) Delrin insulating disc, and (e) copper clustering channel. .... 98

Figure 4-2. Comparison of 'hot' and 'cold' anion photoelectron spectra of GaP<sub>2</sub><sup>-</sup> taken at a wavelength of 355 nm and polarization angle of θ=0°. The spectrum shows only the  $\tilde{A}^2A_1$  state of GaP<sub>2</sub><sup>-</sup>. .... 99

Figure 4-3. Anion photoelectron spectra of GaX<sub>2</sub><sup>-</sup> (X=P, As) taken at the wavelengths and polarization angles indicated. The features marked with an asterisk (\*) are discussed in the text. .... 100

Figure 4-4. Anion photoelectron spectra of Ga<sub>2</sub>X<sup>-</sup> (X=P, As) taken at a wavelength of 355 nm and polarization angles of θ=0° and 90°. The plot of the β parameters is located in the top panel. The features marked with an asterisk (\*) are discussed in the text. .... 101

Figure 4-5. Anion photoelectron spectra of Ga<sub>2</sub>X<sub>2</sub><sup>-</sup> (X=P, As) taken at a wavelength of 355 nm and polarization angle of θ=0°. .... 102

Figure 4-6. Anion photoelectron spectra of Ga<sub>2</sub>X<sub>3</sub><sup>-</sup> (X=P, As) taken at a wavelength of 355 nm and polarization angles of θ=0° and 90°. The dotted line in the lower left panel was taken at 266 nm. .... 103

Figure 4-7. Anion photoelectron spectra of GaX<sub>2</sub><sup>-</sup> (gray solid) superimposed with FC simulation (black line). .... 104

Figure 4-8. Anion photoelectron spectra of Ga<sub>2</sub>X<sup>-</sup> (gray solid) superimposed with FC simulation (black line). Figure 4-9. Anion photoelectron spectra of Ga<sub>2</sub>X<sub>3</sub><sup>-</sup> (gray solid) superimposed with FC simulation (black line). .... 105

#### -5- Anion Photoelectron Spectroscopy of Aluminum Phosphide Clusters ..... 109

Figure 5-1. Photoelectron spectra of Al<sub>x</sub>P<sub>y</sub><sup>-</sup> clusters taken at 266 nm (4.661 eV). All spectra were taken at laser polarization of θ = 55° with respect to the direction of electron collection. .... 131

Figure 5-2 Photoelectron spectra of AlP<sub>2</sub><sup>-</sup> clusters taken at 266 nm (4.661 eV) and 355 nm (3.493 eV). Laser polarization angle is θ=0° and θ=55° with respect to the direction of electron collection. .... 132

Figure 5-3.. Photoelectron spectra of Al<sub>2</sub>P<sup>-</sup> clusters taken at 355 nm (3.493 eV) and 416 nm (2.980 eV). Laser polarization angles are θ=0° and θ=90° with respect to the direction of electron collection. .... 133

Figure 5-4. Photoelectron spectra of Al<sub>2</sub>P<sub>2</sub><sup>-</sup> clusters taken at 266 nm (4.661 eV) and 355 nm (3.493 eV). Laser polarization angles are θ=0° and θ=55° with respect to the direction of electron collection. .... 134

#### -6- Anion Photoelectron Spectroscopy of I<sub>2</sub><sup>-</sup>(CO<sub>2</sub>)<sub>n</sub> (n=1-8) Clusters..... 137

Figure 6-1. Anion photoelectron spectra (solid) of $I_2^-$ and $I_2^-(CO_2)$ measured at photon energy of 4.661 eV (266 nm). Franck-Condon simulation (dashed) of bands A' and A of the $I_2^-(CO_2)$ spectrum is also shown. ....	153
Figure 6-2. Anion photoelectron spectra of $I_2^-(CO_2)_n$ clusters measured at a photon energy of 4.661 eV. The vertical detachment energies for the formation of the X, A', A, and B' states of bare $I_2$ are indicated by the broken vertical lines. ....	154
Figure 6-3. Lowest energy calculated structure for $I_2^-(CO_2)$ based on results from Table 6-2. ....	155
Figure 6-4. Total solvation energy difference $\Delta SE_{tot}^I(n)$ for detachment to the X and A states of $I_2^-(CO_2)_n$ as a function of cluster size n. ....	156
Figure 6-5. Stepwise solvation energy difference $\Delta SE_{step}^X(n)$ for detachment to the X state of $I_2^-(CO_2)_n$ as a function of cluster size n. ....	157
<b>-7-Anion Photoelectron Spectroscopy of Solvated Transition State Precursors..... 160</b>	
Figure 7-1. Anion photoelectron spectra of $IHI^- \cdot (H_2O)$ and $IHI^- \cdot (HI)_{1,2}$ measured at photon energy of 5.821 eV (213 nm). ....	185
Figure 7-2. Anion photoelectron spectra of $BrHBr^- \cdot (H_2O)$ and $BrHBr^- \cdot (HI)_{1,2}$ measured at photon energy of 5.821 eV (213 nm). ....	186
Figure 7-3. Anion photoelectron spectra of $BrHI^- \cdot (HBr)$ and $BrHI^- \cdot (HI)$ measured at photon energy of 5.821 eV (213 nm). ....	187
Figure 7-4. Franck-Condon simulation (dashed) of the $XHX^- \cdot (HX)$ ( $X = I, Br$ ) complexes, experimental spectrum is also shown(solid). ....	188
Figure 7-5. Lowest energy structures calculated for the anions based on results from Tables 1-5. For the $BrHI^- \cdot (HBr)$ complex (B) Iodine occupies the center of the complex. ....	189

## List of Tables

---

<b>-3- Spectroscopy of the low-lying states of the group III-V diatomics, AlP, GaP, InP, and GaAs, via anion photodetachment spectroscopy .....</b>	<b>25</b>
Table 3-1. Comparison of experimental and theoretical molecular constants of AlP. ....	56
Table 3-2. Comparison of experimental and theoretical molecular constants of GaP. ....	57
Table 3-3. Comparison of experimental and theoretical molecular constants of InP. ....	58
Table 3-4. Comparison of experimental and theoretical molecular constants of GaAs. ..	59
<b>-4- Photoelectron spectroscopy of <math>\text{GaX}_2^-</math>, <math>\text{Ga}_2\text{X}^-</math>, <math>\text{Ga}_2\text{X}_2^-</math>, and <math>\text{Ga}_2\text{X}_3^-</math> (<math>\text{X}=\text{P,As}</math>).....</b>	<b>67</b>
Table 4-1. Comparison of geometries and energy separations of $\text{GaP}_2^-/\text{GaP}_2^-$ .....	91
Table 4-2. Comparison of geometries and energy separations of $\text{GaAs}_2^-/\text{GaAs}_2^-$ .....	92
Table 4-3. Comparison of geometries and energy separations of $\text{Ga}_2\text{P}^-/\text{Ga}_2\text{P}^-$ .....	93
Table 4-4. Comparison of geometries and energy separations of $\text{Ga}_2\text{As}^-/\text{Ga}_2\text{As}^-$ .....	94
Table 4-5. Comparison of geometries and energy separations of $\text{Ga}_2\text{As}_3^-/\text{Ga}_2\text{As}_3^-$ and $\text{Ga}_2\text{P}_3^-/\text{Ga}_2\text{P}_3^-$ .....	95
Table 4-6. Photoelectron spectra simulation parameters for active modes in $\text{Ga}_2\text{X}^-$ and $\text{GaX}_2^-$ .....	96
Table 4-7. Neutral structures based on best-fit normal coordinate displacements using calculated anion geometries as reference.....	97
<b>-5- Anion Photoelectron Spectroscopy of Aluminum Phosphide Clusters .....</b>	<b>109</b>
Table 5-1. Estimated adiabatic electron affinities and vertical detachment energies for $\text{Al}_n\text{P}_y^-$ .....	126
Table 5-2. Comparison of geometries and energy separations for $\text{AlP}_2^-/\text{AlP}_2^-$ .....	127
Table 5-3. Comparison of geometries and energy separations for $\text{Al}_2\text{P}^-/\text{Al}_2\text{P}^-$ .....	128
Table 5-4. Comparison of geometries and energy separations for $\text{Al}_2\text{P}_2^-/\text{Al}_2\text{P}_2^-$ .....	129
Table 5-5. Photoelectron spectra simulation parameters for active modes in $\text{Al}_2\text{P}^-$ , $\text{AlP}_2^-$ and $\text{Al}_2\text{P}_2^-$ .....	130
<b>-6- Anion Photoelectron Spectroscopy of <math>\text{I}_2^-(\text{CO}_2)_n</math> (<math>n=1-8</math>) Clusters.....</b>	<b>137</b>
Table 6-1. Total and stepwise shifts (in parentheses) of the bands in the photoelectron spectra of $\text{I}_2^-(\text{CO}_2)_n$ clusters relative to the $\text{I}_2^-$ spectrum as a function of cluster size $n$ . All energies are in meV. ....	142
Table 6-2. Results of electronic structure calculations for $\text{I}_2^-(\text{CO}_2)$ and $\text{I}_2(\text{CO}_2)$ . All bond lengths in Å .....	152
<b>-7- Anion Photoelectron Spectroscopy of Solvated Transition State Precursors.....</b>	<b>160</b>
Table 7-1. Experimental peaks position and labels .....	180
Table 7-2. Results of <i>Ab initio</i> electronic structure calculations for $\text{XHX}^-$ , $\text{H}_2\text{O}$ , $\text{HBr}$ and $\text{HI}$ . All bond lengths in Å.....	181

Table 7-3. Results of <i>Ab initio</i> electronic structure calculations for $\text{XHX}^+ \cdot (\text{H}_2\text{O})$ clusters. All bond lengths in Å.....	182
Table 7-4. Results of <i>Ab initio</i> electronic structure calculations for $\text{IHI}^+ \cdot (\text{HI})_{1,2,3}$ clusters. All bond lengths in Å.....	183
Table 7-5. Results of <i>Ab initio</i> electronic structure calculations for $\text{BrHI}^+ \cdot (\text{HBr})$ and $\text{BrHI}^+ \cdot (\text{HI})$ clusters. All bond lengths in Å. ....	184

## **-1- Introduction**

---

Anion photoelectron spectroscopy (PES) offers numerous advantages over conventional optical techniques. The selection rules allow the observation of both singlet and triplet states unlike optical selection rules. Its moderate to “high” resolution reveals precious information about the electronic structure of the system in question. PES when combined with mass spectrometry allows selection of the atom/molecule of interest and also facilitate the observation and study of size dependent properties of a system. Neutral species, open shell radicals (i.e. I<sub>2</sub>, AIP) and other species that are unstable with respect to dissociation (i.e. transition states, IHI) can generally form bound molecular anions facilitating their production and study using PES. This thesis describes the investigation of a mixed group of molecules. This thesis can be divided into two sections pertaining to the types of species studied: semiconductor clusters and solvated clusters. Chapter 3 discloses the spin-orbit coupling, band lengths, and term energies in AIP, GaP, InP and GaAs diatomics determined using anion photoelectron spectroscopy. For these systems we take advantage of different photoelectron angular distributions of different electronic states to identify up to seven (triplet and single) electronic states in 4 group III-V diatomics. The variation of polarization angle with respect to the direction of electron detection gives the ability to distinguish between transitions of energetically overlapping state. Chapters 4-5 describe the spectroscopy of III-V semiconductor clusters in an effort to understand how their molecular properties evolve as the number of atoms in the cluster is increased, and how their properties correlated with isoelectronic clusters of group V

semiconductors (i.e. Ge, Si). This knowledge will provide a better understanding on how molecular properties evolve into bulk properties. Chapters 6 discuss the spectroscopy of the solvated complexes:  $\text{I}_2^+ \cdot (\text{CO}_2)$ . The study of these species provide a better understating about solute-solvent interactions, as well as details about how the solute can induce changes in the solvent molecules and vice versa. In the remainder of the introduction we will describe our technique to a greater extent and demonstrate its ability to provide important spectroscopic information about the systems studied and further discuss why these systems are relevant to the scientific community.

## I. Anion Photoelectron Spectroscopy

Figure 1-1 illustrates the principle of Anion Photoelectron spectroscopy (PES). In this technique, photons with enough energy are used to remove electrons from negative charge atoms, molecules or clusters ( $M^-$ ). The excess energy of the photon that is not used in the transition to the neutral state(s) ( $M$ ,  $M^*$ ,) is automatically reflected as electron kinetic energy, which is the experimental observable. The kinetic energy of the photoelectrons represent a direct measurement of the energy required to remove a single electron from different orbitals in the anion, therefore revealing the electronic structure of system under study. The kinetic energy (KE) of the photoelectrons is give by equation (1):

$$eKE = h\nu - T_0^{(0)} + T_0^{(-1)} - E_v^{(0)} + E_v^{(-1)} + \dots \quad (1)$$

where  $h\nu$  is the photon energy,  $T_0^{(0)}$  and  $T_0^{(-1)}$  are the electronic energy of the neutral and anion respectively, and  $E_v^{(0)}$  and  $E_v^{(-1)}$  are the vibrational energy of the neutral and anion respectively. Other terms (i.e. rotational energy) are usually ignored because their contribution is negligible compared with electronic and vibrational terms. Assuming the



anions have no internal energy (i.e.  $T_0^{(-1)}, E_v^{(-1)} = 0$ ) the spacing between the peaks in the electron kinetic energy distribution reveal the energies between electronic and vibrational states of the neutral. The intensity of the peaks in the electron kinetic energy distribution provide information about the relative cross-section of the photodetachment process and/or the relative geometry changes between the anion and the neutral states involved. The intensity profile and the extent of vibrational progressions reveal information on how different are the geometries of the neutral states compared to the initial anion state. Photoelectron energy distributions are usually plotted in terms of the electron kinetic energy (eKE) or electron binding energy (eBE) which are energetically related by equation (2)

$$eBE = h\nu - eKE = EA + E_{\text{int}}^{(0)} - E_{\text{int}}^{(-1)} \quad (2)$$

where  $h\nu$  is the photon energy,  $EA$  is the electron affinity, and  $E_{\text{int}}^{(-1)}$  is the internal energy of the resultant neutral state with respect to the neutral ground state.

The angular dependence of the photodetachment intensity for polarized light and randomly oriented molecules is given by equation (3) below

$$\frac{d\sigma}{d\Omega} = \frac{\sigma_{\text{total}}}{4\pi} \left[ 1 + \frac{\beta(eKE)}{2} (3\cos^2\theta - 1) \right] \quad (3)$$

where  $\theta$  is the angle between the electric vector of the photon and the direction of electron ejection,  $\sigma_{\text{total}}$  is the total photodetachment cross section and  $\beta(eKE)$  is the anisotropy parameter ( $-1 \leq \beta \leq 2$ ). Each electronic state usually has a characteristic anisotropy parameter and can be used to distinguish peaks of overlapping electronic transitions. The anisotropy parameter of a peak can be calculated<sup>2</sup> using equation (4)

$$\beta = \frac{I_{0^\circ} - I_{90^\circ}}{\frac{1}{2}I_{0^\circ} + I_{90^\circ}} \quad (4)$$

where  $I_{0^\circ}$  and  $I_{90^\circ}$  are the normalized intensities of the peak taken at the polarization angles  $\theta = 0^\circ$  and  $90^\circ$ .

Anion photoelectron spectroscopy offers many advantages over conventional optical techniques. First, the spin selection rules are more relaxed than in optical spectroscopy where the spin multiplicity cannot change. For example both singlet and triplet neutral states may be observed if starting with a doublet anion, directly yielding their electronic states splitting (i.e. AlP, GaP). Second, the experimental resolution is high enough (8-15 meV) to resolve individual vibrational states within an electronic manifold. In addition to providing valuable vibrational frequencies, frequently the vibrational structure is essential for the proper identification of the electronic state. Vibrational resolution also lead to more accurate determination of band origins, term energies and adiabatic electron affinities, this information if combined with *ab initio* calculations and Frank-Condon simulations could yield valuable structural (i.e. bond lengths, angles) information about the anion and/or neutral complex. Third, the use of anions as a precursors allows mass selection of the anion of interest, ensuring the identity (i.e. mass) and in some cases the unity of system under study. For small molecules a unique isomer is easily generated where as for large clusters there may be many isoenergetic isomers for a particular mass that will complicate the photoelectron spectrum. The corresponding anion of reactive, short-lived, and radical neutral molecules can be generated by a variety of sources including pulsed electric discharge, laser ablation, and the electron gun.

## II. Electronic Structure Evolution of Clusters

Semiconductor clusters have been the subject of intense experimental and theoretical investigations during the last twenty years. Studies of semiconductor clusters have been performed in both the nanoscale and molecular size regimes in order to understand how the structural and spectroscopic properties these species evolve with size. Anion Photoelectron Spectroscopy is particularly well-suited to study the evolution of properties (i.e. electron affinity, electronic structure) of size selected clusters. Smalley and coworkers used magnetic bottle anion photoelectron techniques as a means of observing the electronic structure of mass-selected clusters. The group mainly focused on homonuclear clusters such as  $C_n^-$ ,  $Si_n^-$ , and  $Ge_n^-$ . However they also performed the first study of a heteronuclear III-V semiconductor system, gallium arsenide. Homonuclear clusters are simpler theoretically and experimentally than heteronuclear systems. The low mass resolution and electron kinetic energy resolution prevented them from deriving more than qualitative information from their spectra. Since then several second-generation magnetic bottle anion photoelectron spectrometers have been built. Cheshnovsky and coworkers have added a tilted reflectron to their TOF mass spectrometer enabling them to take photoelectron spectra of mercury clusters up to mass  $\sim 50,000$  amu ( $n = 250$ ). Wang and coworkers have studied transition metal clusters with up to 70 atoms and aluminum clusters with up to 162 atoms. Only the vanadium clusters show a trend in electronic structure that extrapolates to the bulk behavior. In contrast the relatively simple mercury system of Cheshnovsky and coworkers clearly shows this system evolve from the insulator to semiconductor phase<sup>3</sup>. Extrapolation of the data concludes that the band gap closure is complete at  $400 \pm 30$  atoms. This experiment

showed the inadequacy of previous experimental and theoretical methods which conclude that the band gap closure occurs at  $n = 80-100$ . There is clearly a large amount of work to be done on both experimental and theoretical fronts to explain the trends in the electronic structure evolution of metal and semiconductor systems.

Our group has focused its efforts on homonuclear clusters from group IV<sup>4,5</sup> elements and heteronuclear III-V clusters<sup>6-9</sup>. We have gone to great efforts to understand the electronic and vibrational structure of small clusters from these three groups. The  $\text{In}_x\text{P}_y$  ( $x, y = 1-4$ ) photoelectron spectra taken by Xu et al.<sup>10</sup> is the first III-V study published by our group. C.C. (Arnold) Jarrold later revealed the vibrational structure publishing the ZEKE spectra of  $\text{In}_2\text{P}^+$  and  $\text{InP}_2^+$ .<sup>11</sup> Two low-resolution studies (30 meV) of  $\text{Ga}_x\text{P}_y$  ( $x+y \leq 18$ ) and  $\text{In}_x\text{P}_y$  ( $x+y \leq 27$ ) clusters showed the size dependent trend of the electron affinity beginning with stoichiometric clusters having more than 12 atoms. The onset of the size dependent trend coincides with the loss of our ability to resolve electronic structure. For clusters of more than 12 atoms discrete electronic states are no longer observed. The spectra of these two isovalent systems are extremely similar however their bulk properties are quite different. These two studies do not reveal evidence of a band gap at these cluster sizes or photon energies. At this point it became clear that larger clusters and higher energy photons were needed. For this reason we have modified our instrument to look for “band-gap” like structure in larger clusters with higher photon energies with the addition of a magnetic bottle analyzer and 157nm excimer laser as discussed in chapter 2. We look forward for new and exciting results that reveal interesting properties about the electronic structure of “big” semiconductor clusters.

### III. Probing Solute and Solvent Interactions in clusters

The study of solute-solvent interactions has been of profound interest in chemical physics for several decades. Given that most reactions in nature and industry occurs in solution the understating of these interaction is of particular interest. Molecular clusters, particularly charged clusters, offer a unique environment in which the interaction and/or properties of a system can be studied as a function of is size (i.e. mass selection), therefore providing fundamental information about the transition between gas and condense phase. Anion photoelectron spectroscopy provide an excellent tool which could be use to study the properties of a chromophore with the addition of solvent molecules (i.e.  $I^-(H_2O)_n$ )<sup>12</sup>. Important information could be derived from such studies like solvent cage closure, charge transfer, solute and/or solvent structural changes, and cooling effects. Such studies range from straightforward rare gas-halide Van der Waals (i.e.  $Xe_n \cdot I^-$ ) clusters to more complex ultra-fast photofragmentation studies in solvents and clusters (i.e.  $I_2^-(CO_2)_n$ )<sup>13</sup>. Halide-rare gas systems have been widely studied due to their simplicity, these system have reveal fundamental information about solvation effects, clusters structure and potentials<sup>14-21</sup>. Other more complex Van der Waals systems have been studied in order to provide a better understanding between the solute-solvent interaction of polar and/or more complex solvents<sup>12,22-27</sup> (i.e. water, ammonia).

With the latest development of ultra-fast lasers scientists have been able to follow the motion of atoms along a repulsive potential energy surface, such studies include the study of the photodissociation of  $Br_2^-$  and  $I_2^-$ . Studies on the photolysis of  $I_2$  in the gas phase,<sup>28-31</sup> clusters,<sup>32-35</sup> liquids,<sup>36-38</sup> and matrices<sup>39-41</sup> have led to a detailed understanding of many solvent/solute effects. From the gas phase experiments, particularly accurate

potentials have been derived,<sup>28-30</sup> and dissociation times has been measured.<sup>31</sup> In non-polar solvents, dissociation is followed by caging and non-adiabatic curve crossing to the ground electronic state<sup>36</sup>. Also worth mentioning is the recent study solvated transition state study by Liu et al.<sup>42,43</sup>. Liu et al investigated the transition state spectra of the  $X + HI \rightarrow XH + I$  ( $X = I, Br$ ) reactions in argon clusters using anion photoelectron spectroscopy. Argon clustering has resulted in a significant reduction of vibrational hot bands in the spectra, giving much better spectral resolution. This improvement allows them to observe reactive resonances and transitions to hindered rotor states for the  $I + HI$  reaction and new progression due to transitions to the  $I + HI$  ( $v = 1$ ) scattering channel.

#### IV. Figures

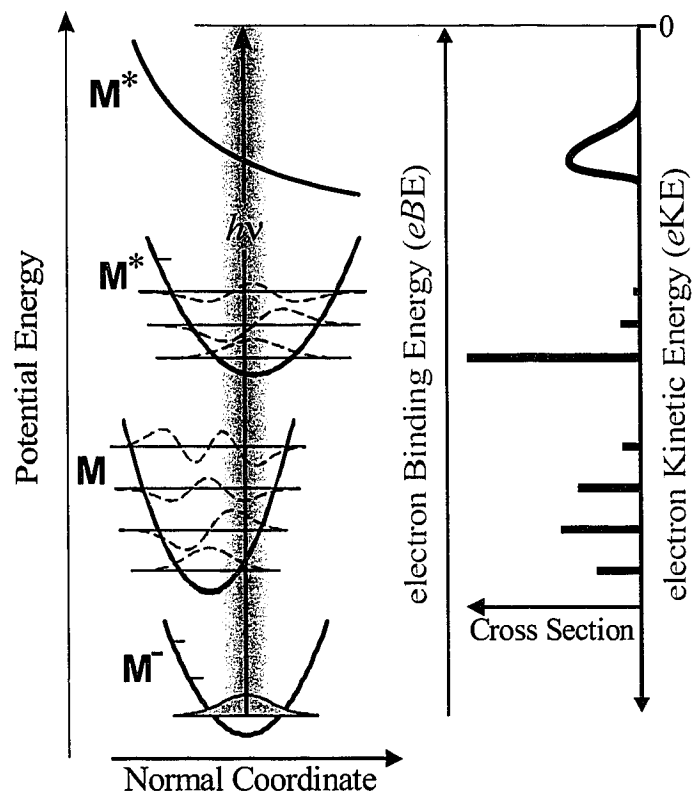


Figure 1-1. Anion Photoelectron Spectroscopy Principle

## V. Reference

- (1) Cooper, J.; Zare, R. N. Photoelectron angular distributions. In *Lectures in Theoretical Physics*; Brittin, W. E., Ed.; Gordon and Breach: New York, 1969; Vol. XI-C; pp 317.
- (2) Ervin, K. M.; Lineberger, W. C. Photoelectron spectroscopy of molecular anions. In *Advances in Gas Phase Ion Chemistry*; JAI Press Inc, 1992; Vol. 1; pp 121.
- (3) Busani, R.; Folkers, M.; Cheshnovsky, O. *Physical Review Letters* **1998**, *81*, 3836.
- (4) Arnold, C. C.; Neumark, D. M. *Journal of Chemical Physics* **1994**, *100*, 1797.
- (5) Arnold, C. C.; Xu, C. S.; Burton, G. R.; Neumark, D. M. *Journal of Chemical Physics* **1995**, *102*, 6982.
- (6) Asmis, K. R.; Taylor, T. R.; Neumark, D. M. *Chemical Physics Letters* **1998**, *295*, 75.
- (7) Gomez, H.; Taylor, T. R.; Neumark, D. M. *Journal of Physical Chemistry A* **2001**, *105*, 6886.
- (8) Taylor, T. R.; Asmis, K. R.; Gomez, H.; Neumark, D. M. *European Physical Journal D* **1999**, *9*, 317.
- (9) Taylor, T. R.; Gomez, H.; Asmis, K. R.; Neumark, D. M. *Journal of Chemical Physics* **2001**, *115*, 4620.
- (10) Xu, C.; Debeer, E.; Arnold, D. W.; Arnold, C. C.; Neumark, D. M. *Journal Of Chemical Physics* **1994**, *101*, 5406.
- (11) Arnold, C. C.; Neumark, D. M. *Canadian Journal Of Physics* **1994**, *72*, 1322.
- (12) Markovich, G.; Pollack, S.; Giniger, R.; Cheshnovsky, O. *Journal of Chemical Physics* **1994**, 9344.
- (13) Alexander, M. L.; Johnson, M. A.; Lineberger, W. C. *Journal of Chemical Physics* **1985**, *82*, 5288.
- (14) Becker, I.; Markovich, G.; Cheshnovsky, O. *Physical Review Letters* **1997**, *79*, 3391.
- (15) Becker, I.; Cheshnovsky, O. *J. Chem. Phys.* **1999**, *110*, 6288.
- (16) Lenzer, T.; Furlanetto, M. R.; Asmis, K. R.; Neumark, D. M. *Journal of Chemical Physics* **1998**, *109*, 10754.
- (17) Lenzer, T.; Yourshaw, I.; Furlanetto, M. R.; Reiser, G.; Neumark, D. M. *Journal of Chemical Physics* **1999**, *110*, 9578.
- (18) Lenzer, T.; Furlanetto, M. R.; Pivonka, N. L.; Neumark, D. M. *Journal of Chemical Physics* **1999**, *110*, 6714.
- (19) Yourshaw, I.; Lenzer, T.; Reiser, G.; Neumark, D. M. *Journal of Chemical Physics* **1998**, *109*, 5247.
- (20) Yourshaw, I.; Zhao, Y. X.; Neumark, D. M. *Journal of Chemical Physics* **1996**, *105*, 351.
- (21) Zhao, Y. X.; Yourshaw, I.; Reiser, G.; Arnold, C. C.; Neumark, D. M. *Journal of Chemical Physics* **1994**, *101*, 6538.



- (22) Hendricks, J. H.; de Clercq, H. L.; Freidhoff, C. B.; Arnold, S. T.; Eaton, J. G.; Fancher, C.; Lyapustina, S. A.; Snodgrass, J. T.; Bowen, K. H. *Journal of Chemical Physics* **2002**, *116*, 7926.
- (23) Kim, J. B.; Wenthold, P. G.; Lineberger, W. C. *Journal of Chemical Physics* **1998**, *108*, 830.
- (24) Kim, J.; Becker, I.; Cheshnovsky, O.; Johnson, M. A. *Chemical Physics Letters* **1998**, 90.
- (25) Davis, A. V.; Zanni, M. T.; Weinkauff, R.; Neumark, D. M. *Chemical Physics Letters* **2002**, *353*, 455.
- (26) Upadhyay, D. M.; Mishra, P. C. *Journal of Molecular Structure-Theochem* **2002**, *584*, 113.
- (27) Markovich, G.; Giniger, R.; Levin, M.; Cheshnovsky, O. *Journal of Chemical Physics* **1991**, 9416.
- (28) Martin, F.; Bacis, R.; Churassy, S.; Verges, J. J. *Mol. Spectrosc.* **1986**, *116*, 71.
- (29) Tellinghuisen, J.; Fei, S.; Zheng, X.; Heaven, M. C. *Chemical Physics Letters* **1991**, *176*, 373.
- (30) Appadoo, D. R. T.; Leroy, R. J.; Bernath, P. F.; Gerstenkorn, S.; Luc, P.; Verges, J.; Sinzelle, J.; Chevillard, J.; Daignaux, Y. J. *Chem. Phys.* **1996**, *104*, 903.
- (31) Bowman, R. M.; Dantus, M.; Zewail, A. H. *Chem. Phys. Lett.* **1989**, *161*, 297.
- (32) Liu, Q. L.; Wang, J. K.; Zewail, A. H. *Nature* **1993**, *364*, 427.
- (33) Wang, J.-K.; Liu, Q. L.; Zewail, A. H. *J. Phys. Chem.* **1995**, *99*, 11309.
- (34) Sanger, K. L.; McClelland, G. M.; Herschbach, D. R. *J. Phys. Chem.* **1981**, *85*, 3333.
- (35) Valentini, J.; Cross, J. J. *Chem. Phys.* **1982**, *77*, 572.
- (36) Chuang, T. J.; Hoffman, G. W.; Eisenthal, K. B. *Chem. Phys. Lett.* **1974**, *25*, 201.
- (37) Nesbitt, D. J.; Hynes, J. T. *J. Chem. Phys.* **1982**, *77*, 2130.
- (38) Harris, A. L.; Brown, J. K.; Harris, C. B. *Annu. Rev. Phys. Chem.* **1988**, *39*, 341.
- (39) Zadoyan, R.; Li, Z.; Ashjian, P.; Martens, C. C.; Apkarian, V. A. *Chem. Phys. Lett.* **1994**, *218*, 504.
- (40) Li, Z.; Zadoyan, R.; Apkarian, V. A.; Martens, C. C. *J. Phys. Chem.* **1995**, *99*, 7453.
- (41) Zadoyan, R.; Li, Z.; Martens, C. C.; Apkarian, V. A. *J. Chem. Phys.* **1994**, *101*, 6648.
- (42) Liu, Z.; Gomez, H.; Neumark, D. M. *Chemical Physics Letters* **2000**, *332*, 65.
- (43) Liu, Z.; Gomez, H.; Neumark, D. M. *Faraday Discussions* **2001**, *118*, 221.

## **-2- *Experimental Improvements***

---

The apparatus used in the experiments is a dual time-of-flight anion photoelectron spectrometer. The original version of this instrument has been described in detail previously<sup>1-4</sup>. Several modifications have been made to improve the overall performance and/or to expand the capabilities of the instrument. First, a new magnetic bottle electron analyzer has been added to the machine in order to study “big” semiconductor clusters. In addition, a new excimer laser (GAM Laser EX50F/250) has joined our lab which is projected to work together with the new magnetic bottle analyzer. Finally new software has been developed for data acquisition, visualization and analysis. The new magnetic bottle design and implementation share similar characteristics with the ones found in the Femtosecond Anion Photoelectron Spectroscopy lab (FPES) and Stimulated Raman Pumping Lab (SRP) in our group. Detailed description of the design and operation of the magnetic bottle electron analyzer can be found in the dissertation of Jeff Greenblatt<sup>5</sup> and Marty Zanni<sup>6</sup>. In this thesis, a general overview of the instrument will be given, followed by a description of features and/or differences in our implementation different from the original Neumark Group “recipe”. The entire modified apparatus is shown in Figure 2-1. Detailed descriptions are presented in the following sections.

### **I. Overview**

The experiments described throughout this thesis were carried out on a dual time-of-flight negative ion photoelectron spectrometer. Anion clusters are generated in the

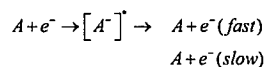
source region (Figure 2-1) using a pulsed molecular beam valve coupled with an electron impact, pulsed discharge or ablation source. The pulsed valve operates at 20 Hz, and the typical pressure in the source region during operation is  $5 \times 10^{-6}$  to  $1 \times 10^{-4}$  torr. Brief descriptions about the operation and use of the different ion sources are given section II. After ions are generated in the source region they enter the first differential region where they are extracted by a pulsed electric field. Ions then enter a time-of-flight mass spectrometer with a linear reflectron stage. The accelerated ions separate in time and space according to their mass to charge ratios, and are selectively detached by a pulsed laser.

Several wavelengths from two distinct laser systems are available for detachment. First the third, fourth and fifth harmonics (355 nm, 3.493 eV, 266 nm, 4.657 eV, 213 nm, 5.821 eV respectively) from a pulsed Nd:YAG laser provide enough energy to photodetach and study molecules with moderate electron affinities and low lying electronic states. For system with high electron affinities or to study multiple electronic states the output of an F<sub>2</sub> excimer laser is used (157 nm, 7.897 eV). Photodetachment and electron kinetic energy analysis can occur at two different locations in the machine. Two different electron analyzers expand the machine capabilities to study a more diverse number of systems. First, moderate to "high" energy resolution is provided by a Field Free Time of Flight electron analyzer. The disadvantage of this electron analyzer is its low collection efficiency, therefore requiring longer acquisition times, and high ion densities. Second, high collection efficiency but low energy resolution is provided by a Magnetic Bottle Flight Time of Flight electron analyzer. The selection of one electron analyzer vs. the other depends strongly on the system under study. The photoelectron

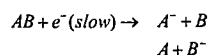
kinetic energy is measured by time-of-flight in a flight tube of 100 cm and 120 cm for the Field Free and Magnetic Bottle analyzers respectively. The Field Free analyzer resolution is 8 - 10 meV for the for an electron kinetic energy (eKE) of 0.65 eV and degrades as  $(eKE)^{3/2}$ . This is suitable for determination of term energies and vibrational structure of small molecules. The Magnetic Bottle resolution depends extensively on the ion velocity. For I<sup>+</sup> with aa extraction voltage of 2500V the resolution is 300-350 meV for an electron kinetic energy (eKE) of 0.65 eV and it also degrades as  $(eKE)^{3/2}$  (Figure 2-2). The Magnetic bottle is intended to study very large systems (i.e. semiconductor clusters) where energy resolution is not critical. Since these large systems numerous degrees of freedom make it impossible to resolve individual vibrational modes. Figure 2-2 shows a comparison of the Time of Flight (TOF) and Energy photoelectron spectra of I<sup>+</sup> collected using 266 nm (4.661 eV) and an extraction voltage of 2500V.

## II. Ion sources

Currently we have three different sources for the production of negative ions. Electron impact, pulsed discharge, and laser ablation. The selection of one source over the other ones depends on the availability and/or the form of the ion precursors (liquid, gas, solid). For gases and some high vapor pressure liquids the electron impact (EI) source has proven to be effective, simple and very stable. In the electron impact source a beam of electrons is accelerated (1000 eV) towards the gas expansion. High energy electrons excite and ionize molecules during the expansion.



Anions are formed by dissociative attachment of slow electrons.



The electron beam can be deflected and (de)focus by means of deflectors and einzel lenses. The EI source provides a soft ionization environment, which is suitable for the generation of relatively cold ions and solvated species.

The pulsed discharge source has proved to be a very stable and efficient alternative to generate cluster ions. Particularly those that cannot be formed by dissociative attachment of slow electrons. In the discharge source an electric pulse is applied few microseconds after the opening of the valve. This pulse is strong and/or long enough to generate a plasma in which bonds are broken and new species are ionized. The magnitude, length, and relative time of the pulse could be changed in order to modify the ions being generated. Some previously hard-to-form ions are easy to obtain from the discharge source. For example, carbon (i.e.  $C_n^+$ ) and carbon hydrides clusters (i.e.  $C_xH_y^+$ ) are generated by discharging rare-gas-buffered  $C_2H_2$ . In addition, clusters formed by the discharge source seem to have a lower vibrational temperature compared with the ablation source.

Anion clusters are generated in a laser ablation source equipped with an (optional) additional liquid nitrogen cooled clustering channel as shown in Figure 2-3. The laser ablation source is used when ion precursors are solid samples (i.e. semiconductors, carbon clusters). In the ablation source the second harmonic 532nm of an Nd:YAG laser (Continuum Minilite II) is focused onto the solid disk target. Two mini motors are used to rotate and translate the disk target simultaneously providing a fresh surface. The speed and direction of the mini motors can be adjusted separately to obtain the best ion quality.

The laser operates at 20 Hz and pulse energies are typically 5.0-7.5 mJ/pulse before being focused onto the target with a 50 cm lens. The resulting plasma is then entrained in a pulse of a rare gas (He or Ar) before continues to travel through a 1.75 inch long copper clustering channel. The copper channel can be cooled by gravimetrically flowing liquid nitrogen through 1/4" diameter copper tubing in thermal contact with the channel. To prevent the valve from cooling, a 1/4" thick insulator made of Delrin is located between the copper channel and the laser ablation assembly. In addition, the laser ablation assembly is heated enough to maintain it at room temperature. Thermocouples are used to ensure that the clustering channel and molecular beam valve are maintained at the appropriate temperatures. The gas pulse exits the clustering channel and passes through a skimmer into a differentially pumped region. The use of the liquid nitrogen cooled clustering channel reduces the internal energy of the ions resulting in much colder and cleaner spectra as shown in Figure 2-3.

### **III. Magnetic Bottle Electron Analyzer**

The magnetic bottle region consists of two elements: a stack of strong permanent magnets (8200 G) located below the ion beam axis, and a weak solenoid (20 G) beginning approximately 12 cm above the beam axis and continuing for 1.2 m, past the electron detector. The permanent magnets are Samarium Cobalt type (Edmund Scientific, CR30309-63) in cylindrical shapes: 1" dia. x 1/4" thick. The arrangement producing the highest electron yield appears to be when 2-3 magnets are stacked on top of one another. However, detection efficiency is also dependent on the proximity of the magnet to the interaction region. The field at the laser interaction point, 0.2-1 cm above the top magnet, is not known precisely, but is estimated to be 2000-1000 G. The major

difference between our design and the other spectrometers in the group is that we choose to place the magnets inside the vacuum region. This configuration is more flexible since allows the magnets to move closer to the interaction region (as close as 2 mm). Also the magnets could be moved away from the interaction region (up to 10 cm) in order to troubleshoot possible problems in the interaction region. The permanent magnets are mounted in a heavy duty linear motion sample holder (MDC part # 147-354). The solenoid consists of a removable plastic (Plexiglas) tube which is placed around the electron flight tube. One layer of Hypernom magnetic shielding surrounds the solenoid, to reduce unrelated magnetic fields. Coated copper magnet wire (18 gauge) is wound at 12 turns per inch for the entire length of the tube. A Kepco high current power supply (ATE 75-8) maintains an adjustable current of up to 8 A.

The magnetic field  $B$  at the center of the solenoid can be calculated by:

$$B = \mu_0 n I \quad (1)$$

where  $\mu_0$  is the magnetic permeability ( $4\pi \times 10^{-7} \text{ H m}^{-1}$ ),  $n$  is the coiling density (turns/unit length), and  $I$  is the current. Thus, a current of 4 A produces a field of 20 G. The choice of wire thickness was based on the maximum voltage of the power supply (75 V). We find, for a ~1150 m length of wire, a resistance of ~12  $\Omega$ , which produces a voltage of 48 V at 4 A, well within these limits. The heat dissipated, 192 W, is not found to be significant over the length of the solenoid, however it is enough to rise the temperature of the solenoid few degrees above room temperature. An ion/neutral detector with three 25 mm micro-channel plates (BURLE, Sturbridge, MA) is mounted at the end of the ion flight path. This detector can be used for initial ion optimization, as well as neutral detection after photodetachment. Ejected photoelectrons are then

collected at the end of the magnetic bottle by a 40mm chevron-mounted multichannel plates (BURLE, Sturbridge, MA) detector. Their arrival times are recorded by a digital oscilloscope (Tektronix TDS544). This data is transferred to a personal computer, where the time of flight spectra is converted into electron kinetic energy spectra.

#### **IV. Data Acquisition Software**

With the introduction of the magnetic bottle electron analyzer, we were obligated to modify the original source code in order to accommodate our new data acquisition requirements. First, the magnetic bottle analyzer requires “shot-to-shot” background subtraction, and possibly longer acquisition times (more than 4  $\mu$ s). Second, we could take advantage of the faster rep-rate of the new laser and push the machine to new boundaries (rather than the old 20Hz). Unfortunately the original compiler has been discontinued (Borland Pascal) and the latest available version was not longer compatible with modern operation systems (Windows ME, Windows 2000, etc.) and modern computer systems. We developed a new software package intended as a replacement of the original data acquisition software (tenure). The new software is a word by word conversion of the original software from Pascal (Borland Pascal V.7) into C++; however we took advantages of available programming tools and add it a new graphical interface illustrated in Figure 2-4. Users familiar with the old tenure code will immediately recognize the new (PES 2000) interface since it is a replica of the old graphical interface. The original data acquisition software was developed by Ricardo B. Metz, and it is described extensively in his disertaion<sup>7</sup>. The code was developed using the most recent version of Borland C++ Builder (v 6.0) programming tools and compiler, therefore we should not confront the problem of a discontinued compiler for at least 10-15 years.



The program capabilities are similar to the original tenure code and only new and/or more pronounced features will be mentioned here.

1. Interactive zoom tool. The program allows the user to zoom in and out any portion of the TOF or energy spectra even while running experiments.
2. Longer acquisition times. The code is capable of collecting scans up to 8  $\mu$ s long (8000 points/1 ns) using the Tektronix scope (TDS 544).
3. Windows Printing. The program can send a hardcopy of the data to any local or network printer. We are no longer limited to generating hardcopy using a plotter.
4. Multiple file formats. PES 2000 is backward compatible with old data files, and it can read and plot a simple ASCII file for visualization purposes.

The graphical interface for the new program is illustrated in Figure 2-4 and 2-5. Figure 2-4 demonstrates the use of the program to collect and plot a time of flight (TOF) mass spectrum, in this case  $\text{Br}^+(\text{HBr})_n$  ( $n \leq 24$ ) clusters. Figure 2-5 demonstrates the ability of the program to collect and plot electron time of flight data (i.e. AIP).

Unfortunately the entire source code for the data acquisition software is too long and complex (555000 lines) to be included in this thesis. However, if it is necessary to modify the code, it is highly recommended that a copy be made for yourself while modifying the code until it is completely bug-free. If the changes are general, update the sub-routine versions, comment thoroughly with dates of modification and place them in the archival directory and put the new version of PES in the /usr/fcf directory for general usage. If not general, keep for yourself.

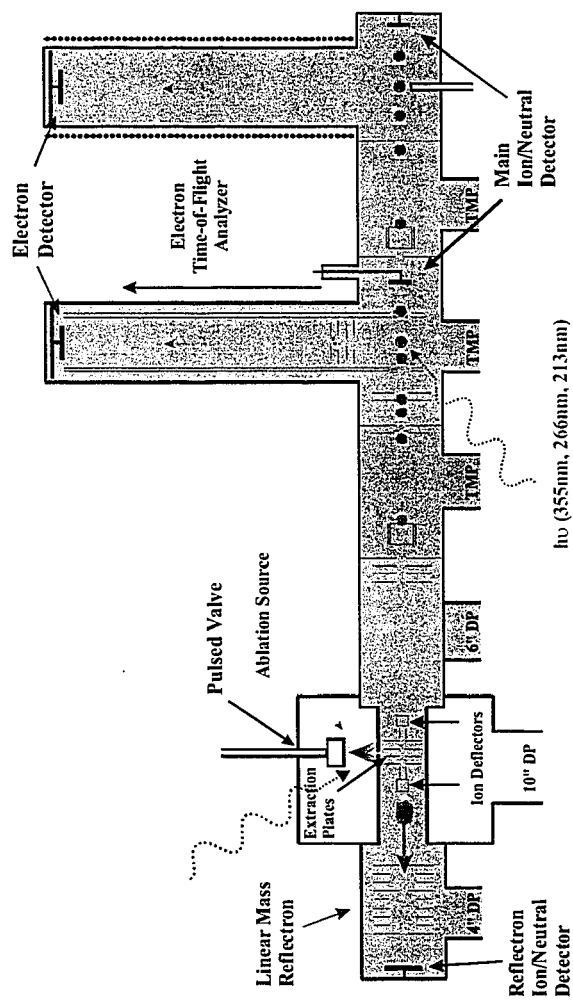


Figure 2-1. Diagram of the dual time-of-flight anion photoelectron spectrometer.

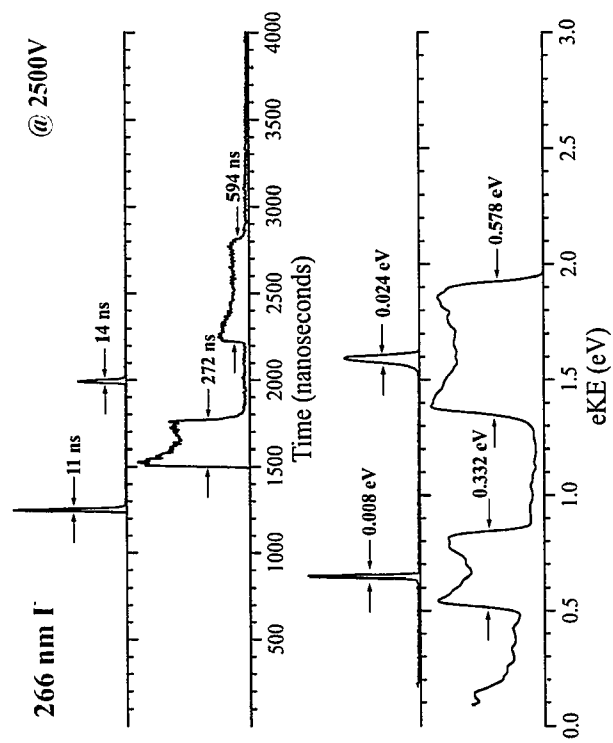
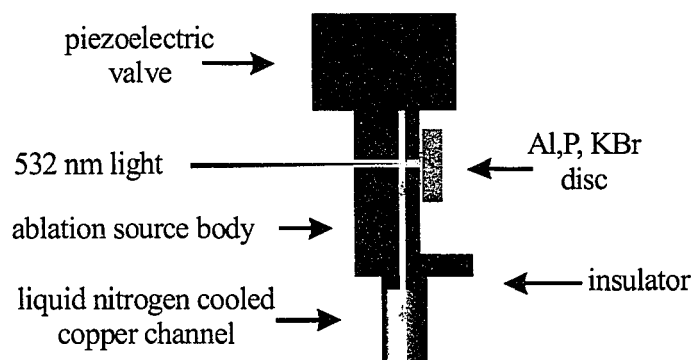


Figure 2-2. Time of Flight (top) and energy photoelectron (bottom) spectra of I<sup>-</sup> collected using 266 nm and ion beam energy of 2500V.



Comparison of spectra taken under different anion temperatures

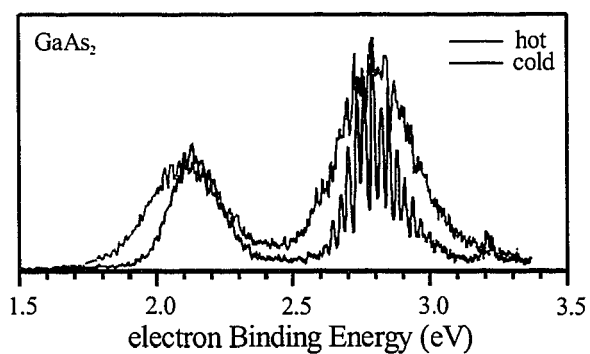


Figure 2-3. Diagram of the laser ablation disc source coupled with a liquid nitrogen cooled clustering channel.

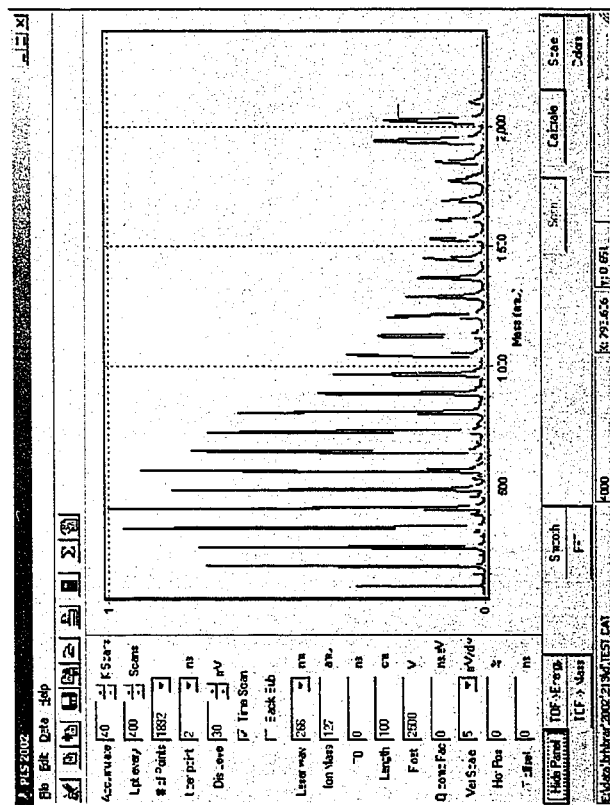


Figure 2-4. Graphical user interface (GUI) of the new data acquisition software PES 2002. Br(HBr)<sub>n</sub> (n = 0-24) clusters mass spectrum illustrates mass spectra capabilities of the program.



### ***-3- Spectroscopy of the low-lying states of the group III-V diatomics, AlP, GaP, InP, and GaAs, via anion photodetachment spectroscopy***

---

The low-lying electronic states of AlP, GaP, InP and GaAs have been probed using anion photoelectron spectroscopy and/or zero electronic kinetic energy spectroscopy. We observe transitions from the anion  $^2\Sigma^+$  and low-lying  $^2\Pi$  states to the triplet ( $^3\Sigma^-$  and  $^3\Pi$  states) and singlet ( $^1\Pi$ ,  $^1\Sigma^+$ , and  $^1\Delta$  states) manifolds of the neutral species. The spectra of the triplet manifolds are particularly complex, with overlapping spin-orbit and vibrational progressions. Spin-orbit splittings, term energies, and vibrational frequencies are reported and compared to previous electronic structure calculations on the anions and neutrals, as well as to those parameters determined previously for the isovalent homonuclear diatomics  $\text{Si}_2$ ,  $\text{Ge}_2$ , and  $\text{Sn}_2$ .

## I. Introduction

The importance III-V compounds in semiconductor devices has stimulated great interest in clusters of group III-V elements. While much of this work has focused on quantum confinement effects in very large clusters<sup>1,2</sup>, the electronic structure of the smallest molecular subunit, the diatomic, is not well characterized. In this paper we present the first systematic experimental studies mapping out the low-lying electronic states of the  $XP^+/XP$  ( $X = Al, Ga, In$ ) and  $GaAs/GaAs^-$  diatomic systems, using anion photoelectron (PE) and zero electron kinetic energy (ZEKE) spectroscopy.

Boron nitride (BN), has received the most experimental attention of all the III-V diatomics. It has been shown to have a  $^3\Pi$  ground state and the triplet states have been well studied by optical spectroscopy,<sup>3-9</sup> and photoelectron spectroscopy of  $BN^-$  yielded the relative energetics of the triplet and singlet manifolds of BN.<sup>10</sup> Photoelectron spectra of  $AlP^-$  and  $InP^-$  were reported but not analyzed by us as part of a study of larger  $Al_nP_n$  and  $In_nP_n$  clusters.<sup>11,12</sup> Lemire *et al.*<sup>13</sup> used resonant two-photon ionization spectroscopy to determine molecular constants for the spin-orbit components of the  $3^3\Pi$  excited state of GaAs, while a laser-induced fluorescence study by Ebben *et al.*<sup>14</sup> showed AlN to have a  $^3\Pi$  ground state. Li *et al.*<sup>15,16</sup> have studied several diatomic systems using matrix absorption experiments, finding vibrational fundamentals for  $GaX$  and  $InX$  ( $X=P, As, Sb$ ), and determining the spin-orbit splitting of the  $^3\Sigma^-$  ground states of  $InAs$  and  $InSb$ .<sup>15</sup> Jin *et al.* measured the first photoelectron spectrum of  $GaAs^-$  from which they were able to extract an electron affinity of  $2.1 \pm 0.1$  eV, but due to their low resolution they were unable to characterize the electronic structure of either the anion or neutral in much detail.



Numerous theoretical studies of III-V clusters and diatomics are available in the literature. GaAs<sup>17-21</sup> has been the most frequently studied of these, but electronic structure calculations on AlP<sup>22,23</sup>, GaP<sup>24,25</sup>, and InP<sup>26</sup> have been reported in recent years. These studies considered bond lengths, vibrational frequencies, and energetics of the ground and low-lying electronic states in both the anionic and neutral species, and in some cases spin-orbit splittings were calculated. Figure 3-1 shows a qualitative picture of the anion and neutral electronic state energies for the four species considered here that emerges from these studies. The anion has a  $^2\Sigma^+$  ground state and a low-lying  $^2\Pi$  excited state. The neutrals are predicted to have a triplet manifold comprised of a  $^3\Sigma^-$  ground state and  $^3\Pi$  excited state, and a higher-lying singlet manifold comprised of the  $^1\Pi$ ,  $^1\Sigma^+$ , and  $^1\Delta$  states. The calculated splittings between states in a given manifold are quite small. For example, the calculated spacing between the  $^3\Sigma^-$  and  $^3\Pi$  states and the  $^1\Pi$  and  $^1\Sigma^+$  states for AlP is 0.11 eV and 0.13 eV respectively, while the spacing between the singlet and the triplet manifold is calculated to be 0.43 eV<sup>22</sup>. This energy level diagram is similar to that previously determined for anionic and neutral Si, Ge, and Sn<sub>2</sub>, the homonuclear isovalent species<sup>27-29</sup>, although some of the state orderings are predicted to be different in the homonuclear molecules.

Negative ion photodetachment offers a unique opportunity to map out the anion and neutral electronic states of the III-V diatomics, because the neutral triplet and singlet states can be accessed from the ground and low-lying anion states. The selection rules governing photoelectron spectroscopy are more relaxed than those for optical spectroscopy, with the major restriction being that only one-electron photodetachment transitions are observed, i.e. those neutral states that result from removal of a single

electron from a negative ion molecular orbital with no additional rearrangement of the remaining electrons. As discussed in previous work on Si<sub>2</sub>, Ge<sub>2</sub>, and Sn<sub>2</sub>, not all possible neutral←anion transitions in Fig. 3-1 are one-electron allowed, most notably the  $^2\Sigma^+ \leftarrow ^3\Sigma^-$  transition between the anion and neutral ground states.<sup>27-31</sup> Nonetheless, as shown in the work presented here, negative ion photodetachment can determine the energetics, vibrational frequencies, and spin-orbit splittings for nearly all of the states shown in Fig. 3-1. As a result, in addition to obtaining a complete picture of the low-lying electronic states for each species, one also can follow trends in the diatomic electronic structure with elemental composition, in particular the transition from Hund's case (a) to case (c) coupling as one moves down the group III and group V columns of the periodic table.

## II. Experimental

The operation of the anion photoelectron (PE) and Zero Electron Kinetic Energy (ZEKE) spectrometers is similar in principle. Both experiments generate negative ions with a laser ablation/pulsed-molecular beam source, mass-select them by time-of-flight (TOF), and photodetach them with a pulsed laser. However, the electron detection schemes are very different, providing a much higher resolution (2-3 cm<sup>-1</sup>) for ZEKE than in PES (65-80 cm<sup>-1</sup>). Although the ZEKE technique has superior resolution one can only obtain photoelectron angular distributions from PES.

### A. Photoelectron spectrometer

In the anion photoelectron spectrometer,<sup>32,33</sup> cluster anions are generated in a laser ablation/pulsed molecular beam source. For AIP clusters a rotating and translating pellet made of 50–80% aluminum powder-200 mesh (Aldrich), 10-30% red phosphorus (Aldrich), and 5-20% KBr (Fisher Scientific) is ablated with the second harmonic (532

nm) of a pulsed Nd:YAG laser. For the other clusters a rotating and translating single crystal disc of GaP, InP, or GaAs (Crystallode Inc.) is ablated with the second harmonic (532 nm) of a pulsed Nd:YAG laser. The laser pulses are typically 5.0-7.5 mJ/pulse before focusing onto the target with a 50 cm lens. The resulting plasma is entrained in a supersonic beam of helium and passes through a 1 ¼ inch long liquid nitrogen cooled clustering channel described elsewhere.<sup>34</sup> The gas pulse exits the clustering channel and passes through a skimmer into a differentially pumped region. Negative ions in the beam are extracted perpendicular to their flow direction by a pulsed electric field and injected into a linear reflectron TOF mass spectrometer,<sup>35,36</sup> affording a mass resolution  $m/\Delta m$  of 2000. Due to the natural isotope abundance of gallium ( $\text{Ga}^{69}:\text{Ga}^{71}$ , 100.0:66.4) each cluster stoichiometry has a mass distribution. In each case the most intense mass peak corresponding to  $\text{Ga}^{69}\text{As}^{75}$  and  $\text{Ga}^{69}\text{P}^{31}$  was studied.

Ions of the desired mass are selectively photodetached with photons having wavelengths of 355 nm (3.493 eV), 416 nm (2.977 eV), and 498 nm (2.490 eV). The 355 nm wavelength is obtained by tripling the fundamental of a pulsed Nd:YAG laser. The first and second Stokes lines generated by passing the third harmonic (355 nm) through a high pressure Raman cell filled with hydrogen (325 psig) produce the 416 nm and 498 nm light, respectively. The electron kinetic energy ( $eKE$ ) distribution is determined by TOF analysis in a 1 m field-free flight tube. The energy resolution is 8-10 meV at 0.65 eV  $eKE$  and degrades as  $(eKE)^{3/2}$  at higher  $eKE$ . The data in electron kinetic energy is converted to electron binding energy ( $eBE$ ) by subtracting it from the photon energy. All data are plotted in  $eBE$  as described by equation (1) where  $EA$  is the adiabatic electron affinity,  $E^\circ$  is the internal energy of the neutral, and  $E^-$  is the internal energy of the anion.

$$eBE = h\nu - eKE = EA + E^o - E^- \quad (1)$$

The angular dependence of the photodetachment intensity for polarized light and randomly oriented molecules is given by equation (2) below<sup>37</sup>

$$\frac{d\sigma}{d\Omega} = \frac{\sigma_{total}}{4\pi} [1 + \beta(eKE) \cdot P_2(\cos \theta)] \quad (2)$$

where  $\theta$  is the angle between the electric vector of the photon and the direction of electron ejection,  $\sigma_{total}$  is the total photodetachment cross section and  $\beta(eKE)$  is the asymmetry parameter ( $-1 \leq \beta \leq 2$ ). Each neutral $\leftarrow$ anion photodetachment transition has a characteristic asymmetry parameter that can sometimes be used to distinguish peaks of overlapping electronic transitions. The asymmetry parameter of a peak can be calculated<sup>38</sup> using equation (3)

$$\beta(eKE) = \frac{I_{0^\circ} - I_{90^\circ}}{\frac{1}{2} I_{0^\circ} + I_{90^\circ}} \quad (3)$$

where  $I_{0^\circ}$  and  $I_{90^\circ}$  are the intensities of the peak taken at the polarization angles  $\theta = 0^\circ$  and  $90^\circ$ . The laser polarization can be rotated with respect to the direction of electron detection by using a half-wave plate.

#### B. ZEKE Spectrometer

In the ZEKE spectrometer,<sup>39,40</sup> anions are generated in a similar manner to that described above, except the ablation/molecular beam source employs a rotating and translating rod instead of a disc. The anions pass through a 2 mm skimmer, are collinearly accelerated to 1 keV, and are then separated into clusters according to their masses in a 1-meter TOF tube.

After they enter the detector region, the anion of interest is photodetached by an excimer-pumped dye laser. Once the photoelectrons are produced, a time delay between 200-350 ns is applied before they are extracted coaxially by a DC electric field of approximately 3 V/cm. During this time delay, electrons with velocity components perpendicular to the molecular beam drift out of the extraction zone. Hence, only electrons with trajectories parallel to the molecular beam or zero kinetic energy are extracted. The amount of energy they acquire during the extraction depends on their location in the extraction field, and thus their initial kinetic energies. A gated TOF detection scheme is used to selectively collect the near zero kinetic energy electrons. The resolution of this spectrometer in the absence of rotational broadening is 2-3  $\text{cm}^{-1}$ .

The electron signal is normalized to laser power and ion signal, and averaged over 1200 laser shots per point. The dyes used to obtain the ZEKE spectrum of  $\text{GaAs}^-$  were Coumarin 440, Coumarin 460, Coumarin 480, Coumarin 540, Rhodamine 590, and Rhodamine 610. The dye laser wavelength is calibrated by measuring the absorption spectra of an iodine cell or a Fe-Neon cathode lamp.

### III. Results

Anion PE spectra of  $\text{XP}^-(\text{X} = \text{Al}, \text{Ga}, \text{In})$  and  $\text{GaAs}^-$  taken at a laser polarization angle of  $\theta = \sim 57^\circ$  (the "magic angle", where  $P_2(\cos \theta) = 0$ ) are plotted in Figure 3-2. Each spectrum is composed of two data sets, indicated by a break in the plot around  $\sim 2.4$  eV. The data at lower  $eBE$  (left side) was taken at a wavelength of 498 nm for all the diatomics, while the data at higher  $eBE$  (right side) was collected at a wavelength of 416 nm for  $\text{InP}^-$  and 355nm for the other diatomics. The two groups of peaks correspond to

transitions to the triplet (left side) and singlet (right side) manifolds of neutral XP ( $X = \text{Al, Ga, In}$ ) and GaAs as discussed in the introduction and shown in Figure 3-1.

Inspection of the PE spectra in Figure 3-2 shows that the triplet manifolds for the XP series shift toward lower  $eBE$  as the size of  $X$  increases from Al to In, while the singlet manifolds remain around the same energy. In addition, the triplet manifolds for all four molecules are significantly more congested than the singlet manifolds. The singlet manifolds show two groups of peaks for all species except for AlP, where only three peaks are observed with similar spacing. The triplet manifolds show a fairly complex evolution as the atoms become heavier. In the AlP spectrum, several peaks are evidently partially resolved triplets; this pattern is not evident in the other PE spectra but more peaks appear in total, suggesting that the triplet components are more spread out and appear as individual peaks.

Figures 3-3 and 3-4 show expanded views of the triplet manifolds of XP ( $X = \text{Al, Ga, In}$ ) and GaAs taken at polarization angles of  $\theta = 0^\circ$  (top) and  $\theta = 90^\circ$  (center), and a wavelength of 498 nm. The bottom panels show simulations which are discussed in Section IV. The GaAs PE spectrum taken at  $\theta = 90^\circ$  is superimposed on the ZEKE spectrum. The peaks in the ZEKE spectrum are much narrower than in the PE spectra and every peak in the PE spectrum also appears in the ZEKE spectrum with similar intensity except for peaks  $A_1$  and  $A'$ . Comparison of the  $\theta = 0^\circ$  and  $\theta = 90^\circ$  PE spectra and inspection of the anisotropy parameters  $\beta$  for each peak (top panel) shows a considerable variation in the photoelectron angular distribution among the peaks. Most notably, the single feature  $A$ ,  $A_0$  or  $A_1$  dominates the  $\theta = 0^\circ$  PE spectra for all four species but is much less prominent, if visible at all, in the  $\theta = 90^\circ$  spectra. Moreover,

anisotropy parameters for peaks at lower and higher  $eBE$  than peak A are different.

Hence, it appears that the triplet manifolds are composed of three distinct neutral $\leftarrow$ anion electronic photodetachment transitions.

Figures 3-5 and 3-6 show expanded views of the singlet manifolds of XP (X = Al, Ga, In) and GaAs taken at polarization angles of  $\theta = 0^\circ$  (top) and  $\theta = 90^\circ$  (center), with simulations shown in the bottom panels. The photodetachment wavelength is 416 nm for InP and 355 nm for the other diatomics. The GaAs PE spectrum is superimposed on the ZEKE spectrum. Again, anisotropy parameters for each peak are shown in the top panel. There appear to be two distinct major progressions, labeled A and B, in each spectrum, with the peaks in progression B more intense at  $\theta = 0^\circ$  and the peaks in progression A more intense at  $\theta = 90^\circ$ . Hence, at least two electronic photodetachment transitions contribute to each singlet manifold. The GaP spectrum shows two additional bands, C and D, at higher and lower  $eBE$ , respectively, than the two intense progressions. There is some evidence for additional, low intensity, high and low energy features in the spectra of the other diatomics, but no individual peaks can be resolved.

## IV. Analysis

### A. General

Figure 3-1 is extremely useful for making a detailed assignment of the PE and ZEKE spectra. All of the III-V diatomics are calculated to have the same energy ordering of electronic states shown in Figure 3-1<sup>17-20,22-25,41-44</sup>, except for InP where the  $^1\Sigma$  and  $^1\Delta$  reverse their order<sup>26</sup>. For each energy level, the case (a) term symbol and highest molecular orbital occupancy is shown on the right, and the projection  $\Omega$  of the total angular momentum on the internuclear axis is shown on the left. All one-electron

allowed transitions from both low-lying anion states are shown in Figure 3-1. Based on our previous work on the silicon and germanium dimers, we expect to observe a transition from Hund's case (a) to case (c) coupling as the atoms become heavier, leading, for example, to an observable splitting of the  $^3\Pi_0$  state into its  $^3\Pi_{0+}$  and  $^3\Pi_{0-}$  components. Figure 1-1 shows the one-electron photodetachment transitions from the anion ground  $^2\Sigma^+(\dots\sigma^1\pi^4)$  and low-lying  $^2\Pi(\dots\sigma^2\pi^3)$  states. All neutral states are accessible from the anion ground state except those with the  $(\dots3\sigma^21\pi^2)$  electronic configuration; neutral states with this configuration include the ground  $^3\Sigma^-$  and excited  $^1\Delta$  states. From the anion  $^2\Pi$  state, only the transition to the  $^1\Sigma^+(\dots3\sigma^01\pi^4)$  state is forbidden by the one-electron selection rule.

More quantitative assignments and analyses were carried out by simulating vibrational and electronic structure seen in the PE and ZEKE spectra. Electronic term energies were varied to best match the experimental spectra. Within each electronic band, intensities of individual vibrational transitions are assumed proportional to their Franck-Condon factors (FCF's),  $|\langle v' | v'' \rangle|^2$ , where  $|v'\rangle$  and  $|v''\rangle$  are neutral and anion harmonic oscillator wavefunctions, respectively. The vibrational frequencies are taken directly from the spectra, and the change in bond length upon photodetachment is varied to reproduce the length of the vibrational progression in the experimental spectrum. The anion vibrational temperature was also varied in order to reproduce hot bands in the spectrum originating from vibrationally excited anions. The resulting stick spectrum was then convoluted with a Gaussian function of width comparable to our experimental resolution, usually 8-15 meV.



We begin our analysis by considering the singlet manifolds for all four species. These are considerably easier to analyze than the triplet manifolds and provide information that facilitates analysis of the more complex triplet manifolds.

## B. Singlet Manifolds

### a. AIP

The anisotropy parameters for the AIP singlet manifold suggest that peaks a and A are from one electronic photodetachment band ("A"), and peaks B, B', and B'' are from another ("B"). Peaks a and A are separated by 516 cm<sup>-1</sup>, peaks A and B are separated by 475 cm<sup>-1</sup> and peaks B, B' and B'' are separated by 540 cm<sup>-1</sup>. The low intensity of peak a suggests it is a hot band electronic transition with origin at A, while the equal spacing of peaks B, B', and B'' suggests a vibrational progression with B as the origin.

With reference to Figure 1-1, the neutral <sup>1</sup>Π and <sup>1</sup>Σ<sup>+</sup> states are accessible via one-electron transitions from the anion <sup>2</sup>Σ<sup>+</sup> state, whereas the neutral <sup>1</sup>Π and <sup>1</sup>Δ states are accessible from the anion <sup>2</sup>Π state. The observation of only two strong bands in the singlet manifold of the AIP<sup>+</sup> PE spectrum thus suggests that both originate from a single anion state.

Electronic structure calculations<sup>22</sup> on AIP<sup>+</sup> predict a <sup>2</sup>Σ<sup>+</sup> ground state with a vibrational frequency of 551 cm<sup>-1</sup>, and a <sup>2</sup>Π excited state with a term value of 0.08 eV and a vibrational frequency of 465 cm<sup>-1</sup>. The only calculation on the excited singlet states of AIP was done by Meier *et al.*<sup>23</sup> who found the <sup>1</sup>Π, <sup>1</sup>Σ<sup>+</sup>, <sup>1</sup>Δ states to have term energies of 0.46 eV, 0.56, and 0.83 eV, and vibrational frequencies of 487, 528, and 374 cm<sup>-1</sup> respectively. The anion and neutral calculations are summarized in Table 1-1. If both calculations are correct, then both bands originate from the anion <sup>2</sup>Σ<sup>+</sup> state, since

this state should be the most populated in the ion beam, and bands “A” and “B” would be assigned to the  ${}^1\Pi \leftarrow {}^2\Sigma^+$  and  ${}^1\Sigma^+ \leftarrow {}^2\Sigma^+$  photodetachment transitions, respectively. The observed vibrational spacing of band “B”,  $540\text{ cm}^{-1}$ , is very close to the calculated frequency for the  ${}^1\Sigma^+$  state,  $528\text{ cm}^{-1}$ , consistent with this assignment. This assignment also yields a splitting of  $0.058\text{ eV}$  between the neutral  ${}^1\Pi$  and  ${}^1\Sigma^+$  states, only slightly smaller than the calculated splitting of  $0.10\text{ eV}$ .

If, on the other hand, both bands originated from the anion  ${}^2\Pi$  state, then bands “A” and “B” would be transitions to the neutral  ${}^1\Pi$  and  ${}^1\Delta$  states, respectively. This alternate assignment is in more conflict with theory; the  ${}^1\Pi - {}^1\Delta$  splitting would be much smaller than the calculated splitting of  $0.37\text{ eV}$ , and the vibrational frequency of the  ${}^1\Delta$  state ( $540\text{ cm}^{-1}$ ) would be much larger than the calculated value of  $374\text{ cm}^{-1}$ . For these reasons, the first assignment is preferred, indicating the anion has a  ${}^2\Sigma^+$  ground state with vibrational frequency  $516\text{ cm}^{-1}$  (the spacing between peaks a and A).

#### **b. GaP**

The  $\beta$  parameters plotted in the top panel of 3-5 show that the peaks can be divided into four bands. The two most intense progressions consist of peaks A, A, & A'' and b, B, & B'. The three “A” peaks are spaced by  $400\text{ cm}^{-1}$ , peaks B and B' are spaced by  $435\text{ cm}^{-1}$ , while b and B are spaced by  $445\text{ cm}^{-1}$ . The spacings and intensities of the peaks indicate that A and B are the vibrational origins of two electronic bands, while b is a vibrational hot band.

The photoelectron angular distributions are similar to those for the AlP singlet manifold, in that the relative intensity of the “A” progression is higher at  $\theta=90^\circ$  than at  $\theta=0^\circ$  (even more so for GaP), suggesting the same assignment in which the “A” and “B”

bands correspond to the  $^1\Pi \leftarrow ^2\Sigma^+$  and  $^1\Sigma^+ \leftarrow ^2\Sigma^+$  photodetachment transitions, respectively. This assignment is consistent with electronic structure calculations, the results of which are summarized in Table 1-2. Archibong<sup>24</sup> finds that GaP<sup>-</sup> has a  $^2\Sigma^+$  ground state with a vibrational frequency of 445 cm<sup>-1</sup>, and a  $^2\Pi$  excited state with a term value of 0.064 eV and a vibrational frequency of 371 cm<sup>-1</sup>; the hot band frequency we observe, 445 cm<sup>-1</sup>, is clearly in better agreement with the  $^2\Sigma^+$  state. In addition, the experimental vibrational frequencies of 402 and 433 cm<sup>-1</sup> for the  $^1\Pi$  and  $^1\Sigma^+$  states, respectively, implied by our assignment are in good agreement with the calculated frequencies,<sup>25</sup> 387 and 439 cm<sup>-1</sup>. The  $^1\Sigma^+ - ^1\Pi$  resulting splitting of 0.133 eV is, however, somewhat larger than the calculated splitting, 0.049 eV.<sup>25</sup>

There are two additional weak bands in the GaP singlet manifold. Peaks C, C', and C'' are spaced by 285 cm<sup>-1</sup>. The only electronic state calculated to have a similar frequency is the  $^1\Delta$  state (278 cm<sup>-1</sup>)<sup>25</sup>. This state is also one-electron accessible from the  $^2\Pi$  excited anion state and we assign peaks C, C', and C'' to the  $^1\Delta \leftarrow ^2\Pi$  transition. Peaks D and D' must then be due to the  $^1\Pi \leftarrow ^2\Pi$  transition, the only remaining one-electron transition that can contribute to the singlet manifold. The spacing between these peaks, 400 cm<sup>-1</sup>, matches the vibrational frequency of the  $^1\Pi$  state, but it is also close to the calculated frequency of the anion  $^2\Pi$  state, 371 cm<sup>-1</sup>. Thus, it is not obvious if peaks D and D' represent a vibrational progression in the neutral  $^1\Pi$  state or the anion  $^2\Pi$  state. This point is discussed further in the context of the GaP triplet manifold.

### c. InP and GaAs

The InP and GaAs singlet manifolds in Figure 3-6 each show two vibrational progressions with photoelectron angular distributions similar to those seen in the AlP and

GaP singlet manifolds, so we assign bands “A” and “B” to the  $^1\Pi \leftarrow ^2\Sigma^+$  and  $^1\Sigma^+ \leftarrow ^2\Sigma^+$  photodetachment transitions, respectively. In the InP<sup>-</sup> spectrum, peaks A and A’ are spaced by 319 cm<sup>-1</sup>, while peaks B, B’, and B’’ are spaced by 350 cm<sup>-1</sup>; these correspond to the vibrational frequencies of the  $^1\Pi$  and  $^1\Sigma^+$  states, respectively, and the splitting between the two singlet states is 0.131 eV. These values can be compared to the calculation by Manna *et al.*<sup>26</sup> summarized in Table 1-3. Note that Manna predicts the  $^1\Delta$  state to lie between the  $^1\Pi$  and  $^1\Sigma^+$  states; we cannot verify this since no transitions to the  $^1\Delta$  state are seen in our spectrum. Another feature of interest in the InP singlet manifold is that in the 0° spectrum, there are two partially resolved peaks (peaks C and C’, Figure 3-6), each lying at 9 meV lower *eBE* than peaks A and A’. We believe these are  $^1\Pi \leftarrow ^2\Pi_{3/2}$  transitions, which would place the anion  $^2\Pi_{3/2}$  state 9 meV above the  $^2\Sigma^+$  ground state. This point is discussed further in our analysis of the InP triplet manifold.

The ZEKE spectrum of GaAs<sup>-</sup> shows that peaks A, A’, and A’’ form a progression with a frequency of  $287.0 \pm 0.5$  cm<sup>-1</sup> and peak a is a hot band transition, giving an anion frequency of  $298.0 \pm 0.5$  cm<sup>-1</sup>. Peaks B, B’, and B’’ form another progression with a frequency of  $292.5 \pm 0.5$  cm<sup>-1</sup>, where peak b is a hot band transition with the same anion frequency of 298.0 cm<sup>-1</sup>. The two bands thus originate from the same anion state, as expected. Based on our assignment, the vibrational frequency of the anion  $^2\Sigma^+$  state is 298.0 cm<sup>-1</sup>, and the neutral  $^1\Pi$  and  $^1\Sigma^+$  are states split by  $0.114 \pm 0.001$  eV. We see no significant contributions of transitions from excited anion electronic states.

Our results can be compared to theory with reference to Table 1-4. Balasubramanian’s<sup>42</sup> calculation of 303 cm<sup>-1</sup> for the  $^2\Sigma^+$  ground state frequency is in closer agreement with our measurement than Meier’s value<sup>17</sup> of 248 cm<sup>-1</sup> (MRDCI).

Manna *et al.*<sup>20</sup> have the closest calculated  ${}^1\Pi - {}^1\Sigma^+$  energy separation, 0.082 eV. All other calculations over-estimate this splitting by a factor of two.<sup>17-19</sup>

### C. Triplet Manifolds

As noted in Section III, the photoelectron angular distributions for all the triplet manifolds indicated that each was composed of three distinct electronic photodetachment transitions. Figure 3-1 shows that there are three one-electron transitions from the anion  ${}^2\Sigma^+$  and  ${}^2\Pi$  states to the neutral triplet states: the  ${}^3\Pi \leftarrow {}^2\Sigma^+$ ,  ${}^3\Pi \leftarrow {}^2\Pi$ , and  ${}^3\Sigma^+ \leftarrow {}^2\Pi$  transitions. Our analysis of the singlet manifolds indicates that all four diatomics have  ${}^2\Sigma^+$  anion ground states, so if the energy ordering in Fig. 3-1 is correct, then the  ${}^3\Pi \leftarrow {}^2\Sigma^+$  band will occur at the highest *eBE*, and the  ${}^3\Sigma^+ \leftarrow {}^2\Pi$  at the lowest. These considerations are a reasonable starting point for our analysis of the triplet manifolds. The anion vibrational frequencies determined through observation of hot bands in the singlet manifolds are also useful in analyzing the triplet manifolds.

#### a. AIP

The triplet manifolds of the AIP<sup>+</sup> PE spectra taken at 498 nm and polarization angles of  $\theta = 90^\circ$  and  $\theta = 0^\circ$  are shown in Figure 3-3. From the  $\beta$ -parameters in the top panel we identify three distinct bands, “A”, “B”, and “C”. In band “A”, peaks A and A’ are separated by  $\sim 460\text{ cm}^{-1}$ . The peaks that make up band “B”, peaks b, B, B’, and B”, all appear as partially resolved triplets with an average separation of 9-10 meV. The spacing between peaks b and B is around  $515\text{ cm}^{-1}$ , while the spacing between peaks B, B’, and B” is around  $460\text{ cm}^{-1}$ . Peaks c, C and C’ are very weak, the spacing between c and C is  $\sim 470\text{ cm}^{-1}$  while the peaks C, and C’ are separated by  $\sim 380\text{ cm}^{-1}$ .

The general considerations outlined above suggest that band “B” be assigned to the  $^3\Pi \leftarrow ^2\Sigma^+$  transition, band “A” to the  $^3\Pi \leftarrow ^2\Pi$  transition, and band “C” to the  $^3\Sigma^- \leftarrow ^2\Pi$  transition. Although no clear evidence for transitions from the  $^2\Pi$  state in AIP<sup>+</sup> was seen in the singlet manifold, this state is predicted to lie only 0.08 eV above the  $^2\Sigma^+$  ground state,<sup>22</sup> so some population of this state in the laser ablation source is expected.

According to this assignment, band “A” results from detachment from a  $\sigma$  molecular orbital, whereas bands “B” and “C” result from detachment from the same  $\pi$  orbital. The observation that the anisotropy parameters of bands “B” and “C” are similar but very different from that for band “A” is qualitatively consistent with our assignment of the three bands. We note the triplet manifolds of the PE spectra of Si<sub>2</sub><sup>+</sup> and Ge<sub>2</sub><sup>+</sup> showed three photodetachment transitions with similar polarization dependences as bands “A”-“C” and analogous assignments were made.<sup>28-30</sup>

There are several more stringent tests of this assignment. Taking peak b as a hot band yields an anion vibrational frequency of  $\sim 515\text{ cm}^{-1}$ , essentially identical with the anion  $^2\Sigma^+$  frequency determined from the AIP singlet manifold. Assuming peak c is a vibrational hot band, then band “C” originates from an anionic electronic state with frequency 460-470  $\text{cm}^{-1}$ , in good agreement with the calculated anion frequency of 465  $\text{cm}^{-1}$  for the anion  $^2\Pi$  state.<sup>22</sup> The anion frequencies are thus support the proposed assignment for two of the three bands.

The partially resolved triplet structure of band “B” is consistent with a  $^3\Pi \leftarrow ^2\Sigma^+$  transition, with the triplets corresponding to transitions to the  $\Omega=2,1$ , and 0 fine structure components of the neutral  $^3\Pi$  state. Although no calculations of this fine structure have been reported, the 9-10 meV splitting we observe is comparable to the 7-8 meV splitting

in the analogous  $^3\Pi_u$  state of  $\text{Si}_2$ .<sup>28</sup> The spacing between peaks B, B', and B'' of 460  $\text{cm}^{-1}$  is close to the calculated vibrational frequency of 449  $\text{cm}^{-1}$  for the AIP  $^3\Pi$  state.<sup>23</sup>

In band "A", the spacing between peaks A and A' is also 460  $\text{cm}^{-1}$ , consistent with its assignment as a transition to the  $^3\Pi$  state in AIP. However, if these peaks are from the  $^3\Pi \leftarrow ^2\Pi$  transition, one can have as many as six fine structure contributions to each peak, namely transitions to the  $^3\Pi_2$ ,  $^3\Pi_1$ , and  $^3\Pi_0$  states from each of the (presumably) closely spaced anion  $^2\Pi_{3/2}$  and  $^2\Pi_{1/2}$  fine structure states. If all six transitions were active, one might not expect to resolve them because of differing fine structure splittings in the anion and neutral, but one would expect the peaks A and A' to be at least as broad as the peaks in band "B". This, however, is not the case. A possible explanation is that the neutral fine structure states are not accessed with equal intensity when the  $\sigma$  electron of the anion  $^2\Pi$  state is detached. In fact, the photoelectron spectra of  $\text{Ge}_2^-$  and  $\text{Sn}_2^-$  show a strong  $\Delta\Omega = \pm 1/2$  propensity rule for  $^3\Pi \leftarrow ^2\Pi$  transitions.<sup>27,29,31</sup> If this rule holds for AIP, then photodetachment from the anion  $^2\Pi_{3/2}$  state would yield the neutral  $^3\Pi_2$  and  $^3\Pi_1$  states, while the  $^2\Pi_{1/2}$  state would yield the  $^3\Pi_1$  and  $^3\Pi_0$  states. So long as the anion and neutral fine structure splitting are similar, one would expect four overlapped transitions covering a narrower energy range than the triplets in band "B", consistent with our observations.

Peaks c, C, and C' are assigned to the  $^3\Sigma^- \leftarrow ^2\Pi$  band. As mentioned above, the c-C spacing is consistent with this assignment, as is the C-C' spacing of 379  $\text{cm}^{-1}$ , which is close to the calculated frequency of 359  $\text{cm}^{-1}$  for the neutral  $^3\Sigma^-$  state.<sup>23</sup> Figures 3-3 and 3-5 (bottom) shows the simulation of both the triplet and singlet manifolds of the AIP photoelectron spectrum. The parameters used in this simulation are listed in Table 3-1,

where they can be readily compared to previously determined theoretical values. Since the PE spectra are sensitive only to changes in the bond length upon photodetachment, the calculated anion bond lengths for the two anion states were assumed to be correct, and the neutral bond lengths were varied to reproduce the experimental spectrum.

In the singlet manifold, the vibrational frequency of the  $^1\Pi$  state is taken to be the same as the spacing between peaks A and B in Figure 3-5, so that peak B has a contribution from the transition to the  $^1\Pi$  ( $v=1$ ) level. In the triplet manifold, only a small change in bond length upon photodetachment is needed to reproduce the short vibrational progression associated with band “A”, whereas more substantial changes are needed to reproduce the longer progressions associated with bands “B” and “C”. These trends are consistent with the calculated bond lengths, further supporting our assignment of the photodetachment transitions. In addition, we find good agreement between experimental and theoretical term values for both the anion and neutral states. Finally, although we do not directly observe the  $^3\Sigma^- - ^2\Sigma^+$  photodetachment transition, the adiabatic electron affinity of AIP, which corresponds to the energy difference between the  $v = 0$  levels of these two states, can be extracted our data using the assignments in Table 3-1 via

$$EA = eBE(C) + (eBE(B) - eBE(A)), \quad (3)$$

where A, B, and C are the vibrational origins of the three bands, with B taken to be the energy of the transition to the  $^3\Pi_2$  fine structure component. Eq. 3 yields  $EA(\text{AIP}) = 2.043 \pm 0.020$  eV, close to the theoretical value<sup>22</sup> of 1.90 eV.



#### b. GaP

The triplet manifolds of the GaP<sup>+</sup> PE spectra at  $\theta = 0^\circ$  and  $90^\circ$  in Figure 3-3 share many similarities with the AlP<sup>+</sup> triplet manifolds and a similar assignment should apply. However, the spin-orbit splittings in the  $^3\Pi$  and  $^2\Pi$  states of GaP and GaP<sup>+</sup> should be larger than in the corresponding AlP states. With this in mind, peaks B<sub>1,2,3</sub> and B'<sub>1,2</sub> are assigned to the  $^3\Pi - ^2\Sigma^+$  transition, peaks a, A and A' to the  $^3\Pi \leftarrow ^2\Pi$  transition, and peaks c'-C' to the  $^3\Sigma^- \leftarrow ^2\Pi$  transition. We now examine each of these assignments in more detail.

The five peaks B<sub>1</sub>-B'<sub>2</sub> are approximately equally spaced by 16-18 meV, or 130-145 cm<sup>-1</sup>. This splitting is considerably less than the calculated vibrational frequencies for any GaP<sup>+</sup> or GaP states (see Table 3-2), and is more reasonably assigned to the spin-orbit splitting in the neutral  $^3\Pi$  state. We therefore expect each  $^3\Pi(v') \rightarrow ^2\Sigma^+(v'')$  transition to yield a triplet of peaks with this characteristic spacing. The observed spin-orbit splitting of ~17 meV is about twice the value calculated by Manna.<sup>25</sup> The most straightforward assignment of these peaks is to take B<sub>1</sub> as the  $^3\Pi_2(v'=0) \rightarrow ^2\Sigma^+(v''=0)$  transition, B<sub>2</sub> and B<sub>3</sub> as the transitions to the  $^3\Pi_1$  and  $^3\Pi_0(v'=0)$  levels, respectively, and B'<sub>1</sub> as the  $^3\Pi_2(v'=1) \rightarrow ^2\Sigma^+(v''=0)$  transition. This assignment yields a vibrational frequency of 415 cm<sup>-1</sup> for the  $^3\Pi$ , which disagrees with the calculated vibrational frequency<sup>24,25</sup> of 358 cm<sup>-1</sup>.

Peaks c, C and C' at low *eBE* consist of partially resolved doublets split by 12-14 meV. The doublet splitting could represent the spin-orbit splitting in the  $^2\Pi$  state into its  $^2\Pi_{3/2}$  and  $^2\Pi_{1/2}$  components. Peaks c', c and C are separated by approximately 370 cm<sup>-1</sup>. This spacing agrees with the calculated frequency for the  $^2\Pi$  anion state, suggesting these

three peaks are ( $v'=0 \leftarrow v''=n$ ) hot band transitions originating from the  $^2\Pi_{3/2,1/2}$  states. Peaks C and C' are separated by  $\sim 400 \text{ cm}^{-1}$ , close to the vibrational frequency of the  $^3\Pi$  state given above. While this might suggest that peak C is the origin of the  $^3\Pi \leftarrow ^2\Pi_{3/2,1/2}$  band, this assignment is inconsistent with the electronic state ordering and the number of peaks observed. Instead, we assign peak C as the origin of the  $^3\Sigma \leftarrow ^2\Pi_{3/2,1/2}$  band. Simulation of peaks c', c, C and C' yields a spin-orbit splitting of  $0.014 \pm 0.05 \text{ meV}$  for the  $^2\Pi$  state. For the simulation we used the neutral experimental frequency determined by Li *et al.* of  $286 \text{ cm}^{-1}$ .<sup>16</sup>

Peaks a and A are separated by  $386 \text{ cm}^{-1}$ , while peaks A and A' are separated by  $\sim 405 \text{ cm}^{-1}$ . The relative intensities of these peaks suggest that peak A is the origin of the electronic transition, a is a hot band of the same electronic transition. The a-A splitting is close to the calculated vibrational frequency of the anion  $^2\Pi$  state,  $371 \text{ cm}^{-1}$ , and the A-A' splitting is similar to the frequency obtained from the series of peaks "B" ( $415 \text{ cm}^{-1}$ ). These observations support our assignment of peaks a, A, and A' to the  $^3\Pi \leftarrow ^2\Pi$  transition. The finer structure of peak A ( $A_0$  and  $A_1$  center panel) depends on the individual spin-orbit splittings of the  $^2\Pi$  and  $^3\Pi$  states. From the "B" series of peaks we have determined the splitting in the  $^3\Pi$  state to be 17-18 meV, and from the "C" series of peaks it appears the splitting in the  $^2\Pi$  state is 14 meV. If we assumed GaP will exhibit the same behavior of  $\text{Ge}_2^-$  and  $\text{Sn}_2^-$  showing a strong  $\Delta\Omega=\pm 1/2$  propensity, we should expect four transitions in a range of energy of about 21 meV. Simulation of these four states convoluted with our experimental resolution results in two peaks separated by approximately 17-18 meV, close to the  $A_0 - A_1$  of  $\sim 15 \text{ meV}$ .

Simulations of the GaP singlet and triplet manifold are shown in Figures 3-3 and 3-5, and the parameters used in these simulations are given in Table 3-2. The best simultaneous fit of the two manifolds leads to an assignment of peak D' in the singlet spectrum to the origin of the  $^1\Pi \leftarrow ^2\Pi$  band. The triplet spectrum is the hardest to fit of all those reported in this paper; the contribution from hot bands is larger, and the peak spacing due to vibrational progressions and spin-orbit interactions are comparable. The discrepancy between the experimental and calculated  $^3\Pi$  vibrational frequencies,  $415\text{ cm}^{-1}$  vs.  $358\text{ cm}^{-1}$ , is somewhat troubling, but the experimental value is needed to fit bands "A" and "B". In any case, this is the best fitting of the singlet and triplet manifolds that we have been able to construct. We can determine the electron affinity of GaP in a similar manner to AlP, finding a value of  $1.988 \pm 0.020\text{ eV}$ .

### c. InP

Anion photoelectron spectra of the triplet manifold of InP taken at 416 nm and a polarization angle of  $\theta = 0^\circ$  (top) and  $\theta = 90^\circ$  are shown in . The  $\theta = 0^\circ$  spectrum is dominated by peak A<sub>1</sub>; the intensity of this peak drops off considerably at  $90^\circ$ , where it is one component of a partially resolved doublet with the other component labeled B<sub>1</sub>. Peaks B<sub>1</sub>-B<sub>4</sub> and several peaks at higher eBE are the most prominent features at  $90^\circ$ . In addition there is a progression c-C'' at  $90^\circ$  that is absent at  $0^\circ$ .

Following our analysis of AlP and GaP, we assign peaks A<sub>0</sub>, a, A<sub>1</sub>, and A' to the  $^3\Pi - ^2\Pi$  transition, peaks B<sub>1</sub>-B<sub>4</sub> and higher to the  $^3\Pi - ^2\Sigma^+$  transition, and c-C'' to the  $^3\Sigma^- - ^2\Pi$  transition. However, several features of interest appear in the InP triplet manifold that were not seen for the lighter molecules. The spacings between peaks B<sub>1</sub>-B<sub>4</sub> are 34, 23, and 14 meV. This uneven spacing is in contrast to the equally spaced triplets

in AlP and GaP that were assigned to the  ${}^2\Pi_{2,1,0}$  spin-orbit multiplet. The InP pattern reflects the expected for Hund's case (c) coupling, in which the splitting of the  ${}^3\Pi_0$  component to  ${}^3\Pi_{0+}$  and  ${}^3\Pi_{0-}$  states becomes significant, suggesting that peaks B<sub>1</sub>-B<sub>4</sub> be assigned to transitions to the  ${}^3\Pi_2$ ,  ${}^3\Pi_1$ ,  ${}^3\Pi_{0+}$ , and  ${}^3\Pi_{0-}$  states. Manna *et al.*<sup>26</sup> have calculated the splittings between these states to be 34, 23, and 4 meV, in reasonable agreement with our values.

Peaks A<sub>1</sub> and B<sub>1</sub> form a doublet separated by 9 meV in the  $\theta=90^\circ$  spectrum. This is the same splitting in several doublets of the InP singlet manifold (Figure 3-6). Our assignment of these doublets to transitions originating from the nearly degenerate anion  ${}^2\Pi_{3/2}$  and  ${}^2\Sigma^+$  states is consistent with assigning peak A<sub>1</sub> to the  ${}^3\Pi_2(\nu=0) \leftarrow {}^2\Pi_{3/2}(\nu=0)$  transition. Peak A' appears to comprise more than one transition; likely candidates are the  ${}^3\Pi_1(\nu=0) \leftarrow {}^2\Pi_{3/2}(\nu=0)$  and  ${}^3\Pi_2(\nu=1) \leftarrow {}^2\Pi_{3/2}(\nu=0)$  transitions. Based on our spin-orbit splittings determined above, and the calculated frequency of 290 cm<sup>-1</sup> for the  ${}^3\Pi$  state,<sup>26</sup> these transitions should occur at 34 and 36 meV, respectively, higher *eBE* than peak A<sub>1</sub>. Peak a may be a vibrational hot band of peak A, yielding a vibrational frequency of 245 cm<sup>-1</sup> for the  ${}^2\Pi_{3/2}$  state. Finally, peak A<sub>0</sub>, which lies at 0.042 eV lower *eBE* than peak A<sub>1</sub>, could originate from the anion  ${}^2\Pi_{1/2}$  state, and would correspond to the  ${}^3\Pi_1 \leftarrow {}^2\Pi_{1/2}$  vibrational origin if the anion  ${}^2\Pi_{1/2}$ - ${}^2\Pi_{3/2}$  splitting were 78 meV.

The spacing of peaks c and C is around ~330 cm<sup>-1</sup>, while that for peaks C, C' and C'' is around ~260 cm<sup>-1</sup>, matching the experimental neutral ground state frequency of 258 cm<sup>-1</sup>.<sup>15</sup> We thus assign peak C to the origin of the  ${}^3\Sigma \leftarrow {}^2\Pi_{3/2}$  transition. Using our

assignment we can determine the electron affinity of InP in a similar manner to GaP and AlP, finding a value of  $1.845 \pm 0.020$  eV.

In the absence of any prior experimental or theoretical information on InP<sup>-</sup>, we performed electronic calculations on the anion and few states on the neutral. Geometries and frequencies were obtained using B3LYP (Becke-3-parameter-Lee-Yang-Parr)<sup>45,46</sup> exchange correlation functional and quadratic configuration interaction with double and triple excitation (QCISD(T)), using the LANL2DZ (Los Alamos ECP)<sup>47</sup> basis set in both calculations. Calculations were performed using Gaussian98<sup>48</sup> electronic structure package, and the results are summarized in Table 3-3. The calculated anion frequencies are very close to that determined from the weak hot band c in the PE spectrum.

Based on the above considerations, a full simulation of the singlet and triplet manifolds is shown in Figures 3-4 and 3-6 using the parameters in Table 3-3. The FC simulation was performed assuming Manna's calculated bond lengths for the neutral  $X^3\Sigma^-$  and  $A^3\Pi_2$  states are correct.<sup>26</sup> From those we determine the anion and singlet bond lengths given in Table 3-3. The simulation reproduces nearly all the features in the experimental spectra in both manifolds, and shows, for example, that the peaks to high *eBE* of peaks B<sub>1</sub>-B<sub>4</sub> are transitions to vibrationally excited levels of the neutral  $^3\Pi$  state.

#### d. GaAs

The GaAs triplet manifold (Figure 3-4) is generally similar to the InP triplet manifold and analogous assignments should hold. The ZEKE spectrum, which resembles the 90° spectrum much more than the 0° spectrum, supports our overall assignment scheme in the following sense. Peaks A<sub>0</sub>, A<sub>1</sub>, and A', which should correspond to  $^3\Pi \leftarrow ^2\Pi$  transitions, disappear in both the ZEKE spectrum and the PE spectrum at 90°.

In the isovalent homonuclear molecular  $\text{Si}_2$ , these transitions would involve detachment from a  $\sigma_g$  molecular orbital and are therefore not seen in the anion ZEKE spectrum because detachment from such an orbital cannot result in an  $l=0$  ( $s$ -wave) electron.<sup>49,50</sup> While this ZEKE transition is not strictly forbidden from heteronuclear  $\text{GaAs}^-$ , we might expect it to have a small  $s$ -wave partial cross section near threshold and hence be very weak.

Looking at the peak positions in more detail,  $B_1$ - $B_4$  are spaced by 33, 24, and 19 meV, similar to the spacings for the analogous peaks in InP, and we assign these to the  $^3\Pi_{2,1,0+,-}(\nu'=0) \leftarrow ^2\Sigma^+(\nu''=0)$  transitions. The peaks at higher eBE are assigned to transition to higher vibrational levels in the  $^3\Pi$  state. Manna *et al.*<sup>20</sup> predicted the splitting in the  $^3\Pi$  state to be 60, 66, 4, almost twice the determined values (except for the 0+/0- splitting). Our values are comparable with experimental splittings for the analogous  $^3\Pi$  state in  $\text{Ge}_2$ . The hot band  $b_1$  yields a vibrational frequency of 298  $\text{cm}^{-1}$  for the anion  $^2\Sigma^+$  state, in agreement with our assignment of the singlet manifold.

Peaks  $A_0$ ,  $A_1$ , and  $A'$  appear to have the same assignments as for InP. However, the  $^3\Pi_{3/2} - ^2\Sigma^+$  splitting (between peaks  $A_1$  and  $B_1$ ) is 52 meV, noticeably larger than the value of 9 meV found for InP. The assignment of peak  $A_0$  to the  $^3\Pi_1 \leftarrow ^2\Pi_{1/2}$  transition implies a spin-orbit splitting of 0.067 eV in the anion  $^2\Pi$  state, close to the InP splitting.

Peaks  $c$ ,  $C$  and  $C'$  are assigned to the  $^3\Sigma^- - ^2\Pi$  transition similar to InP. The spacing between peaks  $c$  and  $C$  is around 242  $\text{cm}^{-1}$ , consistent with this band originating from a different anion electronic state than band "B". This frequency is slightly higher than the calculated by Balasubramanian<sup>42</sup> of 216  $\text{cm}^{-1}$ . The spacing between peaks  $C$  and

$C'$  ( $\sim 220\text{ cm}^{-1}$ ) is consistent with the experimental neutral frequency of  $213\text{ cm}^{-1}$  determined by Lemire *et al.*<sup>13</sup> We thus assign peak C as the origin of this band. FC simulations of the singlet and triplet bands were generated using the parameters in Table 3-4. In this case, all bond length changes are reference to the experimental bond length for the  $^3\Sigma^-$  state,  $2.517\text{ \AA}$ , obtained from the rotationally resolved laser-induced fluorescence spectrum of GaAs.<sup>13</sup> We find an electron affinity of  $1.949 \pm 0.020\text{ eV}$  using the same procedure as for the other diatomics. The  $^2\Sigma - ^2\Pi$  splitting is in good agreement with the calculated splitting by Balasubramanian<sup>19</sup> of  $0.099\text{ eV}$ , however most of the theoretical results underestimated the electron affinity by as much of  $0.5\text{ eV}$ . The electron affinities calculated by Balasubramanian and Meier *et al.*,  $1.4 \pm 0.02\text{ eV}$  (SOC1) and  $1.51\text{ eV}$  (MRDCI), respectively, are clearly too low. However, Lou *et al.* report a much closer value of  $1.89\text{ eV}$  employing the more empirical DFT method using the local density functional (LDF).<sup>21</sup>

## V. Discussion

The analysis in Section IV is fairly involved, and an evaluation of its strong and weak points is in order. In general, assignment of the singlet manifolds was straightforward and showed that all the anions have  $^2\Sigma^+$  ground states. In the case of GaP and InP, the energy of the low-lying  $^2\Pi$  state was obtained through the observation of electronic hot bands in the singlet manifold. The combination of photoelectron energy and angular distributions made it possible to distinguish clearly between different electronic photodetachment transitions, even if they were overlapped, and difference in peak spacings facilitated identification of the vibrational origin for each photodetachment transition.

The triplet manifolds are more problematic to assign. The identification and assignment of the  $^3\Pi \leftarrow ^2\Sigma^+$  transitions (the “B” peaks) was generally straightforward because of their polarization dependence and multiplet pattern from spin-orbit splitting in the  $^3\Pi$  state. Our reasoning in Section IVB makes us confident that the assignment of the “A” peaks to the  $^3\Pi \leftarrow ^2\Pi$  transitions is correct, but this assignment does raise a few questions. In particular, at  $\theta=0^\circ$ , at least one peak associated with this transition dominates the PE spectrum, while in the singlet manifolds, electronic hot bands originating from the  $^2\Pi$  state are either small or indistinguishable from the noise, regardless of the laser polarization angle.

The high intensity of the “A” peaks is due in part to a smaller change in geometry for the  $^3\Pi \leftarrow ^2\Pi$  transition compared to the  $^3\Pi \leftarrow ^2\Sigma^+$  transitions for all four species (see Tables 3-(1-4)), resulting in a much narrower Franck-Condon profile for the  $^3\Pi \leftarrow ^2\Pi$  transition. In addition, photodetachment from the  $^2\Sigma^+$  state accesses all the  $\Omega$ -levels of the  $^3\Pi$  state with approximately equal intensity, whereas only one or two transitions to these  $\Omega$ -levels from the anion  $^2\Pi$  state occur with appreciable intensity, further concentrating the  $^3\Pi \leftarrow ^2\Pi$  transition in a smaller number of peaks. These effects may not be the whole story, however. The relative intensity of the “A” peaks is reduced in photoelectron spectra of the triplet manifolds of  $\text{GaP}^-$  and  $\text{GaAs}^-$  at lower wavelengths, suggesting that non-Franck-Condon effects possibly due to the presence of an excited anion electronic state near 498 nm are distorting the intensity profile.

The other issue regarding the  $^3\Pi \leftarrow ^2\Pi$  peaks is the intensity distribution among the  $\Omega$ -levels of the  $^3\Pi$  state. We have invoked a  $\Delta\Omega=\pm 1/2$  propensity rule based on other anion PE spectra to explain the reduced number of peaks, but even in  $\text{InP}$  and  $\text{GaAs}$ ,



where all the spin-orbit transitions are well-separated, the intensities of the transitions that we assigned to the  $\Omega' = 2 \leftarrow \Omega'' = 3/2$  and  $\Omega' = 1 \leftarrow \Omega'' = 3/2$  are not the same. In the case of GaP the splittings in both states are comparable resulting in a broad band difficult to resolve with our resolution. A careful theoretical study of these open-shell photodetachment transitions would be of great use in understanding the observed intensities.

The "C" peaks, assigned to the  $^3\Sigma^+ \leftarrow ^2\Pi$  are very important because they provide the only experimental means of determining the splitting between the neutral  $^3\Pi$  and  $^3\Sigma^+$  states as well as the electron affinity, since the  $^3\Sigma^+ \leftarrow ^2\Sigma^+$  transition which would provide a direct measure of the electron affinity is not one-electron allowed. The key issue with this transition is to be able to assign the vibrational origin, which can generally be done because the anion and neutral vibrational frequencies are different. We expect the error in the electron affinity to be slightly higher than the other determined term energies for this reason, but not to be higher than  $\pm 1.5$  quanta in the anion frequency.

Figure 3-7 shows a graphical comparison of the experimental ground and excited state energetics for the four III-V species studied here as well the homonuclear, isovalent species  $\text{Si}_2$  and  $\text{Ge}_2$ . The figure shows that the electron affinity of the XP diatomics decreases as the mass of X increases from Al to In, while the electron affinities of GaP and GaAs are roughly equal. This trend suggests that the extra electron in the anion is localized more on the group III atom, a reasonable result in that the III-V neutrals are polar molecules with a partial negative charge on the more electronegative group V atom.

The main difference between the homonuclear and heteronuclear diatomics is in the singlet manifold. Electronic structure calculations predict the ordering of the excited singlet states is reversed in homonuclear vs. heteronuclear species, and our experiments confirm this in all cases where transitions to the singlet states are seen; recall that GaP was the only III-V diatomic for which transitions to the  $^1\Delta$  state were observed. Figure 3-7 also shows the consequences of the evolution from Hund's case (a) to (c) coupling, with spin-orbit splittings progressively increasing as the atoms become heavier, and measurable splitting of the  $^3\Pi_0$  state into  $0^+$  and  $0^-$  components for  $\text{Ge}_2$ ,  $\text{InP}$ , and  $\text{GaAs}$ . The consequences of this evolution are also evident in the anions. In  $\text{InP}^-$ , the spin-orbit splitting in the  $^3\Pi$  state results in the  $\Omega=3/2$  component lying only 9 meV above the  $^2\Sigma^+$  state, while in  $\text{Ge}_2^-$  (and  $\text{Sn}_2^-$ ) the  $\Omega=3/2$  level is pushed below the  $^2\Sigma^+$  state.

## VI. References:

- (1) Alivisatos, A. P. *Journal of Physical Chemistry* **1996**, *100*, 13226.
- (2) Alivisatos, A. P. *Berichte Der Bunsen-Gesellschaft-Physical Chemistry Chemical Physics* **1997**, *101*, 1573.
- (3) Douglas, A. E.; Herzberg, G. *Canadian Journal of Research A* **1940**, *18*, 179.
- (4) Mosher, O. A.; Frosch, R. P. *Journal of Chemical Physics* **1970**, *52*, 5781.
- (5) Bredohl, H.; Dubois, I.; Houbrechts, Y.; Nzohabonayo, P. *J. Phys. B: At. Mol. Phys.* **1984**, *17*, 95.
- (6) Bredohl, H.; Dubois, I.; Houbrechts, Y.; Nzohabonayo, P. *Journal of Molecular Spectroscopy* **1985**, *112*, 430.
- (7) Reid, C. J. *International Journal of Mass Spectrometry and Ion Processes* **1993**, *127*, 147.
- (8) Reddy, R. R.; Reddy, A. S. R.; Rao, T. V. R. *Physica B & C* **1985**, *132B+C*, 373.
- (9) Lorenz, M.; Agreiter, J.; Smith, A. M.; Bondybey, V. E. *Journal of Chemical Physics* **1996**, *104*, 3143.
- (10) Asmis, K. R.; Taylor, T. R.; Neumark, D. M. *Chemical Physics Letters* **1998**, *295*, 75.
- (11) Liu, Z.; Gomez, H.; Neumark, D. M. *Faraday Discussions* **2001**, *118*, 221.
- (12) Asmis, K. R.; Taylor, T. R.; Neumark, D. M. *Chemical Physics Letters* **1999**, *308*, 347.
- (13) Lemire, G. W.; Bishea, G. A.; Heidecke, S. A.; Morse, M. D. *Journal of Chemical Physics* **1990**, *92*, 121.
- (14) Ebben, M.; ter Meulen, J. J. *Chemical Physics Letters* **1991**, *177*, 229.
- (15) Li, S.; Van Zee, R. J.; Weltner Jr., W. *Journal of physical chemistry* **1994**, *98*, 2275.
- (16) Li, S.; Van Zee, R. J.; Weltner Jr., W. *Journal of Physical Chemistry* **1993**, *97*, 11393.
- (17) Meier, U.; Peyerimhoff, S. D.; Grein, F. *Chemical Physics* **1991**, *150*, 331.
- (18) Meier, U.; Peyerimhoff, S. D.; Bruna, P. J.; Grein, F. *Journal of Molecular Spectroscopy* **1989**, *134*, 259.
- (19) Balasubramanian, K. *Journal of Physical Chemistry* **1990**, *94*, 7764.
- (20) Manna, B.; Das, K. K. *Journal of Physical Chemistry A* **1998**, *102*, 9876.
- (21) Lou, L.; Wang, L.; Chibante, L. P. F.; Laaksonen, R. T.; Nordlander, P.; Smalley, R. E. *Journal Of Chemical Physics* **1991**, *94*, 8015.
- (22) Bruna, P. J.; Grein, F. *Journal of Physics B-Atomic Molecular and Optical Physics* **1989**, *22*, 1913.
- (23) Meier, U.; Peyerimhoff, S. D.; Bruna, P. J.; Karna, S. P.; Grein, F. *Chemical Physics* **1989**, *130*, 31.
- (24) Archibong, E. F.; St-Amant, A. *Chemical Physics Letters* **2000**, *316*, 151.
- (25) Manna, B.; Das, K. K. *Journal of Molecular Structure (Theochem)* **1999**, *467*, 135.

- (26) Manna, B.; Dutta, A.; Das, K. K. *Journal of Physical Chemistry A* **2000**, *104*, 2764.
- (27) Ho, J.; Polak, M. L.; Lineberger, W. C. *Journal of Chemical Physics* **1992**, *96*, 144.
- (28) Arnold, C. C.; Kitsopoulos, T. N.; Neumark, D. M. *Journal of Chemical Physics* **1993**, *99*, 766.
- (29) Arnold, C. C.; Xu, C. S.; Burton, G. R.; Neumark, D. M. *Journal of Chemical Physics* **1995**, *102*, 6982.
- (30) Kitsopoulos, T. N.; Chick, C. J.; Zhao, Y.; Neumark, D. M. *Journal of Chemical Physics* **1991**, *95*, 1441.
- (31) Moravec, V. D.; Klopčič, S. A.; Jarrold, C. C. *Journal of Chemical Physics* **1999**, *110*, 5079.
- (32) Metz, R. B.; Weaver, A.; Bradforth, S. E.; Kitsopoulos, T. N.; Neumark, D. M. *Journal of Physical Chemistry* **1990**, *94*, 1377.
- (33) Xu, C.; Burton, G. R.; Taylor, T. R.; Neumark, D. M. *Journal of Chemical Physics* **1997**, *107*, 3428.
- (34) Taylor, T. R.; Gomez, H.; Asmis, K. R.; Neumark, D. M. *Journal of Chemical Physics* **2001**, *115*, 4620.
- (35) Mamyurin, B. A.; Shmikk, D. V. *Zhurnal Eksperimental'noi i Teoreticheskoi Fiziki* **1979**, *76*, 1500.
- (36) Markovich, G.; Giniger, R.; Levin, M.; Cheshnovsky, O. *Journal of Chemical Physics* **1991**, *95*, 9416.
- (37) Cooper, J.; Zare, R. N. Photoelectron angular distributions. In *Lectures in Theoretical Physics*; Brittin, W. E., Ed.; Gordon and Breach: New York, 1969; Vol. XI-C; pp 317.
- (38) Ervin, K. M.; Lineberger, W. C. Photoelectron spectroscopy of molecular anions. In *Advances in Gas Phase Ion Chemistry*; JAI Press Inc, 1992; Vol. 1; pp 121.
- (39) Arnold, C. C.; Zhao, Y. X.; Kitsopoulos, T. N.; Neumark, D. M. *Journal of Chemical Physics* **1992**, *97*, 6121.
- (40) Kitsopoulos, T. N.; Waller, I. M.; Loeser, J. G.; Neumark, D. M. *Chemical Physics Letters* **1989**, *159*, 300.
- (41) Balasubramanian, K. *Journal of Chemical Physics* **1987**, *86*, 3410.
- (42) Balasubramanian, K. *Journal Of Molecular Spectroscopy* **1990**, *139*, 405.
- (43) Balasubramanian, K. *Journal of Chemical Physics* **1990**, *92*, 2123.
- (44) Meier, U.; Peyerimhoff, S. D.; Grein, F. *Chemical Physics* **1991**, *150*, 331.
- (45) Becke, A. D. *Journal of Chemical Physics* **1993**, *98*, 1372.
- (46) Lee, C.; Yang, W.; Parr, R. G. *Physical Review B* **1988**, *37*, 785.
- (47) Melius, C. F.; Goddard, W. A., III. *Physical Review A (General Physics)* **1974**, *vol.10*, 1528.
- (48) M. J. Frisch; G. W. Trucks; H. B. Schlegel; G. E. Scuseria; M. A. Robb; J. R. Cheeseman; V. G. Zakrzewski; J. A. Montgomery, J.; R. E. Stratmann; J. C. Burant; S. Dapprich; J. M. Millam; A. D. Daniels; K. N. Kudin; M. C. Strain; O. Farkas; J. Tomasi; V. Barone; M. Cossi; R. Cammi; B. Mennucci; C. Pomelli; C. Adamo; S. Clifford; J. Ochterski; G. A. Petersson; P. Y. Ayala; Q. Cui; K. Morokuma; D. K. Malick; A. D. Rabuck; K. Raghavachari; J. B. Foresman; J. Cioslowski; J. V. Ortiz; A. G. Baboul; B. B. Stefanov; G. Liu; A. Liashenko; P. Piskorz; I. Komaromi; R. Gomperts; R. L. Martin; D.

J. Fox; T. Keith; M. A. Al-Laham; C. Y. Peng; A. Nanayakkara; M. Challacombe; P. M. W. Gill; B. Johnson; W. Chen; M. W. Wong; J. L. Andres; C. Gonzalez; M. Head-Gordon; E. S. Replogle; J. A. Pople. Gaussian 98; Revision A.9 ed.; Gaussian, Inc.: Pittsburgh PA, 1998.

(49) Branscomb, L. M.; Burch, D. S.; Smith, S. J.; Geltman, S. *Physical Review* **1958**, *111*, 504.

(50) Wigner, E. P. *Physical Review* **1948**, *73*, 1002.

(51) Costales, A.; Kandalam, A. K.; Franco, R.; Pandey, R. *Journal of Physical Chemistry B* **2002**, *106*, 1940.

## VII. Tables

Table 3-1. Comparison of experimental and theoretical molecular constants of AIP.<sup>a</sup>

Method	$X^2\Sigma^+$	$A^2\Pi$	$X^3\Sigma_0^+$	$X^3\Sigma_0^+$	$A^3\Pi_2$	$A^3\Pi_1$	$A^3\Pi_1$	$a^1\Pi$	$b^1\Sigma^+$	$c^1\Delta$	EA (eV)
GGA/DNP <sup>b</sup>			0.000 348 2.46								1.90
MRDCI <sup>c</sup>	0.00 551 2.163	0.08 465 2.273									
MRDCI <sup>d</sup>			0.00 359 2.455	0.11 449 2.260		0.54 487 2.228			0.67 528 2.117		
Experiment	0.000 516 2.163	0.082 467 2.273	0.000 379 2.40	0.108 457 2.26	0.117 0.128	0.516 470 2.22			0.574 541 2.10		2.043

<sup>a</sup> For each entry, the first row gives the term energy (in eV), the second row gives the vibrational frequency (in cm<sup>-1</sup>), and the third row gives the bond length (in Å). Experimental term energies and frequencies have uncertainties of  $\pm 0.10$  eV and  $\pm 15$  cm<sup>-1</sup> respectively.

<sup>b</sup> From reference <sup>31</sup>

<sup>c</sup> From reference <sup>22</sup>

<sup>d</sup> From reference <sup>23</sup>

Table 3-2. Comparison of experimental and theoretical molecular constants of GaP.<sup>a</sup>

Method	X <sup>3</sup> Σ <sup>+</sup>	A <sup>3</sup> Π <sub>3/2</sub>	A <sup>3</sup> Π <sub>1/2</sub>	X <sup>3</sup> Σ <sup>+</sup>	X <sup>3</sup> Σ <sup>+</sup>	A <sup>3</sup> Π <sub>2</sub>	A <sup>3</sup> Π <sub>1</sub>	<sup>3</sup> Π	a <sup>1</sup> Π	b <sup>1</sup> Σ <sup>+</sup>	c <sup>1</sup> Δ	EA (eV)
GGA/DNP <sup>b</sup>				0.000 251 2.76								
MRDCI <sup>c</sup>				0.00 266 2.498	0.0006 265 2.496	0.089 358 2.260	0.098 357 2.258	0.103 359 2.257	0.695 387 2.229	0.744 439 2.105	1.094 278 2.478	
CCSD(T) <sup>d</sup>	0.000 447 2.163	0.064 371 <sup>e</sup> 2.291		0.000 297 2.473	0.116 357 <sup>e</sup> 2.263					0.739 445 <sup>e</sup> 2.126		1.86
Experiment	0.000 445 2.163	0.048 386 2.291	0.062	0.000 283.6 <sup>f</sup> 2.45	0.099 415 2.24	0.116 415 2.24	0.134 402 2.25	0.612 433 2.11	0.746 285 2.35	0.946		1.988

<sup>a</sup> For each entry, the first row gives the term energy (in eV), the second row gives the vibrational frequency (in cm<sup>-1</sup>), and the third row gives the bond length (in Å). Experimental term energies and frequencies have uncertainties of ± 0.10 eV and ±15 cm<sup>-1</sup>, respectively.

<sup>b</sup> From reference <sup>31</sup>

<sup>c</sup> From reference <sup>25</sup>

<sup>d</sup> From reference <sup>24</sup>

<sup>e</sup> B3LYP Frequency (cm<sup>-1</sup>)

<sup>f</sup> Experimental value from reference <sup>16</sup>

Table 3-3. Comparison of experimental and theoretical molecular constants of InP.<sup>a</sup>

Method	X <sup>2</sup> Σ <sup>+</sup>	A <sup>2</sup> Π <sub>3/2</sub>	A <sup>2</sup> Π <sub>1/2</sub>	X <sup>2</sup> Σ <sup>+</sup>	X <sup>3</sup> Σ <sup>+</sup>	X <sup>3</sup> Σ <sup>+</sup>	A <sup>3</sup> Π <sub>2</sub>	A <sup>3</sup> Π <sub>1</sub>	A <sup>3</sup> Π <sub>0</sub>	A <sup>1</sup> Π	c <sup>1</sup> Σ <sup>+</sup>	b <sup>1</sup> Δ	EA (eV)
MRDCI <sup>b</sup>				0 251 2.70	0.005 249 2.70	0.262 290 2.51	0.296 289 2.50	0.319 290 2.51	0.323 289 2.51	0.921 327 2.46	1.153 305 2.38	1.053 261 2.68	
B3LYP <sup>c</sup>	0.00 338 2.382			0.00 265 2.526						1.057 343 2.326			1.594
QCISD(T) <sup>c</sup>	0.00 340 2.420			0.00 255 2.558						0.691 329 2.361			1.105
Experiment	0.000 335 2.43	0.009 245 2.51	0.087	0.000 255 2.70		0.151 285 2.51	0.187 285 2.51	0.210	0.224	0.669 319 2.49	0.800 350 2.39		1.845

<sup>a</sup> For each entry, the first row gives the term energy (in eV), the second row gives the vibrational frequency (in cm<sup>-1</sup>), and the third row gives the bond length (in Å).

<sup>b</sup> Experimental term energies and frequencies have uncertainties of ± 0.10 eV and ± 15 cm<sup>-1</sup> respectively.

<sup>c</sup> From reference <sup>26</sup>

<sup>e</sup> Gaussian 98 calculation using Los Alamos Effective Core Potential basis set (LANL2DZ )



Table 3-4. Comparison of experimental and theoretical molecular constants of GaAs.<sup>a</sup>

Method	$X^3\Sigma^+$	$A^3\Pi_{3/2}$	$^3\Pi_{3/2}$	$X^3\Sigma^-$	$A^3\Pi_2$	$^3\Pi_1$	$^3\Pi_0^+$	$^3\Pi_0$	a $^1\Pi$	b $^1\Sigma^+$	c $^1\Delta$	EA(eV)
MRDCI <sup>b</sup>	0.00	0.02		0.00	0.17				0.74	0.90	0.94	1.51
	248	212		202	260				278	277	210	
	2.333	2.471		2.598	2.381				2.350	2.249	2.593	
CASSCF <sup>c</sup>	0.00	0.099		0.00	0.227				0.798	0.963	0.976	1.4
	303	216		215	236				277	279	214	
	2.268	2.426		2.60	2.38				2.34	2.23	2.58	
MRDCI <sup>d</sup>	0.00			0.009	0.091	0.151	0.217	0.221	0.7789	0.861	1.087	
	180			181	234	240	234	231	265	297	189	
	2.673			2.667	2.396	2.388	2.389	2.401	2.356	2.218	2.649	
LDF <sup>e</sup>	0.00			0.00								1.89
	209			209								
	2.65			2.65								
Experiment	0.000	0.052	0.119	0.000	0.0053	0.100	0.133	0.157	0.176	0.717	0.831	1.949
	298	242		213.12 <sup>f</sup>	208.90 <sup>f</sup>	263			287	292.5		
	2.268	2.426		2.517	2.548	2.318			2.328	2.218		

<sup>a</sup> For each entry, the first row gives the term energy (in eV), the second row gives the vibrational frequency (in cm<sup>-1</sup>), and the third row gives the bond length (in Å). Unless otherwise noted in text, experimental term energies and frequencies have uncertainties of  $\pm 0.10$  eV and  $\pm 15$  cm<sup>-1</sup>, respectively.

<sup>b</sup> From reference 14

<sup>c</sup> From reference 16

<sup>d</sup> From reference 20

<sup>e</sup> From reference 21

<sup>f</sup> Experimental values from reference 13

# VIII. Figures

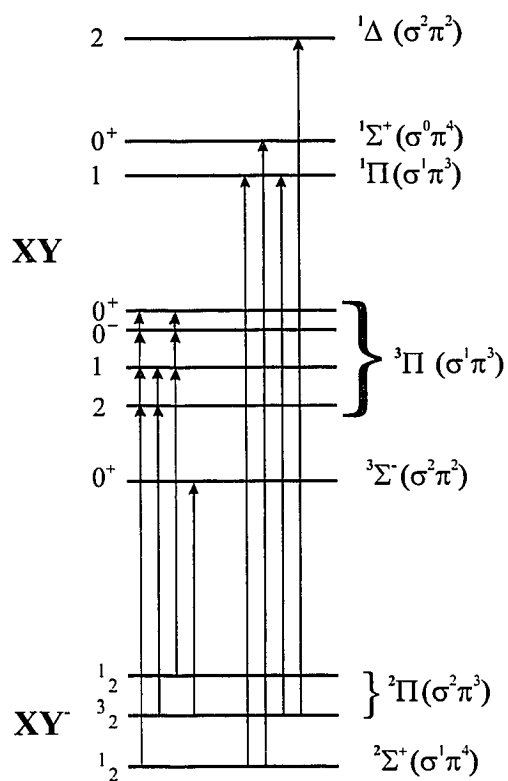


Figure 3-1. Energy level diagram for XY<sup>-</sup>/XY (X = Al, Ga, In and Y = P, As) as derived from *ab initio* calculations.

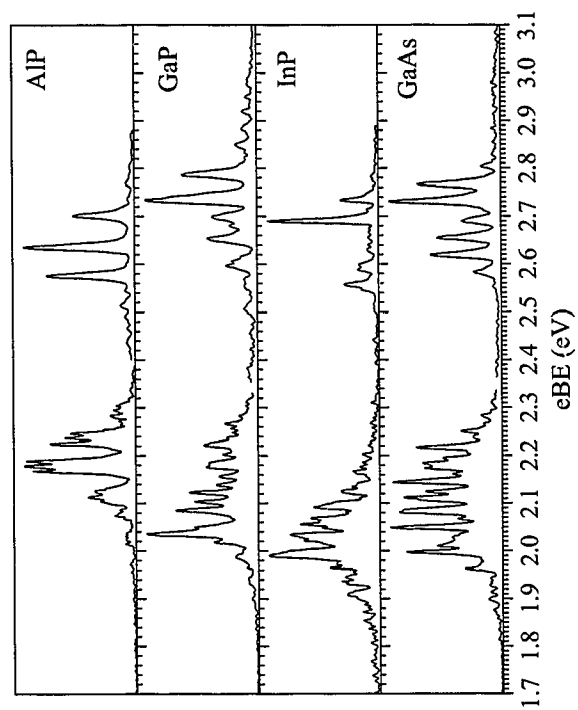


Figure 3-2. Composite plots of the anion photoelectron spectra of XP (X = Al, Ga, In) and GaAs taken at the polarization angle of  $\theta = \sim 54^\circ$ . See text for further description.

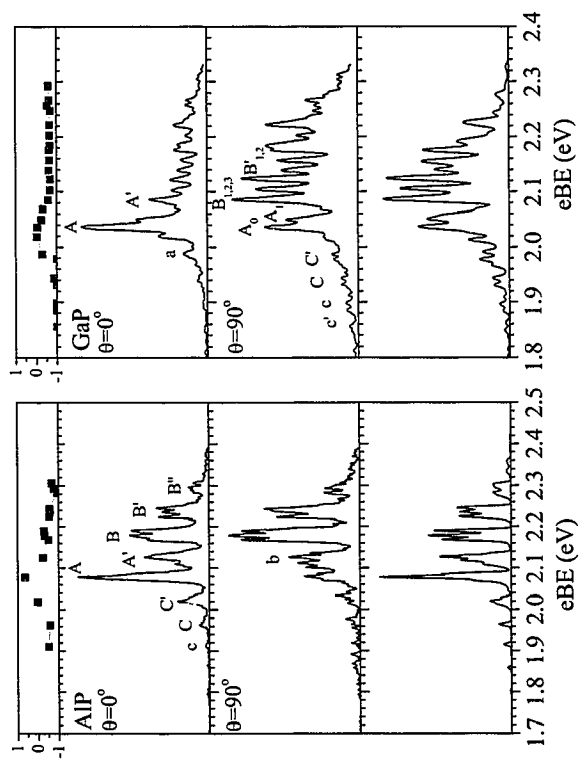


Figure 3-3. Anion photoelectron spectrum AIP<sup>-</sup> and GaP<sup>-</sup> triplet manifold taken at 498 nm and laser polarization of  $\theta = 90^\circ$  and  $\theta = 0^\circ$ . Experimental  $\beta$  parameters at the same photon energy are plotted in the top panel. FC simulation of the  $\theta = 90^\circ$  ( $\theta = 0^\circ$  for AIP) spectrum is shown in the bottom panel.

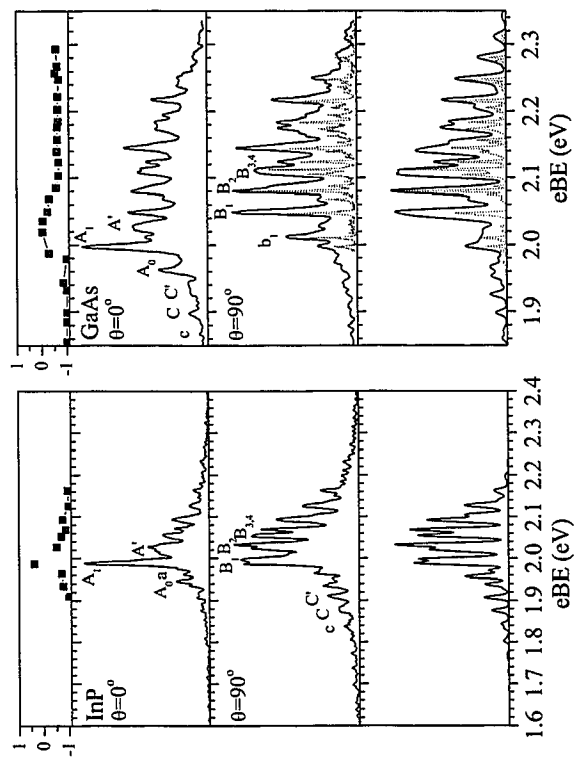


Figure 3-4. Anion photoelectron spectrum InP<sup>-</sup> and GaAs<sup>-</sup> triplet manifold taken at 498 nm and laser polarization of  $\theta = 90^\circ$  and  $\theta = 0^\circ$ . Experimental  $\beta$  parameters at the same photon energy are plotted in the top panel. FC simulation of the  $\theta = 90^\circ$  spectrum is shown in the bottom panel.

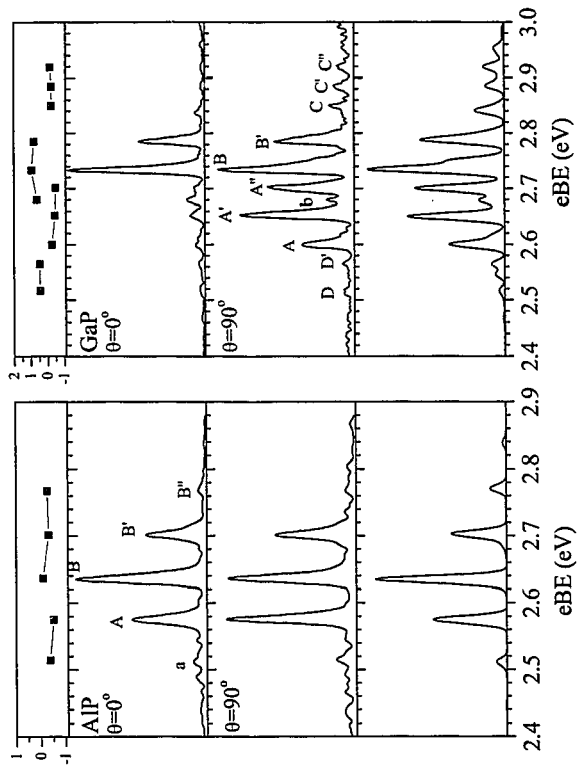


Figure 3-5. Anion photoelectron spectrum AlP<sup>-</sup> and GaP<sup>-</sup> singlet manifold taken at 498 nm and laser polarization of  $\theta = 90^\circ$  and  $\theta = 0^\circ$ . Experimental  $\beta$  parameters at the same photon energy are plotted in the top panel. FC simulation of the  $\theta = 90^\circ$  ( $\theta = 0^\circ$  for AlP) spectrum is shown in the bottom panel.

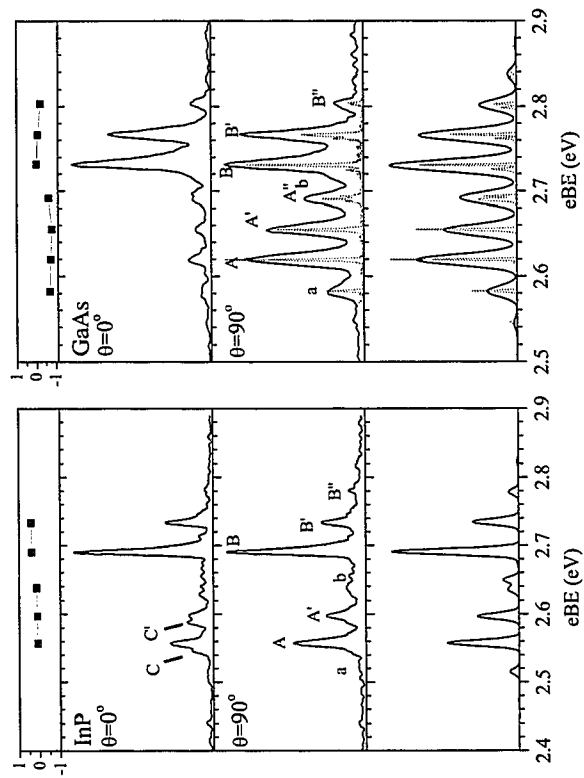


Figure 3-6. Anion photoelectron spectrum InP<sup>-</sup> and GaAs<sup>-</sup> singlet manifold taken at 355 nm (416nm for InP) and laser polarization of  $\theta = 90^\circ$  and  $\theta = 0^\circ$ . Experimental  $\beta$  parameters at the same photon energy are plotted in the top panel. FC simulation of the  $\theta = 90^\circ$  spectrum is shown in the bottom panel.

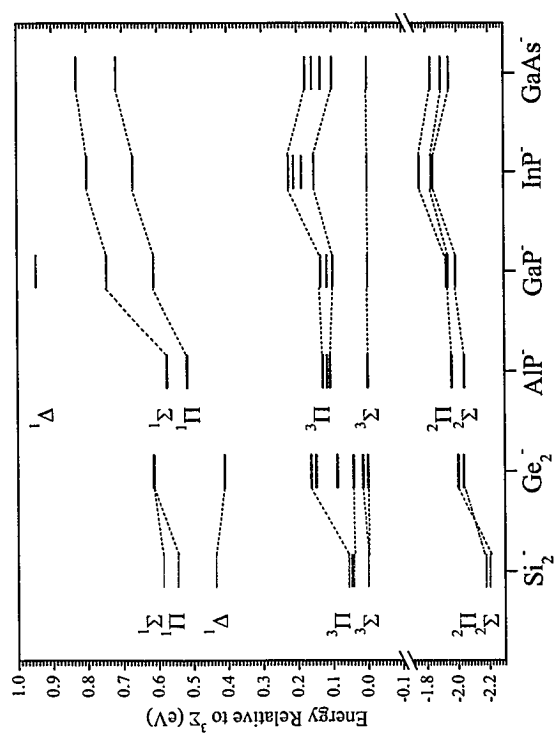


Figure 3-7. Energy level diagram showing the electronic structure of the anion and neutral states of the isoelectronic species,  $\text{Si}_2$ ,  $\text{Ge}_2$ ,  $\text{AlP}$ ,  $\text{GaP}$ ,  $\text{InP}$ , and  $\text{GaAs}$ . The energy is referenced with respect to the  $^3\Sigma$  state for each species.



#### ***-4- Photoelectron spectroscopy of $GaX_2^-$ , $Ga_2X^-$ , $Ga_2X_2^-$ , and $Ga_2X_3^-$ ( $X=P,As$ )***

---

Anion photoelectron spectra taken at various photodetachment wavelengths have been obtained for  $GaX_2^-$ ,  $Ga_2X^-$ ,  $Ga_2X_2^-$ , and  $Ga_2X_3^-$  ( $X=P,As$ ). The incorporation of a liquid-nitrogen cooled channel in the ion source resulted in substantial vibrational cooling of the cluster anions, resulting in resolved vibrational progressions in the photoelectron spectra of all species except  $Ga_2X_2^-$ . Electron affinities, electronic term values, and vibrational frequencies are reported and compared to electronic structure calculations. In addition, similarities and differences between the phosphorus and arsenic-containing isovalent species are discussed.

## I. Introduction

Since the invention of the transistor in 1947, semiconductor materials have become an essential part of the electronics industry. Group III-V materials have shown particular promise as semiconductors and have demonstrated a variety of novel characteristics.<sup>1</sup> While bulk semiconductor materials have been thoroughly studied and are well understood, small molecules made of group III-V elements have received relatively little attention despite their importance in processes such as epitaxial growth and chemical vapor deposition. It has been a goal of our research group to characterize the electronic and vibrational structure of clusters formed from bulk semiconducting materials. This study represents continued progress towards this goal by investigating the electronic and vibrational structure of  $\text{GaX}_2^-$ ,  $\text{Ga}_2\text{X}^-$ ,  $\text{Ga}_2\text{X}_2^-$ , and  $\text{Ga}_2\text{X}_3^-$  ( $\text{X}=\text{P},\text{As}$ ) clusters via anion photoelectron spectroscopy.

Several gas phase and matrix experiments have been carried out in order to characterize the electronic and vibrational spectroscopy of polyatomic  $\text{Ga}_x\text{X}_y$  species. The first systematic experimental studies were carried out by Smalley and co-workers,<sup>2-4</sup> in which  $\text{Ga}_x\text{As}_y$  neutral and anionic clusters with up to 50 atoms were generated by laser ablation and characterized in photodissociation, photodetachment, and photoelectron (PE) spectroscopy experiments. PE spectra of mass-selected  $\text{Ga}_x\text{As}_y^-$  anion clusters showed an even-odd alternation in electron affinities and provided information on the excited state energetics of the neutral clusters.<sup>4</sup> However, the mass resolution was not sufficient to separate clusters with the same number of atoms but differing stoichiometry, and the electron energy resolution ( $>100$  meV) was sufficient to resolve electronic structure only. Li *et al.*<sup>5</sup> have carried out infrared matrix infrared absorption experiments

revealing and measured vibrational frequencies of GaX, GaX<sub>2</sub>, and Ga<sub>2</sub>X (X=P,As). These authors also measured the electron spin resonance spectrum of Ga<sub>2</sub>As<sub>3</sub> in a matrix and concluded that it has a trigonal bipyramidal structure with the unpaired electron shared between the two gallium atoms.<sup>6</sup> Electric dipole polarizabilities of gallium arsenide clusters have been measured by Schlect *et al.*<sup>7</sup>

Taylor *et al.* have carried out two studies on Ga<sub>x</sub>P<sub>y</sub><sup>-</sup> clusters via anion PE spectroscopy. They obtained vertical detachment energies from the PE spectra of size-selected clusters Ga<sub>x</sub>P<sub>y</sub><sup>-</sup> (x+y≤18) at a photon wavelength of 266 nm and an energy resolution of 30 meV.<sup>8</sup> This study showed an odd-even alternation in electron affinities consistent with the open-shell/closed-shell structure of the clusters, similar to the trend seen by Jin *et al.*<sup>4</sup> for Ga<sub>x</sub>As<sub>y</sub> clusters. The size-dependence of electron affinities for the Ga<sub>x</sub>P<sub>y</sub> clusters could be readily extrapolated to the bulk value, a trend also observed in In<sub>x</sub>P<sub>y</sub> clusters.<sup>9</sup> In a more recent, higher resolution (10 meV) study, Taylor *et al.*<sup>10</sup> published preliminary vibrationally-resolved PE spectra of GaP<sub>2</sub><sup>-</sup>, Ga<sub>2</sub>P<sup>-</sup>, and Ga<sub>2</sub>P<sub>3</sub><sup>-</sup> anions and concluded that the anion ground state and the neutral states of GaP<sub>2</sub> and Ga<sub>2</sub>P are bent C<sub>2v</sub> structures. The ground and two excited states of GaP<sub>2</sub> were assigned based on comparison to *ab initio* calculations by Feng and Balasubramanian,<sup>11</sup> but assignment of the Ga<sub>2</sub>P<sup>-</sup> photoelectron spectrum was more problematic. No vibrational structure was seen in the Ga<sub>2</sub>P<sub>2</sub><sup>-</sup> PE spectrum at 10 meV resolution, an interesting result given the observation of vibrational structure in the PE spectra of Si<sub>4</sub><sup>-</sup><sup>12,13</sup> and Ga<sub>2</sub>P<sub>3</sub><sup>-</sup> taken at comparable resolution.

Several theoretical descriptions of polyatomic GaX (X=P,As) clusters have been carried out. Balasubramanian and co-workers have performed a series of complete active

space self-consistent field (CASSCF) and multireference singles and doubles configuration interaction (MRSDCI) calculations, finding geometries and term values for neutral and charged (mainly cationic) gallium arsenide<sup>14-20</sup> and gallium phosphide<sup>11,21-23</sup> clusters with up to five atoms. Graves *et al.*<sup>24</sup> and Al-Laham *et al.*<sup>25</sup> have carried out *ab initio* calculations to determine the ground state of the 1:1 stoichiometric (GaAs)<sub>n</sub> clusters with up to 8 atoms. Lou *et al.*<sup>26,27</sup> calculated structures of stoichiometric and non-stoichiometric Ga<sub>x</sub>As<sub>y</sub> clusters using the local spin density method. Andreoni carried out Car-Parrinello molecular dynamics calculations to study the structures, stability and melting of small stoichiometric GaP, GaAs, and AlAs clusters;<sup>28</sup> a more recent study by Tozzini *et al.*<sup>29</sup> on larger GaP clusters showed evidence for fullerene-like structures for clusters with as few as 20 atoms. Meier *et al.*<sup>30</sup> investigated neutral, cationic, and anionic GaAs<sub>2</sub> and Ga<sub>2</sub>As<sub>2</sub> clusters in a multi-reference configuration interaction (MRD-CI) calculation. Archibong and St. Amant<sup>31</sup> have used coupled cluster singles and doubles (CCSD(T)) and Becke-3-parameter-Lee-Yang-Parr (B3LYP) theoretical methods to study GaP and GaP<sub>2</sub>, calculating term energies and vibrational frequencies of the neutral and anion states. These authors have also found that the ground state of Ga<sub>2</sub>P<sub>2</sub><sup>-</sup> has a nonplanar geometry with C<sub>2v</sub> symmetry,<sup>32</sup> in contrast to the planar rhombic (D<sub>2h</sub>) ground state of neutral Ga<sub>2</sub>P<sub>2</sub>, and propose this change in geometry to be origin for the absence of vibrational structure in the Ga<sub>2</sub>P<sub>2</sub><sup>-</sup> PE spectrum. In support of the electron spin resonance experiment by Van Zee,<sup>6</sup> Arratia-Perez *et al.*<sup>33,34</sup> have calculated the paramagnetic resonance parameters for Ga<sub>2</sub>As<sub>3</sub>, Ga<sub>2</sub>As and GaAs<sub>2</sub>. The electronic absorption spectrum of these and other GaAs clusters was recently calculated by Vasiliev *et al.*<sup>35</sup>

Here we present vibrationally-resolved anion PE spectra of  $\text{GaX}_2^-$ ,  $\text{Ga}_2\text{X}^-$ ,  $\text{Ga}_2\text{X}_3^-$  ( $\text{X}=\text{P,As}$ ) clusters and we also discuss the electronic structure of  $\text{Ga}_2\text{X}_2$ . The addition of a liquid nitrogen cooled clustering channel to our laser ablation disc source results in vibrationally cooler anion cluster precursors than in previous work. This significantly improves the quality of our photoelectron spectra and allows us to more accurately report electron affinities, vibrational frequencies, and term values. The assignment of these spectra is also aided by comparison to our recently reported PE spectra of  $\text{Al}_x\text{P}_y^-$  clusters.<sup>36</sup>

## II. Experimental

The anion photoelectron spectrometer used in this study has been described in detail previously.<sup>37,38</sup> Cluster anions are generated in a laser ablation/pulsed molecular beam source equipped with an additional liquid nitrogen cooled clustering channel as shown in Figure 4-1. The piezo electric molecular beam valve (a) releases a helium gas pulse which intercepts the resulting clusters generated by ablating a rotating and translating single crystal disc (b) of GaP or GaAs (Crystallode Inc.) with the second harmonic (532 nm) of a pulsed Nd:YAG laser (c). The laser pulse energies are typically 5.0-7.5 mJ/pulse and are focused onto the target with a 50 cm lens. The gas pulse continues to travel through a 1.75 inch long copper clustering channel (e). The copper channel is cooled by gravimetrically flowing liquid nitrogen through 1/8" diameter copper tubing in thermal contact with the channel. To prevent the valve from cooling, a 1/4" thick insulator (d) made of Delrin is located between the copper channel and the laser ablation assembly. In addition, the laser ablation assembly is heated enough to maintain it at room temperature. Thermocouples are used to ensure that the clustering channel and

molecular beam valve are maintained at the appropriate temperatures. The gas pulse exits the clustering channel and passes through a skimmer into a differentially pumped region. Negative ions in the beam are extracted perpendicular to their flow direction by a pulsed electric field and injected into a linear reflectron time-of-flight (TOF) mass spectrometer<sup>39,40</sup> with a mass resolution  $m/\Delta m$  of 2000. Due to the natural isotope abundance of gallium ( $\text{Ga}^{69}:\text{Ga}^{71}$ , 100.0:66.4) each cluster stoichiometry has a mass distribution that is fully resolved in our instrument. In each case the most intense mass peak was photodetached.

The ion of interest is selectively photodetached at a photon wavelength of 355 nm (3.493 eV), 416 nm (2.977 eV), or 498 nm (2.490 eV). The 355 nm wavelength is obtained by tripling the fundamental of a pulsed Nd:YAG laser, while light at 416 and 498 nm corresponds to the first and second Stokes lines generated by passing the laser pulse at 355 nm through a high pressure Raman cell filled with hydrogen at 325 psig. The electron kinetic energy ( $eKE$ ) distribution is determined by TOF analysis in a 1 m field-free flight tube. The energy resolution is 8-10 meV at 0.65 eV  $eKE$  and degrades as  $(eKE)^{3/2}$  at higher  $eKE$ . The data in electron kinetic energy is converted to electron binding energy ( $eBE$ ) by subtracting it from the photon energy. All data are plotted in  $eBE$  as described by equation (1) where  $EA$  is the adiabatic electron affinity,  $E^o$  is the internal energy of the neutral, and  $E^-$  is the internal energy of the anion.

$$eBE = h\nu - eKE = EA + E^o - E^- \quad (4)$$

The angular dependence of the photodetachment intensity for polarized light and randomly oriented molecules is given by equation (2) below<sup>41</sup>

$$\frac{d\sigma}{d\Omega} = \frac{\sigma_{total}}{4\pi} \left[ 1 + \frac{\beta(eKE)}{2} (3 \cos^2 \theta - 1) \right] \quad (5)$$

where  $\theta$  is the angle between the electric vector of the photon and the direction of electron ejection,  $\sigma_{total}$  is the total photodetachment cross section and  $\beta(eKE)$  is the asymmetry parameter ( $-1 \leq \beta \leq 2$ ). Each electronic state typically has a characteristic asymmetry parameter and this can be used to distinguish contributions from overlapping electronic transitions. The anisotropy parameter of a peak is calculated<sup>42</sup> using (3)

$$\beta = \frac{I_{0^\circ} - I_{90^\circ}}{\frac{1}{2} I_{0^\circ} + I_{90^\circ}} \quad (3)$$

where  $I_{0^\circ}$  and  $I_{90^\circ}$  are the intensities of the peak taken at the polarization angles  $\theta = 0^\circ$  and  $90^\circ$ . The laser polarization can be rotated with respect to the direction of electron detection by using a half-wave plate.

### III. Results

Figure 4-2 shows a portion of the 355 nm GaP<sub>2</sub> photoelectron spectrum taken at room temperature (HOT) and with liquid nitrogen cooling of the clustering channel (COLD). The HOT spectrum was reported in our earlier work<sup>10</sup> and was assigned to the transition to the  $\tilde{A}(^2A_1)$  excited state of GaP<sub>2</sub>.

These two spectra demonstrate our ability to vibrationally cool the anions prior to photodetachment, yielding a much better-resolved PE spectrum. All spectra reported below were taken under cold conditions.

Figures 4-3, 4-4, 4-5 and 4-6 show the anion photoelectron spectra of  $\text{GaX}_2^-$ ,  $\text{Ga}_2\text{X}^-$ ,  $\text{Ga}_2\text{X}_2^-$ , and  $\text{Ga}_2\text{X}_3^-$  ( $\text{X}=\text{P}, \text{As}$ ), respectively. For all spectra the ordinate is intensity with arbitrary units and the abscissa is in electron binding energy (*eBE*) with units of eV. Spectra of  $\text{Ga}_x\text{P}_y^-$  and  $\text{Ga}_x\text{As}_y^-$  clusters with the same stoichiometry are in general quite similar, the main exception being the excited state (high *eBE*) bands in Figs. 4-4 and 4-5 for  $\text{Ga}_2\text{P}$  and  $\text{Ga}_2\text{As}$ . This similarity also extends to the photoelectron angular distributions, as can be seen by visual comparison of spectra taken at the same photodetachment wavelength but different laser polarization angles. Where possible  $\beta$  has been determined and for  $\text{GaX}_2$  these values are located in Tables 4-(1-2). The values of  $\beta$  for  $\text{Ga}_2\text{X}$  are shown graphically in Figure 4-4 and  $\text{Ga}_2\text{X}_3$  angular distributions are discussed Section IVD. The features marked with the asterisk (\*) appear only in the  $\text{Ga}_2\text{X}$  and  $\text{GaX}_2$  spectra. They are observed in the 'cold' spectra of  $\text{Ga}_2\text{X}^-$  and  $\text{GaX}_2^-$  but are obscured in the 'hot' spectra. They are most significant in the gallium arsenide species and are not significant in spectra taken at 266 nm. Comparison to the PE spectra of  $\text{GaP}^-$  and  $\text{GaAs}^-$  suggests these features are most likely due to photodissociation to  $\text{GaX}^-$  followed by photodetachment of the diatomic anion.<sup>43</sup>

Figure 4-3 shows six panels corresponding to the  $\text{GaX}_2^-$  spectra taken at different wavelengths and polarization angles. The top panels for each species display the spectra taken at 498 nm and  $\theta=90^\circ$ . The lower two panels show spectra taken at 355 nm and  $\theta=90^\circ$  and  $0^\circ$ . The spectra are comprised of two well-separated bands corresponding to



transitions to the ground and first excited states of  $\text{GaX}_2$ . Based on comparison with *ab initio* calculations by Feng,<sup>11</sup> we concluded previously that the anion ground state and neutral states of  $\text{GaP}_2$  have  $C_{2v}$  geometries and assigned the ground and first excited states to the  $\tilde{X}^2B_2$  and  $\tilde{A}^2A_1$  states, respectively.<sup>8,10</sup> This assignment is consistent with more recent calculations by Archibong.<sup>31</sup> Given the similarities between the spectra of  $\text{GaP}_2$  and  $\text{GaAs}_2$  the same assignments should apply to  $\text{GaAs}_2$ . Further support for this assignment is provided in Section IVA. Both states of  $\text{GaX}_2$  exhibit similar extended vibrational progressions, implying a significant geometry change between the anion and neutral states. The  $\tilde{X}^2B_2$  and  $\tilde{A}^2A_1$  bands in the  $\text{GaP}_2^-$  spectra show vibrational progressions with frequencies of 222 and 328  $\text{cm}^{-1}$ , respectively. In the  $\text{GaAs}_2^-$  spectra, the frequencies associated with the  $\tilde{X}^2B_2$  and  $\tilde{A}^2A_1$  bands are 176  $\text{cm}^{-1}$  and 235  $\text{cm}^{-1}$ , respectively, with a somewhat irregular intensity distribution in the  $\tilde{A}^2A_1$  band. Comparison of the 355 nm spectra at  $\theta=0^\circ$  and  $90^\circ$  indicates a strongly negative anisotropy parameter for detachment to the ground state for both species (see Tables 4-1 and 2).

The PE spectra of  $\text{Ga}_2\text{P}^-$  and  $\text{Ga}_2\text{As}^-$  in Fig. 4-4 taken at 355 nm each show two distinct bands: a narrow band ( $X$ ) with no resolved vibrational structure and a higher energy band with some resolved structure. Spectra of band  $X$  taken at 416 nm also showed no vibrational structure. Comparison of the intensities at  $\theta=0^\circ$  and  $90^\circ$  as well as an examination of the anisotropy parameters  $\beta$ , shown graphically for each peak in the top panels of Fig. 4-4, indicate that the higher energy feature is composed of two overlapping transitions labeled  $A$  and  $B$  in Fig. 4-4, with  $A$  having a more positive

anisotropy parameter. Band *A* is vibrationally resolved for both species. Band *B* in the  $\text{Ga}_2\text{P}^-$  spectra is a broad, unresolved feature while it is structured in the  $\text{Ga}_2\text{As}^-$  spectra. The  $\text{Ga}_2\text{P}^-$  spectra are quite similar to the  $\text{Al}_2\text{P}^-$  spectra obtained at 355 nm.<sup>36</sup> In Figure 4-4, feature *A* of  $\text{Ga}_2\text{P}^-$  has the best-resolved vibrational structure yielding a neutral frequency of  $328\text{ cm}^{-1}$ . A hot band transition, labeled as *a*, gives us an anion frequency of  $385\text{ cm}^{-1}$ . It is more difficult to extract vibrational frequencies from the overlapped bands *A* and *B* in the  $\text{Ga}_2\text{As}^-$  spectra, but band *A* is more prominent at  $\theta=0^\circ$  and the first four peaks of this peak are spaced by  $279\text{ cm}^{-1}$ . A more quantitative analysis of this band is presented in the next section.

The use of a cooling channel did not result in the vibrationally-resolved PE spectra for the four-atom clusters  $\text{Ga}_2\text{X}_2^-$ . Figure 4-5 shows the anion photoelectron spectra of  $\text{Ga}_2\text{X}_2^-$  taken at 355 nm and  $\theta=0^\circ$ . Spectra were taken at other polarization angles, but the  $\theta=0^\circ$  spectra are optimal for showing the important spectral features. The spectra show a weak band at low eBE (labeled X) and a stronger band (A) at higher eBE. These spectra resemble those for  $\text{Al}_2\text{P}_2^-$ , the main difference being that the band at higher eBE is vibrationally resolved for  $\text{Al}_2\text{P}_2^-$ .<sup>36</sup>

We are able to resolve vibrational structure in the photoelectron spectra of  $\text{Ga}_2\text{X}_3^-$ . Figure 4-6 shows the photoelectron spectra taken at a wavelength of 355 nm and polarization angles of  $\theta=0^\circ$  and  $90^\circ$ . The spectra taken at  $\theta=90^\circ$  (top panel) shows one electronic state (band X) with an extended progression having a frequency of 213 and 193  $\text{cm}^{-1}$  in  $\text{Ga}_2\text{P}_3$  and  $\text{Ga}_2\text{As}_3$ , respectively. There is additional non-negligible intensity extending toward lower binding energy, more pronounced for  $\text{Ga}_2\text{P}_3$  than for  $\text{Ga}_2\text{As}_3$ . The low eBE signal is more intense in  $\theta=0^\circ$  spectra for both species and appears to

consist of two contributions labeled *a* and *b*. The 266 nm spectrum (dotted line) of  $\text{Ga}_2\text{P}_3^-$  taken at  $\theta=0^\circ$  is shown superimposed on the 355 nm spectra in the lower panel. Peaks *a* and *b* do not appear in the 266 nm spectrum of  $\text{Ga}_2\text{P}_3^-$ .

#### IV. Analysis and Discussion

In this section, the electronic bands and vibrational progressions seen in the  $\text{Ga}_x\text{P}_y^-$  and  $\text{Ga}_x\text{As}_y^-$  PE spectra will be assigned. This process is facilitated by comparison with electronic structure calculations. As discussed in the Introduction, calculations have been performed previously on some of the clusters studied in this paper; the electronic state energies, geometries, and (when available) vibrational frequencies from this earlier work are summarized in Tables 4-(1-5). While these calculated parameters could be directly compared to the experimental PE spectra, it is also very useful to be able to simulate the PE spectra based on electronic structure calculations, and for this the normal coordinate displacements between the anion and various neutral electronic states are needed. Since the force constants required to calculate these displacements are typically not reported, we have carried out our own electronic structure calculations for the anionic and neutral ( $x=1, y=2$ ), (2,1), and (2,3) gallium phosphide and arsenide clusters.

These calculations were performed using the GAUSSIAN98<sup>44</sup> program package. Calculations with GAUSSIAN were performed on the Cray J90 SE cluster at the National Energy Research Scientific Computing Center at the Lawrence Berkeley National Laboratory. The correlation consistent polarized valence basis sets of Dunning and co-workers,<sup>45</sup> denoted by cc-pVxZ where  $x = \text{D}$  (double zeta) and  $\text{T}$  (triple zeta) were used. Additional diffuse functions are especially important for the description of molecular ions

and we therefore mostly used augmented correlation consistent sets of Kendall et al.,<sup>46</sup> denoted by aug-cc-pVxZ ( $x = D, T$ ). The geometries and vibrational frequencies were determined using density functional theory (DFT) with the B3LYP (Becke-3-parameter-Lee-Yang-Parr) exchange correlation functional.<sup>47,48</sup> Except for the (1,2) clusters, only ground states of the neutral clusters were calculated. Our results are listed in Tables 4-(1-5). The tables include normal coordinate displacements  $\Delta Q_i$ , which were calculated using the parallel mode approximation with the anion force constants. This approach allows us to calculate the  $\Delta Q_i$ 's for detachment to neutral excited states for which geometries are available from earlier calculations; these values are also listed in Tables 4-(1-5). Comparison with earlier work shows that our calculations are generally in good agreement with those of Archibong et al.,<sup>31</sup> as expected since the level of theory used in both sets calculations was similar. Agreement with the MRSDCI calculations of Balasubramanian<sup>11,20</sup> is reasonable for  $GaX_2$  and  $Ga_2X_3$  but less so for  $Ga_2X$  species (see Tables 4-3 and 4-4).

Franck-Condon (FC) simulations of the photoelectron spectra were carried out within the parallel-mode approximation assuming harmonic oscillator potentials. Starting from the parameters obtained from the calculations in Tables 4-(1-5), electronic state energies, vibrational frequencies, and normal coordinate changes used as input to the simulations were optimized to best reproduce the experimental PE spectra. The simulations are particularly important for extended progressions where the origin of the state is not definitively observed. When a frequency and normal coordinate change satisfactorily reproduce the spectra, the origin of the transition is shifted by  $\pm 1$  quanta of the neutral frequency and the frequency and normal coordinate change are re-optimized.

Under these conditions, we have found that the experimental data is not as well-reproduced, so error bars for the band origin are assumed to be no larger than  $\pm 1$  quanta of the active neutral frequency.

#### A. $\text{GaX}_2$

Our calculations and the earlier results listed in Tables 4-1 and 4-2 show both  $\text{GaX}_2^-$  species to have a  $^1A_1$  ground state ( $\dots 1b_1^2 4a_1^2 2b_2^2$ ). One-electron detachment from the two highest lying orbitals results in the  $\tilde{X}^2B_2$  ground and  $\tilde{A}^2A_1$  excited neutral states, with all three anion and neutral states having  $C_{2v}$  symmetry. All  $\angle\text{XGX}$  bond angles are acute, implying strong X-X bonds. Term values for the  $^2A_1$  state are calculated to be about 1 eV for  $\text{GaP}_2$  and 0.7 eV for  $\text{GaAs}_2$ , in good agreement with the separation between the two bands in the experimental spectra (Fig. 4-(4-3)), and supporting the assignment of these bands in Section III.

The vibrational progressions of the  $\tilde{X}^2B_2$  states of  $\text{GaP}_2$  and  $\text{GaAs}_2$  are very regular indicating that most of the FC activity is in one vibrational mode; its frequency is  $220\text{ cm}^{-1}$  for  $\text{GaP}_2$  and  $177\text{ cm}^{-1}$  for  $\text{GaAs}_2$ . These values are close to the calculated frequencies for the  $\nu_2$  (Ga-X stretching) mode. (Tables 4-1 and 4-2). The dominance of this mode in the PE spectra is consistent with the calculated normal coordinate displacements. These are considerably larger than for the  $\nu_2$  mode than for the higher frequency  $\nu_1$  mode, since the largest geometry change upon photodetachment to this state is a lengthening of the Ga-X bond accompanied by a decrease in the XGaX bond angle. Our frequencies are also in excellent agreement with the infrared matrix experiments of Li *et al.* where they report the  $\omega_2(a_1)$  fundamentals to be  $220.9\text{ cm}^{-1}$  and  $174.1\text{ cm}^{-1}$  in

GaP<sub>2</sub> and GaAs<sub>2</sub>, respectively.<sup>5</sup> Hence the main vibrational progression in the  $\tilde{X}^2B_2$  PE band of both species is assigned to the  $\nu_2$  mode.

Li *et al.* also observe infrared bands in the matrix absorption spectra of GaP<sub>2</sub> and GaAs<sub>2</sub> at 322 cm<sup>-1</sup> and 231 cm<sup>-1</sup>, respectively, and assigned both bands to the  $\nu_1$  fundamental. This assignment is at odds with the calculations in Tables 4-1 and 4-2 in which considerably higher  $\nu_1$  frequencies are predicted for both species: 690 cm<sup>-1</sup> for GaP<sub>2</sub> and 382.5 cm<sup>-1</sup> for GaAs<sub>2</sub>.<sup>20,31</sup> On the other hand, the experimental IR frequencies are much closer to where the calculations would predict the  $\nu_1\nu_2$  combination band to occur, 349 cm<sup>-1</sup> for GaP<sub>2</sub> and 243 cm<sup>-1</sup> for GaAs<sub>2</sub>, ignoring anharmonic effects. Hence a reassignment of the matrix bands is appropriate.

The  $\tilde{A}^2A_1$  bands of the GaX<sub>2</sub><sup>+</sup> PE spectra are also dominated by a single progression with a frequency of 328 cm<sup>-1</sup> for GaP<sub>2</sub> and 235 cm<sup>-1</sup> for GaAs<sub>2</sub>. Based on comparison with the calculated frequencies and normal coordinate displacements in Tables 4-1 and 4-2, this progression is assigned to the  $\nu_2$  mode for both species. However, while the calculated magnitudes  $|\Delta Q_{1,2}|$  are similar for detachment to the two states (see Table 4-5), the signs of the two displacements are reversed because detachment to the  $\tilde{A}^2A_1$  state results in a shorter Ga-X bond and larger XGaX bond angle.

Fig. 4-7 shows the best fit simulations of the GaX<sub>2</sub><sup>+</sup> photoelectron spectra. The parameters used in these fits are listed in Tables 4-1 and 4-2. The  $\tilde{X}^2B_2$  bands of GaP<sub>2</sub> and GaAs<sub>2</sub> are quite extended, making it difficult to pick out the origin by inspection, but based on our simulations the vibrational origins (indicated by arrows) and hence the

electron affinities are  $1.666 \pm 0.027$  eV and  $1.894 \pm 0.022$  eV for GaP<sub>2</sub> and GaAs<sub>2</sub>, respectively; the error bars correspond to 1 quantum of  $\nu_2$  vibration. Our value for GaP<sub>2</sub> is in good agreement with both calculated values in Table 4-1 obtained by DFT. For GaAs<sub>2</sub>, the experimental electron affinity agrees better with our DFT value, 1.86 eV, than with the other values listed in Table 4-2. Simulations of the  $\tilde{A}^2A_1$  bands yields adiabatic detachment energies of  $2.710 \pm 0.040$  eV and  $2.588 \pm 0.030$  eV for GaP<sub>2</sub> and GaAs<sub>2</sub>, respectively, yielding term values of  $1.044 \pm 0.055$  eV and  $0.694 \pm 0.037$  eV for the  $\tilde{A}^2A_1$  state. The GaP<sub>2</sub> term value determined here agrees with our previously reported value<sup>8,10</sup> of 0.99 eV estimated by the difference in vertical detachment energies of the  $\tilde{X}^2B_2$  and  $\tilde{A}^2A_1$  states.

The PE spectrum showing the second excited  $\tilde{B}^2B_1$  state of GaP<sub>2</sub> is not shown in the current paper, however we mention it briefly in order to reevaluate the term energy. We previously reported the adiabatic detachment energy of the  $B$  state origin to be  $4.324 \pm 0.010$  eV.<sup>10</sup> Subtracting the new electron affinity gives us the improved term value  $T_0(^2B_1)=2.603 \pm 0.029$  eV. In addition, recent calculations by Archibong *et al.*<sup>31</sup> confirm our assignments of the 500 and 589 cm<sup>-1</sup> frequencies to the  $\nu_1(a_1)$  mode of the neutral and anion, respectively, as well as our assignment of the 234 cm<sup>-1</sup> frequency to the  $\nu_2(a_1)$  mode of the neutral. All term values, vibrational frequencies, and assignments for GaP<sub>2</sub> and GaAs<sub>2</sub> are tabulated in Table 4-1 and 4-2, respectively.

Finally, we consider what the PE spectra reveal concerning the geometries of anion and neutral states of GaP<sub>2</sub> and GaAs<sub>2</sub>. For GaP<sub>2</sub>, the magnitudes of the  $\Delta Q_i$ 's used in our best-fit simulations are similar to those obtained from electronic structure

calculations, with a slightly larger  $\Delta Q_2$  needed to fit the  ${}^2B_2$  band, and a slightly smaller  $\Delta Q_2$  required for the  ${}^2A_1$  band. Although our simulations do not depend on the sign of the  $\Delta Q_i$ 's, we assume the signs from the electronic structure calculations are correct. Hence, assuming the calculated anion geometries are correct, we can extract geometries for the  $\tilde{X}^2B_2$  and  $\tilde{A}^2A_1$  states from our signed values of the  $\Delta Q_i$ 's. These geometries are in fact quite close to the calculated geometries, and given the possible inaccuracies associated with our use of the parallel mode approximation we cannot claim that the structures obtained by our analysis represent an improvement over the calculations.

Our best-fit  $\Delta Q_i$ 's for detachment to the  $\tilde{X}^2B_2$  state of GaAs<sub>2</sub> are in excellent agreement with those derived from Balasubramanian's<sup>20</sup> electronic structure values in Table 4-2, indicating that his calculated geometries for the anion and neutral ground state are likely to be accurate. However, while the experimental frequency of 234 cm<sup>-1</sup> for the  $\tilde{A}^2A_1$  band agrees well with Balasubramanian's calculated frequency of 238.7 cm<sup>-1</sup> for the  $\nu_2$  mode, the simulated  $\nu_2$  progression using his geometry is too long and  $\Delta Q_2$  must be reduced significantly, from 0.2302 to 0.130 Å·amu<sup>1/2</sup>. Converting our normal coordinate displacements to geometries (see Table 4-7) shows that the increase in bond angle and decrease in Ga-As bond length upon detachment to the  $\tilde{A}^2A_1$  state are smaller than predicted in Balasubramanian's calculation.

#### B. Ga<sub>2</sub>X

The experimental spectra in Fig. 4-4 and electronic structure calculations in Table 4-3 and 4-4 show that the Ga<sub>2</sub>X<sup>-</sup> PE spectra are more complex than the GaX<sub>2</sub><sup>-</sup> spectra. The Ga<sub>2</sub>X<sup>-</sup> PE spectra show evidence for transitions to three neutral electronic states: the



ground state, responsible for band X, and two low-lying excited states that result in the overlapped bands A and B in Fig. 4-4. While band X is of similar appearance in the  $\text{Ga}_2\text{P}^+$  and  $\text{Ga}_2\text{As}^+$  spectra, the excited state bands are quite different, with the somewhat surprising result that more vibrational structure is seen in the  $\text{Ga}_2\text{As}^+$  spectra. The overall appearance of the  $\text{Ga}_2\text{P}^+$  spectrum is very similar to the  $\text{Al}_2\text{P}^+$  PE spectrum.<sup>36</sup> This similarity suggests that the same state assignments for  $\text{Al}_2\text{P}$  be applied to  $\text{Ga}_2\text{P}$ , namely that band X is the transition to the  $\tilde{X}^2B_2$  ground state, while the vibrationally resolved band A and broad, unresolved band B result from transitions to the  $\tilde{A}^2A_1$  and  $\tilde{B}^2B_1$  excited state, respectively. Carrying this line of reasoning further, it is reasonable to assign band X in the  $\text{Ga}_2\text{As}^+$  spectrum to the transition to the  $\tilde{X}^2B_2$  ground state of  $\text{Ga}_2\text{As}$ , with the excited state assignments being less obvious.

Confirmation of these assignments by comparison with electronic structure calculations is more problematic than for the  $\text{GaX}_2^+$  spectra. Our calculations on both  $\text{Ga}_2\text{X}^+$  anions yield a  $^1A_1$  ground state with  $C_{2v}$  symmetry and the molecular orbital configuration  $(\dots 3a_1^2 1b_2^2 1b_1^2 2b_2^2)$ . However, the neutral species are more complicated. Balasubramanian<sup>30</sup> find that  $\text{Ga}_2\text{As}$  has two nearly degenerate states: a  $^2A'$  ground state of  $C_s$  symmetry, with unequal Ga-As bond lengths, and a  $^2B_2$  state with  $C_{2v}$  symmetry. The  $^2B_2$  state was found to be the ground state at the MRSDCI+Q level of theory, with the  $^2A'$  state lying only 0.025 eV higher. Our DFT calculations on  $\text{Ga}_2\text{P}$  and  $\text{Ga}_2\text{As}$  yield a  $^2B_2$  ground state when restricted to  $C_{2v}$  symmetry, but the  $\nu_3$  frequency is imaginary in both cases indicating that the  $C_{2v}$  structure is not an energy minimum. At the MRSDCI level, Feng<sup>11</sup> finds a  $^2B_1$  ground state for  $\text{Ga}_2\text{P}$  and a  $^2B_2$  excited state lying only 0.09 eV higher, but these calculations were restricted to  $C_{2v}$  symmetry.

We simulated the  $\text{Ga}_2\text{As}^-$  spectrum using Balasubramanian's geometries and frequencies for the anion and the  $^2A'$  and  $^2B_2$  neutral states<sup>20</sup> (since no frequencies are given for the neutral  $^2B_2$  state, we used the anion vibrational frequencies), and the force constants from our DFT calculation on the anion. Simulation of the  $^2A'$  state yields an extended progression in the  $\nu_3$  mode which would have been easily seen in our spectrum. On the other hand, simulation of the  $^2B_2$  band using the *ab initio* parameters yields a single broad, unstructured peak, similar to the experimental band *X*. The width of the simulated peak depends strongly on the assumed anion temperature. The structured bands *A* and *B* were fit with anion temperature  $T = 250$  K (see below), so this temperature was also used to fit band *X*. The best-fit simulation, shown in Fig. 4-8, was obtained with the  $\Delta Q_i$  values in Table 4-6, both of which are smaller than the corresponding *ab initio* values. Using Balasubramanian's anion geometry as a reference, the optimized geometry of the  $\text{Ga}_2\text{As}$  ground state is given in Table 4-7; it differs from Balasubramanian's calculated geometry for the neutral  $^2B_2$  state (Table 4-4) in that its bond angle is about  $13^\circ$  larger. Nonetheless, assigning band *X* to the  $^2B_2$  state is still reasonable since its calculated properties are in better agreement with experiment than any other state, and the same assignment holds for band *X* in the  $\text{Ga}_2\text{P}^-$  PE spectrum. Based on the simulation of band *X*, the electron affinity of  $\text{Ga}_2\text{As}$  is  $2.428 \pm 0.020$  eV, and we estimate the electron affinity of  $\text{Ga}_2\text{P}$  to be  $2.481 \pm 0.020$  eV.

The best-fit simulation of band *A* in the  $\text{Ga}_2\text{P}^-$  PE spectrum, shown in Fig. 4-8, yields anion and neutral frequencies of  $385$  and  $328$   $\text{cm}^{-1}$ , respectively, for the  $\nu_1$  mode, with the anion frequency derived from the hot band transition *a*. The frequency of the  $\nu_2$  mode was assumed to be  $56$   $\text{cm}^{-1}$ , the same value as was calculated for the anion. The

normal coordinate displacements  $\Delta Q_1$  and  $\Delta Q_2$  (Table 4-6) were chosen to reproduce the length of the progression and the widths of the individual peaks, respectively. The term value for the neutral state responsible for band A is 0.268 eV. As stated above, based on comparison with the  $\text{Al}_2\text{P}^+$  PE spectrum, this state is assigned as the  $\tilde{A}^2A_1$  state. While this state has not been calculated for  $\text{Ga}_2\text{P}$ , we can determine its geometry from our normal coordinate displacements and the calculated anion geometry in Table 4-3, assuming the signs of the  $\Delta Q_i$ 's are the same as for detachment to the  $\tilde{A}^2A_1$  state of  $\text{Al}_2\text{P}$ ;<sup>49</sup> this geometry is given in Table 4-7.

The differing anisotropy parameters for the overlapped bands *A* and *B* in the  $\text{Ga}_2\text{As}^+$  PE spectra confirm that they arise from transitions to distinct electronic states. The two bands were simulated by assuming activity in a single high frequency vibrational mode with a frequency of 200  $\text{cm}^{-1}$  for band A and 279  $\text{cm}^{-1}$  for band B, and an anion vibrational frequency of 245  $\text{cm}^{-1}$ ; these presumably correspond to the  $\nu_1$  modes for both states. In addition, a small  $\Delta Q_2$  value was used to match the experimental peak widths (Table 4-6). Term values for bands *A* and *B* were found to be 0.209 and 0.280 eV, respectively. The 200  $\text{cm}^{-1}$  frequency for band *A* agrees with the calculated  $\nu_1$  frequency of 194.5  $\text{cm}^{-1}$  for the  $^2B_1$  state of  $\text{Ga}_2\text{As}$ .<sup>20</sup> Based on this comparison, one is tempted to assign band *A* to the  $^2B_1$  state and band *B* to the  $^2A_1$  state. However, the normal coordinate displacements used to simulate band *A* are noticeably smaller than those found using Balasubramanian's anion and neutral geometries. As a consequence the change in bond angle upon photodetachment (Table 4-7) is considerably smaller than predicted by his calculations, so this assignment, like the assignment of band *X*, is reasonable but not as compelling as the assignments made for the  $\text{GaX}_2^+$  spectra.

### C. $\text{Ga}_2\text{X}_2^-$

The anion photoelectron spectra of  $\text{Ga}_2\text{X}_2^-$  at 355 nm are not vibrationally resolved, even using the liquid-nitrogen cooled ion source configuration. We can nonetheless discuss band assignments based on calculations by Archibong and St-Amant<sup>32</sup> on  $\text{Ga}_2\text{P}_2^-$  and our PE spectra of isovalent  $\text{Al}_2\text{P}_2^-$ .<sup>36</sup> The absence of vibrational structure in the  $\text{Ga}_2\text{X}_2^-$  PE spectra is at first surprising, given that clear vibrational structure was seen in the PE spectra of  $\text{Si}_4^-$  and  $\text{Ge}_4^-$ .<sup>12,13,50</sup> However, while photodetachment of  $\text{Si}_4^-$  and  $\text{Ge}_4^-$  involves transitions between planar rhombus ( $D_{2h}$ ) geometries of the anion and neutral species, the calculations by Archibong on  $\text{Ga}_2\text{P}_2$  and  $\text{Al}_2\text{P}_2$  indicate that the anion ground states of both species are non-planar, distorted tetrahedral  $^3B_1$  states with  $C_{2v}$  symmetry, the  $^1A_g$  neutral ground states have planar rhombus geometries, and most of the low-lying excited neutral states have  $C_{2v}$  structures.<sup>32,51</sup> Hence, large changes upon the dihedral angle upon photodetachment can result in extensive progressions in the low-frequency umbrella ( $\nu_3$ ) mode that would not be resolved in our spectrum, since its calculated frequency is around  $50\text{ cm}^{-1}$  in the various  $\text{Ga}_2\text{P}_2$  anion and neutral states. On the basis of calculated energetics, band X in the  $\text{Ga}_2\text{P}_2^-$  spectrum was assigned<sup>32</sup> to a transition from the anion  $^3B_1$  state to the neutral  $^1A_g$  ground state, while the more intense band A was assigned to a transition to the neutral  $^3B_2$  state with a distorted tetrahedral structure.

The  $\text{Ga}_2\text{P}_2^-$  and  $\text{Al}_2\text{P}_2^-$  are similar in that each has a low intensity peak (band X) at low eBE followed by a more intense band (band A) at higher eBE. However, band A in the  $\text{Al}_2\text{P}_2^-$  spectrum is vibrationally resolved with a distinct progression in the  $320\text{ cm}^{-1}$   $\nu_2$  mode and was assigned to the neutral  $^3A_2$  state.<sup>36</sup> The calculated dihedral angle for this state was only  $10^\circ$  larger than in the anion, and simulations showed that progressions in

the low-frequency umbrella mode were not long enough to wash out the higher frequency  $\nu_2$  progression. The absence of an analogous progression in band A of the  $\text{Ga}_2\text{P}_2^-$  spectrum suggests a larger change in dihedral angle upon photodetachment to the neutral excited state. Unfortunately these angles were not given in Archibong's paper on  $\text{Ga}_2\text{P}_2$  species.

#### D. $\text{Ga}_2\text{X}_3$

The  $\text{Ga}_2\text{X}_3^-$  PE spectra are each dominated by a single band (X) which shows a well-resolved progression in a single vibrational mode for both species. This band presumably results from a photodetachment transition between anion and neutral states of the same symmetry, with geometry changes that activate only one totally symmetric mode in the PE spectrum. Electronic structure calculations on  $\text{Ga}_2\text{As}_3$  predict a  $^2A_2''$  ground state in  $D_{3h}$  symmetry with a trigonal bipyramidal structure,<sup>19,26,34</sup> while calculations on  $\text{Ga}_2\text{P}_3$  predict a similar state to be nearly degenerate with a Jahn-Teller distorted  $^2B_1$  state.<sup>21</sup> In addition, matrix electron spin resonance experiments on  $\text{Ga}_2\text{As}_3$  indicate a  $D_{3h}$  structure.<sup>6</sup> The appearance of band X in the PE spectra is therefore consistent with the anions of both species having trigonal bipyramidal structures, and our DFT electronic structure calculations (Table 4-5) find this to be the case, with  $^1A_1'$  closed shell ground states found for both anions. Our DFT calculations for the neutral species yield states with geometries very similar to the  $^2A_2''$  states calculated previously.

Simulations of band X for both species are shown in Fig. 4-9. The geometries and frequencies used in these simulations are very close to those obtained in our DFT calculations. Hence the simulations confirm that band X results from transitions between trigonal bipyramidal structures of the anion and neutral. The vibrational origins of band

X occur at  $2.991 \pm 0.026$  eV for X=P and  $2.783 \pm 0.024$  eV for X=As, in reasonable agreement with our calculated energetics.

The simulations are dominated by a progression in the  $\nu_2$  mode, a totally symmetric Ga-Ga stretch mode activated by the substantial decrease in the Ga-Ga bond length upon photodetachment. This is consistent with from the nature of the  $a_2''$  orbital from which detachment occurs, which is antibonding between the apical Ga and equatorial P atoms.<sup>34</sup> We note that the photoelectron spectrum of  $\text{Si}_5^-$  also shows vibrational structure attributed to similar structures and geometry changes upon photodetachment.<sup>13</sup>

The vibrational origins given above correspond to the electron affinities of  $\text{Ga}_2\text{P}_3$  and  $\text{Ga}_2\text{As}_3$  only if band X represents the transition between the anion and neutral ground electronic states. The presence of bands *a* and *b* complicates this issue. The photoelectron angular distributions associated with these bands differs from that of band X, with the relative intensities of bands *a* and *b* clearly higher at  $\theta=0^\circ$  than at  $\theta=90^\circ$ . Hence, these two bands must arise from a different electronic photodetachment transition than band X, although it is less clear if they themselves arise from two distinct electronic transitions or instead represent a single extended transition.

There are several possible origins for these bands. They can originate from low-lying excited electronic states of the anion, or from transitions to lower-lying neutral states than the  $^2A_2'' D_{3h}$  state responsible for band X. As mentioned above, calculations by Feng<sup>21</sup> on  $\text{Ga}_2\text{P}_3$  predict a  $^2B_1$  state to be nearly degenerate with the  $^2A_2''$  state; the  $^2B_1$  state arises from Jahn-Teller distortion of a low-lying  $^2E'$  state of  $\text{Ga}_2\text{P}_3$ . It is certainly possible that bands *a* and *b*, which show no vibrational structure, arise from

photodetachment from the anion ground state to this  ${}^2B_1$  state, since a transition to a structure of different symmetry generally results in the activation of multiple vibrational modes. However, the apparent origin of band *b* is more than 0.5 eV below that of band *X* in the  $\text{Ga}_2\text{P}_3^-$  PE spectrum, about an order of magnitude larger than the calculated splitting between the  ${}^2B_1$  and  ${}^2A_2''$  states. Alternatively, since Feng's calculation on neutral  $\text{Ga}_2\text{P}_3$  indicates the presence of a low-lying, unfilled  $e'$  orbital, there is likely to be a low-lying  ${}^3E'$  electronic state of the anion which can undergo Jahn-Teller distortion, and transitions from this state to the neutral  ${}^2A_2''$  state are also possible candidates for bands *a* and *b*. Similar considerations apply to the  $\text{Ga}_2\text{As}_3^-$  PE spectra, although no low-lying  ${}^3E'$  states were found in calculations on  $\text{Ga}_2\text{As}_3$ .<sup>19</sup> Finally, bands *a* and *b* bear some resemblance to the PE spectra of the tetra-atomic  $\text{Ga}_2\text{X}_2^-$  species, even if they occur at somewhat lower eBE than the bands in the  $\text{Ga}_2\text{X}_2^-$  PE spectra. Hence these bands may result from photodissociation to vibrationally hot  $\text{Ga}_2\text{X}_2^-$  fragments followed by photodetachment of these fragments. This explanation is consistent with the observation that bands *a* and *b* are not seen at 266 nm.

## V. Conclusions

We have presented and discussed the anion photoelectron spectra of  $\text{GaX}_2^-$ ,  $\text{Ga}_2\text{X}^-$ ,  $\text{Ga}_2\text{X}_2^-$ , and  $\text{Ga}_2\text{X}_3^-$  ( $\text{X}=\text{P},\text{As}$ ). With the aid of electronic structure calculations and Franck-Condon simulations, we identify the structural and electronic symmetry of the electronic states observed and where possible have assigned the vibrational modes. The  $\text{GaX}_2^-$  anion and neutral species are shown unambiguously to be of  $\text{C}_{2v}$  symmetry and we assign the two neutral states observed to the  $\tilde{X}^2B_2$  and  $\tilde{A}^2A_1$  states. Assignments of the ground and excited state bands in the  $\text{Ga}_2\text{P}^-$  and  $\text{Ga}_2\text{As}^-$  PE spectra

were based on comparison to recent experimental work on  $\text{Al}_2\text{P}^-$  as well as electronic structure calculations, with all assigned anion and neutral states having  $C_{2v}$  symmetry. The  $\text{Ga}_2\text{X}$  species appear to be problematic from the perspective of electronic structure calculations, so the assignments are not as firm as for the  $\text{GaX}_2$  species. The absence of vibrational structure in the  $\text{Ga}_2\text{X}_2^-$  PE spectra is discussed in light of recent calculations predicting a non-planar, distorted tetrahedral ground state for the  $\text{Ga}_2\text{P}_2^-$  anion, in contrast to the planar rhombus structures found for  $\text{Si}_4^-$  and  $\text{Ge}_4^-$ . Finally, the dominant bands in the  $\text{Ga}_2\text{X}_3^-$  spectra are vibrationally resolved and are attributed to transitions between anion and neutral states with trigonal bipyramidal geometries, similar to  $\text{Si}_5^-$ .



Table 4-1. Comparison of geometries and energy separations of GaP<sub>2</sub>/GaP<sub>2</sub>.

Reference	Species	Stat <sup>e</sup>	Level	$\theta$ (°)	Ga-P (Å)	P-P (Å)	$\Delta E$ (eV)	$\nu_1(a_1)$	$\nu_2(a_1)$	$\nu_3(b_2)$	$\beta_{355}$
Feng <i>et al.</i> <sup>a</sup>	GaP <sub>2</sub>	<sup>2</sup> B <sub>2</sub>	MRSDCI	43.9	2.658	1.987	0.0				
	GaP <sub>2</sub>	<sup>2</sup> A <sub>1</sub>	MRSDCI	56.0	2.308	2.167	1.07				
	GaP <sub>2</sub>	<sup>2</sup> B <sub>1</sub>	MRSDCI	55.8	2.400	2.246	2.33				
Archibong <i>et al.</i> <sup>b</sup>	GaP <sub>2</sub>	<sup>1</sup> A <sub>1</sub>	B3LYP	48.9	2.481	2.056	-1.73 (-1.75)	590	260	240	
	GaP <sub>2</sub>	<sup>2</sup> B <sub>2</sub>	B3LYP	43.6	2.657	1.972	0.0 (0.0)	690	210	139	
	GaP <sub>2</sub>	<sup>2</sup> A <sub>1</sub>	B3LYP	54.9	2.311	2.129	0.98 (.78)	532	328	355	
	GaP <sub>2</sub>	<sup>2</sup> B <sub>1</sub>	MP2-F19 <sup>c</sup>	49.8	2.574	2.168	2.81(2.55)	513	247	249	
	GaP <sub>2</sub>	<sup>2</sup> B <sub>1</sub>	MP2-F19 <sup>c</sup>	49.8	2.574	2.168	2.81(2.55)	513	247	249	
Theory	GaP <sub>2</sub>	<sup>1</sup> A <sub>1</sub>	B3LYP	48.9	2.490	2.061	-1.722	584	258	237	
	GaP <sub>2</sub>	<sup>2</sup> B <sub>2</sub>	B3LYP	43.5	2.667	1.980	0	685	208	137	
	GaP <sub>2</sub>	<sup>2</sup> A <sub>1</sub>	B3LYP	54.9	2.317	2.135	0.997	526	326	349	
Experiment <sup>d</sup>	GaP <sub>2</sub>	<sup>1</sup> A <sub>1</sub>	PES				-1.666 ± 0.041	589			
	GaP <sub>2</sub>	<sup>2</sup> B <sub>2</sub>	PES				0.0		222		-0.81
	GaP <sub>2</sub>	<sup>2</sup> B <sub>2</sub>	MATRIX <sup>e</sup>	52			0.0	322 <sup>f</sup>	220.9		
	GaP <sub>2</sub>	<sup>2</sup> A <sub>1</sub>	PES				1.044 ± 0.101		328		+0.18
	GaP <sub>2</sub>	<sup>2</sup> B <sub>1</sub>	PES				2.603 ± 0.051	500	234		
	GaP <sub>2</sub>	<sup>2</sup> B <sub>1</sub>	PES				2.603 ± 0.051	500	234		

<sup>a</sup> Reference 11.

<sup>b</sup> Ref. 31. CCSD(T)-FC/B3LYP value in parentheses. Frequencies calculated with B3LYP.

<sup>c</sup> CCSD(T)/MP2-F19 values in parentheses. Frequencies calculated with MP2-F19.

<sup>d</sup> This work, except as noted.

<sup>e</sup> Reference 5.

<sup>f</sup> See discussion in text.

Table 4-2. Comparison of geometries and energy separations of GaAs<sub>2</sub>/GaAs<sub>2</sub>.

Reference	Species	State	Level	$\theta$ (°)	Ga-As (Å)	As-As (Å)	$\Delta E$ (eV)	$\nu_1(a_1)$	$\nu_2(a_1)$	$\nu_3(b_2)$	$\beta_{\text{ass}}$
Balasubramanian <sup>a</sup>	GaAs <sub>2</sub>	<sup>1</sup> A <sub>1</sub>	MRSDCI	52.7	2.586	2.296	-1.50(-1.61)	329.6	198.1	152.1	
	GaAs <sub>2</sub>	<sup>2</sup> B <sub>2</sub>	MRSDCI	45.9	2.80	2.184	0.0	382.5	162.5	80.3	
	GaAs <sub>2</sub>	<sup>2</sup> A <sub>1</sub>	MRSDCI	60.7	2.4	2.425	0.71(0.65)	311.6	238.7	161.9	
	GaAs <sub>2</sub>	<sup>2</sup> B <sub>1</sub>	MRSDCI								
Meier <sup>b</sup>	GaAs <sub>2</sub>	<sup>1</sup> A <sub>1</sub>	FCle	49.6	2.73	2.29	-1.42				
	GaAs <sub>2</sub>	<sup>2</sup> B <sub>2</sub>	FCle	46.6	2.27	2.87	0.0				
	GaAs <sub>2</sub>	<sup>2</sup> A <sub>1</sub>	FCle	58.4	2.44	2.50	0.65				
Theory	GaAs <sub>2</sub>	<sup>1</sup> A <sub>1</sub>	B3LYP	52.2	2.601	2.290	-1.856	331	200	150	
	GaAs <sub>2</sub>	<sup>2</sup> B <sub>2</sub>	B3LYP	46.4	2.783	2.195	0.000	381	166	87	
Experiment <sup>c</sup>	GaAs <sub>2</sub>	<sup>1</sup> A <sub>1</sub>	PES				-1.894 ± 0.033				
	GaAs <sub>2</sub>	<sup>2</sup> B <sub>2</sub>	PES				0.0		176		-0.65
	GaAs <sub>2</sub>	<sup>2</sup> B <sub>2</sub>	MATRIX <sup>d</sup>	38			0.0		174.1		
	GaAs <sub>2</sub>	<sup>2</sup> A <sub>1</sub>	PES				0.694 ± 0.077		235		+0.70
	GaAs <sub>2</sub>	<sup>2</sup> B <sub>1</sub>	PES								

<sup>a</sup> Reference 11. Values in parenthesis are MRSDCI+Q.<sup>b</sup> Reference 10.<sup>c</sup> This work, except as noted.<sup>d</sup> Reference 5.

Table 4-3. Comparison of geometries and energy separations of Ga<sub>2</sub>P/Ga<sub>2</sub>P<sup>+</sup>.

Reference	Species	State	Level	$\theta$ (°)	Ga-P (Å)	Ga-Ga (Å)	$\Delta E$ (eV)	$v_1(a_1)$	$v_2(a_1)$	$v_3(b_2)$
Feng <i>et al.</i> <sup>a</sup>	Ga <sub>2</sub> P	<sup>2</sup> B <sub>1</sub>	MRSDCI	111.0	2.419		0.0			
	Ga <sub>2</sub> P	<sup>2</sup> B <sub>2</sub>	MRSDCI	90.0	2.300		0.09			
	Ga <sub>2</sub> P	<sup>2</sup> $\Pi_u$	MRSDCI	180.0	2.391		0.16			
Theory	Ga <sub>2</sub> P <sup>+</sup>	<sup>1</sup> A <sub>1</sub>	B3LYP	108.2	2.283	3.700	-2.449	323	56	396
	Ga <sub>2</sub> P	<sup>2</sup> B <sub>2</sub>	B3LYP	99.9	2.282	3.496	0.000	312	57	173i
Experiment <sup>b</sup>	Ga <sub>2</sub> P <sup>+</sup>	<sup>1</sup> A <sub>1</sub>	PES				-2.481 ± 0.015	375 ± 25		
	Ga <sub>2</sub> P	X	PES				0.0			
	Ga <sub>2</sub> P	X	MATRIX	85.7			0.0			280.5
	Ga <sub>2</sub> P	A	PES				0.268 ± 0.025	311		
	Ga <sub>2</sub> P	B	PES				-0.4 <sup>c</sup>			

<sup>a</sup> Reference 11.

<sup>b</sup> All work is ours except matrix work from Reference<sup>5</sup>.

<sup>c</sup> Vertical detachment energy with respect to the neutral ground state.

Table 4.4. Comparison of geometries and energy separations of Ga<sub>2</sub>As/Ga<sub>2</sub>As<sup>+</sup>.

Reference	Species	State	Level	$\theta$ (°)	Ga-As (Å)	Ga-Ga (Å)	$\Delta E$ (eV)	$v_1(a_1)$	$v_2(a_1)$	$v_3(b_2)$
Balasubramanian <sup>a</sup>	Ga <sub>2</sub> As <sup>+</sup>	<sup>1</sup> A <sub>1</sub>	MRSDCI	98.5	2.37		-2.20(-2.17)	240.5	46.5	275.3
	Ga <sub>2</sub> As	<sup>2</sup> A <sub>1</sub>	MRSDCI	90.3	2.83, 2.534		0.0(0.025)	182.7	50.4	265.6
	Ga <sub>2</sub> As	<sup>2</sup> B <sub>2</sub>	MRSDCI	79.9	2.407		0.09(0.0)			
	Ga <sub>2</sub> As	<sup>2</sup> B <sub>1</sub>	MRSDCI	108.2	2.52		0.16(0.22)	194.5	43.0	225.0
Theory	Ga <sub>2</sub> As <sup>+</sup>	<sup>1</sup> A <sub>1</sub>	B3LYP	106.3	2.384	3.816	-2.429	244	46.7	277
	Ga <sub>2</sub> As	<sup>2</sup> B <sub>2</sub>	B3LYP	95.4	2.392	3.540	0.000	229	46.7	173.2i
Experiment <sup>b</sup>	Ga <sub>2</sub> As <sup>+</sup>	<sup>1</sup> A <sub>1</sub>	PES				-2.457 ± 0.015	245		
	Ga <sub>2</sub> As	X	PES				0.0			
	Ga <sub>2</sub> As	X	MATRIX					160		204.7
	Ga <sub>2</sub> As	A	PES				0.209 ± 0.040	200		
	Ga <sub>2</sub> As	B	PES				0.28	279		
	Ga <sub>2</sub> As									

<sup>a</sup> Reference<sup>20</sup>.

<sup>b</sup> All work is ours except matrix work from Reference<sup>5</sup>.

Table 4-5. Comparison of geometries and energy separations of Ga<sub>2</sub>As<sub>3</sub>/Ga<sub>2</sub>As<sub>3</sub><sup>+</sup> and Ga<sub>2</sub>P<sub>3</sub>/Ga<sub>2</sub>P<sub>3</sub><sup>+</sup>

Reference	Species	State	Level	P-P (Å)	Ga-Ga (Å)	Ga-P (Å)	ΔE (eV)	Frequencies (cm <sup>-1</sup> ) <sup>a</sup>
Theory	Ga <sub>2</sub> P <sub>3</sub> <sup>-</sup>	<sup>1</sup> A <sub>1</sub> <sup>+</sup>	B3LYP	2.248	4.488	2.593	-2.912	508, 182 (A <sub>1</sub> <sup>+</sup> ) 279 (A <sub>2</sub> <sup>''</sup> ) 101, 391 (E <sup>+</sup> ) 206 (E <sup>''</sup> )
		<sup>2</sup> A <sub>2</sub> <sup>''</sup>	B3LYP	2.317	4.183	2.483	0.0	470, 210 (A <sub>1</sub> <sup>+</sup> ) 243 (A <sub>2</sub> <sup>''</sup> ) 117, 365 (E <sup>+</sup> ) 262 (E <sup>''</sup> )
Experiment	Ga <sub>2</sub> P <sub>3</sub> <sup>-</sup> Ga <sub>2</sub> P <sub>3</sub>	<sup>1</sup> A <sub>1</sub> <sup>+</sup>	PES				-2.991	
		<sup>2</sup> A <sub>2</sub> <sup>''</sup>	PES				0.0	213
Theory	Ga <sub>2</sub> As <sub>3</sub> <sup>-</sup>	<sup>1</sup> A <sub>1</sub> <sup>+</sup>	B3LYP	As-As (Å) 2.486	Ga-Ga (Å) 4.619	Ga-As (Å) 2.719	-2.694 ±0.026	169, 297 (A <sub>1</sub> <sup>+</sup> ) 205 (A <sub>2</sub> <sup>''</sup> ) 82, 226 (E <sup>+</sup> ) 124 (E <sup>''</sup> )
		<sup>2</sup> A <sub>2</sub> <sup>''</sup>	B3LYP	2.558	4.279	2.600	0.0	286, 190 (A <sub>1</sub> <sup>+</sup> ) 184 (A <sub>2</sub> <sup>''</sup> ) 100, 220 (E <sup>+</sup> ) 164 (E <sup>''</sup> )
Experiment	Ga <sub>2</sub> As <sub>3</sub> <sup>-</sup> Ga <sub>2</sub> As <sub>3</sub>	<sup>1</sup> A <sub>1</sub> <sup>+</sup>	PES				-2.783 ±0.024	
		<sup>2</sup> A <sub>2</sub> <sup>''</sup>	PES				0.0	193

<sup>a</sup> Active vibrational mode in PE spectrum in bold.

Table 4-6. Photoelectron spectra simulation parameters for active modes in Ga<sub>2</sub>X<sup>+</sup> and GaX<sub>2</sub><sup>+</sup>

Molecule	State	PES-FCF active modes				Temp (K)
		$\nu_1$ (cm <sup>-1</sup> )	$\Delta Q_1$ (Å·amu <sup>1/2</sup> ) <sup>a</sup>	$\nu_2$ (cm <sup>-1</sup> )	$\Delta Q_2$ (Å·amu <sup>1/2</sup> ) <sup>a</sup>	
GaP <sub>2</sub> <sup>+</sup>	<sup>1</sup> A <sub>1</sub>	590		260		
GaP <sub>2</sub>	<sup>2</sup> B <sub>2</sub>	690	0.029	222 <sup>b</sup>	-0.220 (-0.188)	275
GaP <sub>2</sub>	<sup>2</sup> A <sub>1</sub>	532	-0.023	328 <sup>b</sup>	0.160 (0.186)	275
GaAs <sub>2</sub> <sup>+</sup>	<sup>1</sup> A <sub>1</sub>	330		198		
GaAs <sub>2</sub>	<sup>2</sup> B <sub>2</sub>	386	0.033	176 <sup>b</sup>	-0.191 (-0.189)	300
GaAs <sub>2</sub>	<sup>2</sup> A <sub>1</sub>	312	-0.037 (-0.056)	235 <sup>b</sup>	0.130 (0.230)	300
Ga <sub>2</sub> P <sup>+</sup>	<sup>1</sup> A <sub>1</sub>			375 <sup>b</sup>		
Ga <sub>2</sub> P	<sup>2</sup> B <sub>2</sub>		0.010		-0.181	
Ga <sub>2</sub> P	<sup>2</sup> B <sub>1</sub>		0.051	311 <sup>b</sup>	0.055	275
Ga <sub>2</sub> As <sup>+</sup>	<sup>1</sup> A <sub>1</sub>	46.5		240.5		250
Ga <sub>2</sub> As	X		0.013 (0.043)		-0.191 (-0.4261)	250
Ga <sub>2</sub> As	A	46.7	0.090 (0.183)	200 <sup>b</sup>	0.061 (0.306)	250
Ga <sub>2</sub> As	B		0.080	279 <sup>b</sup>	0.065	

<sup>a</sup> Normal coordinate displacements from electronic structure calculations shown in parentheses when different from those used in best-fit simulation.

<sup>b</sup> Observed experimental progression.

Table 4-7. Neutral structures based on best-fit normal coordinate displacements using calculated anion geometries as reference.

Species	State <sup>a</sup>	$\theta$ (°)	Ga-P (Å)	P-P (Å)
GaP <sub>2</sub> <sup>-b</sup>	<sup>1</sup> A <sub>1</sub>	48.9	2.481	2.056
GaP <sub>2</sub>	<sup>2</sup> B <sub>2</sub>	44.6	2.719	2.068
GaP <sub>2</sub>	<sup>2</sup> A <sub>1</sub>	52.5	2.324	2.054
		$\theta$ (°)	Ga-As (Å)	As-As (Å)
GaAs <sub>2</sub> <sup>-c</sup>	<sup>1</sup> A <sub>1</sub>	52.7	2.586	2.296
GaAs <sub>2</sub>	<sup>2</sup> B <sub>2</sub>	46.4	2.785	2.198
GaAs <sub>2</sub>	<sup>2</sup> A <sub>1</sub>	56.9	2.489	2.373
		$\theta$ (°)	Ga-P (Å)	Ga-Ga (Å)
Ga <sub>2</sub> P <sup>-d</sup>	<sup>1</sup> A <sub>1</sub>	108.2	2.283	3.700
Ga <sub>2</sub> P	(X) <sup>2</sup> B <sub>2</sub>	N/C		
Ga <sub>2</sub> P	(A) <sup>2</sup> A <sub>1</sub>	109.1	2.327	3.798
		$\theta$ (°)	Ga-As (Å)	Ga-Ga (Å)
Ga <sub>2</sub> As <sup>-e</sup>	<sup>1</sup> A <sub>1</sub>	98.5	2.37	3.591
Ga <sub>2</sub> As	(X) <sup>2</sup> B <sub>2</sub>	93.1	2.401	3.486
Ga <sub>2</sub> As	(A) <sup>2</sup> B <sub>1</sub>	100.7	2.429	3.740

<sup>a</sup> For Ga<sub>2</sub>X species, corresponding band in PE spectrum is indicated in parentheses.

<sup>b</sup> Anion geometry from Ref. <sup>31</sup>

<sup>c</sup> Anion geometry from Ref. <sup>11</sup>

<sup>d</sup> Anion geometry from our DFT (B3LYP) calculation

<sup>e</sup> Anion geometry from Ref. <sup>20</sup>

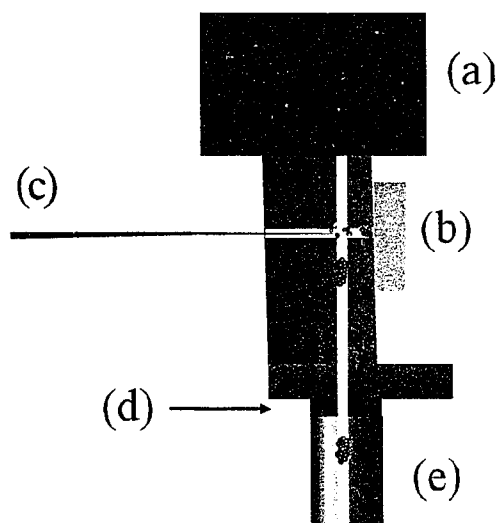


Figure 4-1. Diagram of the liquid nitrogen cooled clustering channel coupled with the laser ablation disc source. The diagram is labeled as follows: (a) pulsed piezo electric valve, (b) disc ablation target, (c) incident laser beam, (d) Delrin insulating disc, and (e) copper clustering channel.



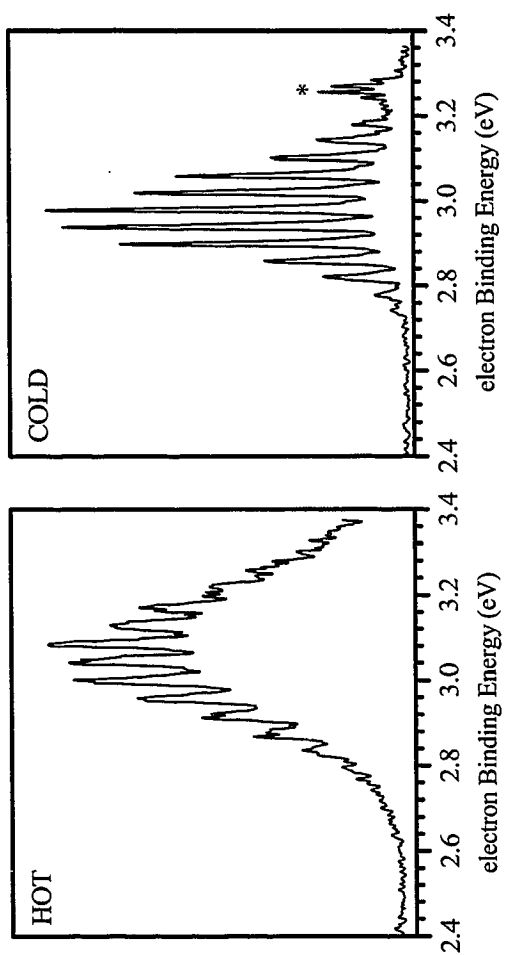


Figure 4-2. Comparison of 'hot' and 'cold' anion photoelectron spectra of GaP<sub>2</sub> taken at a wavelength of 355 nm and polarization angle of  $\theta=0^\circ$ . The spectrum shows only the  $\bar{A}^2 A_1$  state of GaP<sub>2</sub>.

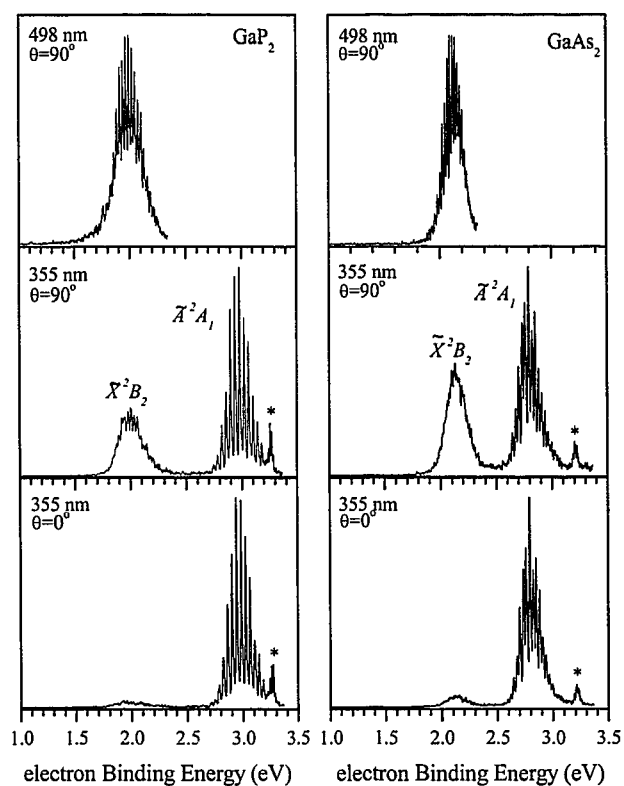


Figure 4-3. Anion photoelectron spectra of  $\text{GaX}_2^-$  ( $\text{X}=\text{P}, \text{As}$ ) taken at the wavelengths and polarization angles indicated. The features marked with an asterisk (\*) are discussed in the text.

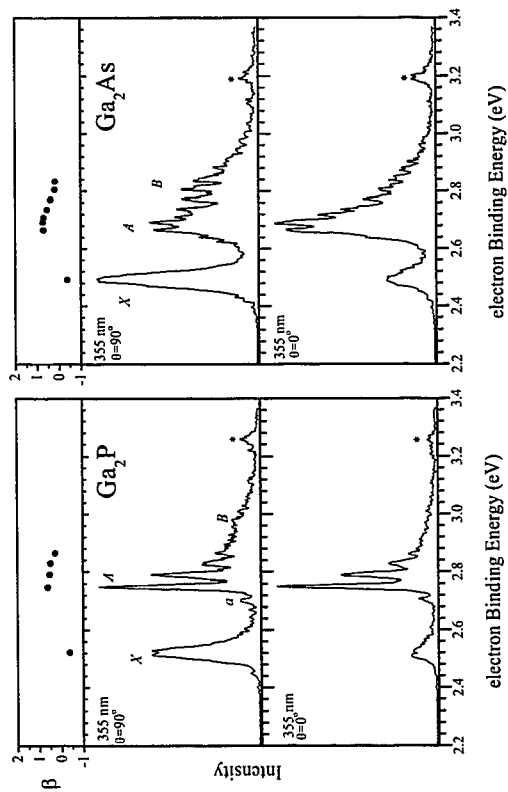


Figure 4-4. Anion photoelectron spectra of  $\text{Ga}_2\text{X}$  ( $\text{X}=\text{P}, \text{As}$ ) taken at a wavelength of 355 nm and polarization angles of  $\theta=0^\circ$  and  $90^\circ$ . The plot of the  $\beta$  parameters is located in the top panel. The features marked with an asterisk (\*) are discussed in the text.

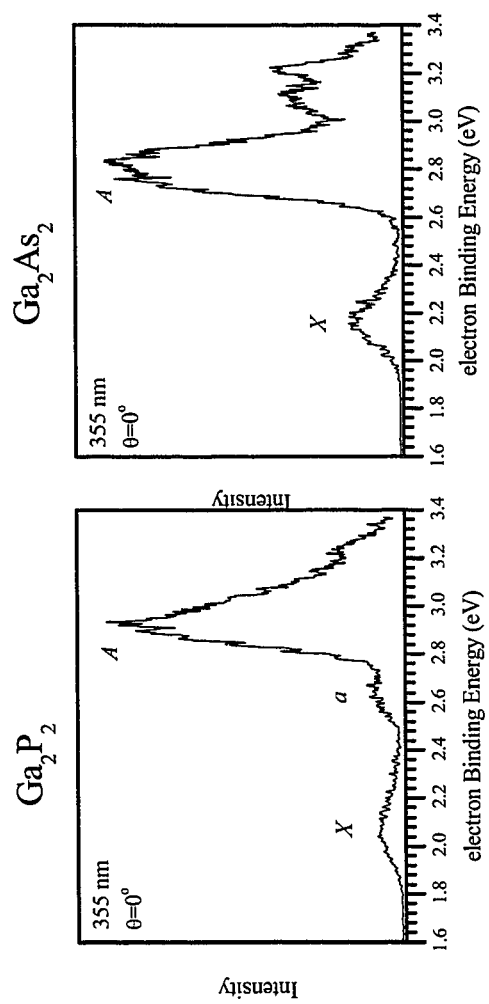


Figure 4-5. Anion photoelectron spectra of  $\text{Ga}_2\text{X}_2^-$  ( $\text{X}=\text{P}, \text{As}$ ) taken at a wavelength of 355 nm and polarization angle of  $\theta=0^\circ$ .

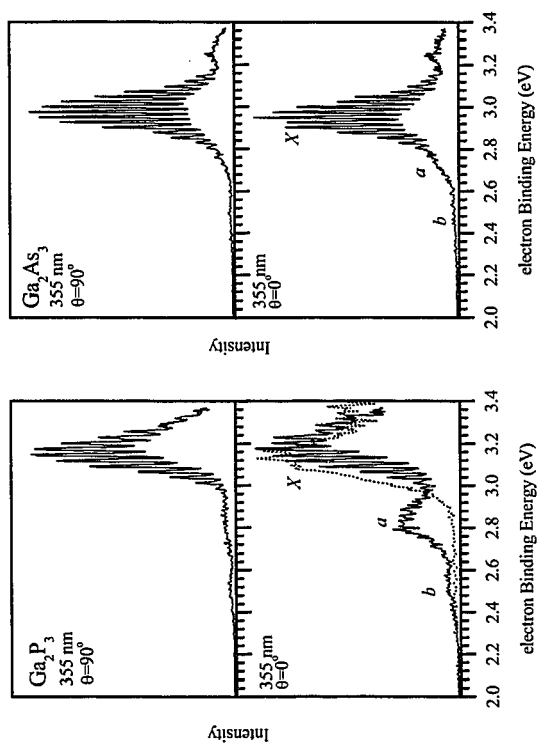


Figure 4-6. Anion photoelectron spectra of  $\text{Ga}_2\text{X}_3$ - ( $\text{X}=\text{P}, \text{As}$ ) taken at a wavelength of 355 nm and polarization angles of  $\theta=0^\circ$  and  $90^\circ$ . The dotted line in the lower left panel was taken at 266 nm.

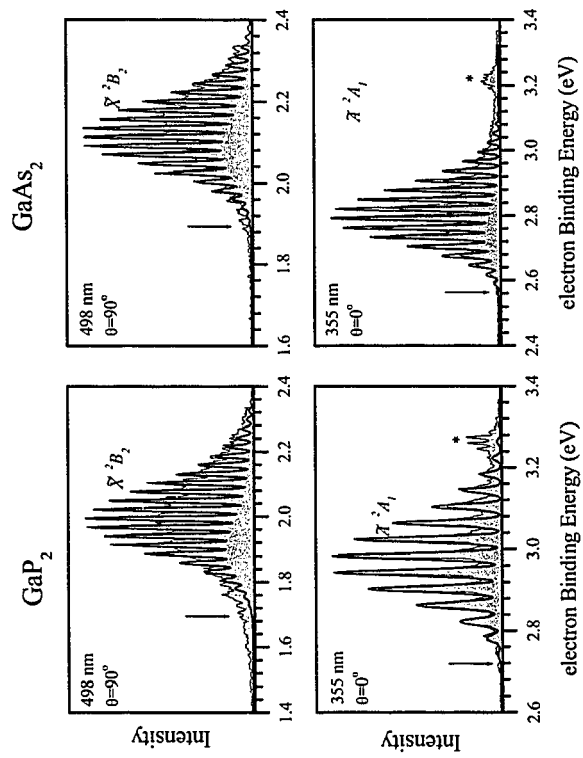


Figure 4-7. Anion photoelectron spectra of  $\text{GaX}_2^-$  (gray solid) superimposed with FC simulation (black line).

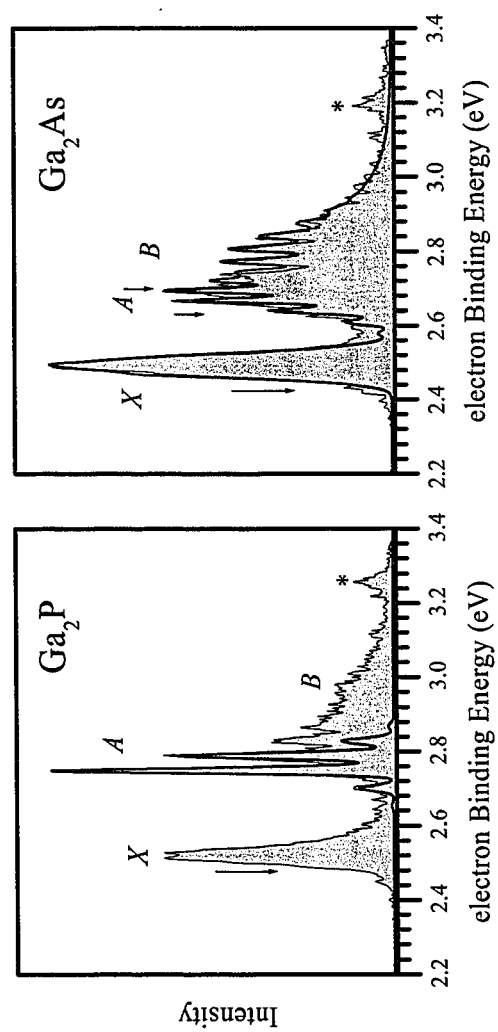


Figure 4-8. Anion photoelectron spectra of  $\text{Ga}_2\text{X}$ - (gray solid) superimposed with FC simulation (black line).

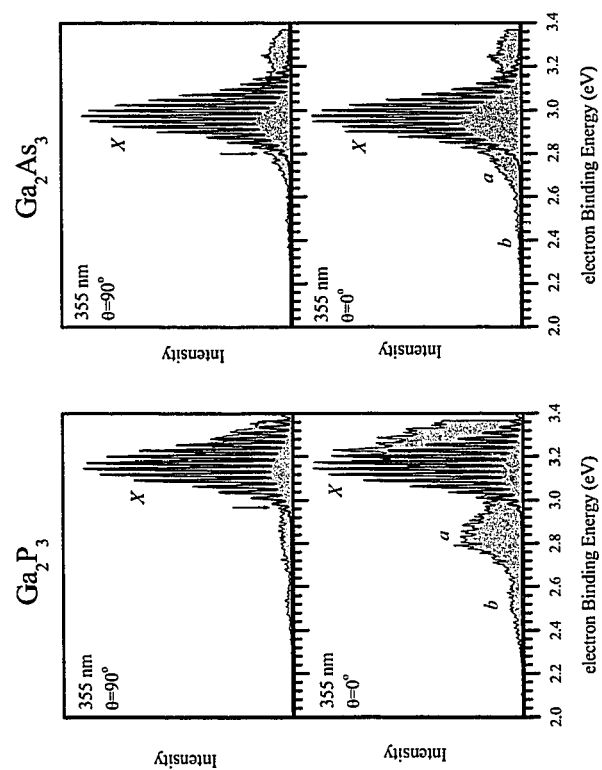


Figure 4-9. Anion photoelectron spectra of  $\text{Ga}_2\text{X}_3$  (gray solid) superimposed with FC simulation (black line).



## VI. References

- <sup>1</sup> P. P. Jenkins, A. N. Macinnes, M. Tabibazar, and A. R. Barron, *Science* **263**, 1751 (1994).
- <sup>2</sup> S. C. O'Brien, Y. Liu, Q. Zhang, J. R. Heath, F. K. Tittel, R. F. Curl, and R. E. Smalley, *J. Chem. Phys.* **84**, 4074 (1986).
- <sup>3</sup> Y. Liu, Q. L. Zhang, F. K. Tittel, R. F. Curl, and R. E. Smalley, *J. Chem. Phys.* **85**, 7434 (1986).
- <sup>4</sup> C. Jin, K. J. Taylor, J. Conceicao, and R. E. Smalley, *Chem. Phys. Lett.* **175**, 17 (1990).
- <sup>5</sup> S. Li, R. J. Van Zee, and W. Weltner, *J. Phys. Chem.* **97**, 11393 (1993).
- <sup>6</sup> R. J. Van Zee, S. Li, and W. Weltner Jr., *J. Chem. Phys.* **98**, 4335 (1993).
- <sup>7</sup> S. Schlect, R. Schaefer, J. Woenckhaus, and J. A. Becker, *Chem. Phys. Lett.* **246**, 315 (1995).
- <sup>8</sup> T. R. Taylor, K. R. Asmis, C. Xu, and D. M. Neumark, *Chem. Phys. Lett.* **297**, 133 (1998).
- <sup>9</sup> K. R. Asmis, T. R. Taylor, and D. M. Neumark, *Chem. Phys. Lett.* **308**, 347 (1999).
- <sup>10</sup> T. R. Taylor, K. R. Asmis, H. Gomez, and D. M. Neumark, *European Physical Journal D* **9**, 317 (1999).
- <sup>11</sup> P. Y. Feng and K. Balasubramanian, *Chem. Phys. Lett.* **265**, 41 (1997).
- <sup>12</sup> T. N. Kitsopoulos, C. J. Chick, A. Weaver, and D. M. Neumark, *J. Chem. Phys.* **93**, 6108 (1990).
- <sup>13</sup> C. Xu, T. R. Taylor, G. R. Burton, and D. M. Neumark, *J. Chem. Phys.* **108**, 1395 (1998).
- <sup>14</sup> K. Balasubramanian, *J. Chem. Phys.* **87**, 3518 (1987).
- <sup>15</sup> K. Balasubramanian, *Chem. Rev.* **90**, 93 (1990).
- <sup>16</sup> K. Balasubramanian, *Chem. Phys. Lett.* **171**, 58 (1990).
- <sup>17</sup> K. K. Das and K. Balasubramanian, *J. Chem. Phys.* **94**, 6620 (1991).
- <sup>18</sup> D. W. Liao and K. Balasubramanian, *J. Chem. Phys.* **96**, 8938 (1992).
- <sup>19</sup> M. Z. Liao, D. G. Dai, and K. Balasubramanian, *Chem. Phys. Lett.* **239**, 124 (1995).
- <sup>20</sup> K. Balasubramanian, *J. Phys. Chem.* **104**, 1969 (2000).
- <sup>21</sup> P. Y. Feng and K. Balasubramanian, *Chem. Phys. Lett.* **265**, 547 (1997).
- <sup>22</sup> P. Y. Feng and K. Balasubramanian, *Chem. Phys. Lett.* **258**, 387 (1996).
- <sup>23</sup> P. Y. Feng and K. Balasubramanian, *Chem. Phys. Lett.* **288**, 1 (1998).
- <sup>24</sup> R. M. Graves and G. E. Scuseria, *J. Chem. Phys.* **95**, 6602 (1991).
- <sup>25</sup> M. A. Al-Laham and K. Raghavachari, *Chem. Phys. Lett.* **187**, 13 (1991).
- <sup>26</sup> L. Lou, L. Wang, L. P. F. Chibante, R. T. Laaksonen, P. Nordlander, and R. E. Smalley, *J. Chem. Phys.* **94**, 8015 (1991).
- <sup>27</sup> L. Lou, P. Nordlander, and R. E. Smalley, *J. Chem. Phys.* **97**, 1858 (1992).
- <sup>28</sup> W. Andreoni, *Phys. Rev. B* **45**, 4203 (1992).
- <sup>29</sup> V. Tozzini, F. Buda, and A. Fasolino, *Phys. Rev. Lett.* **85**, 4554 (2000).
- <sup>30</sup> U. Meier, S. D. Peyerimhoff, and F. Grein, *Chem. Phys.* **150**, 331 (1991).
- <sup>31</sup> E. F. Archibong and A. St-Amant, *Chem. Phys. Lett.* **316**, 151 (2000).
- <sup>32</sup> E. F. Archibong and A. St-Amant, *Chem. Phys. Lett.* **330**, 199 (2000).
- <sup>33</sup> R. Arratia-Perez and L. Hernandez-Acevedo, *J. Chem. Phys.* **110**, 10882 (1999).
- <sup>34</sup> R. Arratia-Perez and L. Hernandez-Acevedo, *J. Chem. Phys.* **109**, 3497 (1998).
- <sup>35</sup> I. Vasiliev, S. Ogut, and J. R. Chelikowsky, *Phys. Rev. B* **60**, R8477 (1999).

- <sup>36</sup> H. Gomez, T. R. Taylor, and D. M. Neumark, *Journal Of Physical Chemistry A* (in press).
- <sup>37</sup> R. B. Metz, A. Weaver, S. E. Bradforth, T. N. Kitsopoulos, and D. M. Neumark, *J. Phys. Chem.* **94**, 1377 (1990).
- <sup>38</sup> C. Xu, G. R. Burton, T. R. Taylor, and D. M. Neumark, *J. Chem. Phys.* **107**, 3428 (1997).
- <sup>39</sup> B. A. Mamyrin and D. V. Shmikk, *JETP* **49**, 762 (1979).
- <sup>40</sup> G. Markovich, R. Giniger, M. Levin, and O. Cheshnovsky, *J. Chem. Phys.* **95**, 9416 (1991).
- <sup>41</sup> J. Cooper and R. N. Zare, in *Lectures in Theoretical Physics*, Vol. XI-C, edited by S. Geltman, K. T. Mahanthappa, and W. E. Brittin (Gordon and Breach, New York, 1969), p. 317.
- <sup>42</sup> K. M. Ervin and W. C. Lineberger, in *Advances in Gas Phase Ion Chemistry*, Vol. 1 (JAI Press Inc, 1992), p. 121.
- <sup>43</sup> H. Gomez, T. R. Taylor, K. R. Asmis, and D. M. Neumark, (manuscript in preparation).
- <sup>44</sup> Gaussian 98, M. J. Frisch, G. W. Trucks, H. B. Schlegel, G. E. Scuseria, M. A. Robb, J. R. Cheeseman, V. G. Zakrzewski, J. J. A. Montgomery, R. E. Stratmann, J. C. Burant, S. Dapprich, J. M. Millam, A. D. Daniels, K. N. Kudin, M. C. Strain, O. Farkas, J. Tomasi, V. Barone, M. Cossi, R. Cammi, B. Mennucci, C. Pomelli, C. Adamo, S. Clifford, J. Ochterski, G. A. Petersson, P. Y. Ayala, Q. Cui, K. Morokuma, D. K. Malick, A. D. Rabuck, K. Raghavachari, J. B. Foresman, J. Cioslowski, J. V. Ortiz, A. G. Baboul, B. B. Stefanov, G. Liu, A. Liashenko, P. Piskorz, I. Komaromi, R. Gomperts, R. L. Martin, D. J. Fox, T. Keith, M. A. Al-Laham, C. Y. Peng, A. Nanayakkara, M. Challacombe, P. M. W. Gill, B. Johnson, W. Chen, M. W. Wong, J. L. Andres, C. Gonzalez, M. Head-Gordon, E. S. Replogle, and J. A. Pople (Gaussian, Inc., Pittsburgh PA, 1998).
- <sup>45</sup> T. H. Dunning, Jr., *J. Chem. Phys.* **90**, 1007 (1989).
- <sup>46</sup> R. A. Kendall, T. H. Dunning, and R. J. Harrison, *J. Chem. Phys.* **96**, 6796 (1992).
- <sup>47</sup> C. Lee, W. Yang, and R. G. Parr, *Phys. Rev. B* **37**, 785 (1988).
- <sup>48</sup> A. D. Becke, *J. Chem. Phys.* **98**, 1372 (1993).
- <sup>49</sup> P. Y. Feng and K. Balasubramanian, *Chem. Phys. Lett.* **318**, 417 (2000).
- <sup>50</sup> G. R. Burton, C. Xu, C. C. Arnold, and D. M. Neumark, *J. Chem. Phys.* **104**, 2757 (1996).
- <sup>51</sup> E. F. Archibong, R. M. Gregorius, and S. A. Alexander, *Chem. Phys. Lett.* **321**, 253 (2000).

## ***-5- Anion Photoelectron Spectroscopy of Aluminum Phosphide Clusters***

---

Anion photoelectron spectra of size selected  $\text{Al}_x\text{P}_y^-$  ( $x, y \leq 4$ ) clusters have been taken at photodetachment wavelengths of 266 nm (4.661 eV), 355 nm (3.493) and 416 nm (2.980 eV). The spectra show transitions to multiple neutral electronic states, and several of these bands are vibrationally resolved. We report electron affinities, term values, and vibrational frequencies of the corresponding neutral and anion states where possible. Detailed assignments are proposed for the  $\text{AlP}_2^-$ ,  $\text{Al}_2\text{P}^-$ , and  $\text{Al}_2\text{P}_2^-$  spectra with the aid of electronic structure calculations. Results are compared with comparably sized  $\text{Ga}_x\text{P}_y^-$  and  $\text{In}_x\text{P}_y^-$  clusters.

## I. Introduction

Semiconductor clusters have been the subject of intense experimental and theoretical investigations during the last twenty years. Research in this area is motivated by the desire to understand how properties of macroscopic semiconductors that make them so important in the electronics industry are affected when they are greatly reduced in size. Studies of semiconductor clusters have been performed in both the nanoscale and molecular size regimes in order to understand how the structural and spectroscopic properties these species evolve with size. The nanoscale experiments<sup>1,2</sup> have primarily explored how finite size alters the properties of bulk materials, while experiments in the molecular size regime probe aim at a detailed understanding of the much more abrupt changes in structure and spectroscopy as a cluster is built up from its elemental constituents one atom at a time. The latter studies have been greatly aided by the development of new theoretical methods and faster computers, enabling more complex and accurate calculations on ground and excited states, and allowing more detailed comparison with experiments.

One of the most powerful experimental tools in the study of clusters has been anion photoelectron spectroscopy (PES), a technique that yields the electronic and vibrational spectroscopy of size-selected clusters.<sup>3</sup> This method and its higher resolution counterpart, zero kinetic energy (ZEKE) photodetachment spectroscopy, have been applied to both of elemental<sup>4-11</sup> and binary<sup>12-15</sup> semiconductor clusters. Recent work in our group on has focused on III-V semiconductor clusters; results have been reported for  $B_xN_y$ ,<sup>16-18</sup>  $Ga_xP_y$ ,<sup>19</sup> and  $In_xP_y$  clusters<sup>20</sup> with as many as 27 atoms. In this

publication we report anion photoelectron spectra of aluminum phosphide clusters  $\text{Al}_x\text{P}_y^-$  with  $x, y \leq 4$ .

AIP clusters are attractive targets of study compared to III-V clusters with heavier atoms because they have higher vibrational frequencies, facilitating the observation of vibrational progressions in their photoelectron spectra. In addition, the smaller number of electrons makes them more amenable to electronic structure calculations. While no experimental studies have been performed to date on AIP clusters, a series of electronic structure calculations have predicted that small AIP clusters adopt the two and three-dimensional characteristic of  $\text{Si}_n$  and  $\text{Ga}_x\text{As}_y$  clusters, rather than the linear geometries found for carbon<sup>21</sup> and some  $\text{B}_x\text{N}_y$  clusters.<sup>16,17</sup>

*Ab initio* calculations on properties of  $\text{Al}_x\text{P}_y$  clusters have been carried out by several groups.<sup>22-30</sup> Raghavachari<sup>24</sup> calculated minimum energy structures for  $(\text{AlP})_n$  using Hartree-Fock (HF) and fourth order Møller-Plesset (MP4) perturbation theory, followed by quadratic configuration interaction QCISD(T). Ramakrishna<sup>26</sup> used density functional theory (DFT) to explore structures for  $(\text{AlP})_n$  clusters up to 12 atoms, finding significantly different structures than for  $\text{Si}_{2n}$  clusters for  $n \geq 3$ . Balasubramanian and Feng<sup>27,28,30</sup> performed higher level *ab initio* calculations on a series of  $\text{Al}_x\text{P}_y$  neutral and charged clusters with four or fewer atoms. They calculated ground and excited state geometries and energies using complete active space self-consistent field (CASSCF) and multi-reference singles-doubles configuration interaction (MRSDCI) levels of theory with a basis set composed of relativistic effective core potentials and valence Gaussian basis sets. Archibong et al<sup>29</sup> calculated structures and detachment energies for  $\text{AlP}_2^-$ ,  $\text{Al}_2\text{P}_2^-$ , and their neutral counterparts at the DFT and CCSD(T) levels of theory. They

reported ground and excited state electronic energies and vibrational frequencies for the neutral and anionic species. Archibong's work differs from that of Balasubramanian in that  $\text{Al}_2\text{P}_2$  was not restricted to  $D_{2h}$  (planar rhombic) symmetry, and indeed  $\text{Al}_2\text{P}_2^-$  was found to have a non-planar ground state.

The spectra reported in this paper represent the first experimental study in the electronic structure of aluminum phosphide clusters in the molecular size regime. We obtain electron affinities (EAs), vertical detachment energies for the ground and low-lying electronic states of the neutral clusters, and vibrational frequencies in some cases. In general, photoelectron spectra of  $\text{Al}_x\text{P}_y^-$ , are reasonably similar to isoelectronic species  $\text{Ga}_x\text{As}_y^-$  and  $\text{In}_x\text{P}_y^-$ . Photoelectron spectra of the small clusters are compared directly to *ab initio* calculations by Balasubramanian et al.<sup>27,28,30</sup> and Archibong et al.<sup>29</sup> in order to assign the observed electronic transitions.

## II. Experimental

The anion photoelectron spectrometer used in this study has been described in detail previously.<sup>31,32</sup> Cluster anions are generated in a laser ablation/pulsed molecular beam source. A rotating and translating pellet made of 50–80% aluminum powder-200 mesh (Aldrich), 10-30% red phosphorus (Aldrich), and 5-20% KBr (Fisher Scientific) is ablated with the second harmonic (532 nm) of a pulsed Nd:YAG laser. The laser pulses are typically 5.0-7.5 mJ/pulse and are focused onto the target with a 50 mm lens. The resulting plasma is entrained in a supersonic beam of argon. The gas pulse continues to travel through a 1.75-inch long copper-clustering channel cooled with liquid nitrogen, then passes through a skimmer into a differentially pumped region. The cooling

channel<sup>33</sup> reduces spectral congestion in the PE spectra from vibrationally excited anions.

Negative ions in the beam are extracted perpendicular to their flow direction by a pulsed electric field and injected into a linear reflectron time-of-flight (TOF) mass spectrometer. The accelerated ions separated in time and space according to the mass-to-charge ratio, achieving a mass resolution of  $m/\Delta m \approx 2000$ . The ions of interest are selectively photodetached with photons having wavelengths of 266 nm (4.661 eV), 355 nm (3.493 eV) and 416 nm (2.980 eV). The photon wavelengths, 266 and 355 nm, were obtained by frequency quadrupling and tripling the fundamental of a pulsed Nd:YAG laser. To generate light at 416 nm, the third harmonic was passed through a Raman cell filled with hydrogen at high pressure (325 psig). The electron kinetic energy (eKE) distribution is determined by TOF analysis in a 1 m field-free flight tube. The energy resolution is 8-10 meV at 0.65 eV eKE and degrades as  $(\text{eKE})^{3/2}$  at higher eKE.

The angular dependence of the photodetachment intensity for polarized light and randomly oriented molecules is given by<sup>34</sup>

$$\frac{d\sigma}{d\Omega} = \frac{\sigma_{total}}{4\pi} \left[ 1 + \frac{\beta(\text{eKE})}{2} (3\cos^2\theta - 1) \right] \quad (1)$$

where  $\theta$  is the angle between the electric vector of the photon and the direction of electron ejection,  $\sigma_{total}$  is the total photodetachment cross section and  $\beta(\text{eKE})$  is the anisotropy parameter ( $-1 \leq \beta \leq 2$ ), which can be calculated using

$$\beta = \frac{I_{0^\circ} - I_{90^\circ}}{\frac{1}{2}I_{0^\circ} + I_{90^\circ}} \quad (2)$$

Here  $I_{0^\circ}$  and  $I_{90^\circ}$  are the intensities of the peak taken at the polarization angles  $\theta = 0^\circ$  and  $90^\circ$ . The laser polarization can be rotated with respect to the direction of electron detection with a half-wave plate. Each electronic photodetachment transition has a characteristic asymmetry parameter and this can be used to distinguish overlapping electronic transitions.

### III. Results

Figure 5-1 shows photoelectron (PE) spectra of twelve  $\text{Al}_x\text{P}_y^-$  clusters taken at photon energy of 4.661 eV. In these spectra the electron binding energy (eBE) is related to the internal energy of the anion and neutral by

$$eBE = EA + E^0 + E^- \quad (3)$$

Here EA is the adiabatic electron affinity, and  $E^0$  and  $E^-$  are the internal energies of the neutral and anion, respectively. The PE spectra show peaks corresponding to transitions to different electronic states in the neutral, with the lowest-lying state occurring at the lowest eBE. At 266 nm, the  $\text{AlP}^-$  and  $\text{Al}_2\text{P}^-$  spectra show resolved vibrational structure, and less well-resolved vibrational features are also seen superimposed on the lowest eBE peaks in the PE spectra of  $\text{Al}_3\text{P}^-$ ,  $\text{Al}_2\text{P}_3^-$  and  $\text{Al}_3\text{P}_3^-$ . All the spectra in Fig.5-1 were taken at a laser polarization of  $\theta = 55^\circ$  with respect to the electron detection angle, the “magic angle” for which intensities are independent of the photoelectron anisotropy parameter. Spectra were obtained at other polarization angles for all clusters, but no significant effect on peak intensities was observed at 266 nm.

The spectra directly yield vertical detachment energies (VDEs) for each neutral electronic state, using  $\text{VDE} = eBE_{\text{max}}$ , where  $eBE_{\text{max}}$  is the electron binding energy at the band maximum for the state in question. Where possible, these maxima are marked by



asterisks in Fig. 5-1, and the corresponding VDE's are given in Table 5-1. For each cluster in Table 5-1, the electronic bands are labeled X, A, B, C, etc., in order of increasing VDE. In addition, estimated adiabatic electron affinities (EA's) are listed in Table 5-1 and are indicated in each spectra in Fig. 5-1 by an arrow. The more precise EA's in Table 5-1 are obtained from vibrationally resolved PE spectra and the determination of these values is described below. For PE spectra with no vibrational resolution, estimated EA's are taken at the point of inflection at lowest eBE. In all PE spectra the determination of EA's is facilitated by use of the liquid nitrogen cooling channel, as this reduces the contribution of vibrationally excited anions in the spectra.

Figs. 5-(2-4) show PE spectra of  $\text{AlP}_2^-$ ,  $\text{Al}_2\text{P}^-$ , and  $\text{Al}_2\text{P}_2^-$  at higher detachment wavelengths. Electrons with the same eBE are slower at these wavelengths compared to 266 nm, so the energy resolution is higher and more vibrational structure is resolved. In addition, we generally find a stronger dependence of the spectra on laser polarization angle than at 266 nm; anisotropy parameters for each electronic band at 355 nm are listed in Tables 5-(2-4).

Fig. 5-2 shows PE spectra of  $\text{AlP}_2^-$  at 266 nm and at 355 nm. The two spectra at 355 nm were taken at polarization angles  $\theta = 55^\circ$  and  $0^\circ$ . The overall profile of the spectrum at  $\theta = 55^\circ$  is similar to the 266 nm spectrum, as expected at the magic angle, but band X is considerably less intense in the  $\theta = 0^\circ$  spectrum. The 355 nm spectra show clearly resolved vibrational progressions in bands X and A; both bands are dominated by a single progression with vibrational frequencies of 300 and  $425\text{ cm}^{-1}$  respectively.

Fig. 5-3 shows the photoelectron spectra of  $\text{Al}_2\text{P}^-$  taken at the wavelengths of 355 nm at polarization angles of  $\theta = 0^\circ$  and  $90^\circ$  and at 416 nm at  $\theta = 90^\circ$ . Features X, A and

B exhibit distinctly different polarization dependences at 355 nm. At 416 nm one can barely resolve a vibrational progression in band X with a peak spacing of  $\sim 70\text{ cm}^{-1}$ . Peaks A1-A4, associated with a transition to electronically excited  $\text{Al}_2\text{P}^*$ , show much better resolved structure than band X; peaks A2-A4 are spaced by  $\sim 420\text{ cm}^{-1}$ , while peaks A1 and A2 are spaced by  $450\text{ cm}^{-1}$ . There is a broad feature (B) at higher eBE.

In Fig. 5-4, the  $\text{Al}_2\text{P}_2^+$  photoelectron spectra at 266 nm shows four peaks labeled X, A, B and C, with peak A the most intense. The 355 nm,  $\theta = 55^\circ$  photoelectron spectrum shows resolved vibrational structure in band A with frequency  $320\text{ cm}^{-1}$ . At  $\theta = 0^\circ$  an additional resolved band a' at higher eBE is seen with a characteristic peak spacing of  $420\text{ cm}^{-1}$ .

#### IV. Analysis and Discussion

In this section the assignment of electronic states and vibrational progressions in the PE spectra are considered. Analysis of the  $\text{AlP}^+$  spectrum will be covered in a separate publication along with spectra of related diatomic species. Here we concentrate on  $\text{AlP}_2^+$ ,  $\text{Al}_2\text{P}^+$ , and  $\text{Al}_2\text{P}_2^+$ , with some discussion of the larger clusters at the end of this section. In addition, the  $\text{Al}_x\text{P}_y^+$  PE spectra are compared to previously results on  $\text{Ga}_x\text{P}_y^+$  and  $\text{In}_x\text{P}_y^+$  clusters.

Assignment of the  $\text{Al}_x\text{P}_y^+$  spectra is facilitated by comparison with the electronic structure calculations of Archibong *et al.*<sup>29</sup> and Balasubramanian *et al.*<sup>27,28,30</sup> These calculations report electronic state energies, geometries, and vibrational frequencies for several  $\text{Al}_x\text{P}_y$  neutral and charged clusters. Results at the highest level of theory reported by each group are listed in Table 5-(2-4) for  $\text{AlP}_2$ ,  $\text{Al}_2\text{P}$ , and  $\text{Al}_2\text{P}_2$ . While we can directly compare our experimental band origins and vibrational frequencies to these

calculations, it is also valuable to simulate the PE spectra within the Franck-Condon approximation in order to determine how well the calculated changes in geometry upon photodetachment compare to experiment. These simulations are best done using normal coordinates determined from *ab initio* force constants for the anion and neutral, and since these values are typically not reported, we have performed our own *ab initio* calculations on several anion and neutral clusters both as a check on previous reports and to generate a set of force constants with which to simulate the PE spectrum. These calculations were performed on anionic and neutral ground states of  $\text{AlP}_2$ ,  $\text{Al}_2\text{P}$ , and  $\text{Al}_2\text{P}_2$  using GAUSSIAN98<sup>35</sup> program package. The correlation consistent polarized valence basis sets of Dunning and co-workers,<sup>36</sup> denoted by cc-pVxZ where x=D (double zeta) and T (triple zeta) were used. Additional diffuse functions are especially important for the description of molecular ions and we therefore mostly used augmented correlation consistent sets of Kendall et al,<sup>37</sup> denoted by aug-cc-pVxZ (x = D,T). The geometries and vibrational frequencies were determined using density functional theory (DFT) with the B3LYP (Becke-3-parameter-Lee-Yang-Parr) exchange correlation functional.<sup>38,39</sup> Results from our calculations are also listed in Tables 5-(2-4).

Franck-Condon simulations were calculated using the parallel mode approximation. Using the anion and neutral geometries from the electronic structure calculations and the negative ion normal coordinates, we determine the normal mode displacements between the anion and various neutral electronic states for each cluster. These displacements and the calculated anion and neutral frequencies served as the starting point in the simulations and were then modified in order to best reproduce the experimental PE spectra. The anion vibrational temperature was also varied in order to

reproduce hot bands in the spectrum originating from vibrationally excited anions. The resulting stick spectrum is then convoluted with a gaussian function of width comparable to our experimental resolution, usually 8-15 meV. The simulations provide a detailed comparison with theory and also aid in determining the vibrational origin of electronic bands in which the origin is not obvious by inspection.

Simulation parameters for the  $\text{AlP}_2^-$ ,  $\text{Al}_2\text{P}^+$ , and  $\text{Al}_2\text{P}_2^-$  spectra are listed in Table 5-5. Because several of the vibrational progressions are quite extended, we can obtain vibrational frequencies with higher accuracy than our experimental resolution; error bars for the vibrational frequencies (see Table 5-5) are as low as  $10\text{ cm}^{-1}$ . In addition, for well-resolved bands, the error in determining the vibrational origin of a particular band is no larger than  $\pm 1$  quantum in the most active neutral vibrational frequency.

Electronic structure calculations by Feng and Balasubramanian<sup>30</sup> and by Archibong et al.<sup>29</sup> find that  $\text{AlP}_2^-$  has an  $^1\text{A}_1$  ground state, while  $\text{AlP}_2$  has a  $\tilde{\text{X}}^2\text{B}_2$  ground state and low lying  $\tilde{\text{A}}^2\text{A}_1$  excited state. The geometries are similar in all three calculations in Table 5-2 and show  $\text{AlP}_2$  and  $\text{AlP}_2^-$  to be acute triangles with  $\angle \text{P-Al-P}$  ranging from  $45^\circ$ - $56^\circ$ , indicating strong P-P bonding in all cases. Archibong calculates a higher EA (1.92 vs. 1.31 eV) and smaller  $\tilde{\text{X}} - \tilde{\text{A}}$  splitting (0.41 vs 0.63 eV) than Feng. The  $\nu_1$ ,  $\nu_2$ , and  $\nu_3$  vibrational modes correspond respectively to P-P stretching, Al-P stretching, and an antisymmetric stretch mode, which is inactive since the relevant anion and neutral electronic states all have  $\text{C}_{2v}$  symmetry.

Turning to the  $\text{AlP}_2^-$  spectra in Fig. 5-2, it appears by inspection that the origin of band X is at  $\text{eBE} \approx 2.0\text{ eV}$ , and that the VDE's of bands X and A differ by about 0.4 eV. These energetics agree well with those calculated by Archibong assuming band X and A

correspond to transitions to the  $\tilde{X}^2B_2$  and  $\tilde{A}^2A_1$  states of  $AlP_2$ , respectively. Based on Archibong's anion and neutral geometries and our anion force constants and normal coordinates, we find  $\Delta Q_1 = 0.057 \text{ \AA} \cdot \text{amu}^{1/2}$ ,  $\Delta Q_2 = 0.188 \text{ \AA} \cdot \text{amu}^{1/2}$  for detachment to the  $\tilde{X}^2B_2$  state and  $\Delta Q_1 = 0.009 \text{ \AA} \cdot \text{amu}^{1/2}$ ,  $\Delta Q_2 = 0.182 \text{ \AA} \cdot \text{amu}^{1/2}$  for detachment to the  $\tilde{A}^2A_1$  state. Hence for both transitions nearly all the FC activity is in the  $\nu_2$  mode, at least within the parallel mode approximation. Fig. 5-2 (bottom) shows the best-fit simulation to the  $AlP_2^-$  PE spectrum, obtained using the parameters in Table 5-5. There is generally good agreement between the simulation parameters and the electronic structure parameters calculated by Archibong, the main difference being that  $\Delta Q_2$  needed to be increased slightly to reproduce the  $\tilde{X}^2B_2$  band.

The calculations by Feng and Balusubramanian<sup>30</sup> on  $Al_2P^-$  and  $Al_2P$  show a strong dependence on the level of theory, particularly for the anion and some of the neutral excited states. At the highest level (MRSDCI + Q),  $Al_2P^-$  has a  $^1A_1$  ground state lying 1.90 eV below the neutral  $^2B_2$  ground state, while the  $^2A_1$  and  $^2B_1$  excited states are calculated to lay 0.43 and 0.58 eV, respectively, above the neutral ground state. At the DFT(B3LYP) level of theory, the calculated<sup>30</sup> symmetric stretch and bend frequencies for the ground state are  $\nu_1 = 435 \text{ cm}^{-1}$  and  $\nu_2 = 76 \text{ cm}^{-1}$ ; the lower frequency mode matches the spacing in band X of the experimental spectrum in Fig. 5-3.

The normal coordinate displacements analysis for  $Al_2P/Al_2P^-$  were determined using our calculated force constants at the DFT level of theory and the MRSDCI+Q geometries from Feng in Table 5-3. The calculated  $\angle Al-P-Al$  bend angle changes significantly upon photodetachment to the ground state, from  $93.7^\circ$  to  $77^\circ$ . We expect an extended bend progression in the PE spectrum, similar to what was seen in the ZEKE

spectrum of  $\text{InP}_2^-$  by Arnold et al.<sup>14</sup> Based on the calculations, the normal coordinate displacements are  $\Delta Q_1 = 0.120 \text{ \AA} \cdot \text{amu}^{1/2}$  and  $\Delta Q_2 = 0.379 \text{ \AA} \cdot \text{amu}^{1/2}$  for detachment to the  $\tilde{X}^2\text{B}_2$  state. A Franck-Condon simulation using these values is shown in Fig. 5-3 (bottom) and is quite similar in appearance to the experimental band X, so we assign band X to the  $^2\text{B}_2 \leftarrow ^1\text{A}_1$  photodetachment transition. From the simulation we estimate a vibrational origin and adiabatic electron affinity of  $2.513 \pm 0.020 \text{ eV}$ .

The progression A1-A4 could correspond to either of the two close-lying excited states in Table 5-3. In order to distinguish these, we note that at the MRSDCI+Q level of theory, the calculated bend angles for the  $^2\text{A}_1$  and  $^2\text{B}_1$  states are  $106.0^\circ$  and  $114.1^\circ$ , respectively, and that the  $^2\text{A}_1$  angle is considerably closer to the angle in the anion. The relatively narrow peaks A1-A4 are therefore more likely to result from a transition to the  $^2\text{A}_1$  state than to the  $^2\text{B}_1$  state. These peaks were simulated in Fig. 5-3 using the parameters in Table 5-5. The simulations yield frequencies of  $450 \text{ cm}^{-1}$  and  $421 \text{ cm}^{-1}$  for the anion and neutral respectively, assigning A2 as the origin and A1 as a hot band. By analogy to the ground state this frequency is assigned to the symmetric stretch. The peak widths result from relatively short, unresolved bend progressions. The adiabatic detachment energy (ADE) to the  $^2\text{A}_1$  state is  $2.859 \pm 0.007 \text{ eV}$ , while the term value for the  $^2\text{A}_1$  state is  $0.346 \pm 0.021 \text{ eV}$ , in reasonable agreement with the calculated value; the larger error bar in the term value reflects the uncertainty in the vibrational origin of band X. We assign the broad band B to the  $^2\text{B}_1$  state, with a very approximate term value of  $0.5 \text{ eV}$ .

The PE spectrum of  $\text{Al}_2\text{P}_2^-$  at 266 nm shows transitions to at least four electronic states labeled X, A, B, and C in the top panel of Fig. 5-4. At 355 nm, where the electron

energy resolution is higher for the same eBE, band X shows no vibrational structure, but band A shows a resolved progression with frequency  $320\text{ cm}^{-1}$ . These observations suggest a larger geometry change upon photodetachment to the ground state of  $\text{Al}_2\text{P}_2$  than to its first excited state. This interpretation is consistent with the *ab initio* calculations of Archibong et al,<sup>29</sup> in which the anion is found to have a nonplanar  $^2\text{B}_1$  ground state of  $\text{C}_{2v}$  symmetry, whereas  $\text{Al}_2\text{P}_2$  has a  $^1\text{A}_g$  planar rhombus ( $\text{D}_{2h}$ ) ground state, in agreement with the earlier calculation by Feng,<sup>28</sup> and a low-lying  $^3\text{A}_2$  excited state with the same symmetry as the anion.

FC simulations provide a more quantitative interpretation of these PE spectra.

The solid line in the bottom panel of Fig. 5-4 shows a simulated spectrum incorporating transitions to three  $\text{Al}_2\text{P}_2$  electronic states and was determined as follows. Based on Archibong's geometries and frequencies and our force constants, the normal coordinate displacement for photodetachment to the  $\text{Al}_2\text{P}_2$  ground state is given in Table 5-4. These displacements should result in a very long progression in the low frequency ( $\nu_3 = 88\text{ cm}^{-1}$ ) breathing mode of  $\text{Al}_2\text{P}_2$  upon photodetachment, as well as modest excitation in the symmetric P-P ( $\nu_1$ ) and Al-P ( $\nu_2$ ) stretches. Simulation of this progression using Archibong's geometries and an electron affinity of  $2.15 \pm 0.05\text{ eV}$  yields a ground state band that extends from 1.9 to 2.7 eV. With appropriate scaling, the simulation of this band resembles band X in our spectra, as can be seen from the low eBE portion of the simulated spectrum in Fig. 5-4. The low intensity of band X presumably results from a combination of being spread out over a large electron energy range and a low photodetachment cross section.

Photodetachment to the  $^3A_2$  excited state also results in activity in the three totally symmetric modes, but there is considerably less activity in the  $\nu_3$  mode. The dotted line in the bottom panel of Fig. 5-4 shows an FC simulation of this transition based on Archibong's geometries; it is dominated by a progression in the  $\nu_2$  mode with a calculated frequency of  $314\text{ cm}^{-1}$ . This progression resembles the experimental band A but is too short. Better agreement (solid line, Fig. 5-4, bottom) is obtained by increasing  $\Delta Q_2$  from  $0.107\text{ Å}\cdot\text{amu}^{1/2}$  to  $0.154\text{ Å}\cdot\text{amu}^{1/2}$ , and increasing the  $\nu_2$  frequency slightly to  $320\text{ cm}^{-1}$ ; the other  $\Delta Q$  values are given in Table 5-3. The simulation yields the adiabatic detachment energy for band A of  $2.643 \pm 0.010\text{ eV}$ , resulting in a term value of  $0.49 \pm 0.05\text{ eV}$  for the  $^3A_2$  state, slightly lower than the calculated values in Table 5-4.

Band a' in the  $\text{Al}_2\text{P}_2^-$  photoelectron spectra shows a short progression of peaks spaced by  $420\text{ cm}^{-1}$ . In the bottom panel of Fig. 5-4, this band is simulated assuming a single active mode with  $\Delta Q = 0.169\text{ Å}\cdot\text{amu}^{1/2}$  and term value  $0.846\text{ eV}$ . This state lies close to the calculated term value for the  $^3B_2$  excited state, but the calculated frequencies of  $563\text{ cm}^{-1}$  and  $266\text{ cm}^{-1}$  for the  $\nu_1$  and  $\nu_2$  modes do not agree well with the experimental peak spacing. Also, based on the calculated geometry in Table 5-4, there should be more than one active normal mode; the normal coordinate displacements are  $\Delta Q_1 = 0.045\text{ Å}\cdot\text{amu}^{1/2}$ ,  $\Delta Q_2 = 0.163\text{ Å}\cdot\text{amu}^{1/2}$ , and  $\Delta Q_3 = 0.695\text{ Å}\cdot\text{amu}^{1/2}$ . These are similar to the displacements for detachment to the ground state, so one expects a broad, unresolved band dominated by a progression in the low frequency  $\nu_3$  mode. We tentatively assign band a' to the  $^3B_2$  electronic state based on the calculated energetics, but it is clear that the calculated structure and frequencies do not agree with experiment.



The spectra for the other four atom clusters in Fig. 5-1,  $\text{AlP}_3^-$  and  $\text{Al}_3\text{P}^-$ , can be tentatively assigned by comparison with electronic structure calculations by Feng and Balasubramanian,<sup>27</sup> in which the energies and geometries of the neutral ground and excited states were calculated at the CASSCF and MRSDCI levels of theory. The calculations predict that  $\text{AlP}_3$  and  $\text{Al}_3\text{P}$  have  $^3\text{A}_2$  and  $^1\text{A}_1$  ground states, respectively, both with  $\text{C}_{3v}$  symmetry.  $\text{AlP}_3$  has close-lying  $^3\text{E}$  and  $^1\text{E}$  excited states lying 0.31 and 0.40 above the ground state, both of which presumably undergo Jahn-Teller distortion. The PE spectrum of  $\text{AlP}_3^-$  is comprised of three bands; the VDE's of band A and B are 0.28 and 0.64 eV higher than the VDE of band X. These energies suggest assigning band X to the  $^3\text{A}_2$  ground state, band A to the overlapped  $^3\text{E}$  and  $^1\text{E}$  states, and band B to a higher lying state not considered in the calculation.

The  $\text{Al}_3\text{P}^-$  photoelectron spectrum also has three distinctive peaks that are narrower and considerably better separated than in the  $\text{AlP}_3^-$  spectrum. Band X shows partially resolved peaks separated by  $340\text{ cm}^{-1}$ , and from the apparent origin of this band we obtain an EA of  $2.051 \pm 0.020\text{ eV}$ . Based in the differences on the VDEs, peaks X and A are separated by 0.87 eV, while peak X and B are separated by 1.30 eV. The large gap between electronic states qualitatively agrees with electronic structure calculations on  $\text{Al}_3\text{P}$ , which predict two low-lying electronic states,  $^3\text{E}$  and  $^1\text{A}_2$ , also with  $\text{C}_{3v}$  symmetry, to lie 1.86 eV and 2.46 eV, respectively, above the ground state. However, the calculated excitation energies are clearly larger than in the experimental spectrum.

Consideration of the molecular orbital configurations presented by Feng and Balasubramanian suggests that  $\text{AlP}_3^-$  and  $\text{Al}_3\text{P}^-$  both have  $^2\text{E}$  ground states. The widths of band X in the PE spectra indicate a much larger geometry change upon photodetachment

to the neutral ground state for  $\text{AlP}_3^-$  than for  $\text{Al}_3\text{P}^-$ , possibly indicating more substantial Jahn-Teller distortion in  $\text{AlP}_3^-$ . To date no calculations have been performed on either anion.

The  $\text{Al}_3\text{P}_3^-$  PE spectrum (Fig. 5-1) is the only other spectrum for which vibrational structure is resolved; band X shows a partially resolved progression with a peak spacing of  $630\text{ cm}^{-1}$ , and based on the apparent origin of this progression the EA of  $\text{Al}_3\text{P}_3$  is  $2.450 \pm 0.020\text{ eV}$ . Band X is well-separated from band A with their VDE's differing by  $1.18\text{ eV}$ . Raghavachari and co-workers<sup>24</sup> performed an extensive search for the ground state geometry of  $\text{Al}_3\text{P}_3$  in an electronic structure calculation. At the highest level of theory applied (QCISD(T)), this structure was found to be an Al-capped trigonal bi-pyramid with  $C_3$  symmetry. A similar result was found by Ramakrishna<sup>26</sup> in a more recent calculation using DFT within the local density approximation (LDA).

While it is difficult to say anything definitive about the  $\text{Al}_3\text{P}_3$  structure from the experimental PE spectrum, the narrow width of band X ( $280\text{ meV}$ ) and the fact that we can observe any vibrational structure in a cluster of this size suggests that the geometries of the negative ion and neutral are similar. Raghavachari also calculated vibrational frequencies for several  $\text{Al}_3\text{P}_3$  structures at the HF/6-31G\* level of theory. The highest frequency for the low energy structure mentioned above was a totally symmetric mode ( $a'$ ) with frequency  $551\text{ cm}^{-1}$ , a noticeably lower frequency than the experimental value. In fact, only one  $\text{Al}_3\text{P}_3$  isomer was found to have a frequency as large as our value: planar ( $D_{3h}$ )  $\text{Al}_3\text{P}_3$  with an  $e'$  mode at  $631\text{ cm}^{-1}$ . This was the next-lowest energy isomer found by Raghavachari, so it is possible that  $\text{Al}_3\text{P}_3^-$  has a similar but lower-symmetry geometry, resulting in activity of the  $e'$  mode in the photoelectron spectrum. Higher level

calculations of the vibrational frequencies for the various  $\text{Al}_3\text{P}_3$  isomers would help to resolve this issue.

We conclude by comparing the  $\text{Al}_x\text{P}_y^-$  PE spectra to those previously reported for  $\text{Ga}_x\text{P}_y^-$  and  $\text{In}_x\text{P}_y^-$  clusters.<sup>13,19,40</sup> In general, EA's for comparably sized AlP and GaP clusters are similar and somewhat higher than for InP clusters. For example, the EA's of  $\text{Al}_3\text{P}_3$ ,  $\text{Ga}_3\text{P}_3$ , and  $\text{In}_3\text{P}_3$  are 2.450 eV, 2.50 eV, and 1.40 eV, respectively. Most of the  $\text{Al}_x\text{P}_y^-$  photoelectron spectra in Fig. 5-1 are similar in appearance to the corresponding  $\text{Ga}_x\text{P}_y^-$  PE spectra; the spectra that differ the most are  $\text{AlP}_2^-$ ,  $\text{Al}_4\text{P}^-$ ,  $\text{Al}_2\text{P}_3^-$ , and  $\text{Al}_3\text{P}_2^-$ . Even though the  $\text{AlP}_2^-$  and  $\text{GaP}_2^-$  spectra appear dissimilar, they have both been assigned to transitions to a neutral  $^3\text{B}_2$  ground state and  $^2\text{A}_1$  excited state, but the splitting is considerably larger in  $\text{GaP}_2$  (1.25 vs. 0.41 eV).<sup>40</sup> In any case, comparison of the PE spectra indicates that most but not all AlP and GaP neutral and anion clusters in the size range we have studied have similar geometric and electronic structure.

## V. Tables

Table 5-1. Estimated adiabatic electron affinities and vertical detachment energies for  $\text{Al}_x\text{P}_y^-$

Cluster $\text{Al}_x\text{P}_y$ $x,y$	Mass (amu)	Adiabatic EA (eV) <sup>a</sup>	Vertical Detachment energies (eV)		
			X	A	B
1,1	58				
1,2	89	1.933 ± 0.007	2.21	2.65	
1,3	120	2.06	2.58	2.85	3.21
1,4	151	2.64	2.93	3.40	
2,1	85	2.513 ± 0.020	2.55	2.83	2.98
2,2	116	2.15	2.33	2.73	3.42
2,3	147	2.739 ± 0.020	2.92		3.86
3,1	112	2.051 ± 0.020	2.12	2.99	3.43
3,2	143	2.58	2.82		
3,3	174	2.450 ± 0.020	2.63	3.81	
4,1	139	1.98	2.40	2.58	3.21
4,2	170	2.25	2.37	3.13	3.63

<sup>a</sup> Unless otherwise noted, Electron Affinities (EA) and VDEs have uncertainties of ±50 and ±25 meV respectively

Table 5-2. Comparison of geometries and energy separations for  $\text{AlP}_2/\text{AlP}_2^-$ .

Reference	Species	State	Level	$\theta$ ( $^\circ$ )	Al-P ( $\text{\AA}$ )	P-P ( $\text{\AA}$ )	$\Delta E$ (eV)	$\omega_1(a_1)$	$\omega_2(a_1)$	$\omega_3(b_2)$	$\beta_{\text{SS}}$
Feng <i>et al.</i> <sup>a</sup>	$\text{AlP}_2^-$	$^1A_1$	MRSDCI+Q	50.2	2.440	2.070	-1.31				
	$\text{AlP}_2^-$	$^2B_2$		45.0	2.599	1.989	0.00	650	271	140	
	$\text{AlP}_2$	$^2A_1$		56.4	2.268	2.143	0.63				
	$\text{AlP}_2$	$^2A_2$		44.6	2.653	2.013	1.28				
Archibong <i>et al.</i> <sup>b</sup>	$\text{AlP}_2^-$	$^1A_1$	CCSD(T)	50.8	2.422	2.078	-1.92	578	378	304	
	$\text{AlP}_2^-$	$^2B_2$	B3LYP	45.4	2.580	1.990	0.00	693	286	157	
	$\text{AlP}_2$	$^2A_1$	B3LYP	55.6	2.286	2.132	0.41	563	442	388	
	$\text{AlP}_2$	$^2B_1$	B3LYP	50.3	2.178	2.178	2.53	506	303	225	
This work Theory	$\text{AlP}_2^-$	$^1A_1$	B3LYP <sup>c</sup>	50.2	2.437	2.066	-1.25	585	358	286	
	$\text{AlP}_2^-$	$^2B_2$		44.4	2.618	1.978	0.00	687	283	152	
Experiment	$\text{AlP}_2^-$	$^1A_1$	PES				-1.933 <sup>d</sup>				
	$\text{AlP}_2^-$	$^2B_2$					0.000		306		-0.51
	$\text{AlP}_2$	$^2A_1$					0.410		425		0.89

<sup>a</sup> Ref. 30

<sup>b</sup> Ref. 29

<sup>c</sup> Results using DFT (B3LYP) with the aug-cc-pVTZ basis set

<sup>d</sup> Experimental electron affinities and term energies for  $\text{AlP}_2/\text{AlP}_2^-$  have an uncertainty of  $\pm 7$  meV and  $\pm 10$  meV respectively.

Table S-3. Comparison of geometries and energy separations for  $\text{Al}_2\text{P}/\text{Al}_2\text{P}^*$ .

Reference	Species	State	Level	$\theta$ ( $^\circ$ )	Al-P ( $\text{\AA}$ )	Al-Al ( $\text{\AA}$ )	$\Delta E$ (eV)	$\omega_1(a_1)$	$\omega_2(a_1)$	$\omega_3(b_2)$	$\beta_{355}$
Feng <i>et al.</i> <sup>a</sup>	$\text{Al}_2\text{P}^*$	$^1\text{A}_1$	MRSDCI+Q	93.7	2.249	3.282	-1.90				
	$\text{Al}_2\text{P}$	$^2\text{B}_2$		77.0	2.250	2.801	0.00	435	76	208	
	$\text{Al}_2\text{P}$	$^2\text{A}_1$		106.0	2.304	3.680	0.43				
	$\text{Al}_2\text{P}$	$^2\text{B}_1$		114.1	2.378	3.991	0.58				
This work Theory	$\text{Al}_2\text{P}^*$	$^1\text{A}_1$	B3LYP <sup>b</sup>	107.7	2.256	3.644	-2.39	426	78	498	
	$\text{Al}_2\text{P}$	$^2\text{B}_2$		95.0	2.243	3.307	0.00	430	69	230	
Experiment	$\text{Al}_2\text{P}^*$	$^1\text{A}_1$	PES				-2.513 <sup>c</sup>	450			
	$\text{Al}_2\text{P}$	$^2\text{B}_2$					0.000		$\sim 70$		-0.95
	$\text{Al}_2\text{P}$	$^2\text{A}_1$					0.346	421			-0.05
	$\text{Al}_2\text{P}$	$^2\text{B}_1$					0.5				

<sup>a</sup> Ref. 30<sup>b</sup> Results using DFT (B3LYP) with the aug-cc-pVTZ basis set<sup>c</sup> Experimental Electron Affinities and Term energies for  $\text{Al}_2\text{P}/\text{Al}_2\text{P}$  have an uncertainty of  $\pm 20$  meV and  $\pm 23$  meV respectively.

Table 5-4. Comparison of geometries and energy separations for  $\text{Al}_2\text{P}_2/\text{Al}_2\text{P}_2^-$ .

Reference	Specie c	State	Level	$\theta$ ( $^\circ$ ) (P/AlP)	Al-P (Å)	P-P (Å)	$\phi$ AlPPA	$\Delta E$ (eV)	Frequencies $\nu_a$ ( $\text{cm}^{-1}$ )
Feng <i>et al.</i> <sup>a</sup>	$\text{Al}_2\text{P}_2^-$	$^2\text{B}_{1g}$	D <sub>2h</sub>	55.3	2.417	2.242	180	-1.33	
	$\text{Al}_2\text{P}_2$	$^1\text{A}_g$	D <sub>2h</sub>	49.2	2.521	2.100	180	0.00	
	<i>et al.</i> <sup>b</sup>	$^2\text{B}_1$	C <sub>2v</sub>	54.3	2.434	2.222	148	-1.83	468,307,74( <i>a<sub>1</sub></i> ) 312( <i>a<sub>2</sub></i> )
		$^1\text{A}_g$	D <sub>2h</sub>	48.5	2.529	2.067	180	0.00	395( <i>b<sub>1</sub></i> ) 193( <i>b<sub>2</sub></i> )
Archibong	$\text{Al}_2\text{P}_2$	$^3\text{A}_2$	C <sub>2v</sub>	59.0	2.366	2.331	159	0.70	588,274( <i>a<sub>2</sub></i> ) 276( <i>b<sub>1g</sub></i> )
	$\text{Al}_2\text{P}_2^-$	$^3\text{B}_2$	C <sub>2v</sub>	47.1	2.610	2.085	115	1.08	340( <i>b<sub>1u</sub></i> ) 159( <i>b<sub>2u</sub></i> ) 88( <i>b<sub>1u</sub></i> )
	This work	$^2\text{B}_1$	C <sub>2v</sub>	54.4	2.440	2.231	149	-1.87	440,314,59( <i>a<sub>1</sub></i> ) 312( <i>a<sub>2</sub></i> )
		$^1\text{A}_g$	D <sub>2h</sub>	48.3	2.536	2.073	180	0.00	239( <i>b<sub>1</sub></i> ) 328( <i>b<sub>2</sub></i> )
Experiment	$\text{Al}_2\text{P}_2$	$^3\text{A}_2$	C <sub>2v</sub>	59.5	2.370	2.341	160	0.60	563,266,83( <i>a<sub>1</sub></i> ) 37( <i>a<sub>2</sub></i> )
	$\text{Al}_2\text{P}_2^-$	$^2\text{B}_1$	C <sub>2v</sub>					-2.15 <sup>c</sup>	109( <i>b<sub>1</sub></i> ) 289( <i>b<sub>2</sub></i> )
	$\text{Al}_2\text{P}_2$	$^3\text{A}_2$	D <sub>2h</sub>					0.000	475,304,67( <i>a<sub>1</sub></i> ) 241( <i>a<sub>2</sub></i> )
	$\text{Al}_2\text{P}_2^-$	$^3\text{B}_2$ <sup>d</sup>	C <sub>2v</sub>					0.493	395( <i>b<sub>1</sub></i> ) 193( <i>b<sub>2</sub></i> )
								0.846	585,273( <i>a<sub>2</sub></i> ) 274( <i>b<sub>1g</sub></i> )
									339( <i>b<sub>1u</sub></i> ) 158( <i>b<sub>2u</sub></i> ) 87( <i>b<sub>3u</sub></i> )
									437,312,55( <i>a<sub>1</sub></i> ) 309( <i>a<sub>2</sub></i> )
									327( <i>b<sub>1</sub></i> ) 235( <i>b<sub>2</sub></i> )

<sup>a</sup> Ref. 28

<sup>b</sup> Ref. 29

<sup>c</sup> Experimental Electron Affinities and Term energies for  $\text{Al}_2\text{P}_2/\text{Al}_2\text{P}_2^-$  have an uncertainty of  $\pm 50$  meV.

<sup>d</sup> Tentative assignment

Table 5-5. Photoelectron spectra simulation parameters for active modes in  $\text{Al}_2\text{P}^+$ ,  $\text{AlP}_2^+$  and  $\text{Al}_2\text{P}_2^+$ .

Molecule	Band	State	PES-FCF active modes						Temp (K)
			$\nu_1$ ( $\text{cm}^{-1}$ )	$\Delta Q_1$ ( $\text{\AA}\cdot\text{amu}^{1/2}$ )	$\nu_2$ ( $\text{cm}^{-1}$ )	$\Delta Q_2$ ( $\text{\AA}\cdot\text{amu}^{1/2}$ )			
$\text{AlP}_2^+$ $\text{AlP}_2$		$^1\text{A}_1$	578		360				
	X	$^2\text{B}_2$	693	0.057	$306 \pm 10^a$	0.234 (0.188) <sup>b</sup>			360
	A	$^2\text{A}_1$	563	0.009	$425 \pm 10^a$	0.190 (0.182)			360
$\text{Al}_2\text{P}^+$ $\text{Al}_2\text{P}$		$^1\text{A}_1$	$450 \pm 20^a$		78				
	X <sup>c</sup>	$^2\text{B}_2$	430	0.120	69	0.379			350
	A	$^2\text{A}_1$	$421 \pm 15^a$	0.125 (0.095)	69	0.255 (0.297)			350
$\text{Al}_2\text{P}_2^+$ $\text{Al}_2\text{P}_2$			$\nu_1$	$\Delta Q_1$	$\nu_2$	$\Delta Q_2$	$\nu_3$ ( $\text{cm}^{-1}$ )	$\Delta Q_3$ ( $\text{\AA}\cdot\text{amu}^{1/2}$ )	
		$^2\text{B}_1$	464		304		79		
	X <sup>c</sup>	$^1\text{A}_g$	588	0.085	274	0.130	88	0.656	400
	A	$^3\text{A}_2$	440	0.026	$320 \pm 12^a$	0.154 (0.107)	59	0.104	400
	a <sup>*</sup>	$^3\text{B}_2$	$420 \pm 15^a$	0.169 (0.049)	266			(0.695)	400

<sup>a</sup> Observed experimental progression

<sup>b</sup> Values from normal coordinate analysis included in parenthesis, if different from simulation parameters.

<sup>c</sup> Change in normal coordinate base on calculated geometries and force constants



# VI. Figures

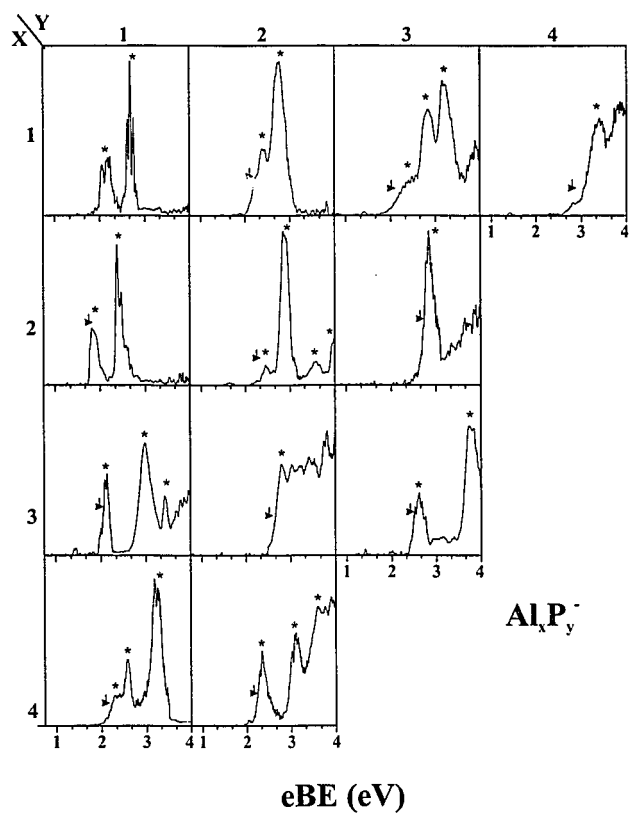


Figure 5-1. Photoelectron spectra of  $\text{Al}_x\text{P}_y^-$  clusters taken at 266 nm (4.661 eV). All spectra were taken at laser polarization of  $\theta = 55^\circ$  with respect to the direction of electron collection

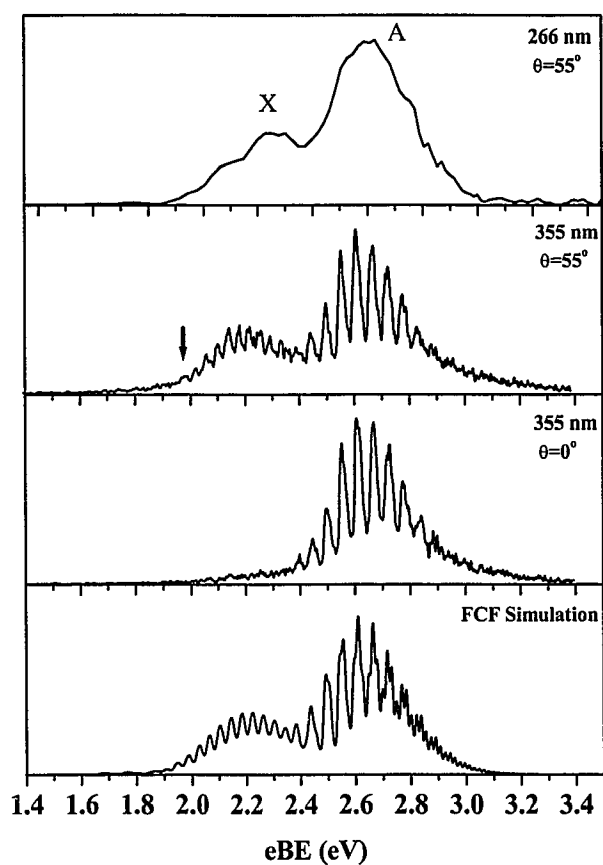


Figure 5-2 Photoelectron spectra of  $\text{AlP}_2^+$  clusters taken at 266 nm (4.661 eV) and 355 nm (3.493 eV). Laser polarization angle is  $\theta=0^\circ$  and  $\theta=55^\circ$  with respect to the direction of electron collection

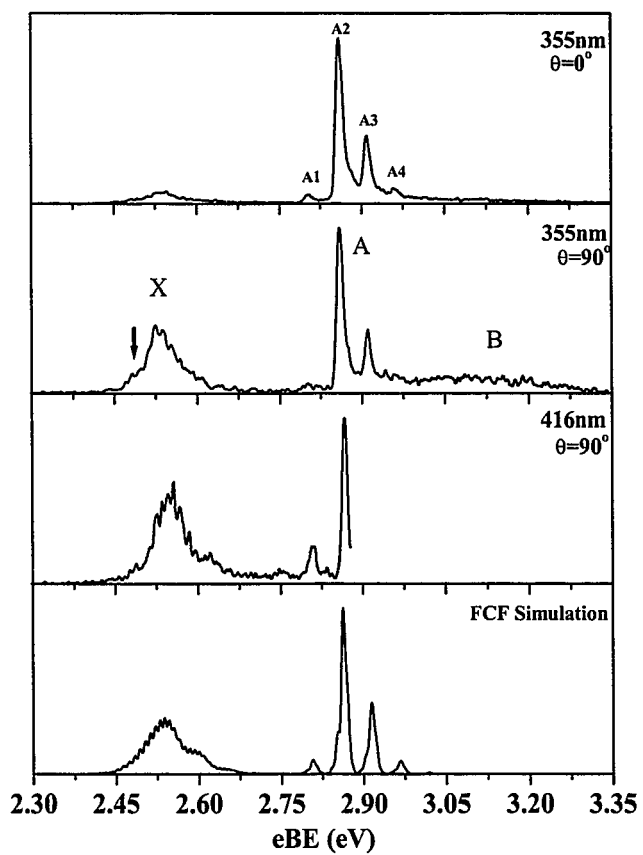


Figure 5-3.. Photoelectron spectra of  $\text{Al}_2\text{P}^+$  clusters taken at 355 nm (3.493 eV) and 416 nm (2.980 eV). Laser polarization angles are  $\theta=0^\circ$  and  $\theta=90^\circ$  with respect to the direction of electron collection.

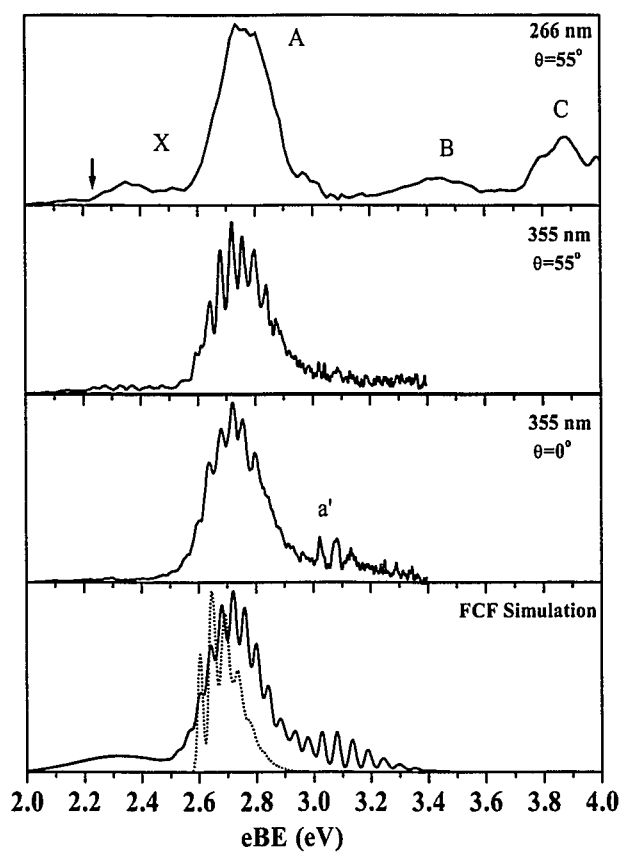


Figure 5-4. Photoelectron spectra of  $\text{Al}_2\text{P}_2^+$  clusters taken at 266 nm (4.661 eV) and 355 nm (3.493 eV). Laser polarization angles are  $\theta = 0^\circ$  and  $\theta = 55^\circ$  with respect to the direction of electron collection.

## VII. References

- (1) Alivisatos, A. P. *J. Phys. Chem.* **1996**, *100*, 13226.
- (2) Alivisatos, A. P. *Berichte Der Bunsen-Gesellschaft-Physical Chemistry Chemical Physics* **1997**, *101*, 1573.
- (3) Ervin, K.; Lineberger, W. C. Photoelectron spectroscopy of molecular anions. In *Advances in Gas Phase Ion Chemistry*; Adams, N. G., Babcock, L. M., Eds.; JAI Press: Greenwich, CT, 1992; Vol. 1; pp 121.
- (4) Cheshnovsky, O.; Yang, S. H.; Pettiette, C. L.; Craycraft, M. J.; Liu, Y.; Smalley, R. E. *Chem. Phys. Lett.* **1987**, *138*, 119.
- (5) Kitsopoulos, T. N.; Chick, C. J.; Weaver, A.; Neumark, D. M. *J. Chem. Phys.* **1990**, *93*, 6108.
- (6) Polak, M. L.; Ho, J.; Gerber, G.; Lineberger, W. C. *J. Chem. Phys.* **1991**, *95*, 3053.
- (7) Arnold, C. C.; Neumark, D. M. *J. Chem. Phys.* **1993**, *99*, 3353.
- (8) Burton, G. R.; Xu, C. S.; Arnold, C. C.; Neumark, D. M. *J. Chem. Phys.* **1996**, *104*, 2757.
- (9) Xu, C. S.; Taylor, T. R.; Burton, G. R.; Neumark, D. M. *J. Chem. Phys.* **1998**, *108*, 1395.
- (10) Negishi, Y.; Kawamata, H.; Hayase, T.; Gomei, M.; Kishi, R.; Hayakawa, F.; Nakajima, A.; Kaya, K. *Chem. Phys. Lett.* **1997**, *269*, 199.
- (11) Lippa, T. P.; Xu, S. J.; Lyapustina, S. A.; Nilles, J. M.; Bowen, K. H. *J. Chem. Phys.* **1998**, *109*, 10727.
- (12) Jin, C.; Taylor, K. J.; Conceicao, J.; Smalley, R. E. *Chem. Phys. Lett.* **1990**, *175*, 17.
- (13) Xu, C. S.; Debeer, E.; Arnold, D. W.; Arnold, C. C.; Neumark, D. M. *J. Chem. Phys.* **1994**, *101*, 5406.
- (14) Arnold, C. C.; Neumark, D. M. *Can. J. Phys.* **1994**, *72*, 1322.
- (15) Thomas, O. C.; Xu, S. J.; Lippa, T. P.; Bowen, K. H. *J. Clust. Sci.* **1999**, *10*, 525.
- (16) Asmis, K. R.; Taylor, T. R.; Neumark, D. M. *J. Chem. Phys.* **1999**, *111*, 8838.
- (17) Asmis, K. R.; Taylor, T. R.; Neumark, D. M. *J. Chem. Phys.* **1999**, *111*, 10491.
- (18) Asmis, K. R.; Taylor, T. R.; Neumark, D. M. *Euro. Phys. J. D* **1999**, *9*, 257.
- (19) Taylor, T. R.; Asmis, K. R.; Xu, C. S.; Neumark, D. M. *Chem. Phys. Lett.* **1998**, *297*, 133.
- (20) Asmis, K. R.; Taylor, T. R.; Neumark, D. M. *Chem. Phys. Lett.* **1999**, *308*, 347.
- (21) VanOrden, A.; Saykally, R. J. *Chem. Rev.* **1998**, *98*, 2313.
- (22) Bruna, P. J.; Grein, F. *Journal of Physics B (Atomic, Molecular and Optical Physics)* **1989**, *22*, 1913.
- (23) Meier, U.; Peyerimhoff, S. D.; Bruna, P. J.; Karna, S. P.; Grein, F. *Chem. Phys.* **1989**, *130*, 31.
- (24) Allaham, M. A.; Trucks, G. W.; Raghavachari, K. *J. Chem. Phys.* **1992**, *96*, 1137.
- (25) Rodriguez-Hernandez, P.; Munoz, A. *Semiconductor Science and Technology* **1992**, *7*, 1437.
- (26) Tomasulo, A.; Ramakrishna, M. V. *J. Chem. Phys.* **1996**, *105*, 10449.
- (27) Feng, P. Y.; Balasubramanian, K. *Chem. Phys. Lett.* **1999**, *301*, 458.
- (28) Feng, P. Y.; Balasubramanian, K. *J. Phys. Chem. A* **1999**, *103*, 9093.

- (29) Archibong, E. F.; Gregorius, R. M.; Alexander, S. A. *Chem. Phys. Lett.* **2000**, *321*, 253.
- (30) Feng, P. Y.; Balasubramanian, K. *Chem. Phys. Lett.* **2000**, *318*, 417.
- (31) Xu, C. S.; Burton, G. R.; Taylor, T. R.; Neumark, D. M. *J. Chem. Phys.* **1997**, *107*, 3428.
- (32) Metz, R. B.; Weaver, A.; Bradforth, S. E.; Kitsopoulos, T. N.; Neumark, D. M. *J. Phys. Chem.* **1990**, *94*, 1377.
- (33) Moravec, V. D.; Jarrold, C. C. *J. Chem. Phys.* **1998**, *108*, 1804.
- (34) Cooper, J.; Zare, R. N. Photoelectron angular distributions. In *Lectures in Theoretical Physics*; Geltman, S., Mahanthappa, K. T., Brittin, W. E., Eds.; Gordon and Breach: New York, 1969; Vol. XI-C; pp 317.
- (35) M. J. Frisch; G. W. Trucks; H. B. Schlegel; G. E. Scuseria; M. A. Robb; J. R. Cheeseman; V. G. Zakrzewski; J. A. Montgomery, J.; R. E. Stratmann; J. C. Burant; S. Dapprich; J. M. Millam; A. D. Daniels; K. N. Kudin; M. C. Strain; O. Farkas; J. Tomasi; V. Barone; M. Cossi; R. Cammi; B. Mennucci; C. Pomelli; C. Adamo; S. Clifford; J. Ochterski; G. A. Petersson; P. Y. Ayala; Q. Cui; K. Morokuma; D. K. Malick; A. D. Rabuck; K. Raghavachari; J. B. Foresman; J. Cioslowski; J. V. Ortiz; A. G. Baboul; B. B. Stefanov; G. Liu; A. Liashenko; P. Piskorz; I. Komaromi; R. Gomperts; R. L. Martin; D. J. Fox; T. Keith; M. A. Al-Laham; C. Y. Peng; A. Nanayakkara; M. Challacombe; P. M. W. Gill; B. Johnson; W. Chen; M. W. Wong; J. L. Andres; C. Gonzalez; M. Head-Gordon; E. S. Replogle; J. A. Pople. Gaussian 98; Revision A.9 ed.; Gaussian, Inc.: Pittsburgh PA, 1998.
- (36) Dunning, T. H., Jr. *J. Chem. Phys.* **1989**, *90*, 1007.
- (37) Kendall, R. A.; Dunning, T. H.; Harrison, R. J. *J. Chem. Phys.* **1992**, *96*, 6796.
- (38) Lee, C.; Yang, W.; Parr, R. G. *Phys. Rev. B* **1988**, *37*, 785.
- (39) Becke, A. D. *J. Chem. Phys.* **1993**, *98*, 1372.
- (40) Taylor, T. R.; Asmis, K. R.; Gomez, H.; Neumark, D. M. *Euro. Phys. J. D* **1999**, *9*, 317.

## **-6- *Anion Photoelectron Spectroscopy of $I_2^-(CO_2)_n$ ( $n=1-8$ ) Clusters***

---

We report the anion photoelectron spectra of  $I_2^-(CO_2)_n$  clusters ( $n = 1-8$ ) measured at a photon energy of 4.661 eV. Assignment of the spectra is aided by electronic structure calculations on  $I_2^-(CO_2)$ . The experiment yields size-dependent vertical and adiabatic detachment energies for the formation of the ground state and low-lying valence-excited states of the neutral cluster. Vertical detachment energies are successively blue-shifted with increasing cluster size, indicating a stronger stabilization of the anionic cluster relative to the neutral counterpart. In addition, a short progression in the  $CO_2$  bending mode is observed in the  $n=1$  and 2 clusters, indicating that the  $CO_2$  solvent species are slightly bent ( $\sim 2.5^\circ$ ) in the anion clusters. The trends in the total and stepwise solvation energies are discussed in terms of cluster geometries solute-solvent interactions.

## I. Introduction

Molecular clusters offer a unique opportunity to study effects of solvation in chemistry. By investigating clusters in which a chromophore is weakly bound to distinct solvent species, one can follow the evolution of chromophore properties as the number and type solvent species are varied, with the ultimate goal of understanding how the chromophore spectroscopy and dynamics evolve as one progresses from a gas phase to condensed phase environment. Studies of ionic clusters of this type have proved particularly fruitful, because charged clusters can be readily mass-selected, making it relatively straightforward to track cluster properties with size.<sup>1,2</sup> Anion photoelectron spectroscopy is one of the most versatile techniques for probing size-selected clusters, as it yields energetic and spectroscopic information on both the cluster anion and the neutral cluster formed by photodetachment. In this paper, we report anion photoelectron spectra of  $\text{I}_2^-(\text{CO}_2)_n$  clusters with up to 8  $\text{CO}_2$  solvent species.

Clusters of  $\text{I}_2^-$  are an excellent model system for understanding how the dynamics of a fundamental process, the photodissociation of  $\text{I}_2^-$ , are affected by clustering. In a series of landmark experiments, Lineberger and co-workers excited the  $\text{I}_2^-$  chromophore in  $\text{I}_2^-(\text{CO}_2)_n$  and  $\text{I}_2^-(\text{Ar}_n)$  clusters from its  $\tilde{X}^2\Sigma_u^+$  ground state to the repulsive  $\tilde{A}'^2\Pi_{g,1/2}$  and  $\tilde{B}^2\Sigma_g^+$  excited states.<sup>3-9</sup> They observed that a relatively small number of solvent species resulted in caging and recombination of the recoiling  $\text{I} + \text{I}^-$  photofragments, and measured overall time constants for relaxation of the highly vibrationally excited, clustered  $\text{I}_2^-$  formed by recombination. These experiments are complemented by transient absorption experiments on  $\text{I}_2^-$  in solution by Barbara and co-workers,<sup>10,11</sup> and by time-resolved photoelectron spectroscopy experiments on  $\text{I}_2^-(\text{CO}_2)_n$  and  $\text{I}_2^-(\text{Ar}_n)$  clusters in our



group.<sup>12-17</sup> Molecular dynamics simulations on these clusters have been carried out by Parson,<sup>18-21</sup> Coker,<sup>22,23</sup> and co-workers.

However, the interpretation of the dynamics experiments is still somewhat limited by the absence of spectroscopic data on the anion clusters. In particular, experimental information on the solvent binding energies and geometries would be very useful. In addition, in all simulations except one,<sup>24</sup> the CO<sub>2</sub> solvent molecules are treated as rigid, linear species, whereas it is known from earlier photoelectron spectroscopy studies<sup>25,26</sup> that the CO<sub>2</sub> molecules are slightly bent in clusters with *atomic* halides. It is therefore of interest to determine whether the solute-solvent interaction in I<sub>2</sub><sup>-</sup>(CO<sub>2</sub>)<sub>n</sub> clusters is strong enough to distort the CO<sub>2</sub> geometry.

In the present study, we address these issues by measuring the anion photoelectron spectra of I<sub>2</sub><sup>-</sup> and I<sub>2</sub><sup>-</sup>(CO<sub>2</sub>)<sub>n</sub> clusters (n = 1-8). We describe the experimental setup and the source conditions for the production of I<sub>2</sub><sup>-</sup>(CO<sub>2</sub>)<sub>n</sub> clusters. The spectra show vibrational structure indicating that the CO<sub>2</sub> molecules are slightly bent in the anion clusters. The observed shifts of the bands in the photoelectron spectra with increasing solvation are discussed in terms of possible cluster geometries and changes in solvation energy as a function of cluster size and electronic state. Electronic structure calculations have been carried out on I<sub>2</sub><sup>-</sup>, I<sub>2</sub><sup>-</sup>(CO<sub>2</sub>), and I<sub>2</sub>(CO<sub>2</sub>) to aid in the interpretation of the anion photoelectron spectra.

## II. Experiment

The negative ion time-of-flight TOF photoelectron (PE) spectrometer used in this study has been described in detail previously.<sup>27,28</sup> Briefly, I<sub>2</sub><sup>-</sup>(CO<sub>2</sub>)<sub>n</sub> clusters are prepared by coexpanding iodine vapor with 4–40 psi of a 5% CO<sub>2</sub>/Ar mixture at room temperature

through a pulsed molecular beam valve with a  $\sim 0.75$  mm diameter orifice. The valve is operated at a repetition rate of 20 Hz. Negative ions are generated by a 1 keV, 300 mA electron beam that crosses the gas jet just downstream of the nozzle, in the continuum flow region of the expansion. The ions are extracted perpendicularly to the expansion by means of a pulsed electric field into a linear reflection time-of-flight (TOF) mass spectrometer at an average beam energy of 2.5 keV. The mass resolution  $m/\Delta m = 2000$ . At the spatial focus of the mass spectrometer, ions are intersected and photodetached by a fixed frequency laser pulse from a Nd:YAG laser running at 20 Hz. The laser firing delay with respect to the pulsed extraction field is varied until optimal temporal overlap is achieved with the ions of the desired mass. The fourth harmonic of the Nd:YAG laser at 266 nm (4.661 eV) was used in the present study.

Photodetached electrons are detected at the end of a 1 m magnetically shielded flight tube, mounted orthogonally to the laser and ion beam, and are energy-analyzed by TOF. The electron detector, a 75 mm diameter chevron microchannel plate configuration with a flat anode, subtends a solid angle of 0.0044 sr, so that 0.035% of the detached photoelectrons are detected. The instrumental resolution is 8–10 meV for an electron kinetic energy (eKE) of 0.65 eV and degrades as  $(\text{eKE})^{3/2}$ . Under typical conditions, the ion density in the laser interaction region is about  $10^5$  /cm<sup>3</sup> for  $\text{I}_2^-$  and decreases with increasing cluster size. Approximately 30% of the ions are photodetached at 266 nm and about one electron is detected per laser shot. A typical spectrum requires 300,000–600,000 laser shots. Ultraviolet photons efficiently eject electrons from metal surfaces, resulting in a residual background photoelectron contribution of typically one electron

per ten laser shots at 266 nm, primarily at low eKE. Background spectra were recorded on a daily basis, summed, and then subtracted from the acquired data.

All photoelectron spectra presented here are plotted as a function of the electron kinetic energy (eKE, bottom axis) and electron binding energy (eBE, top axis), where

$$eBE = h\nu - eKE \quad (4)$$

and  $h\nu$  is the photon energy of the detachment laser. The angle between the laser polarization and the direction of electron collection can be varied by means of a half-wave plate. All spectra reported here were measured at a laser polarization angle of 90°.

### III. Results

#### A. Photoelectron spectra

The anion PE spectra of  $I_2^-$  and  $I_2^-(CO_2)$  at 266 nm are shown in Fig 6-1. The bare  $I_2^-$  spectrum is comprised of transitions to six electronic states of  $I_2$  with energies centered at eKE = 1.422 eV (X), 0.875 eV (A'), 0.783 eV (A), 0.533 eV (B'), 0.422 eV (B''), and 0.239 eV (B), where the band labeling corresponds to the accepted notation for the  $I_2$  electronic states. The corresponding vertical detachment energies (VDE's), defined as the electron binding energy at each band maximum, are 3.235 eV (X), 3.782 eV (A'), 3.874 eV (A), 4.124 eV (B'), 4.235 eV (B'') and 4.235 eV (B). Vibrational structure is observed in the X, A', and A bands, but this structure is less resolved than in the previously reported PE spectrum of  $I_2^-$  at 355 nm<sup>29</sup> due to lower electron energy resolution at higher eKE.

The  $I_2^-(CO_2)$  PE spectrum has the same general appearance at the bare  $I_2^-$  spectrum. Five of the six electronic bands (i.e. all except B) appear in the  $I_2^-(CO_2)$  spectrum, but the VDE's for these bands are all higher by 135-140 meV. Band X in the

$I_2^-$  spectrum is wider than the corresponding band in the  $I_2^-(CO_2)$  spectrum. This effect is attributed to fewer vibrational hot bands in the cluster PE spectrum, and has been seen in previous PE spectra of  $I_2^-(Ar)$  and  $I_3^-(Ar)$ .<sup>30,31</sup> In contrast, bands A' and A in  $I_2^-(CO_2)$  are considerably broader than their counterparts in the bare  $I_2^-$  spectrum, and a new feature, band a, appears at 80 meV ( $\sim 670\text{ cm}^{-1}$ ) lower eKE than band A; this spacing is close to the bending frequency of  $CO_2$  ( $667\text{ cm}^{-1}$ ).

The 266 nm PE spectra of  $I_2^-(CO_2)_n$  ( $n = 0 - 8$ ) clusters are shown in Fig. 6-2. The spectra of these clusters remain similar in form, except for a continuous shift of all bands to lower eKE, i.e., higher electron binding energy (eBE). While band X remains mostly unchanged with the addition of the  $CO_2$  molecules, bands A and A' become noticeably broader. Peak a in the  $I_2^-(CO_2)$  spectrum appears as a small shoulder in the  $I_2^-(CO_2)_2$  spectra and it disappears and/or is overlapped in the larger clusters by the broadening of bands A' and A. The  $n=6$  cluster is the largest for which both bands A' and A are energetically accessible at 266 nm, whereas the weaker bands B' and B'' are out of range for  $n>2$ .

The shifts in VDE for bands X, A, A' and B' are listed in Table 6-1. These shifts are determined by horizontally displacing the band of interest to achieve the best overlap with the corresponding feature in the  $I_2^-(CO_2)$  spectrum. Table 6-1 shows the total shifts relative to  $I_2^-$  as well as the stepwise shifts (in parentheses) relative to  $I_2^-(CO_2)_{n-1}$ , i.e., the shift from the addition of the  $n^{\text{th}}$   $CO_2$  molecule. The estimated error bars for the energy shifts are  $\pm 7\text{ meV}$  for bands A', A, and B' and  $\pm 10\text{ meV}$  for band X.

Table 6-1. Total and stepwise shifts (in parentheses) of the bands in the photoelectron spectra of  $I_2^-(CO_2)_n$  clusters relative to the  $I_2^-$  spectrum as a function of cluster size  $n$ . All energies are in meV.

$n$	$X (^1\Sigma_g^+)$	$A' (^3\Pi_{2u})$	$A (^3\Pi_{1u})$	$B' (^3\Pi_{0u})$
0	0	0	0	0
1	139 (+139)	136 (+136)	135 (+135)	140 (+140)
2	250 (+111)	260 (+124)	260 (+125)	255 (+115)
3	345 (+95)	339 (+79)	340 (+80)	
4	425 (+80)	420 (+81)	415 (+75)	
5	500 (+75)	492 (+72)	483 (+68)	
6	580 (+80)	569 (+77)	559 (+76)	
7	662 (+82)	661 (+92)		
8	745 (+83)			

## B. Electronic structure calculations

Electronic structure calculations were performed to assist in the interpretation of the data presented above. These calculations are aimed at determining the geometries of the binary  $I_2^-(CO_2)$  and  $I_2(CO_2)$  complexes.  $I_2/I_2^-$  and  $I_2/I_2^-(CO_2)$  geometries were optimized at the UHF (unrestricted Hartree-Fock) and HF levels of theory for the anion and neutral respectively, then further explored using MP2 (Moller-Plesset), and density functional theory (DFT) with the B3LYP (Becke-3-parameter-Lee-Yang-Parr) exchange correlation functional.<sup>32,33</sup> The STO-3G\*, and 6-311\*\* basis sets were used. Calculations were performed using Gaussian98 electronic structure package,<sup>34</sup> and the results are summarized in Table 6-2. Experimental data on  $CO_2$ ,  $I_2$ , and  $I_2^-$  are included in Table 6-2 for comparison.<sup>29,35,36</sup>

Several configurations for the anion complex were explored at UHF/STO-3G\* and UHF/6-311G\*\*, but only the global minimum structure is reported and studied further at higher levels of theory. This structure, shown in Fig 6-3, has  $C_{2v}$  symmetry, with the  $CO_2$  molecule lying in the plane that bisects the I-I bond. This structure is similar to previous structures calculated using Monte Carlo<sup>18</sup> and molecular dynamics<sup>37</sup>

simulations. However, the electronic structure calculations at all levels of theory predict that the CO<sub>2</sub> in I<sub>2</sub><sup>-</sup>(CO<sub>2</sub>) is slightly bent, with a deviation from linearity of ~2.6° to ~5.7° depending on the level of theory. In Table 6-2, the “experimental” result for the bond angle is based on the Franck-Condon analysis described in the next section.

The neutral I<sub>2</sub>(CO<sub>2</sub>) cluster has a local minimum structure similar to the global minimum for the anion. The major differences are that the CO<sub>2</sub> is very nearly linear in the neutral complex, and the distance between the C atom and the I<sub>2</sub> center-of-mass, R<sub>I-C</sub> in Table 6-2, is considerably longer. Both effects are consistent with a weaker intermolecular interaction in the neutral complex.

Table 6-2 shows that the agreement between the experimental and calculated I<sub>2</sub><sup>-</sup> geometries and frequencies is considerably better in the MP2 than in the B3LYP calculation, while for neutral I<sub>2</sub> both calculations compare equally well with experiment. The MP2/6-311G\*\* and B3LYP/6-311G\*\* calculations show that the bond lengths of bare I<sub>2</sub><sup>-</sup> and I<sub>2</sub> are essentially unchanged upon complexation with CO<sub>2</sub>, and R<sub>C-O</sub> in the neutral and anion clusters is very close to the experimental value for bare CO<sub>2</sub>. The CO<sub>2</sub> is slightly more bent in the B3LYP/6-311G\*\* calculation (176.1 vs 176.6°). The biggest difference between the two calculations is that R<sub>I-C</sub> is noticeably larger for the anion and neutral complexes in the B3LYP/6-311G\*\* calculation, as is the increase in R<sub>I-C</sub> upon photodetachment (1.256 vs. 0.357 Å). Vibrational frequencies for the anion and neutral complexes were calculated at the MP2/6-311G\*\* and B3LYP/6-311G\*\* level of theory and the results for the three totally symmetric modes from the MP2/6-311G\*\* calculation are included in Table 6-2. MP2/6-311G\*\* population analysis of the I<sub>2</sub><sup>-</sup>(CO<sub>2</sub>) complex indicates that ~1.7% of the total negative charge has migrated from the I<sub>2</sub><sup>-</sup> anion to the

CO<sub>2</sub> molecule. The CO<sub>2</sub> distortion is correlated with the degree of charge transfer, which ranges from 0.3% to 2.0% depending upon the level of theory. However, distortion of the CO<sub>2</sub> can also result purely from electrostatic effects, as discussed in previous work on X(CO<sub>2</sub>) clusters.<sup>26</sup>

#### IV. Analysis and Discussion

In this section, we first focus on the geometries of the I<sub>2</sub><sup>+</sup>(CO<sub>2</sub>) and I<sub>2</sub><sup>•</sup>(CO<sub>2</sub>) binary complexes by a Franck-Condon analysis of the photoelectron spectrum in Fig. 6-1. We then analyze and discuss the cluster energetics as revealed by the PE spectra in Fig. 6-2.

##### A. Franck-Condon analysis

We have performed Franck-Condon simulations of bands A and A' in the I<sub>2</sub><sup>+</sup>(CO<sub>2</sub>) and I<sub>2</sub><sup>•</sup>(CO<sub>2</sub>)<sub>2</sub> PE spectra in order to analyze the new feature (a) in the spectra and to characterize the vibrational temperature of the negative ions. The simulations are superimposed on the I<sub>2</sub><sup>+</sup>(CO<sub>2</sub>) PE spectrum in Figure 6-1, and are largely based on the MP2/6-311G\*\* results in Table 6-2, since this calculation yielded significantly better I<sub>2</sub>-parameters than the B3LYP/6-311G\*\* calculation. Using the calculated MP2/6-311G\*\* geometries, frequencies and force constants for the anion and neutral ground state complex, and experimental frequencies and distances for the I<sub>2</sub> A and A' electronic states,<sup>38,39</sup> we have simulated the photoelectron spectra within the parallel mode approximation using three totally symmetric vibrational modes: the I-I stretch, the CO<sub>2</sub> bend and the low-frequency I-C stretch motion. The CO<sub>2</sub> bending angle and frequency and the anion temperature were optimized in order to reproduce the spectra. The change in normal coordinate for the low frequency I-C stretch was set at the value obtained from

the MP2/6-311G\*\* geometries; we assumed this displacement is independent of the neutral I<sub>2</sub> electronic state.

The parameters determined from the fit are  $680 \pm 20$  cm<sup>-1</sup> for the CO<sub>2</sub> bend frequency,  $177.5 \pm 1.0^\circ$  for the OCO bend angle, and  $80 \pm 20$  K for the cluster temperature. The CO<sub>2</sub> frequency and bend angle were chosen to reproduce the position and intensity of band a. The simulations confirm that peak a is due to excitation of one quantum of the CO<sub>2</sub> bend in the neutral complex with I<sub>2</sub> in its A state. In principle, similar features should be associated with each neutral state of I<sub>2</sub> accessed in the photoelectron spectra. However, the analogous feature associated with band A' lies under band A, and for band X it is obscured by the extended progression in the I-I stretch. The simulations also show that the broadening of bands A and A' relative to the bare I<sub>2</sub>-spectrum is mainly due to vibrational activity in the I-C stretch due to the increase in RI-C upon photodetachment; this broadening is reproduced satisfactorily using  $\Delta R_{I-C} = 0.357$  Å from the MP2/6-311G\*\* calculation.

The OCO bend angle obtained from our Franck-Condon analysis is slightly larger than that obtained from the two highest level calculations in Table 6-2, possibly reflecting the need for more diffuse functions in the basis sets used in the anion calculations. The CO<sub>2</sub> in I<sub>2</sub><sup>-</sup>(CO<sub>2</sub>) is more linear than in the I<sup>-</sup>·CO<sub>2</sub> complex, for which the CO<sub>2</sub> angle is  $174.5 \pm 1.5^\circ$ <sup>26</sup>. This result may reflect the delocalization of the I<sub>2</sub><sup>-</sup> charge over the two centers, reducing the effective potential between the charge and the CO<sub>2</sub> quadrupole. Although the analog of peak a is not clearly resolved in PE spectra of the larger clusters, these spectra do show a shoulder where this peak would be expected, so we expect bent CO<sub>2</sub> molecules to be present in the larger clusters as well.



## B. Cluster Energetics

As has been discussed in earlier work,<sup>25,30</sup> the shifts in the VDE's with number of CO<sub>2</sub> molecules in Table 6-1 are a measure of the differences in anion and neutral solvent binding energies. The positive shifts with increasing  $n$  seen here indicate that binding in the anion is stronger than in the neutral, as expected, since the leading  $-1/r^3$  charge-quadrupole attractive term in the anion is absent in the neutral.

More quantitatively, the shifts can be interpreted in terms of the stepwise solvation energies  $SE_{\text{step}}^i(n)$  and  $SE_{\text{step}}^-(n)$ , defined as the solvent dissociation energies for the loss of a single CO<sub>2</sub> molecule from  $I_2^-(\text{CO}_2)_n$  or  $I_2^-(\text{CO}_2)_n$ , respectively; the superscript  $i$  indicates the  $I_2$  neutral electronic state. The total solvation energy  $SE_{\text{tot}}(n)$ , defined for the anion and neutral clusters, is given by the sum over the stepwise solvation energies  $SE_{\text{step}}(x)$ :

$$SE_{\text{tot}}(n) = \sum_{x=1}^n SE_{\text{step}}(x) \quad (5)$$

The VDE's are related to the stepwise solvation energy difference  $\Delta SE_{\text{step}}^i(n)$ , *i.e.*, the difference in the stepwise solvation energy of the neutral,  $SE_{\text{step}}^i(n)$ , and of the anionic cluster,  $SE_{\text{step}}^-(n)$ , as follows:

$$VDE^i(n) - VDE^i(n-1) = SE_{\text{step}}^-(n) - SE_{\text{step}}^i(n) \equiv \Delta SE_{\text{step}}^i(n) \quad (6)$$

The total solvation energy difference  $\Delta SE_{\text{tot}}^i(n)$  is then given by:

$$VDE^i(n) - VDE^i(0) = \sum_{x=1}^n \Delta SE_{\text{step}}^i(x) \equiv \Delta SE_{\text{tot}}^i(n) \quad (7)$$

Strictly speaking, one should use adiabatic detachment energies (ADE's) rather than VDE's in Eqs. (6) and (7), where the ADE is defined as the energy gap between the

vibrational ground states of the anion and neutral electronic state in question (and is equal to the electron affinity when the neutral electronic state is the ground state). Accurate determination of ADE's is difficult in the absence of resolved vibrational structure in the PE spectrum. Since the addition of CO<sub>2</sub> solvent molecules results in relatively minor changes in the shape of each band, we assume that the shifts in ADE's are equal to the shifts in the VDE's and use the latter in Eqs. (6) and (7).

In Figure 6-4, the total solvation energy differences for the A and X states,  $\Delta SE_{\text{tot}}^{\text{A}}(n)$  and  $\Delta SE_{\text{tot}}^{\text{X}}(n)$ , are plotted as a function of cluster size.  $\Delta SE_{\text{tot}}^{\text{A}'}(n)$  is essentially identical to  $\Delta SE_{\text{tot}}^{\text{A}}(n)$  and has therefore been omitted from Fig. 6-4. The small differences between  $\Delta SE_{\text{tot}}^{\text{A}}(n)$  and  $\Delta SE_{\text{tot}}^{\text{X}}(n)$  may not be significant. For all three states,  $\Delta SE_{\text{tot}}^i(n)$  increases monotonically with cluster size, but the slope drops considerably above  $n=2$ . At  $n = 8$ , the largest cluster studied, the anion cluster is stabilized by 745 meV relative to the neutral cluster in the X state.

Trends in the solvation energies are emphasized by plotting the stepwise solvation energy difference for the X state,  $\Delta SE_{\text{step}}^{\text{X}}(n)$ , as a function of the cluster size  $n$  in Figure 6-5. The first CO<sub>2</sub> molecule is bound by 139 meV more strongly in the anion than in the neutral.  $\Delta SE_{\text{step}}^{\text{X}}(n)$  decreases steadily from  $n = 1$  to  $n = 4$  and then remains nearly constant from  $n = 4 - 8$ , over which range each CO<sub>2</sub> stabilizes the anion by ~80 meV relative to the neutral.

The results in Fig. 6-5 differ significantly from those seen previously for I<sub>2</sub>Ar<sub>*n*</sub> and IHI'Ar<sub>*n*</sub> clusters,<sup>30,40</sup> for which  $\Delta SE_{\text{step}}(n)$  was relatively constant for the first six Ar atoms and then decreased sharply. The earlier results were consistent with molecular

dynamics simulations on  $I_2^+Ar_n$  clusters<sup>21,41</sup> that predicted the first six Ar atoms form a ring around the waist of the anion core, allowing each Ar atom to interact strongly with the partial negative charge residing on each Ar atom. Subsequent Ar atoms can be adjacent to only a single I atom, hence their binding energy in the anion is lowered.

The  $\Delta SE_{step}(n)$  trends in  $I_2^+Ar_n$  clusters were interpreted largely in terms of effects in the anion rather than the neutral clusters, and it is reasonable to make the same assumption for  $I_2^+(CO_2)_n$  clusters. In other words, we attribute the steep drop in  $\Delta SE_{step}^X(n)$  in Fig. 6-5 for  $n=1-4$  to decreases in  $SE_{step}^-(n)$  over this size range, so that the first  $CO_2$  binds the most strongly in the anion, with each successive  $CO_2$  binding less strongly until  $n=4$ , above which the binding energies are relatively constant. This interpretation is justified in part because the anion binding energies are stronger than the neutral binding energies, so that one would expect larger absolute variations with  $n$  in  $SE_{step}^-(n)$  than in  $SE_{step}^X(n)$ .

One can then view the overall trend in Fig. 6-5 as a competition between  $I_2^+CO_2$  interactions and  $CO_2 \cdot CO_2$  interactions. The  $I_2^+CO_2$  interaction is most favorable for the geometry in Fig. 6-3, which maximizes the attraction between the partial positive charge on the carbon atom and the negatively charged I atoms while minimizing the repulsion between the partial negative charges on the O and I atoms. On the other hand, in  $CO_2$  dimer, the two  $CO_2$ 's are parallel but displaced in order to maximize attraction between the electropositive C atom and electronegative O atoms.<sup>42-44</sup> Hence, if the first two or three  $CO_2$  molecules added to the  $I_2^+$  are aligned to lie in the plane that bisects the  $I_2^+$  bond, as predicted in the simulations by Amar and Perera,<sup>37</sup> they will be in an unfavorable orientation with respect to one another because of the proximity of the O

atoms in adjacent CO<sub>2</sub> molecules, resulting in a progressively lower binding energy as more CO<sub>2</sub> molecules are added. Note that in I<sup>-</sup>(CO<sub>2</sub>)<sub>n</sub> clusters,<sup>25</sup> where there is no I<sub>2</sub><sup>-</sup> axis to align the CO<sub>2</sub> molecules, the solvent shifts are relatively flat for the first several CO<sub>2</sub> molecules, lying between 140 and 150 meV for n=1-4. The flattening in Fig. 6-5 for n>4 suggests that subsequent CO<sub>2</sub> molecules primarily interact with one rather than two I atoms, so that the alignment with respect to the I<sub>2</sub><sup>-</sup> axis is less important than in the smaller clusters. This interpretation is consistent with molecular dynamics simulations of the structures of the larger cluster anions.<sup>18,22,37</sup> Given the large variation of binding energies, one might certainly expect different distortions from linearity for the inequivalently bound solvent molecules.

According to Eqs. (6) and (7), the photoelectron spectra are sensitive only to the differences in the anion and neutral solvent binding energies. Hence, more experimental information is needed to extract the actual anion/neutral solvation energies. Papanikolas et al<sup>4</sup> found that excitation of I<sub>2</sub><sup>-</sup>(CO<sub>2</sub>)<sub>n</sub> clusters at 720 nm (1.75 eV) results in the loss of 7 CO<sub>2</sub> molecules from clusters with 10<n<22, yielding an average binding energy of 0.25 eV. However, aside from being an average value, it is also an upper bound, because each CO<sub>2</sub> molecule leaves with non-zero kinetic energy. More recently, we have used femtosecond stimulated emission pumping (FSEP) to vibrationally excite the I<sub>2</sub><sup>-</sup> chromophore in I<sub>2</sub><sup>-</sup>(CO<sub>2</sub>)<sub>n</sub> clusters and observe the number of CO<sub>2</sub> molecules that evaporate over a wide range of vibrational excitation energies.<sup>45</sup> The FSEP results, when combined with the VDE shifts measured here, yield a best-fit solvent binding energy of SE<sub>step</sub> = 95 meV for neutral I<sub>2</sub>(CO<sub>2</sub>)<sub>n</sub> clusters, assumed to be independent of n, so that in

the anion clusters,  $SE_{\text{sep}}^-(n) = 234$  meV for the first  $\text{CO}_2$  and 178 meV for the 8th  $\text{CO}_2$ .

Details of this analysis are presented in the FSEP paper.

## V. Conclusions

The photoelectron spectra of  $\text{I}_2^-(\text{CO}_2)_n$  clusters presented here yield new insights into the structure and energetics of these clusters. The spectra show that the interaction between the  $\text{I}_2^-$  and  $\text{CO}_2$  constituents of the cluster is sufficient to distort the  $\text{CO}_2$  from linearity, and this distortion is reproduced in electronic structure calculations on the binary  $\text{I}_2^-(\text{CO}_2)$  complex. Franck-Condon simulations of the  $\text{I}_2^-(\text{CO}_2)$  spectrum show this distortion is only  $2.5^\circ$ , but inclusion of this distortion may be desirable in future molecular dynamics simulations of structures and energetics of larger  $\text{I}_2^-(\text{CO}_2)_n$  clusters. The PE spectra also yield trends in cluster energetics through shifts in the vertical detachment energies with increasing cluster size, implying that in the anion clusters, the binding energy of each successive  $\text{CO}_2$  drops significantly for the first four solvent molecules, after which little variation occurs. This drop in binding energy is attributed to competing  $\text{I}_2^-/\text{CO}_2$  and  $\text{CO}_2/\text{CO}_2$  interactions.

Table 6-2. Results of electronic structure calculations for  $I_2$  ( $CO_2$ ) and  $I_2(CO_2)$ . All bond lengths in Å.

Species	Level of Theory	$R_{I-I}$	$R_{C-O}$	$R_{I-C}$	$\angle OCO$ (°)
$I_2(CO_2)$	UHF/STO-3G*	3.08824	1.18843	3.2464	174.284
	MP2/STO-3G*	3.07215	1.23000	3.4111	177.441
$CO_2$	UHF/6-311G**	3.35077	1.13566	3.8436	176.833
	MP2/6-311G**	3.28406	1.16900	3.4413	176.560
	B3LYP/6-311G**	3.39261	1.16140	3.9702	176.104
	Experiment		1.1621 <sup>58</sup>		177.5 <sup>59</sup>
$I_2(CO_2)$	HF/STO-3G*	2.58153	1.18794	4.3963	179.941
	MP2/STO-3G*	2.57985	1.23084	3.9436	179.959
$CO_2$	HF/6-311G**	2.70317	1.13527	4.7373	179.876
	MP2/6-311G**	2.71495	1.16904	3.7983	179.810
	B3LYP/6-311G**	2.75683	1.16084	5.2261	179.874
	Experiment		1.1615 <sup>1</sup>		180.0
$I_2^-$		$R_{I-I}$	$\omega_e$ (cm <sup>-1</sup> )		
	MP2/6-311G**	3.28490	109.22		
	B3LYP/6-311G**	3.40281	83.53		
	Experiment	3.205 <sup>60</sup>	110 <sup>5</sup>		
$I_2$	MP2/6-311G**	2.71441	222.15		
	B3LYP/6-311G**	2.73693	206.55		
	Experiment	2.666 <sup>61</sup>	214.57		

Vibrational frequencies in cm<sup>-1</sup> for the totally symmetric modes of  $I_2(CO_2)/I_2(CO_2)$  are (5941, 110724, 598612, 1332/1330) from MP2/6-311\*\* calculation.

<sup>58</sup> Reference <sup>35</sup>  
<sup>59</sup> This work.  
<sup>60</sup> Reference <sup>29</sup>  
<sup>61</sup> Reference <sup>36</sup>

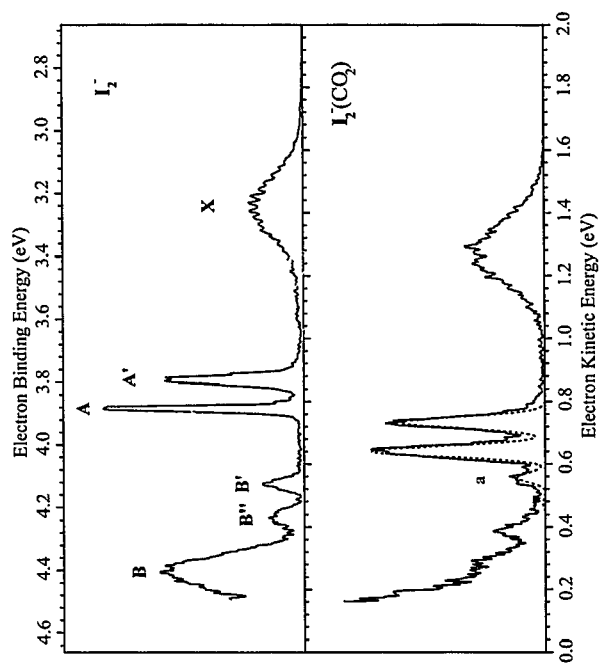


Figure 6-1. Anion photoelectron spectra (solid) of  $I_2^-$  and  $I_2^-(CO_2)$  measured at photon energy of 4.661 eV (266 nm). Franck-Condon simulation (dashed) of bands A' and A of the  $I_2^-(CO_2)$  spectrum is also shown.

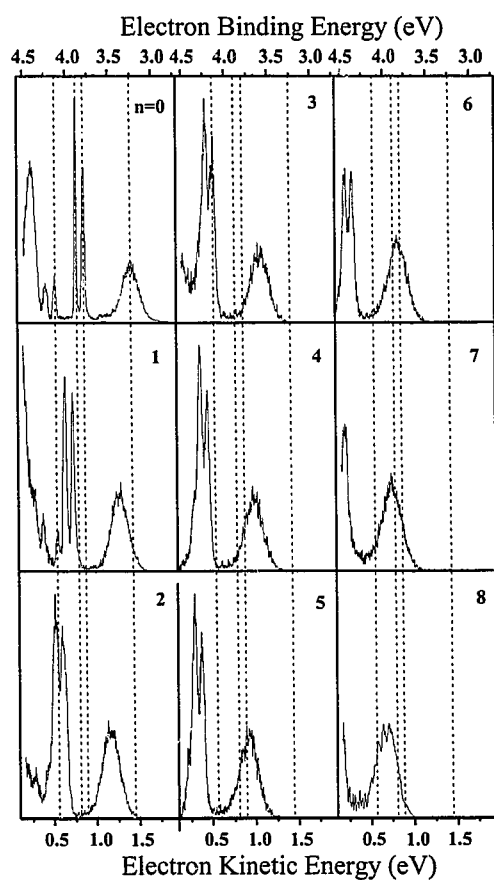


Figure 6-2. Anion photoelectron spectra of  $I_2(CO_2)_n$  clusters measured at a photon energy of 4.661 eV. The vertical detachment energies for the formation of the  $X$ ,  $A'$ ,  $A$ , and  $B'$  states of bare  $I_2$  are indicated by the broken vertical lines.



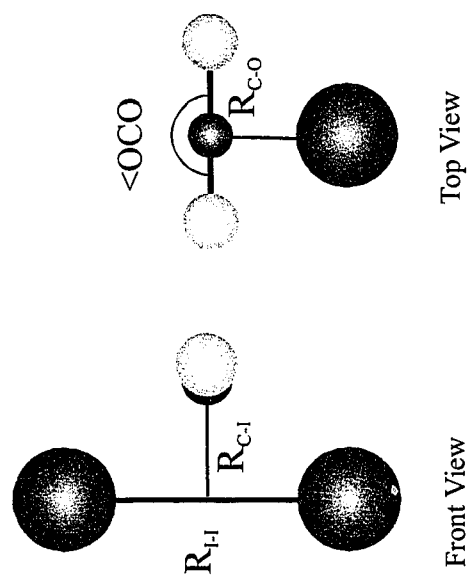


Figure 6-3. Lowest energy calculated structure for  $I_2 \cdot (CO_2)$  based on results from Table 6-2.

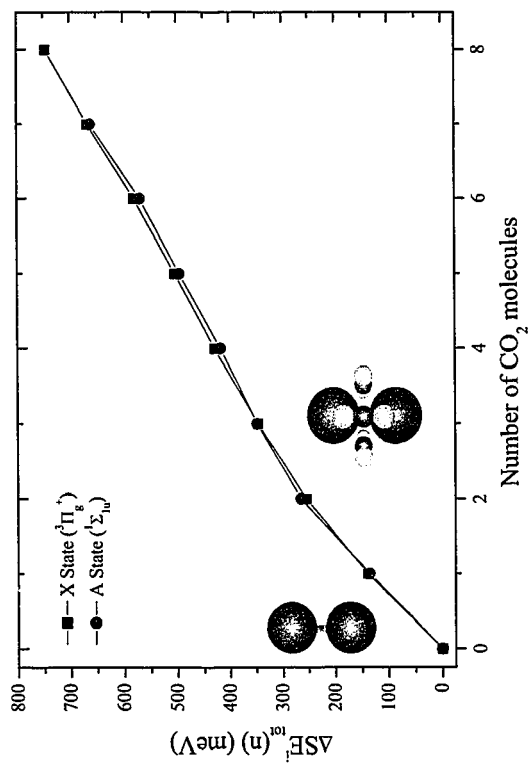


Figure 6-4. Total solvation energy difference  $\Delta SE_{\text{tot}}^I(n)$  for detachment to the X and A states of  $I_2^-(\text{CO}_2)_n$  as a function of cluster size  $n$ .

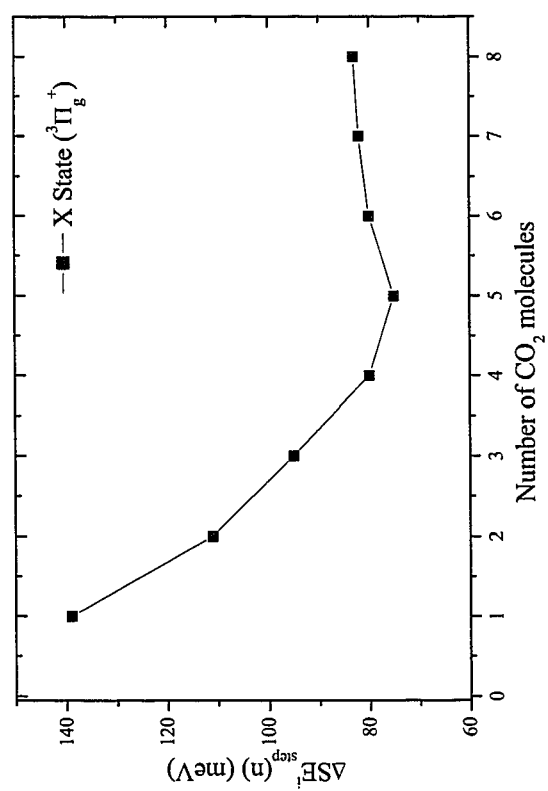


Figure 6-5. Stepwise solvation energy difference  $\Delta SE_{\text{step}}^X(n)$  for detachment to the X state of  $\text{I}_2(\text{CO}_2)_n$  as a function of cluster size  $n$ .

## VI. References

- <sup>1</sup> A. W. Castleman, Jr. and K. H. Bowen, Jr., *J. Phys. Chem.* **100**, 12911 (1996).
- <sup>2</sup> M. A. Duncan, *Int J Mass Spectrom* **200**, 545 (2000).
- <sup>3</sup> D. Ray, N. E. Levinger, J. M. Papanikolas, and W. C. Lineberger, *J. Chem. Phys.* **91**, 6533 (1989).
- <sup>4</sup> J. M. Papanikolas, J. R. Gord, N. E. Levinger, D. Ray, V. Vorsa, and W. C. Lineberger, *J. Phys. Chem.* **95**, 8028 (1991).
- <sup>5</sup> J. M. Papanikolas, V. Vorsa, M. E. Nadal, P. J. Campagnola, H. K. Buchenau, and W. C. Lineberger, *J. Chem. Phys.* **99**, 8733 (1993).
- <sup>6</sup> J. M. Papanikolas, V. Vorsa, M. E. Nadal, P. J. Campagnola, J. R. Gord, and W. C. Lineberger, *J. Chem. Phys.* **97**, 7002 (1992).
- <sup>7</sup> V. Vorsa, P. J. Campagnola, S. Nandi, M. Larsson, and W. C. Lineberger, *J. Chem. Phys.* **105**, 2298 (1996).
- <sup>8</sup> V. Vorsa, S. Nandi, P. J. Campagnola, M. Larsson, and W. C. Lineberger, *J. Chem. Phys.* **106**, 1402 (1997).
- <sup>9</sup> A. Sanov, T. Sanford, S. Nandi, and W. C. Lineberger, *J. Chem. Phys.* **111**, 664 (1999).
- <sup>10</sup> A. E. Johnson, N. E. Levinger, and P. F. Barbara, *J. Phys. Chem.* **96**, 7841 (1992).
- <sup>11</sup> P. K. Walhout, J. C. Alfano, K. A. M. Thakur, and P. F. Barbara, *J. Phys. Chem.* **99**, 7568 (1995).
- <sup>12</sup> B. J. Greenblatt, M. T. Zanni, and D. M. Neumark, *Science* **276**, 1675 (1997).
- <sup>13</sup> B. J. Greenblatt, M. T. Zanni, and D. M. Neumark, *Faraday Discuss.*, 101 (1997).
- <sup>14</sup> B. J. Greenblatt, M. T. Zanni, and D. M. Neumark, *J. Chem. Phys.* **112**, 601 (2000).
- <sup>15</sup> B. J. Greenblatt, M. T. Zanni, and D. M. Neumark, *J. Chem. Phys.* **111**, 10566 (1999).
- <sup>16</sup> A. V. Davis, M. T. Zanni, C. Frischkorn, M. Elhanine, and D. M. Neumark, *J Electron Spectrosc. and Related Phenom.* **112**, 221 (2000).
- <sup>17</sup> D. M. Neumark, *Annu. Rev. Phys. Chem.* **52**, 255 (2001).
- <sup>18</sup> J. M. Papanikolas, P. E. Maslen, and R. Parson, *J. Chem. Phys.* **102**, 2452 (1995).
- <sup>19</sup> N. Delaney, J. Faeder, P. E. Maslen, and R. Parson, *J. Phys. Chem. A* **101**, 8147 (1997).
- <sup>20</sup> J. Faeder, N. Delaney, P. E. Maslen, and R. Parson, *Chem. Phys.* **239**, 525 (1998).
- <sup>21</sup> J. Faeder and R. Parson, *J. Chem. Phys.* **108**, 3909 (1998).
- <sup>22</sup> V. S. Batista and D. F. Coker, *J. Chem. Phys.* **106**, 7102 (1997).
- <sup>23</sup> C. J. Margulis and D. F. Coker, *J. Chem. Phys.* **110**, 5677 (1999).
- <sup>24</sup> B. M. Ladanyi and R. Parson, *J. Chem. Phys.* **107**, 9326 (1997).
- <sup>25</sup> D. W. Arnold, S. E. Bradforth, E. H. Kim, and D. M. Neumark, *J. Chem. Phys.* **102**, 3510 (1995).
- <sup>26</sup> D. W. Arnold, S. E. Bradforth, E. H. Kim, and D. M. Neumark, *J. Chem. Phys.* **102**, 3493 (1995).
- <sup>27</sup> R. B. Metz, A. Weaver, S. E. Bradforth, T. N. Kitsopoulos, and D. M. Neumark, *J. Phys. Chem.* **94**, 1377 (1990).
- <sup>28</sup> C. Xu, G. R. Burton, T. R. Taylor, and D. M. Neumark, *J. Chem. Phys.* **107**, 3428 (1997).

- <sup>29</sup> M. T. Zanni, T. R. Taylor, B. J. Greenblatt, B. Soep, and D. M. Neumark, *J. Chem. Phys.* **107**, 7613 (1997).
- <sup>30</sup> K. R. Asmis, T. R. Taylor, C. S. Xu, and D. M. Neumark, *J. Chem. Phys.* **109**, 4389 (1998).
- <sup>31</sup> T. R. Taylor, K. R. Asmis, M. T. Zanni, and D. M. Neumark, *J. Chem. Phys.* **110**, 7607 (1999).
- <sup>32</sup> A. D. Becke, *J. Chem. Phys.* **98**, 1372 (1993).
- <sup>33</sup> C. Lee, W. Yang, and R. G. Parr, *Phys. Rev. B* **37**, 785 (1988).
- <sup>34</sup> M. J. Frisch, G. W. Trucks, H. B. Schlegel, G. E. Scuseria, M. A. Robb, J. R. Cheeseman, V. G. Zakrzewski, J. J. A. Montgomery, R. E. Stratmann, J. C. Burant, S. Dapprich, J. M. Millam, A. D. Daniels, K. N. Kudin, M. C. Strain, O. Farkas, J. Tomasi, V. Barone, M. Cossi, R. Cammi, B. Mennucci, C. Pomelli, C. Adamo, S. Clifford, J. Ochterski, G. A. Petersson, P. Y. Ayala, Q. Cui, K. Morokuma, D. K. Malick, A. D. Rabuck, K. Raghavachari, J. B. Foresman, J. Cioslowski, J. V. Ortiz, A. G. Baboul, B. B. Stefanov, G. Liu, A. Liashenko, P. Piskorz, I. Komaromi, R. Gomperts, R. L. Martin, D. J. Fox, T. Keith, M. A. Al-Laham, C. Y. Peng, A. Nanayakkara, M. Challacombe, P. M. W. Gill, B. Johnson, W. Chen, M. W. Wong, J. L. Andres, C. Gonzalez, M. Head-Gordon, E. S. Replogle, and J. A. Pople, *Gaussian 98* (Gaussian, Inc., Pittsburgh PA, 1998).
- <sup>35</sup> G. Herzberg, *Infrared and raman spectra of polyatomic molecules*. (Van Nostrand, New York, 1945).
- <sup>36</sup> G. Herzberg, *Spectra of diatomic molecules*. (Van Nostrand, New York, 1950).
- <sup>37</sup> F. G. Amar and L. Perera, *Z. Phys. D* **20**, 173 (1991).
- <sup>38</sup> X. N. Zheng, S. L. Fei, M. C. Heaven, and J. Tellinghuisen, *J. Chem. Phys.* **96**, 4877 (1992).
- <sup>39</sup> D. R. T. Appadoo, R. J. Leroy, P. F. Bernath, S. Gerstenkorn, P. Luc, J. Verges, J. Sinzelle, J. Chevillard, and Y. Daignaux, *J. Chem. Phys.* **104**, 903 (1996).
- <sup>40</sup> Z. Liu, H. Gomez, and D. M. Neumark, *Faraday Discuss.* **118**, 221 (2001).
- <sup>41</sup> V. S. Batista and D. F. Coker, *J. Chem. Phys.* **110**, 6583 (1999).
- <sup>42</sup> M. A. Walsh, T. H. England, T. R. Dyke, and B. J. Howard, *Chem. Phys. Lett.* **142**, 265 (1987).
- <sup>43</sup> K. W. Jucks, Z. S. Huang, D. Dayton, R. E. Miller, and W. J. Lafferty, *J. Chem. Phys.* **86**, 4341 (1987).
- <sup>44</sup> K. W. Jucks, Z. S. Huang, R. E. Miller, G. T. Fraser, A. S. Pine, and W. J. Lafferty, *J. Chem. Phys.* **88**, 2185 (1988).
- <sup>45</sup> R. Wester, A. V. Davis, A. E. Bragg, and D. M. Neumark, *Phys. Rev. Lett.* (submitted).

## ***-7- Anion Photoelectron Spectroscopy of Solvated Transition State Precursors***

---

Photoelectron spectra have been collected for several clusters of the type  $\text{XHX}^-(\text{M})$  ( $\text{X} = \text{Br}, \text{I}$ ) and  $\text{BrHI}^-(\text{M})$ , where  $\text{M} = \text{H}_2\text{O}, \text{HBr}$  and  $\text{HI}$ . The results of these experiments are interpreted in terms of the solvated anions and the solvated transition state species  $\text{X} + \text{HX} \rightarrow \text{XH} + \text{X}$  ( $\text{X} = \text{I}, \text{Br}$ ). Addition of one water molecule to  $\text{XHX}^-$  leads to a shift of the  $\text{IHI}^-$  and  $\text{BrHBr}^-$  spectra to lower electron kinetic energies by 355 and 455 meV, respectively. Addition of  $\text{HBr}$  or  $\text{HI}$  molecules distorts the transition state precursor altering significantly the Franck-Condon overlap between the anion and the neutral reaction surface. These experiments are an extension of previous work done in transition state spectroscopy and dynamics in clusters by our group.

## I. Introduction

Characterization of the transition state region of a chemical reaction is of fundamental importance in chemical reaction dynamics. In the past decades, there have been extensive experimental and theoretical studies on transition state spectroscopy and dynamics in the gas phase<sup>1-5</sup>. However, in addition to gas phase chemical reactions, which play an important role in our environment, solution phase chemistry offers a completely different set of conditions under which chemical reactions can take place. In fact, exploitation of solvent effects on chemical reaction rates is one of the main tools used in organic chemistry. Therefore, the effects which solvent molecules have on the dynamics of chemical reactions are of great interest. It has been shown that interactions on the molecular scale, particularly in the first solvent shell, play a vital role in solvation and condensed phase reactions dynamics.<sup>6,7</sup> One method to address this issue is to probe the transition state region of a chemical reaction in size selected clusters. By studying the changes which occur in the photoelectron spectra as a function of clusters size we are able to probe the effect of solvation at the transition state of a bimolecular reaction.

Previously in this group photoelectron spectroscopy of stable negative ions has been used to study transition state species for gas phase bimolecular chemical reactions. The reactions studied include several heavy-light-heavy hydrogen transfer systems<sup>4,5,8,9</sup>, hydrogen abstraction reactions<sup>10</sup> and fundamental hydroxyl radical reactions<sup>11</sup>. This technique has also been used very successfully to study the transition state region of the prototypical  $F + H_2$  reaction<sup>12,13</sup>. In those experiments, the photoelectron spectrum is collected for an anion whose geometry is very similar to that of a transition state species for the chemical reaction of interest. The region of the potential energy surface which is

studied by photodetachment of this 'precursor anion' is determined by the Franck-Condon overlap between the anion and the neutral reaction surface.

The transition state spectrum of the I + HI reaction was first reported by Weaver *et al.*<sup>4</sup>. A well-resolved progression belonging to the antisymmetric stretch vibration of the neutral complex  $[\text{IHI}]^\ddagger$  was observed. A higher resolution study of  $\text{IHI}^-$  by Waller *et al.*<sup>14</sup> using anion Zero Electron Kinetic Energy (ZEKE) spectroscopy revealed more underlying structure in each of the three peaks observed by Weaver *et al.*<sup>4</sup>. The most interesting result of the higher resolution study was the observation of the symmetric stretch vibration, which is associated with reactive resonances in the transition state. Transitions to the hindered rotor states of the neutral IHI complex were also observed in the ZEKE spectrum. The photoelectron spectrum of  $\text{BrHI}^-$  was observed by Bradforth *et al.*<sup>10</sup>. The Br + HI reaction represents an asymmetric hydrogen transfer reaction which is an interesting chemical system for transition state spectroscopy. The observed spectrum showed a progression due to the asymmetric motion of the hydrogen atom in the dissociating BrHI complex.

Arnold *et al.*<sup>15,16</sup> performed the first study of transition state spectroscopy of  $\text{IHI}^-$  in clusters. They used size selected  $\text{IHI}^-(\text{N}_2\text{O})_n$  clusters as precursors and measured the photoelectron spectra of these anion clusters to probe the transition state. In the observed spectra the overall features resembled those observed for  $\text{IHI}^-$  but were shifted to lower electron kinetic energies due to the effect of solvation. They also found that the spacing of the antisymmetric stretch progression was different in  $\text{IDI}^-(\text{N}_2\text{O})$  compared to bare  $\text{IDI}^-$ . This result was qualitatively explained by considering a small but observable change in anion geometry resulting from the interaction between the anion and solvating



species, shifting the Franck-Condon region to a larger I-I distance with an accompanying change in the neutral vibrational level spacing.

More recently Liu *et al.*<sup>17,18</sup> employed anion photoelectron spectroscopy to explore the effect of argon clustering in the IHI and BrHI transition states. Argon clustering exerts little effect in the transition state complex and the anion precursor. This effect is reflected by a small shift of the photoelectron spectrum to lower electron kinetic energy, and minimal changes in the peaks spacing. On the other hand argon clustering significantly reduced the contribution of vibrational hot bands to the spectra, giving much better spectral resolution. This enhancement allows the observation of reactive resonances and transitions to hindered rotor states for the I + HI reaction only observed before using higher resolution ZEKE spectroscopy. Also a new progression due to transitions to the I + HI ( $v = 1$ ) scattering channel was observed. Appearance of this progression together with the symmetric stretch vibration in the  $v_3' = 2$  level indicates that the photodetachment process accesses both symmetric stretch and direct scattering wavefunctions of the I + HI reaction. The addition of multiple argon atoms is reflected by the successive shifts in the photoelectron spectra to lower kinetic energy. Also a small change in peak spacing is observed for large clusters. This is attributed to a small bond change in the IHI<sup>-</sup> complex in the clusters.

In the present work, we employ anion photoelectron spectroscopy to investigate the effects of more strongly solvating species on clustered transition state precursors. We present results on the bimolecular reactions  $X + HX \rightarrow XH + X$  ( $X = Br, I$ ) in clusters by measuring the photoelectron spectra of BrHBr<sup>-</sup>, IHI<sup>-</sup> and BrHI<sup>-</sup> in H<sub>2</sub>O, HBr and HI clusters. H<sub>2</sub>O, HBr and HI are predicted to bind strongly to the charge in the anion

precursor, causing possibly structural changes in the transition state "precursor. It is of particular interest the understanding of structural changes in the anion induced by solvation, if we are going to understand effects on neutral TS dynamics. These changes could result in a different overlap with the transition state region, therefore revealing new information about the neutral potential. Recent experimental and theoretical results by Pivonka *et al.*<sup>19</sup> revealed that the addition of HBr molecules to  $\text{BrHBr}^-$  break the symmetry of transition state precursor. Their results indicate that only one solvent molecule (HBr) is required to produce this effect resulting in clusters of the form  $\text{Br}^- \dots (\text{HBr})_n$ . In this work we explore the effects of these structural changes on the photoelectron spectra of transition state precursors.

## II. Experiment

The negative ion time-of-flight TOF photoelectron (PE) spectrometer used in this study has been described in detail previously<sup>9,20</sup> and only relevant details will be given here.  $\text{BrHBr}^-(\text{HBr})_n$ ,  $\text{IHI}^-(\text{HI})_n$  and  $\text{BrHI}^-(\text{HX})$  ( $X = \text{Br}, \text{I}$ ) clusters are prepared by coexpanding 4–40 psi of a HBr and/or HI argon mixture at room temperature through a pulsed molecular beam valve with a ~0.25 mm diameter orifice. The concentrations of HBr and/or HI are modified depending on the size of the clusters of interest. Typical concentration values range between 0.01–1.0 % HI/HBr in Argon. Water-containing clusters are generated by adding couple drops of distilled water to the gas lines. Negative ions are generated by a 1 keV, 300 mA electron beam that crosses the gas jet just downstream of the nozzle, in the continuum flow region of the expansion. The ions are extracted perpendicularly to the expansion by means of a pulsed electric field into a linear reflection time-of-flight (TOF) mass spectrometer at an average beam energy of 2.5 keV.

The mass resolution is  $m/\Delta m = 2000$ . At the spatial focus of the mass spectrometer, ions are intersected and photodetached by a fixed frequency laser pulse from an Nd:YAG laser running at 20 Hz. The fifth harmonic of the Nd:YAG laser at 213 nm (5.821 eV) was used in the present study.

Photodetached electrons are detected at the end of a 1 m magnetically shielded flight tube, mounted orthogonally to the laser and ion beam, and are energy-analyzed by TOF. The instrumental resolution is 8–10 meV for an electron kinetic energy (eKE) of 0.65 eV and degrades as  $(\text{eKE})^{3/2}$ . Approximately 25% of the ions are photodetached at 213 nm and about one electron is detected per laser shot. A typical spectrum requires 300,000–600,000 laser shots. Ultraviolet photons efficiently eject electrons from metal surfaces, resulting in a residual background photoelectron contribution of typically one electron per ten laser shots at 213 nm, primarily at low eKE. Background spectra were recorded on a daily basis, summed, and then subtracted from the acquired data.

All photoelectron spectra presented here are plotted as a function of the electron kinetic energy (eKE). In the photoelectron spectra the eKE is related to the internal energy of the anion and neutral complex by

$$\text{eKE} = h\nu - EA - T_0 - E_v^0 + E_v^- \quad (1)$$

In equation (1)  $h\nu$  is the photon energy of the detachment laser,  $EA$  is the electron affinity of the complex and  $T_0$  the term value for various electronic states.  $E_v^0$  and  $E_v^-$  represent the vibrational energy of the neutral and anion complex respectively. The angle between the laser polarization and the direction of electron collection can be varied by means of a half-wave plate. All spectra reported here were measured at a laser polarization angle of  $90^\circ$ .

### III. Results

**Photoelectron spectra** The photoelectron spectra (PE) of  $\text{XHX}^+(\text{H}_2\text{O})$ , and  $\text{XHX}^+(\text{HX})_{1,2}$  ( $\text{X}=\text{Br}, \text{I}$ ) collected at  $h\nu = 5.821 \text{ eV}$  are shown in figures 7-1 and 7-2 along with the spectra of  $\text{IHI}^-$  and  $\text{BrHBr}^-$ . Figure 7-3 shows the photoelectron spectra of  $\text{BrHI}^-$  solvated by  $\text{HBr}$  and  $\text{HI}$  along with the spectra of  $\text{BrHI}^-$ . Peak positions for each spectrum are given in Table 7-1. The  $h\nu = 5.821 \text{ eV}$  spectra reveal similar structure than previously reported spectra.<sup>21</sup> Previous studies in our laboratory on  $\text{IHI}^-$ ,  $\text{BrHBr}^-$  and  $\text{BrHI}^-$  have assigned the features as photodetachment transitions to the unstable  $\text{IHI}$ ,  $\text{BrHBr}$  and  $\text{BrHI}$  complexes, respectively. The main progressions of  $\text{IHI}^-$  ( $A_1, A_2, A_3$ ) and  $\text{BrHBr}^-$  ( $A_1, A_2, A_3$ ) were attributed to the antisymmetric hydrogen vibrational motion ( $\nu_3$ ) of the complex prior to dissociation to  $\text{X} + \text{HX}$  ( $\text{X} = \text{I}, \text{Br}$ ) and the vibrational assignment is  $\nu_3' = 0, 2$  and  $4$ . The progression  $A_1, A_2, A_3$  in  $\text{BrHI}^-$  results from the same vibrational motion ( $\nu_3$ ) but with a slightly different vibrational assignment ( $\nu_3' = 0, 1$  and  $3$ )<sup>10</sup>. For  $\text{IHI}^-$  and  $\text{BrHI}^-$ , the peaks located at low electron kinetic energy (B) are separated by approximately the spin-orbit splitting of iodine ( $0.943 \text{ eV}$ )<sup>22</sup>. At high electron kinetic energy figures 7-(1-3) reveal peaks (\*) corresponding to photodetachment of bare halides ( $\text{X}^-$ ). These atoms are likely to emerge from the photodissociation followed by photodetachment of the clusters.

In general, the  $\text{IHI}^+(\text{H}_2\text{O})$  and  $\text{BrHBr}^+(\text{H}_2\text{O})$  spectra appear as broadened, shifted versions of the  $\text{IHI}^-$  and  $\text{BrHBr}^-$  spectra. The overall features of the spectra are similar to those of their corresponding bare ions. The peak spacing and relative intensities remain mostly unchanged for each complex compared with the bare ion. The spectral shifts of

$\text{IHI}^{\bullet}(\text{H}_2\text{O})$  and  $\text{BrHBr}^{\bullet}(\text{H}_2\text{O})$  against  $\text{IHI}^-$  and  $\text{BrHBr}^-$  are measured to be about  $355 \pm 0.020$  meV and  $455 \pm 0.020$  meV (from peaks  $A_1$  and  $A_1$  on each spectrum), respectively.

In contrast, photoelectron spectra of species solvated by HI or HBr show a totally different envelope than their corresponding bare ions; they exhibit fewer and broader peaks. The peaks are shifted by  $431 \pm 0.020$  meV and  $626 \pm 0.020$  meV for  $\text{IHI}^{\bullet}(\text{HI})$  and  $\text{BrHBr}^{\bullet}(\text{HBr})$  respectively (from peaks  $A_1$  and  $A_1$ ). In addition from Table 7-1 the peak spacing for each specie is considerably different than the analogous bare ion. The  $\text{IHI}^{\bullet}$  peak spacings are:  $A_{1,2} = \sim 1300 \text{ cm}^{-1}$ ,  $A_{2,3} = \sim 1400 \text{ cm}^{-1}$  and  $A_{3,4} = \sim 1550 \text{ cm}^{-1}$ , while the peak spacings for  $\text{IHI}^{\bullet}(\text{HI})_{1,2}$  are:  $A-A' = \sim 2200 \text{ cm}^{-1}$ ,  $A'-A'' = 2200 \text{ cm}^{-1}$ . The A-B separation for  $\text{IHI}^{\bullet}(\text{HI})$  spectrum each spectrum is  $0.901 \pm 0.030$  eV. This value is comparable to the spin orbit splitting in atomic iodine  $0.943 \text{ eV}^{22}$  similar to bare  $\text{IHI}^{\bullet}$ . The  $\text{BrHBr}^{\bullet}$  peak spacings are:  $A_{1,2} = 1550 \text{ cm}^{-1}$  and  $A_{2,3} = 1700 \text{ cm}^{-1}$ , while the peak spacings for  $\text{BrHBr}^{\bullet}(\text{HBr})$  is:  $A-A' = \sim 2400 \text{ cm}^{-1}$ . For  $\text{BrHBr}^{\bullet}(\text{HBr})_2$  only one peak is accessible at 213nm due to the large shift to lower electron kinetic energy following the addition of an additional HBr.

The  $\text{BrHI}^{\bullet}(\text{HI})$  and  $\text{BHI}^{\bullet}(\text{HBr})$  (figure 7-3) spectra show some similarities. Both spectra are shifted by approximately 540 meV with respect to  $\text{BrHI}^-$  (from peaks  $A_1$  and  $A_1$ ). They also show a relatively shorter progression compared with bare  $\text{BrHI}^-$ . Both show a visible progression of around  $\sim 2500 \text{ cm}^{-1}$ ; this value is slightly smaller than the HBr frequency<sup>23</sup> of  $2648 \text{ cm}^{-1}$ . The  $\text{BrHI}^{\bullet}(\text{HBr})$  progression is less congested than the observed for  $\text{BrHI}^{\bullet}(\text{HI})$ . The A-B separation for each spectrum is  $0.920 \pm 0.030$  eV. This value is comparable to the spin orbit splitting in atomic iodine  $0.943 \text{ eV}^{22}$  analogous to  $\text{BrHI}^-$ .

#### A. Electronic structure calculations

Electronic structure calculations were performed to assist in the interpretation of the data presented above. These calculations are aimed at determining the geometries of the solvated complexes. Geometries were optimized at the HF and UHF(unrestricted Hartree-Fock) levels of theory for the anion and neutral respectively, then further explored using density functional theory (DFT) with the B3LYP (Becke-3-parameter-Lee-Yang-Parr) exchange correlation functional.<sup>24,25</sup> The STO-3G\*, 3-21G\*\*, 6-311\*\* and aug-cc-pVDZ basis sets were used during the study. However for Iodine containing clusters the biggest basis set used is 6-311\*\*. Calculations were performed using Gaussian98 electronic structure package,<sup>26</sup> and the results are summarized in Tables 7-(2-5). The calculated anion structures are shown in Figure 7-5. Experimental and *ab initio* results for H<sub>2</sub>O, HI and HBr are included in Table 7-2 for comparison.

##### a. $\text{XHX}^-(\text{H}_2\text{O})$

For the  $\text{XHX}^-(\text{H}_2\text{O})$  clusters several configurations for the anion complexes were explored at HF/STO-3G\* and HF/6-311G\*\*. Several local minimum structures were found for the anion complex. However only the global minimum structure are reported and further studied at higher levels of theory. Calculated minimum structures include several single hydrogen bonded and two double hydrogen bonded clusters. All single hydrogen bonded configurations have the charge localized in one of the halogen with the water molecule bound to the halogen containing the charge ( $\text{XH}\cdots\text{X}^-\cdots\text{H}_2\text{O}$ ). In these configurations the symmetry of both the  $\text{XHX}^-$  ( $D_{1h}$ ) complex and water molecule ( $C_{2v}$ ) is broken. These configurations have  $C_s$  symmetry. The double hydrogen bonded structures exhibit  $C_{2v}$  symmetry where each hydrogen is bonded to one halogen. These structures share similarities with previously calculated  $\text{FHF}^-(\text{H}_2\text{O})$  clusters by Li *et al.*<sup>27</sup>

The main difference between Li's and our results is that we found the double hydrogen bonded structure where the symmetry of the  $\text{XHX}^-$  ( $\text{C}_{2v}$ ) complex is preserved to be the global minimum. His results show this structure as a local minimum. The calculated global minimum for  $\text{XHX}^\bullet \cdot (\text{H}_2\text{O})$  ( $\text{X} = \text{I}, \text{Br}$ ) is illustrated in Figure 7-1 (A). Bond lengths and angles for the complex at different levels of theory are summarized in Table 7-3. The lowest single hydrogen bonded structure ( $\text{C}_s$ ) for  $\text{BrHBr}^\bullet \cdot (\text{H}_2\text{O})$  is also included for comparison. This structure is calculated to lie  $\sim 100$  meV above the  $\text{C}_{2v}$  complex. Vibrational analysis of this structure reveals no imaginary frequencies further supporting a global minimum. At all levels of theory the anion complex is planar with  $\text{C}_{2v}$  symmetry. Results indicate that the water molecule bound to both the halogen atoms equally, and the charge of the complex is delocalized equally among the halogen atoms. The attraction in the complex is strong enough to cause small changes in the water and  $\text{XHX}^-$  molecules. The  $\text{XHX}^-$  angle change from  $180^\circ$  in the bare ion to  $\sim 177^\circ$  for both  $\text{IHI}^-$  and  $\text{BrHBr}^-$  with the largest basis set. The angle for the water molecule changes from  $104.5^\circ$  to  $\sim 102^\circ$  for both anions. No significant change is noted for all bond lengths ( $\text{HX}$  or  $\text{OH}$ ) in the solvated complex.

#### **b. $\text{IHI}^\bullet \cdot (\text{HI})_n$**

The  $\text{IHI}^\bullet \cdot (\text{HI})_n$  structures show similar characteristics with experimental and theoretical results on clusters of the type  $\text{XHX}^\bullet \cdot (\text{HX})_n$  ( $\text{X} = \text{F}, \text{Br}$ ) ions<sup>19,28,29</sup>. All clusters have a configuration where the charge is localized on a central halogen, therefore breaking the symmetry of the  $\text{XHX}^-$  complex. The structure are better described by an iodide anion ( $\text{I}^-$ ) solvated by HI molecules ( $\text{I}^\bullet \cdot (\text{HI})_n$ ). The  $\text{IHI}^\bullet \cdot (\text{HI})$  complex has  $\text{C}_{2v}$  symmetry (Figure 7-1 B). In this configuration, an iodine atom is surrounded by two HI molecules. Population analysis reveals that more than 58% of the complex charge is

located in the central halogen atom, indicating that the anion complex behaves more like a single halogen solvated by two HI (i.e.  $I^-(HI)_2$ ). The  $IHI^-(HI)_2$  complex exhibit an ammonia like structure with  $C_{3v}$  symmetry. This complex have an iodine center which carries most of the complex charge (51%) analogous to  $IHI^-(HI)$ , although in this case it is surrounded by three HI molecules (i.e.  $I^-(HI)_3$ ). The  $IHI^-(HI)_3$  has a methane type structure near  $T_d$  symmetry, where the center iodine carries around 49% percent of the charge. With the addition of more HI molecules the H-I bond distance become smaller; resembling the free HI bond length. On the other hand the  $I^...HI$  distance increases, suggesting that the solute-solvent interaction become smaller with the addition of solvent (HI) molecules. Theoretical results for  $IHI^-(HI)_{1,2,3}$  clusters are summarized in Table 7-4.

#### c. $BrHI^-(HX)_n$

The  $BrHI^-(HX)$  ( $X = Br, I$ ) structures show similar characteristics with the results on  $IHI^-(HI)$  clusters. The results reveal that in both clusters the charge is mostly localized in a central iodine atom resulting in complexes of the type  $I^-(HBr)_2$  and  $I^-(HBr)(HI)$ . The HI and HBr bond lengths in the clusters are longer compared with free HI and HBr with an increase of 10% and 7% respectively. In  $I^-(HBr)(HI)$ , the HI molecule is significantly closer to the central iodine than HBr, suggesting a stronger interaction between the central  $I^-$  and the HI. This is also confirmed by the larger change in bond length in HI compared to HBr. Results for  $BrHI^-(HX)$  clusters are summarized in Table 7-5.



#### IV. Analysis and Discussion

To analyze the  $\text{XHX}^-(\text{M})_n$  ( $\text{X} = \text{I}, \text{Br}; \text{M} = \text{H}_2\text{O}, \text{HBr}, \text{HI}$ ) data presented above, several points need to be considered in more detail. We are interested in understanding how the solvent molecule interacts with the anion and the neutral complex to produce the observed differences from the  $\text{XHX}^-$  spectrum. We will first consider how the binding within the clusters leads the observed shift of the  $\text{XHX}^-(\text{M})_n$  spectra relative to the spectrum of  $\text{XHX}^-$ . Then, the changes in the photoelectron spectrum will be discussed in terms of the photodetachment of an anion cluster containing a geometrically distorted chromophore ( $\text{XHX}^-$ ) to a neutral complex in which there is a minimal interaction between the solvent molecule and the  $[\text{XHX}]^+$  species. As a result of the  $\text{XHX}^-$  perturbation the Franck-Condon region for  $\text{XHX}^-(\text{M})$  photodetachment is different from that of  $\text{XHX}^-$ . Therefore changes in the photoelectron spectra should yield information about different regions of the neutral potential energy surface. The results are discussed in term of calculated anion and neutral geometries.

We will begin our discussion with water-solvated (i.e. hydrated) clusters. Based in our experience with solvated clusters<sup>30-34</sup>, we know the shift in the photoelectron spectra is caused by a larger stabilization of the anion complex with respect to the neutral complex. Under most conditions, the interactions in the neutral molecule are negligible compared with the interaction in the anion complex. In this case the shift in the photoelectron spectra would directly yield the electrostatic stabilization ( $E_{\text{stab}}$ ) of the anion complex. However this is not necessarily the case for water or the other solvents (HX). Their large dipole moments could lead to significant interactions in the neutral complex. This must be taken into account for the real determination of the stabilization

energy  $E_{\text{stab}}$ . The shift of the  $\text{XHX}^+(\text{H}_2\text{O})$  (349 meV for  $\text{X} = \text{I}$  and 438 meV for  $\text{X} = \text{Br}$ ) complex is comparable with the shift determined by Markovich et al.<sup>31,32</sup> for  $\text{I}^+(\text{H}_2\text{O})$  and  $\text{Br}^+(\text{H}_2\text{O})$  clusters of 450 and 550 meV respectively. The significant reduction in the stabilization energy compared with  $\text{X}^+(\text{H}_2\text{O})$  clusters could be explained in term of possible cluster structures. Further discussion will be presented below.

The  $\text{IHI}^+(\text{HI})$  spectrum is shifted by 431 meV, the addition of a second HI shift the spectra by another 315 meV. The  $\text{BrHBr}^+(\text{HBr})$  spectrum is shifted by 626 meV. The addition of a second HBr shifts the spectra by another 385 meV. The spectral shift for  $\text{IHI}^+(\text{HI})$  is comparable with the  $\text{I}^+(\text{H}_2\text{O})$ , however the  $\text{BrHBr}^+(\text{HBr})$  shift is significantly higher than  $\text{Br}^+(\text{H}_2\text{O})$ .  $\text{BrHI}^+(\text{HBr})$  and  $\text{BrHI}^+(\text{HI})$  are shifted to the same extent (~540 meV) and they exhibit similar vibrational structure. It is important to point out that the shift for  $\text{BrHI}^+(\text{HBr})$  and  $\text{BrHI}^+(\text{HI})$  are almost identical, however they are two different “solvents” molecules. This might indicate that the ion stabilization highly depend in the “solute” molecule rather than the solvent molecule. For the  $\text{XHX}^+(\text{M})$  clusters, the most significant solute-solvent interaction is dipole-charge. This interaction should be largely responsible for the observed spectrum shift, and ion stabilization. Based on this observation we should expect the spectral shift for  $\text{H}_2\text{O}$  to be largest, followed by HBr, with HI producing the smaller shift. However this is not the observed trend. These differences are closely correlated to the cluster structures and will be discussed below.

$\text{XHX}^+(\text{H}_2\text{O})$  and  $\text{XHX}^+$  photoelectron spectra show similar characteristics. This indicates that photodetachment of the  $\text{XHX}^+(\text{H}_2\text{O})$  complex accesses a transition state potential energy surface comparable to neutral XHX surface. In order to observe similar

structure between the  $\text{XHX}^-(\text{H}_2\text{O})/\text{XHX}^-$  photoelectron spectra the Frank-Condon overlap between the anion and neutral surfaces should be similar for both systems. This indicates that the changes in the anion and neutral complex cause by the water molecule are minimal. This is supported by our electronic structure calculations which predict small changes in the solute and solvent molecules. Our results also predict that the symmetry of the  $\text{XHX}^-$  complex is maintained. This is important for the observation of the transition state structure. Breaking the symmetry of the  $\text{XHX}^-$  complex would likely cause photodetachment to access the exit or entrance channel of the transition state potential energy surface (see  $\text{IHI}^-$  and  $\text{BrHI}^-$  discussion below). The main differences in the photoelectron spectra are the shift and the broadening in the vibrational bands. We know that the shift is caused by the ion stabilization of cause by the addition of the water. The broadening in the vibrational bands is probably caused by the excitation of low frequency Van der Waals modes upon photodetachment. Going back to the difference in the observed shift compared with  $\text{X}^-(\text{H}_2\text{O})$ , we suspect that the formation of a double vs. single hydrogen bonded structure have a significant role in the ion stabilization.  $\text{X}^-(\text{H}_2\text{O})$  clusters have a single hydrogen bonded structure<sup>35</sup>, while our calculation indicate that  $\text{XHX}^-(\text{H}_2\text{O})$  have a double hydrogen bonded structure. In order for  $\text{XHX}^-(\text{H}_2\text{O})$  to accommodate the second hydrogen bond the  $\text{XHX}$  and water angles are distorted by  $\sim 3^\circ$  each. This would cause stress in the anion complex, which would be reflected in a further reduction in the ion stabilization energy. Similar phenomena are observed for the  $\text{SO}_2^-(\text{H}_2\text{O})$  complex.<sup>36</sup> We suspect that the formation of a single hydrogen bonded clusters would require the migration of the charge to one of the halogens. This would likely be followed by the symmetry breaking of the water and  $\text{XHX}^-$  molecules. We

believe this process is energetically less favorable than the formation of a double hydrogen bond which is followed by a small change in the water and XHX angle. The lowest  $C_s$  local minimum is calculated to lie  $\sim 100$  meV above the  $C_{2v}$  structure, further supporting our observation.

$IHI^+(HI)$  and  $BrHBr^+(HBr)$  photoelectron spectra show similar characteristics. They both display shorter and broader progressions compared with the bare ions. The peak spacing is also significantly bigger, much closer to free HI and HBr for  $IHI^+(HI)$  and  $BrHBr^+(HBr)$  respectively. Previous experimental and theoretical results for  $BrHBr^+(HBr)_{1,2,3}$  clusters reveal that the addition of HBr to the  $BrHBr^+$  complex distorts the symmetry of the complex.<sup>19</sup> The theoretical calculations reveal that the resulting complexes contain a central halogen carrying the most of charge surrounded by HBr molecules. Based in similarities in their photoelectron spectra and our theoretical calculations we conclude that  $IHI^+(HI)$  clusters exhibit similar behavior, where that charge is localized in a central iodine surrounded by multiple HI (i.e.  $I^+(HI)_2$ ). By altering the symmetry of the  $XHX^+$  complex we are consequently probing a different region of the neutral surface. In the case of  $IHI^+(HI)$  we believe that we are probing the entrance or exit channel of the  $I_A + HI_B \rightarrow I_AH + I_B$  reaction. This is reflected in the HI progression in the photoelectron spectra. We anticipate the length of the vibrational progression to be a result of a change in bond length in the surrounding HX molecules upon photodetachment. As established by Pivonka's *et al.* results and our theoretical results the HX bond length in the anion complex is considerably longer than in the bare HX molecule. The interaction in the neutral complex is expected to be considerably smaller than in the anion complex, resulting in a HX bond length significantly closer to

free HX. Upon detachment the HX bond length decreases. We are able to simulate the HX progression in the  $X^{\bullet}(HX)_2$  photoelectron spectra using the vibrational frequencies obtained from the *ab initio* calculations. The change in the HX bond length was varied in order to reproduce the length of the vibrational progression. The peak widths were largely determined by displacement in low frequency Van der Waals modes. The change in the HX bond length required to reproduce the experimental data is in good agreement with the calculated values. A Franck-Condon simulation of the  $X^{\bullet}(HX)_2$  photoelectron spectra is shown in Figure 7-4. Experimental HI bond lengths obtained from the simulation are included in Table 7-4.

$BrHI^{\bullet}(HBr)$ ,  $BrHI^{\bullet}(HI)$  and  $BrHI^{\bullet}$  exhibit similar structure. All show a visible progression of around  $2500\text{ cm}^{-1}$ , however  $BrHI^{\bullet}(HBr)$  progression is less congested.  $Br + HI \rightarrow BrH + I$  is a typical asymmetric hydrogen transfer reaction. The Franck-Condon region of anion photodetachment lies in the  $I + HBr$  product valley<sup>10</sup>. As a result the photoelectron spectra show mostly HBr motion along the exit valley. Since the anion is already asymmetric, with most of the charge located on the iodine atom, the addition of an additional HBr or HI molecule does not significantly change the spectrum envelope. The spectra show a shorter vibrational progression because the solute-solvent interaction becomes smaller with the addition of more solvent molecules. Therefore the change in bond length upon detachment is smaller. Similar to  $IHI^{\bullet}(HI)$  we were able to simulate the  $BrHI^{\bullet}(HX)$  ( $X = Br, I$ ) photoelectron spectra. For  $BrHI^{\bullet}(HBr)$  we used a single HBr vibrational mode, while for  $I^{\bullet}(HI)(HBr)$  two modes were used (HI and HBr). The only assumption used is that the HBr and HI motion in  $I^{\bullet}(HI)(HBr)$  are not coupled and

could be considered as separate harmonic oscillators. Results for  $\text{BrHI} \cdot (\text{HX})$  ( $\text{X} = \text{Br}, \text{I}$ ) are summarized in table 7-5.

## V. Conclusions

For  $\text{XHX} \cdot \text{H}_2\text{O}$  the symmetry of the bihalide complex is preserve. This is somewhat due to a double hydrogen bonded structure in the anion complex. Previously observe transition state features are also observed for the solvated clusters indicating that one water does not significantly perturb the transition state or TST precursor. For the other clusters  $\text{XHX} \cdot (\text{M})_{1,2}$  ( $\text{M} = \text{HBr}, \text{HI}$ ), charge localization is responsible for breaking the symmetry of the  $\text{XHX}^-$  complex. This is reflected by a large difference in the photoelectron spectra compared to the bare ion. As a result, the anion photoelectron spectrum probes a region of the neutral potential energy surface distant from the transition state.

## VI. References:

- <sup>1</sup> A. H. Zewail, *Science* 242, 1645 (1988).
- <sup>2</sup> P. R. Brooks, *Chemical Review* 88, 407 (1988).
- <sup>3</sup> G. C. Schatz, *J. Phys. Chem.* 94, 6157 (1990).
- <sup>4</sup> A. Weaver, R. B. Metz, S. E. Bradforth, and D. M. Neumark, *J. Phys. Chem.* 92, 5558 (1988).
- <sup>5</sup> D. M. Neumark, *Accts. Chem. Res.* 26, 33 (1993).
- <sup>6</sup> S. Leutwyler and J. Bosiger, *Faraday Discussions of the Chemical Society*, 225 (1988).
- <sup>7</sup> B. M. Ladanyi and J. T. Hynes, *J. Am. Chem. Soc.* 108, 585 (1986).
- <sup>8</sup> R. B. Metz and D. M. Neumark, *J. Chem. Phys.* 97, 962 (1992).
- <sup>9</sup> R. B. Metz, A. Weaver, S. E. Bradforth, T. N. Kitsopoulos, and D. M. Neumark, *J. Phys. Chem.* 94, 1377 (1990).
- <sup>10</sup> S. E. Bradforth, A. Weaver, D. W. Arnold, R. B. Metz, and D. M. Neumark, *J. Chem. Phys.* 92, 7205 (1990).
- <sup>11</sup> D. W. Arnold, C. S. Xu, and D. M. Neumark, *J. Chem. Phys.* 102, 6088 (1995).
- <sup>12</sup> D. E. Manolopoulos, K. Stark, H. J. Werner, D. W. Arnold, S. E. Bradforth, and D. M. Neumark, *Science* 262, 1852 (1993).
- <sup>13</sup> S. E. Bradforth, D. W. Arnold, D. M. Neumark, and D. E. Manolopoulos, *J. Chem. Phys.* 99, 6345 (1993).
- <sup>14</sup> I. M. Waller, T. N. Kitsopoulos, and D. M. Neumark, *J. Phys. Chem.* 94, 2240 (1990).
- <sup>15</sup> D. W. Arnold, *Ph. D. Dissertation*, University of California, Berkeley, 1994.
- <sup>16</sup> D. M. Neumark, in *Advances in Molecular Vibrations and Collision Dynamics*, edited by J. M. a. R. Brauman, M.A. (JAI Press, Greenwich, CT, 1991), Vol. 1A, pp. 165.
- <sup>17</sup> Z. Liu, H. Gomez, and D. M. Neumark, *Chem. Phys. Lett.* 332, 65 (2000).
- <sup>18</sup> Z. Liu, H. Gomez, and D. M. Neumark, *Faraday Discuss* 118, 221 (2001).

- <sup>19</sup> N. L. Pivonka, C. Kaposta, G. v. Helden, G. Meijer, L. Woste, D. M. Neumark, and K. R. Asmis, *J. Phys. Chem.* in press (2002).
- <sup>20</sup> C. Xu, G. R. Burton, T. R. Taylor, and D. M. Neumark, *J. Chem. Phys.* 107, 3428 (1997).
- <sup>21</sup> I. Prigogine and S. A. Rice, *Advances in chemical physics. Volume LXXXI.* (Wiley, New York, 1992).
- <sup>22</sup> H. Hotop and W. C. Lineberger, *Journal of Physical and Chemical Reference Data* 14, 731 (1985).
- <sup>23</sup> G. Herzberg and J. W. T. Spinks, *Molecular spectra and molecular structure.* (Van Nostrand Reinhold, Princeton, N.J., 1945).
- <sup>24</sup> A. D. Becke, *J. Chem. Phys.* 98, 1372 (1993).
- <sup>25</sup> C. Lee, W. Yang, and R. G. Parr, *Phys. Rev. B* 37, 785 (1988).
- <sup>26</sup> M. J. Frisch et al, *Gaussian 98* (Gaussian, Inc., Pittsburgh PA, 1998).
- <sup>27</sup> G. P. Li, B. Reinhart, and I. P. Hamilton, *J. Chem. Phys.* 115, 5883 (2001).
- <sup>28</sup> I. G. Shenderovich et al, *Berichte Der Bunsen-Gesellschaft-Physical Chemistry Chemical Physics* 102, 422 (1998).
- <sup>29</sup> S. A. Perera and R. J. Bartlett, *J. Am. Chem. Soc.* 122, 1231 (2000).
- <sup>30</sup> G. Markovich, L. Perera, M. L. Berkowitz, and O. Cheshnovsky, *J. Chem. Phys.* 105, 2675 (1996).
- <sup>31</sup> G. Markovich, S. Pollack, R. Giniger, and O. Cheshnovsky, *J. Chem. Phys.* 101, 9344 (1994).
- <sup>32</sup> G. Markovich, R. Giniger, M. Levin, and O. Cheshnovsky, *J. Chem. Phys.* 95, 9416 (1991).
- <sup>33</sup> K. R. Asmis, T. R. Taylor, C. S. Xu, and D. M. Neumark, *J. Chem. Phys.* 109, 4389 (1998).
- <sup>34</sup> H. Gomez, T. R. Taylor, and D. M. Neumark, *J. Chem. Phys.* 116, 6111 (2002).
- <sup>35</sup> P. Ayotte, G. H. Weddle, J. Kim, J. Kelley, and M. A. Johnson, *J. Phys. Chem. A* 103, 443 (1999).
- <sup>36</sup> E. A. Woronowicz, W. H. Robertson, G. H. Weddle, M. A. Johnson, E. M. Myshakin, and K. D. Jordan, *J. Phys. Chem. A* 106, 7086 (2002).



- <sup>37</sup> *G. Herzberg, Electronic spectra and electronic structure of polyatomic molecules. (Van Nostrand, New York, 1966).*
- <sup>38</sup> *G. Herzberg, Spectra of diatomic molecules. (Van Nostrand, New York, 1956).*

Table 7-1. Experimental peaks position and labels

Species	Position (eV) <sup>a</sup>
IHI <sup>+</sup>	1.879(A <sub>1</sub> ), 1.719(A <sub>2</sub> ), 1.545(A <sub>3</sub> ), 1.353(A <sub>4</sub> )
IHI <sup>+</sup> •(H <sub>2</sub> O)	1.502(A <sub>1</sub> ), 1.375(A <sub>2</sub> ), 1.187(A <sub>3</sub> ), 0.982(A <sub>4</sub> )
IHI <sup>+</sup> •(HI)	1.425(A), 1.160(A'), 0.899(A''), 0.522(B)
IHI <sup>+</sup> •(HI) <sub>2</sub>	1.099(A), 0.835(A'), 0.584(A'')
BrHBr <sup>+</sup>	1.327(A <sub>1</sub> ), 1.125(A <sub>2</sub> ), 0.914(A <sub>3</sub> )
BrHBr <sup>+</sup> •(H <sub>2</sub> O)	0.872(A <sub>1</sub> ), 0.680(A <sub>2</sub> ), 0.465(A <sub>3</sub> )
BrHBr <sup>+</sup> •(HBr)	0.693(A), 0.397(A')
BrHBr <sup>+</sup> •(HBr) <sub>2</sub>	0.306(A)
BrHI <sup>+</sup>	1.935(A <sub>1</sub> ), 1.615(A <sub>2</sub> ), 1.365(A <sub>3</sub> ), 1.045(B <sub>1</sub> ), 0.739(B <sub>2</sub> )
BrHI <sup>+</sup> •(HBr)	1.391(A), 1.081(A'), 0.817(A''), 0.485(B)
BrHI <sup>+</sup> •(HI)	1.409(A), 1.103(A'), 0.846(A''), 0.502(B)

<sup>a</sup> Error ± 0.025 eV

Table 7-2. Results of *Ab initio* electronic structure calculations for  $\text{XHX}^+$ ,  $\text{H}_2\text{O}$ ,  $\text{HBr}$  and  $\text{HI}$ . All bond lengths in Å.

Species		Method	$A_{\text{H-X-H}}$	$R_{\text{X-H}}$ (Å)	Frequencies ( $\text{cm}^{-1}$ )
$\text{IHI}^+$	$D_{\text{IH}}$	B3LYP/3-21G**	180.0	1.9844	132,575,575,1079
		B3LYP/6-311G**	180.0	1.9543	141,601,601,906
$\text{BrHBr}^+$	$D_{\text{IH}}$	B3LYP/6-311++G**	180.0	1.7311	198,700,700,801
		B3LYP/aug-cc-pVDZ	180.0	1.7292	197,703,703,829
$\text{H}_2\text{O}$	$C_{2v}$		$A_{\text{H-O-H}}$	$R_{\text{O-H}}$ (Å)	Frequencies ( $\text{cm}^{-1}$ )
		B3LYP/3-21G**	103.94	0.9966	1692,3415,3555
		B3LYP/6-311++G**	105.04	0.9622	1602,3815,3920
		B3LYP/aug-cc-pVDZ	104.73	0.9648	1614,3801,3906
		Experiment <sup>a</sup>	104.5	0.965	1595,3755,3656
$\text{HBr}$	$C_{\text{IH}}$		$R_{\text{O-H}}$ (Å)	Frequency ( $\text{cm}^{-1}$ )	
		B3LYP/6-311++G**	1.4267	2593	
		B3LYP/aug-cc-pVDZ	1.4314	2595	
		Experiment <sup>b</sup>	1.4144	2648.97	
$\text{HI}$	$C_{\text{IH}}$	B3LYP/3-21G**	1.6387	2308	
		B3LYP/6-311G**	1.6260	2337	
		Experiment <sup>b</sup>	1.60916	2309.01	

<sup>a</sup> From Reference <sup>37</sup>

<sup>b</sup> From Reference <sup>38</sup>

Table 7-3. Results of *Ab initio* electronic structure calculations for  $\text{HX}^+ \cdot (\text{H}_2\text{O})$  clusters. All bond lengths in Å.

Species		Method	$\text{A}_{\text{H}\cdots\text{X}}$	$\text{R}_{\text{H}\cdots\text{X}}$ (Å)	$\text{R}_{\text{H}\cdots\text{X}}$ (Å)	$\text{R}_{\text{O}\cdots\text{H}}$ (Å)	$\text{A}_{\text{H}\cdots\text{O}\cdots\text{H}}$	$\text{A}_{\text{H}\cdots\text{X}\cdots\text{H}}$
$\text{HI}^+ \cdot (\text{H}_2\text{O})$	$\text{C}_{2v}$	B3LYP/3-21G**	175.75	2.8726	1.947	0.9703	101.22	67.53
		B3LYP/6-311G**	177.14	2.9726	1.9498	0.9705	101.99	67.73
$\text{BrHBr}^+ \cdot (\text{H}_2\text{O})$	$\text{C}_{2v}$	B3LYP/6-311++G**	176.18	2.7367	1.7306	0.9672	101.08	70.86
		B3LYP/aug-cc-pvdz	176.90	2.7302	1.7288	0.9711	101.34	70.58
$\text{Cs}$		B3LYP/6-311++G**	179.41	2.5528	1.6067	0.9745	103.73	
					1.9063	0.9634		
		B3LYP/aug-cc-pvdz	179.05	2.4871	1.6111	0.9792	101.98	
					1.8799	0.9643		

Table 7-4. Results of *Ab initio* electronic structure calculations for  $\text{IH}^+ \bullet (\text{HI})_{1,2,3}$  clusters. All bond lengths in Å.

Species	Method	$A_{\text{H} \dots \text{H}}$ (Å)	$R_{\text{H}}^{\text{H}}$ (Å)	$R_{\text{H} \dots \text{X}}$ (Å)	$A_{\text{H} \dots \text{H}_2}$
$\text{IH}^+ \bullet (\text{HI})$ Experiment	$\text{C}_{2v}$ B3LYP/3-21G**	107.68	1.780	2.196	177.60
	B3LYP/6-311++G**	107.57	1.753	2.254	177.73
			1.742		
$\text{IH}^+ \bullet (\text{HI})_2$ Experiment	$\text{C}_{3v}$ B3LYP/3-21G**	107.85	1.728	2.332	178.98
	B3LYP/6-311G**	108.09	1.698	2.414	179.45
			1.709		

Table 7-5. Results of *Ab initio* electronic structure calculations for BrH<sup>+</sup> • (HBr) and BrH<sup>+</sup> • (HI) clusters. All bond lengths in Å.

Species		Method	A <sub>II-I-II</sub>	R <sub>I...II</sub> (Å)	R <sub>I...III</sub> (Å)	R <sub>II-Br</sub> (Å)	R <sub>II-I</sub> (Å)
BrH <sup>+</sup> • (HI)	C <sub>s</sub>	B3LYP/3-21G**	110.18	2.3441	2.1349	1.5054	1.8103
		B3LYP/6-311G**	110.58	2.3865	2.1981	1.4981	1.7731
		Experiment				1.477	1.678
BrH <sup>+</sup> • (HBr)	C <sub>2v</sub>	B3LYP/3-21G**	114.85	2.2774		1.5235	
		B3LYP/6-311G**	100.46	2.3398		1.5116	
		Experiment				1.549	

## VII. Figures

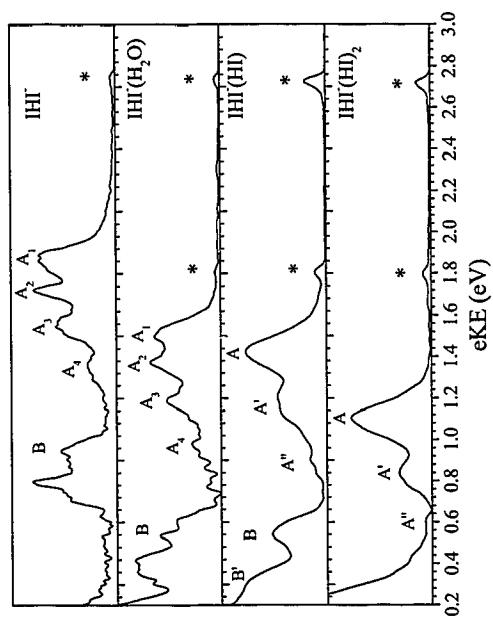


Figure 7-1. Anion photoelectron spectra of IHI<sup>•</sup> • (H<sub>2</sub>O) and IHI<sup>•</sup> • (HI)<sub>1,2</sub> measured at photon energy of 5.821 eV (213 nm).

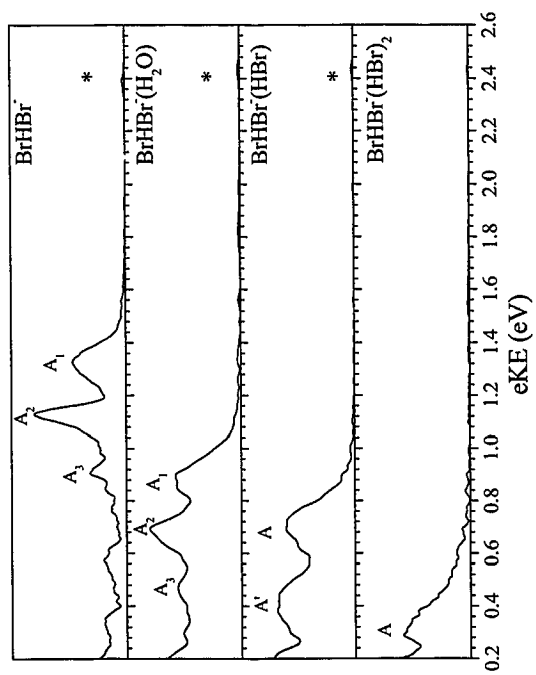


Figure 7-2. Anion photoelectron spectra of BrHBr<sup>-</sup>•(H<sub>2</sub>O) and BrHBr<sup>-</sup>•(H)<sub>1,2</sub> measured at photon energy of 5.821 eV (213 nm).



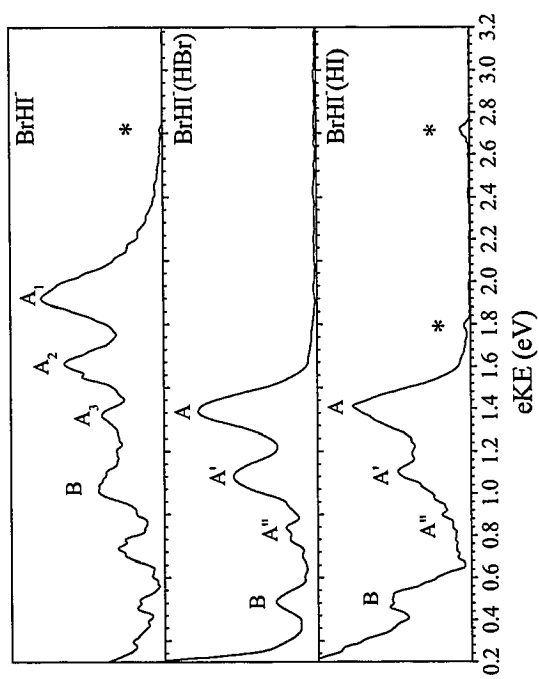


Figure 7-3. Anion photoelectron spectra of  $\text{BrHI}^- \cdot (\text{HBr})$  and  $\text{BrHI}^- \cdot (\text{HI})$  measured at photon energy of 5.821 eV (213 nm).

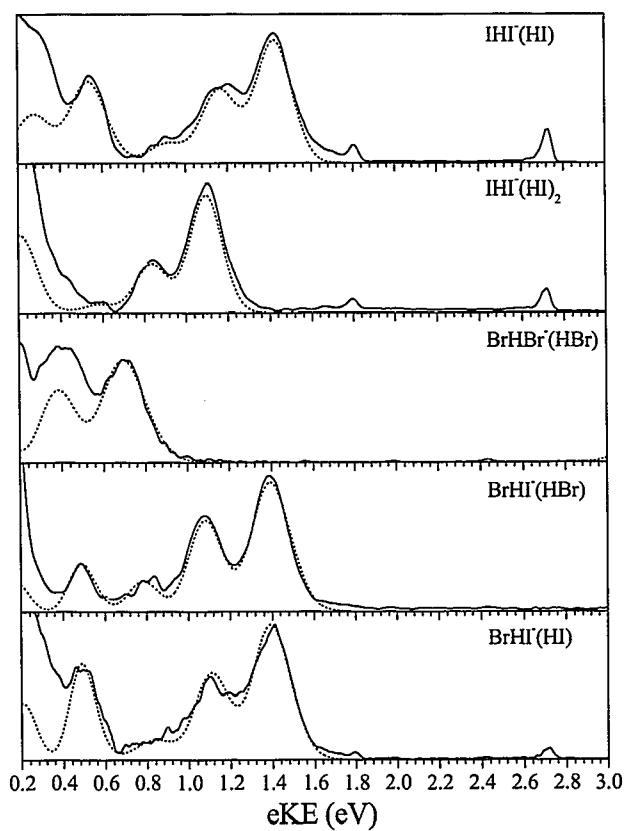


Figure 7-4. Franck-Condon simulation (dashed) of the  $\text{XHX}^+(\text{HX})$  ( $\text{X} = \text{I}, \text{Br}$ ) complexes, experimental spectrum is also shown (solid).

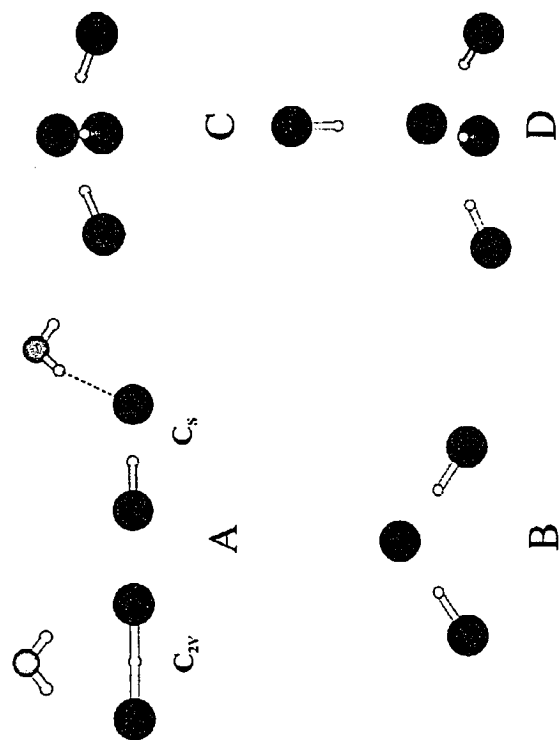


Figure 7-5. Lowest energy structures calculated for the anions based on results from Tables 1-5. For the  $\text{BrHI} \cdot (\text{HBr})$  complex (B) Iodine occupies the center of the complex.

## *Appendix A: Frank-Condon Simulation Program*

---

### **I. Introduction**

As demonstrated throughout this thesis, the analysis of data collected using anion photoelectron spectroscopy requires the ability to calculate the Franck-Condon factors (FCF's) for the photodetachment process being studied. This appendix describes and contains the source code for a computer program PESN, which has been developed to compute the Frank-Condon overlap between the eigenvectors of two general one-dimensional potential energy surfaces (one for the anion and one for the neutral in the case of anion photoelectron spectroscopy). While the core of the code only calculates one-dimensional FCF's, combination band calculations can be made within the separable normal coordinate approximation. In addition, the code is set up to calculate FCF's for photodetachment transitions to multiple electronic states and convolute them all together for direct comparison with the experimental data.

This code is intended as a replacement for the old and slow "FC Analysis program" (a.k.a. PES). The program was designed with speed and simplicity in mind since the spectrum simulation process is an iterative and monotonous one. Many of the features available in the old code (PES) are available in the new program (PESN). Several features have been eliminated for simplicity and other need to be implemented in the future (see to do list). The code is currently set up to be used in the analysis of anion photoelectron data (PES), however the code is general and simple enough to be easily modified to simulate Zero Electron Kinetic Energy (ZEKE) spectroscopy data.

The PESN program is designed to be user friendly and reasonably simple. The concept behind the program is that the user will be attempting to fit the experimental data by an iterative simulation process (a.k.a. "by eye"). Before running the program the user must create an input file with the relevant information about the states involved in the simulation. This process is done by running a secondary program called writep from "write parameters". This program prompts for the variables needed to perform the simulation.

There are many features of PESN which have been developed for the analysis over the last years. Now, I will attempt to summarize the capabilities of PESN.

1. Multiple Electronic States – The program is capable of calculating FCF's of up to 15 different electronic states, scaling each state to the relative photodetachment cross-section (value specified by user for each state), after which it will convolute all states together.
2. Multiple Vibrational Modes (for each electronic state) – PESN treats multiple vibrational modes in the separable normal mode approximation. For multimode simulations, combination bands arise. The positions are calculated by summation of terms for individual mode vibrational levels and the intensities are determined by taking the product of individual mode FCF's.
3. Different Temperatures for Individual Vibrational Modes – PESN allows you to account for anion vibrational excitation which is not equilibrated between the different normal modes.

4. Simultaneous Generation of Convolved and Stick Spectrum – The program automatically generates separate output files with stick spectra and convoluted spectra for easy comparison of peak positions and intensities.
5. Diagnostic Output Features – PESN provides several files which summarize the FCF calculations and serve as diagnostics for the assignment of spectral features.
6. Multiple Platforms - PESN is not limited to powerful workstations. It is currently available for Linux, Silicon Graphics (SGI) and Windows (Win32, using cygwin port).

## II. Usage

PESN is without a doubt user friendly and fast. There are a minimum of 12 questions asked to collect the required information for the simulation. In order to generate an input file containing the simulation parameters the user must run the program "writep". The first question, "Enter the filename to be created?" is asked in order to determine the file name to store the simulation parameters. The file will be called "FILENAME.in". The input file must have the right format in order for PESN to read it, so it is recommended to use "writep" to generate the initial file. This file can be modified for future use and will be read in automatically by PESN. The code then asks about the calculations to be done. Either a diatomic or polyatomic simulation can be chosen. Then the program will read the simulation parameters from the keyboard. After the input file is generated the user can use the command "PESN -iFILENAME" to perform the simulation based on the parameters in the file "FILENAME.in". The successful execution of the program will generate a series of files that contain the simulated spectra as well as other useful information about the calculation. The file "FILENAME.dat"

contains the simulated spectrum convoluted with the experimental resolution. The file "FILENAME.stick" contains the simulated stick spectrum convoluted. The file "FILENAME.out" contains an explanation about the input parameters, as well as some other useful information used to troubleshoot problems with the code.

The input information needed by the program is shown in sample input file shown below, as well as sample of the output files generated by the execution of the command "PESN -iFILENAME":

#### Sample file - O2.in

```
d
  16.00000      16.00000
  1
  1
    2.5
  300.00000
 1090.00000      1580.00000
    0.00000      0.00000
 15   50
    1.35000      1.20700
    1.00000
    30.00000
```

#### Program output for O2.in

Mon Aug 12 03:20:35 2002

```
!!   Welcome to PES 2000 v0.01   !!
      Harry Gomez - Neumark Group
```

```
Input data file      = o2.in
Output files         = o2
```

```
d
  16.00000      16.00000      Molecule Type
  1                                     Diatomic Mases
  1                                     Electronic states
    2.500                                     Modes for State 1
  300.00000                                     Origin of band
 1090.00000      1580.00000      Temp for state 1
    0.00000      0.00000      Frequencies (A N) mode 1
 15   50                                     Anharmonicities (A N) mode 1
    1.35000      1.20700      Vibrational levels (A N)
                                     Atomic distances (A N) mode 1
```

```

1.000000          Scale factor for state 1
30.000000          Energy resolution
Reduce mass 8 = 1.32843e-23
End of Input file
HOFCF for state 1 and mode 1.. done ..
Generating spectrum.. done ..

```

#### Sample file - O2.out

```

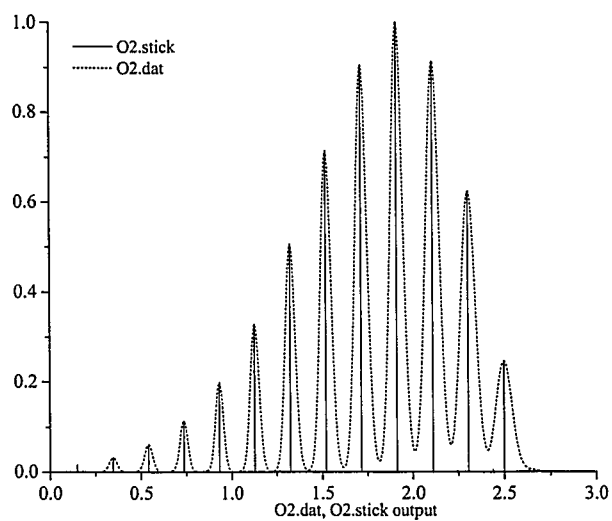
d
1 16.00000 16.00000 Molecule Type
1 Diatomic masses
1 Electronic states
2.500 Modes for State 1
300.00000 Origin of band
1090.00000 Temp for state 1
0.00000 1580.00000 Frequencies (A N) mode 1
0.00000 0.00000 Anharmonicities (A N) mode 1
15 50 Vibrational levels (A N)
1.35000 1.20700 Atomic distances (A N) mode 1
1.00000 Scale factor for state 1
30.00000 Energy resolution
Reduce mass 8.000000 = 1.328432e-23
End of Input File

Anion population distribution for state 1
na = Anion vib Level N
na = 0 Pop = 0.9946335
na = 1 Pop = 0.0053377
na = 2 Pop = 0.0000286
na = 3 Pop = 0.0000002

```

Graphical representaion of files - O2.dat and O2.stick





### III. Advanced usage/Modifications

If it is necessary to modify the code, it is recommended that a copy be made for yourself while modifying the code until it is completely bug-free. If the changes are general, update the sub-routine versions, comment thoroughly with dates of modification and place them in the archival directory and put the new version of PES in the /usr/fcf directory for general usage. If not general, keep for yourself. Once modifications are made the program can be compiled using:

"make -f makefile"

This invokes the makefile "makefile" which contains all of the compilation information. This file must be updated when routine versions are changed:

#### Source file -makefile

```
#
#
CC=g++
#
CFLAGS=-Wall -g -O3 -ansi -funroll-loops -mcpu=i686
#
INSDIR=/home/harry/bin
PEXE = pesn
WEXE = writep
#
#
all:pesn writep
#
#
rebuild:clean all
#
pesn: init.h pesn.o simfcf.o hofcf.o readp.o combination.o misc.o
$(CC) $(CFLAGS) -o $(PEXE) misc.o pesn.o simfcf.o hofcf.o readp.o
combination.o
#
#
pesn.o:misc.o init.h pesn.cpp
$(CC) $(CFLAGS) -c pesn.cpp
#
simfcf.o:pesn.o init.h simfcf.cpp
$(CC) $(CFLAGS) -c simfcf.cpp
#
hofcf.o:init.h hofcf.cpp
$(CC) $(CFLAGS) -c hofcf.cpp
#
#
readp.o:init.h readp.cpp
$(CC) $(CFLAGS) -c readp.cpp
#
combination.o:init.h combination.cpp
$(CC) $(CFLAGS) -c combination.cpp
#
misc.o:init.h misc.cpp
$(CC) $(CFLAGS) -c misc.cpp
#
writep: writep.cpp init.h
$(CC) $(CFLAGS) -o $(WEXE) writep.cpp
#
#
install: all
cp -f $(PEXE) $(INSDIR)
```

```

cp -f $(WEXE) $(INSDIR)
#
#
clean:
rm *.o $(PEXE) $(WEXE)
#

```

#### IV. To do list

There are several features in the code which have not been implemented that were available in the old code. These features were not implemented since are rarely use and hence hard to implement and troubleshoot. Within the features that would be nice to add to the PESN program in the feature are;

1. Capability to simulate anhamonic potentials using Morse wavefunctions
2. Capability to calculate Frank-Condon overlap of general potentials numerically
3. Add graphical user interface to the PESN program to facilitate simulation and comparison of experimental data.

## V. Description of files

- a. **init.h** – contains variable definitions and most program parameters
- b. **pesn.cpp** – Main program controls and call all other routines.
- c. **reap.cpp** – Subroutine to read parameters simulation parameters.
- d. **hofcf.cpp** – Subroutine that calculates Harmonic Franck-Condon factors.
- e. **simfcl.cpp** – Subroutine that sort transition lines and generate stick and convoluted photoelectron spectra.
- f. **misc.cpp** – Subroutine with miscellaneous functions used by the main program and subroutines.
- g. **writcp.cpp** – Program to create and format the input file and input parameters.

## VI. Source code listing

```
a. init.h
/*****
init.h
Variables initialization, program parameters
*****/

#include <math.h>
#include <stdio.h>
#include <iostream.h>
#include <stdlib.h>
#include <time.h>

const double ATMASS = 1.6605402E-24;
const double PI = 3.14159265359;
const double H = 6.6260755E-27;
const double HB = 6.6260755E-27/3.14159265359;
const double C = 2.99792458E10; //speed of light in cm
const double CTEMP = 8.61735E-5; //change Temp K ==> eV
const double CWEV = 8065.479; //change cm-1 ==> eV
const double K = 1.380658E-23; //Boltzman C

//Laser energies
const double w157 = 7.89708;
const double w193 = 6.42054;
const double w213 = 5.82085;
const double w248 = 4.99936;
const double w266 = 4.66106;
const double w299 = 4.14663;
const double w355 = 3.49251;
const double w416 = 2.98039;
const double w498 = 2.48964;
const double w532 = 2.33053;
```

```

const unsigned int MAXNLEV = 128; //2^7 //Max number of neutral levels
const unsigned int MAXALEV = 32; //2^5 //Max number of anion levels
const unsigned int MAXMODES = 6;
const unsigned int MAXSTATES = 16; //2^2 //Max number of electronic
states

const double MAXRES = 5e5; // Max Resolution for spectrum 1e3 == 0.001
const long unsigned int MAXSIM = 250000; //simulation array BIG !
typedef double sim[2][MAXSIM];

const float FCFCOFF = 1E-8; //FCF min cut off

typedef double QQI[MAXMODES][MAXALEV][MAXNLEV];
typedef double QQs[MAXALEV][MAXNLEV];

typedef double combi[2][262144];

//Structure with all simulation parameters and simulated data
struct fcf {
    unsigned int mode;
    float temp;
    double wea[MAXMODES]; //anion freq
    double wen[MAXMODES]; //neutral freq
    double xewea[MAXMODES]; //anion anharmonicity
    double xewen[MAXMODES]; //neutral anharmonicity
    unsigned int na[MAXMODES];
    unsigned int nn[MAXMODES];
    float ra[MAXMODES];
    float rn[MAXMODES];
    QQI fcfi;
    float orig;
    QQI fcfe;
    float scale; //scale factor for simulation
    combi comb;
    long unsigned int combnn;
};

```

#### **b. pesn.cpp**

```

/*****

pesn.cpp
Main Program file
Othe subroutines are called from this file

*****/
#include <math.h>
#include <stdio.h>
#include <iostream.h>
#include <stdlib.h>
#include <string.h>
#include <time.h>
#include "init.h"

int fixres; //Fix resolution
double eres ; // 2* ERES is the energy resolution

```

```

FILE *infile,*outfile,*debugf;
char filename[128],readfile[128],ofile[128];

double redmass,redmass2;

int error;
int debug;
time_t t;

struct fcf fcfs[MAXSTATES];

//Display usage funtion
extern void usage(void);

//Display help information
extern void help(void);

//Calculated Harmonic Franck-Condon Factors
extern void HOFcf(const unsigned int &state,const unsigned int &mode,
    struct fcf &fcfs);

//Simulated Spetrum
extern void simfcf(const unsigned int &states,struct fcf
    fcfs[MAXSTATES]);

//Read parameters
extern void readp(unsigned int &states,double &res,
    double &redmass,struct fcf fcfs[MAXSTATES]);

//Calculate Combination bands
extern void combination(const unsigned int &modes,struct fcf &sfcf);

int main (int argc, char *argv[])
{
    unsigned int nn,na;
    unsigned int state,states;
    unsigned int mode;
    int error = 1;

    time(&t);
    printf("%s\n",ctime(&t));
    printf("!!\tWelcome to PES 2000 v0.01\t!!\n");
    printf("\tHarry Gomez - Neumark Group\n");

    while ((argc > 1) && (argv[1][0] == '-'))
    {
        switch(argv[1][1])
        {
            case 'd':
                debug = atoi(&argv[1][2]);
                if (debug > 5) debug = 0;
                cout <<"Debug level \t\t\t= "<< debug <<"\n";
                break;
            case 'i':
                strcpy(filename,&argv[1][2]);

```

```

strcpy(readfile,filename);
strcat(readfile,".in");
cout <<"Input data file \t\t=" << readfile <<"\n";
infile = fopen(readfile,"r");
error = 0;
if (infile == NULL)
{
    cout <<"\nFile \""<<readfile<<"\" not found\n";
    usage();
}
break;
case 'o':
    strcpy(filename,&argv[1][2]);
    break;
case 'h':
    help();
    break;
case 'r':
    fixres = 1;
    //fix resolution not  $\sim(EKE)^{3/2}$ 
    break;

default:
    cerr << "!!\tBad option\t\t=" << argv[1] <<"\t!!\n\n";
    usage();
}
--argc;
++argv;
}

if (error)
{
    usage();
}

cout <<"Output files \t\t\t=" << filename <<"\n";

ofile = filename;
strcat(ofile,".out");
outfile = fopen(ofile,"w");

//Read parameters from file file.in
readp(states,eres,redmass,fcfs);

//Calculate HO-FCF Factors

for (state = 1;state <= states; ++state)
    for (mode = 1; mode <= fcfs[state].mode; ++mode)
    {
        cout <<"HOFCF for state "<<state<<" and mode "
            <<mode <<".. "<<flush;
        HOFCF(state,mode,fcfs[state]);
        cout <<" done ..\n";

        //if Debug Print output
        if (debug == 3)

```

```

        for (na = 0; na <= fcfs[state].na[mode]; ++na)
            for (nn = 0; nn <= fcfs[state].nn[mode]; ++nn)
            {
                printf("na =%3d nn =%3d Ev =%8.5f QQ = %8.5f \n",na,nn,
                    fcfs[state].fcfe[mode][na][nn],
                    fcfs[state].fcfi[mode][na][nn]);
            }
    }

//End of HO-FCF Calc

//Combination Bands calculatoin

for (state = 1;state <= states; ++state)
{
    if (fcfs[state].mode > 1)
    {
        cout <<"Calculating combination bands for state "<<state
            <<".. "<<flush;
        combination(fcfs[state].mode,fcfs[state]);
    }
}

//Simulation subroutine
simfcf(states,fcfs);

fclose(infile);
fclose(outfile);

return(0);
}

c. readp.cpp
/*****
readp.cpp
read input file parameters

*****/
#include <math.h>
#include <stdio.h>
#include <iostream.h>
#include <stdlib.h>
#include "init.h"

extern FILE *infile,*outfile;
extern char readfile[128];
extern int debug;

void readp(unsigned int &states,double &res,
    double &redmass,struct fcf fcfs[MAXSTATES]);

/*****

```



```

void readp(unsigned int &states,double &res,
           double &redmass,struct fcf fcfs[MAXSTATES])
{
    char type[20];
    float mass1,mass2;
    unsigned int state;
    unsigned int mode;

    //    printf("Diatomic(d) of Poliatomic(p) ?\n");
    fgets(type,sizeof(type),infile);
    cout <<'\\n' << type[0] << "\\t\\t\\tMolecule Type\\n";

    fprintf(outfile,"\\n");
    fprintf(outfile,"%c\\t\\t\\tMolecule Type\\n",type[0]);

    if (type[0] == 'd')
    {
        fscanf(infile,"%f %f",&mass1,&mass2);
        printf("%15.5f\\t\\tDiatomic Mases\\n",mass1,mass2);
        fprintf(outfile,"%15.5f\\t\\tDiatomic masses\\n",
                mass1,mass2);
        redmass = ((mass1*mass2)/(mass1+mass2))*ATMASS;
    }
    else
    {
        fscanf(infile,"%lf",&redmass);
        printf("%15.5f\\t\\tReduce Mass\\n",redmass);
        fprintf(outfile,"%15.5f\\t\\tReduce mass\\n",redmass);
        redmass = redmass * ATMASS;
    }

    fscanf(infile,"%4d",&states);
    printf("%4d\\t\\t\\tElectronic states \\n",states);
    fprintf(outfile, "%4d\\t\\t\\tElectronic states \\n",states);

    for(state = 1; state <= states; ++state)
    {

        fscanf(infile,"%4d",&fcfs[state].mode);
        if (fcfs[state].mode > MAXMODES)
        {
            cout <<"!! Modes for state "<<state<<" > MAXMODES... !!\\n";
            cout <<"!! Please fix input file = "<<readfile <<" !!\\n";
            cout <<"exit..";
            exit(8);
        }

        printf("%4d\\t\\t\\tModes for State %d\\n",fcfs[state].mode,state);
        fprintf(outfile,"%4d\\t\\t\\tModes for State %d\\n",
                fcfs[state].mode,state);
    }
}

```

```

fscanf(infile,"%f",&fcfs[state].orig);
printf("%15.3f\t\t\tOrigin of band\n",fcfs[state].orig);
fprintf(outfile,"%15.3f\t\t\tOrigin of band\n",fcfs[state].orig);

fscanf(infile,"%f",&fcfs[state].temp);
if (fcfs[state].temp == 0)
{
    cout << "!! Min teperature 0.100 K !!\n";
    fcfs[state].temp = 0.1;
}
printf("%15.5f\t\t\tTemp for state %d\n",fcfs[state].temp,state);
fprintf(outfile,"%15.5f\t\t\tTemp for state %d\n",fcfs[state].temp,state);

for (mode = 1; mode <= fcfs[state].mode; ++mode)
{
    fscanf(infile,"%lf %lf",
        &fcfs[state].wea[mode],&fcfs[state].wen[mode]);
    printf("%15.5f%15.5f\t\tFrequencies (A N) mode %d\n",
        fcfs[state].wea[mode],fcfs[state].wen[mode],mode);
    fprintf(outfile,"%15.5f%15.5f\t\tFrequencies (A N) mode %d\n",
        fcfs[state].wea[mode],fcfs[state].wen[mode],mode);

    fscanf(infile,"%lf %lf",
        &fcfs[state].xwea[mode],&fcfs[state].xwen[mode]);
    printf("%15.5f%15.5f\t\tAnharmonicities (A N) mode %d\n",
        fcfs[state].xwea[mode],fcfs[state].xwen[mode],mode);
    fprintf(outfile,"%15.5f%15.5f\t\tAnharmonicities (A N) mode %d\n",
        fcfs[state].xwea[mode],fcfs[state].xwen[mode],mode);

    fscanf(infile,"%d %d",
        &fcfs[state].na[mode],&fcfs[state].nn[mode]);

    if ((fcfs[state].na[mode] >= MAXALEV) || (fcfs[state].nn[mode] >= MAXNLEV))
    {
        cout << "!! Vib Levels for state "<< state << ", mode "
            << mode << ", > MAX... !!\n";
        cout << "!! Please fix input file = "<< readfile << " !!\n";
        cout << "exit..";
        exit(8);
    }

    printf("%6d%6d\t\t\tVibrational levels (A N)\n",
        fcfs[state].na[mode],fcfs[state].nn[mode]);
    fprintf(outfile,"%6d%6d\t\t\tVibrational levels (A N)\n",
        fcfs[state].na[mode],fcfs[state].nn[mode]);

    fscanf(infile,"%f %f",

```

```

        &fcfs[state].ra[mode],&fcfs[state].rn[mode]);
    printf("%15.5f%15.5f\tAtomic distances (A N) mode %d\n",
        fcfs[state].ra[mode],fcfs[state].rn[mode],mode);
    fprintf(outfile,"%15.5f%15.5f\tAtomic distances (A N) mode
%d\n",
        fcfs[state].ra[mode],
        fcfs[state].rn[mode],mode);

} //End of mode loop

fscanf(infile,"%f",&fcfs[state].scale);
printf("%15.5f\t\tScale factor for state %d \n",
    fcfs[state].scale,state);
fprintf(outfile,"%15.5f\t\tScale factor for state %d \n",
    fcfs[state].scale,state);

} //End of state loop

fscanf(infile,"%lf",&res);
if ((res == 0) || (res < 0.1))
{
    res = 0.1 ;
    cout <<"!! Min resolution = 0.1 !! 0.01 ==> stick !!\n";
}
printf("%15.5f\t\tEnergy resolution\n",res);
fprintf(outfile,"%15.5f\t\tEnergy resolution\n",res);

cout <<"Reduce mass " <<redmass/ATMASS<<" = " << redmass << "\n";
fprintf(outfile,"Reduce mass %f = %e\n",redmass/ATMASS,redmass);

cout <<"End of Input file \n";
fprintf(outfile,"End of Input File\n\n");

res = res /1000; //change of res from meV ==> eV

return;

}

```

#### d. hofcf.cpp

```

/*****

```

```

hofcf.cpp
Subroutine to calculate harmonic Frank-Condon Factors

```

```

*****/

```

```

#include <math.h>
#include <stdio.h>
#include <iostream.h>
#include <stdlib.h>
#include "init.h"

```

```

extern double redmass;
extern int debug;

```

```

extern FILE *outfile;
extern int MIN(int a,int b);

extern double FAC(float N);

void HOFcf(const unsigned int &state,const unsigned int &mode,
           struct fcf &fcfs);

//*****
void HOFcf(const unsigned int &state,const unsigned int &mode,
           struct fcf &fcfs)
{
    double alf,den,xnum,del;
    double evwea,evwen;
    double evxwea,evxwen;
    double evtemp;
    double raw,rnw; //atomic distances in cm
    unsigned int nla,nln;

    double boltz[MAXALEV];

    unsigned int imax,jmax,lmax,ll,ii,jj;
    float nd,nf;
    double sum, prod;

    Qqs QQINT,QQ;

    raw = fcfs.ra[mode] * 1E-8;
    rnw = fcfs.rn[mode] * 1E-8;

    evwea = fcfs.wea[mode]/CWEEV;
    evwen = fcfs.wen[mode]/CWEEV;

    evxwea = fcfs.xwea[mode]/CWEEV;
    evxwen = fcfs.xwen[mode]/CWEEV;

    evtemp = fcfs.temp*CTEMP;

    alf = sqrt(fcfs.wea[mode]/fcfs.wen[mode]);
    den = 1.0 + pow(alf,2);
    xnum = 1.0 - pow(alf,2);

    if (rnw==raw) raw=raw+0.0000001E-8;

    del = (rnw-raw)*2.0*PI*sqrt(C * fcfs.wea[mode] * redmass/H);

    for (nla = 0; nla <= fcfs.na[mode]; ++nla)
    {
        boltz[nla]=exp(-(evwea*(nla)/evtemp));
    }
    //calculate boltzman dist of anion states

}

// //Normalize thermal distribution to 1

```

```

// sum = 0;
// for (nla = 0; nla <= fcfs[state].na[mode]; ++nla)
//   if (sum <= boltz[nla]) sum = boltz[nla];
// for (nla = 0; nla <= fcfs[state].na[mode]; ++nla)
//   boltz[nla] = boltz[nla]/sum;

//Normalize thermal distribution to SUM = 1

sum = 0;
for (nla = 0; nla <= fcfs.na[mode]; ++nla)
  sum = sum + boltz[nla];
for (nla = 0; nla <= fcfs.na[mode]; ++nla)
  boltz[nla] = boltz[nla]/sum;

//Optimization of anion levels
for (nla = 0; nla <= fcfs.na[mode]; ++nla)
{
  if (boltz[nla] <= 1e-5)
  {
    fcfs.na[mode] = nla;
  }
}

if (boltz[fcfs.na[mode]] >= 1e-3)
{
  cout << "\n!! Largest anion level populatio > 1% !!\n";
  cout << "Consider increasing anion leves for this mode\n";
  cout << "Population distribution for state "<<state<<'\n';
  for (nla = 0; nla <= fcfs.na[mode]; ++nla)
    printf("na =%4d Pop =%15.7f\n",nla,boltz[nla]);
}

if (debug == 1)
{
  cout << "Population distribution for state "<<state<<'\n';
  for (nla = 0; nla <= fcfs.na[mode]; ++nla)
    printf("na =%4d Pop =%15.7f\n",nla,boltz[nla]);
}

//Print population distribution
{
  fprintf(outfile,"Anion population distribution for state %d\n",
    state);
  fprintf(outfile,"na = Anion vib Level N\n");
  for (nla = 0; nla <= fcfs.na[mode]; ++nla)
    fprintf(outfile,"na =%4d Pop =%15.7f\n",nla,boltz[nla]);
  fprintf(outfile,"\n\n");
}

//FCF calculation
for (nla = 0; nla <= fcfs.na[mode]; ++nla)
{
  for (nln = 0; nln <= fcfs.nn[mode]; ++nln)
  {
    sum=0;
    lmax=MIN(nln,nla) ;

```

```

for (ll = 0; ll <= lmax; ++ll)
{
    if (fmod((nln-ll),2) == 1) imax=(nln-ll-1)/2;
    else imax=(nln-ll)/2;
    for (ii = 0; ii <= imax; ++ii)
    {
        if (fmod((nla-ll),2) == 1) jmax=(nla-ll-1)/2;
        else jmax=(nla-ll)/2;
        for (jj = 0; jj <= jmax; ++jj)
        {
            prod = 1;
            if (ll != 0)
                prod=prod * (1/FAC(ll)) * (pow((4*alf/den), ll));
            if (ii != 0)
                prod = prod * (1/FAC(ii)) * (pow((xnum/den), ii));
            if (jj != 0)
                prod=prod * (1/FAC(jj)) * (pow((-xnum/den), jj));
            nd = nln-2*ii-ll;
            if (nd != 0)
                prod = prod * (1/FAC(nd)) * (pow((-2*alf*del/den), nd));
            nf = nla-2*jj-ll;
            if (nf != 0)
                prod = prod * (1/FAC(nf)) * (pow((2*del/den), nf));

            sum = sum + prod;
        }
    }
    QQINT[nla][nln] = sum * sqrt((FAC(nln)*FAC(nla))/
                                pow(2, (nln+nla)));
    QQ[nla][nln] = pow(QQINT[nla][nln],2);
}

for (nla = 0; nla <= fcfs.na[mode]; ++nla)
{
    sum = 0;
    for (nln = 0; nln <= fcfs.nn[mode]; ++nln)
    {
        if (sum <= QQ[nla][nln]) sum = QQ[nla][nln];
    }
    for (nln = 0; nln <= fcfs.nn[mode]; ++nln)
    {
        QQ[nla][nln]=QQ[nla][nln]/sum;

        fcfs.fcfe[mode][nla][nln] = fcfs.orig - evwen * nln + evxewen
* pow(nln,2)
        + evwea*nla - evxewea * pow(nla,2);
    }
}

if (debug == 1)
{
    fprintf(outfile, "Franck-Condon Factor Tables\n");
    fprintf(outfile, "na = Anion Level\tnn = Neutral Level\n");
}

```

```

for (nla = 0; nla <= fcfs.na[mode]; ++nla)
{
    for (nln = 0; nln <= fcfs.nn[mode]; ++nln)
    {
        fcfs.fcfi[mode][nla][nln] = QQ[nla][nln] * boltz[nla] ;

        if (debug == 1)
        {
            fprintf(outfile,"na =%3d nn =%3d Q =%15.6e QQ =%15.8f\n",
                nla,nln,QQINT[nla][nln], fcfs.fcfi[mode][nla][nln]);
        }
        if (debug == 5 )
        {
            printf("na =%3d nn =%3d QINT =%15.6e QQ =%15.8f\n",
                nla,nln,QQINT[nla][nln], fcfs.fcfi[mode][nla][nln]);

            // fprintf(infile,"%5d%5d%15.8f%15.8f\n",
            //nla,nln,QQe[mode][nla][nln],QQb[mode][nla][nln]);
        }

        if (debug == 1) fprintf(outfile,"\n");
        if (debug == 5) cout << '\n';
    }
}

return;
}

```

#### e. simfcf.cpp

```

/*****

simfcf.cpp
Simulation of FCF data points

*****/

#include <math.h>
#include <stdio.h>
#include <iostream.h>
#include <stdlib.h>
#include <string.h>
#include "init.h"

long unsigned int MAXPTS; // points for simulation
extern double eres; // 2* ERES is the energy resolution
double RANGEf;
double step,res;
long int range,rangeg;

extern int fixres;
extern int debug;

FILE *stickf,*simf;
char stick[128],simu[128];

```

```

extern char filename[128];

//Qsort implementaion
void Partition (sim &table, long int first, long int last,
               long int &PivotIndex );

void Qsort (sim &table, long int first, long int last);

//Gaussian fuction (resolution)
double GAUSS(const sim &simul,const long int &ii);

double LORTZ(const sim &simul,const long int &ii);

void simfcf(const unsigned int &states,struct fcf sfcf[MAXSTATES]);

//*****

void Partition (sim &table, long int first, long int last,
               long int &PivotIndex )
{
    double pivot;
    long int up,down;
    double tempx,tempy;

    up = first;  down = last;
    pivot = table[0][first];

    do{
        // move up to the next location > pivot
        while(( table[0][up] <= pivot ) && ( up < last ) )
            up++;
        // move down to the next location <= pivot
        while ( table[0][down] > pivot )
            down--;

        if (up < down)
        {
            tempx = table[0][up];
            tempy = table[1][up];
            table[0][up] = table[0][down];
            table[1][up] = table[1][down];
            table[0][down] = tempx;
            table[1][down] = tempy;
        }

    } while (up < down );

    //put pivot value where it belongs and define PivotIndex
    {
        tempx = table[0][first];
        tempy = table[1][first];
        table[0][first] = table[0][down];
        table[1][first] = table[1][down];
        table[0][down] = tempx;
    }
}

```



```

        table[1][down] = tempy;
    }
    PivotIndex = down;
}

void Qsort (sim &table, long int first, long int last)
{
    long int PivotIndex;

    if( first < last)
    {
        Partition(table, first,last, PivotIndex );
        Qsort(table, first, PivotIndex-1);
        Qsort(table, PivotIndex+1,last);
    }
}

double GAUSS(const sim &simul,const long int &ii)
{
    double result,resolution;
    long unsigned int index;
    long unsigned int top,bottom,lrange;

    //Spectral Resolution fixed
    if ((fixres != 1) && (simul[0][ii] > 1 ))
    {
        resolution = res * pow(sqrt(simul[0][ii]),3);
        lrange = range * int(sqrt(simul[0][ii]));
    }
    else
    {
        resolution = res;
        lrange = range;
    }

    bottom = ii - lrange;    top = ii + lrange;

    if (bottom < 0) bottom = 0;
    if (top > MAXPTS) top = MAXPTS;

    result = 0;

    for (index = bottom; index <= top; ++index)
    {
        result = result + simul[1][index] * 0.5 *
            exp(-(pow(simul[0][index] - simul[0][ii],2)/resolution));
    }

    return(result);
}

double LORT2(const sim &simul,const long int &ii)

```

```

{
    double result,resolution;
    long unsigned int index;
    long unsigned int top,bottom,lrange;

    //Spectral Resolution fixed
    if ((fixres != 1) && (simul[0][ii] > 1 ))
    {
        resolution = res * pow(sqrt(simul[0][ii]),3);
        lrange = range * int(sqrt(simul[0][ii]));
    }
    else
    {
        resolution = res;
        lrange = range;
    }

    bottom = ii - lrange;    top = ii + lrange;

    if (bottom < 0) bottom = 0;
    if (top > MAXPTS) top = MAXPTS;

    result = 0;

    for (index = bottom; index <= top; ++index)
    {
        result = result + simul[1][index] * 0.5 *
            exp(-(pow(simul[0][index] - simul[0][index],2)/resolution));
    }

    return(result);
}

//Simulation Subroutine
void simfcf(const unsigned int &states,struct fcf sfcf[MAXSTATES])
{
    sim asim,simul;
    long unsigned int counter,count,co;
    unsigned int state,mode,tmp;
    int unsigned nla,nln;
    long unsigned int ii;
    double emax,emin;
    double norm,norma;
    double tmpint;
    long int tmpener;

    cout << "Generating spectrum.. " <<flush;

    strcpy(stick,filename);
    strcat(stick,".stick");
    strcpy(simu,filename);
    strcat(simu,".dat");
    stickf = fopen(stick,"w");
    simf = fopen(simu,"w");

```

```

counter = 0;

//Sorting vibrational contributions
for (state = 1; state <= states; ++state)
{
    if (sfcf[state].mode > 1)
    {
        for (nln = 0; nln <= sfcf[state].combnn; ++nln)
        {
            simul[0][counter] = sfcf[state].comb[0][nln];
            simul[1][counter] = sfcf[state].comb[1][nln]
                * sfcf[state].scale;
            counter = ++counter;
        }
    }
    else
    {
        for (mode = 1; mode <= sfcf[state].mode; ++mode)
        for (nla = 0; nla <= sfcf[state].na[mode]; ++nla)
        for (nln = 0; nln <= sfcf[state].nn[mode]; ++nln)
        {
            if ((sfcf[state].fcfe[mode][nla][nln] > 0.0) &&
                (sfcf[state].fcfi[mode][nla][nln] > FCFCOFF))
            {
                simul[0][counter] = sfcf[state].fcfe[mode][nla][nln];
                simul[1][counter] = sfcf[state].fcfi[mode][nla][nln]
                    * sfcf[state].scale;
                counter = ++counter;
            }
        }
    }
}

counter = counter - 1;

if (debug == 1) cout << "\nCOUNTERa = "<< counter;

Qsort(simul,0,counter);

co = 0;
for (count = 0; count <= counter; ++count)
{
    tmpener = int(simul[0][count] * MAXRES);
    tmpint = simul[1][count];
    tmp = 0;
    while (tmpener == (int(simul[0][(count + tmp + 1)] * MAXRES)))
    {
        tmpint = tmpint + simul[1][(count + tmp + 1)];
        tmp = ++tmp;
    }
    asim[0][co] = tmpener/MAXRES ;
    asim[1][co] = tmpint;
    count = count + tmp;
    co = ++co;
}

```

```

counter = co - 1;
if (debug == 1) cout <<"\nCOUNTERb = "<< counter;

emin = asim[0][0];
emax = asim[0][counter];

if (debug == 1)
{
    cout <<"\nEmax = "<< emax;
    cout <<"\nEmin = "<< emin;
}

if (emin <= 0.5)
{
    emin = 0;
}
else
{
    emin = emin - 0.5;
}

emax = emax + 0.5;

if (eres <= 0.001)
{
    MAXPTS = int((emax - emin + 0.0001*counter)/0.0001);
    rangeg = int(1500 * .005/eres);
}
else if (eres <= 0.005)
{
    MAXPTS = int((emax - emin + 0.00049*counter)/0.00049);
    rangeg = int(1500 * .005/eres);
}
else
{
    MAXPTS = int((emax - emin + 0.00099*counter)/0.00099);
    rangeg = int(1500 * .005/eres);
}

if (debug == 1) cout <<"\nMAXPTSa = "<< MAXPTS<<"\n";

if (debug == 2)
{
    for (ii = 0; ii <= counter; ++ii)
        printf("%5ld%12.8f%12.8f\n",ii,asim[0][ii],asim[1][ii]);
    cout <<"\n";
}

step = (emax - emin)/(MAXPTS - counter);

if (debug == 1) cout <<"Step = "<< step <<"\n";

res = pow(eres,2);

```

```

range = int(res / step * range);

if (eres <= 0.001)
{
    range = range * 2;
}

if (debug == 1)
{
    cout <<"RANGE = "<< range<<"\n";
    cout <<"Fixres = "<< fixres <<"\n";
}

for (ii = 0; ii <= MAXPTS; ++ii)
{
    if (ii <= counter)
    {
        simul[0][ii] = asim[0][ii];
        simul[1][ii] = asim[1][ii];
    }
    else
    {
        simul[0][ii] = emin + (ii - (counter))*step;
        simul[1][ii] = 0.0 ;
    }
}

Qsort(simul,0,MAXPTS);

co = 0;
for (count = 0; count <= MAXPTS; ++count)
{
    tmpener = int(simul[0][count] * MAXRES * 10);
    tmpint = simul[1][count];
    tmp = 0;
    while (tmpener == (int(simul[0][(count + tmp + 1)] * MAXRES *
10)))
    {
        tmpint = tmpint + simul[1][(count + tmp + 1)];
        tmp = ++tmp;
    }
    asim[0][co] = tmpener/(MAXRES * 10) ;
    asim[1][co] = tmpint;
    count = count + tmp;
    co = ++co;
}

MAXPTS = co - 1;

if (debug == 1) cout <<"MAXPTSb = "<< MAXPTS<<"\n";

norma = 0;
for (ii = 0; ii <= MAXPTS; ++ii)
{
    if (norma <= asim[1][ii]) norma = asim[1][ii];
}

```

```

    }

    norm = 0;
    for (ii = 0; ii <= MAXPTS; ++ii)
    {
        fprintf(stickf, "%15.8f %15.5e\n", asim[0][ii], asim[1][ii]/norma);
        simul[0][ii] = asim[0][ii];
        simul[1][ii] = GAUSS(asim, ii);
        if (norm <= simul[1][ii]) norm = simul[1][ii];
    }

    for (ii = 0; ii <= MAXPTS; ++ii)
    {
        simul[1][ii] = simul[1][ii]/norm;
        fprintf(simf, "%15.8f%15.5e\n", simul[0][ii], simul[1][ii]);
    }

    if (debug == 6)
    {
        for (ii = 0; ii <= MAXPTS; ++ii)
        {
            printf("%15.8f%15.5e\n", simul[0][ii], simul[1][ii]);
        }
    }

    fclose(stickf);
    fclose(simf);
    cout << "done ..\n";
}

```

#### f. misc.cpp

```

/*****

misc.cpp
Miscelaneos funtions used by pesn

*****/

#include <math.h>
#include <stdio.h>
#include <iostream.h>
#include <stdlib.h>
#include <time.h>
#include "init.h"

int MIN(int a, int b);

//Factorial function
double FAC(float N);

//Usage display
void usage(void);

```

```

//Help display
void help(void);

void LPartition (combi table,int first,int last,int &PivotIndex );

void LQsort (combi table, int first, int last);

//*****

int MIN(int a,int b)
{
    int result;

    if (a <= b) result = a;
    else result = b;

    return(result);
}

double FAC(float N)
{
    //Factorial Funtion double(double)
    double result;
    int i;

    if (N < 0) N = -N;

    if (N == 0) result = 1;
    if (N == 1) result = 1;

    result =1;

    if (N > 1) {
        for (i = 2; i <= N; ++i)
            result = result*i;
    }
    return(result);
}

void usage(void)
{
    cerr <<"Usage is \"pesn -options\" \n";
    cerr <<"Options:\n";
    cerr <<"\t-d\t\t\tDebug level (Max = 3)\n";
    cerr <<"\t-i<file_name>\t\tinput file (without extension)\n";
    cerr <<"\t-o<file_name>\t\toutput files (optional)\n";
    cerr <<"\t-h\t\t\tDisplay help information\n";
    exit(8);
}

void help(void)
{
    cerr <<"This program calculates Frank condon Factor (FCFs) \n";
    cerr <<"starting from an anion state to multiple neutral\n";

```

```

cerr <<"states.\n\n";

cerr <<"Usage is \"pesn -options\" \n";
cerr <<"Options:\n";
cerr <<"\t-d\t\t\tDebug level (Max = 3)\n";
cerr <<"\t-i<file_name>\t\twithout extension\n";
cerr <<"\t-o<file_name>\t\toutput files (optional)\n";
cerr <<"\t-h\t\t\tDisplay help information\n";
cerr<<"Example:\n\tpesn -idata -ooutput -dl\n\n";
cerr<<"This command line will run the program using data.in\n";
cerr<<"inputfile, generating the following output files:\n\n";
cerr<<"output.stick\t\t\tstick spectrum\n";
cerr<<"output.out\t\t\tFCFs infomation \n";
cerr<<"output.dat\t\t\ttsimulated spectrum\n\n";
cerr<<"With Debug level = 1\n\n";
cerr<<"The input file can be generated using \"writep\"\n";
cerr<<"\"write parameters\" command.\n\n";
exit(8);
}

void LPartition (combi table, int first, int last,
                int &PivotIndex)
{
    double pivot;
    int up,down;
    double tempx,tempy;

    up = first;  down = last;
    pivot = table[0][first];

    do{
        // move up to the next location > pivot
        while(( table[0][up] <= pivot ) && ( up < last ) )
            up++;
        // move down to the next location <= pivot
        while ( table[0][down] > pivot )
            down--;

        if (up < down)
        {
            tempx = table[0][up];
            tempy = table[1][up];
            table[0][up] = table[0][down];
            table[1][up] = table[1][down];
            table[0][down] = tempx;
            table[1][down] = tempy;
        }

    } while (up < down );

    //put pivot value where it belongs and define PivotIndex
    {
        tempx = table[0][first];
        tempy = table[1][first];
        table[0][first] = table[0][down];
        table[1][first] = table[1][down];
    }
}

```



```

        table[0][down] = tempx;
        table[1][down] = tempy;
    }

    PivotIndex = down;
}

void LQsort (combi table, int first, int last)
{
    int PivotIndex;

    if( first < last)
    {
        LPartition(table, first,last, PivotIndex );
        LQsort(table, first, PivotIndex-1);
        LQsort(table, PivotIndex+1,last);
    }
}

```

#### **g. writep.cpp**

```

/*****
writep.cpp
Program to generate input file for pesn
*****/
#include <math.h>
#include <stdio.h>
#include <iostream.h>
#include <stdlib.h>
#include <string.h>
#include "init.h"

FILE *outfile;

int main(void)
{
    char writefile[128];

    float res;
    char type[0];
    float mass1,mass2,redmass;
    unsigned int state,states;
    unsigned int mode,modes;
    int right;
    float scale;
    float temp,wea,wen,xewea,xewen,ra,rn,origin;
    int na,nn;

    printf("!!\tWelcome to PES 2000 v0.001\t!!\n");

```

```

printf("Enter the file name to be created: \n");
cin >>writefile;
strcat(writefile, ".in");
cout << "File to be created \t\t: "<<writefile<<"\n";
outfile = fopen(writefile, "w");

right = 1;
while (right)
{
    printf("Diatomic(d) of Poliatomic(p) ?\n");
    cin >>type;
    if ((type[0] == 'd') || (type[0] == 'p'))
    {
        printf("%c\n", type[0]);
        fprintf(outfile, "%c\n", type[0]);
        right = 0;
    }
    else
    {
        cout << "Small caps please \n" ;
    }
}

right =1;
while (right)
{
    if (type[0] == 'd')
    {
        cout<<"Enter Mass1 and Mass2 separate by spaces \n";
        cin >> mass1 >> mass2;
        printf("%15.5f %15.5f\n", mass1, mass2);
        fprintf(outfile, "%15.5f%15.5f\n", mass1, mass2);
    }
    else
    {
        printf("Enter reduce mass (Default = 2)\n");
        cin >> redmass;
        printf("%15.5f\n", redmass);
        fprintf(outfile, "%15.5f\n", redmass);
    }
    right = 0;
}

right =1;
while (right)
{
    cout << "How many electronic states (MAX = 15) \n";
    cin >> states;
    if ((states >0) && (states <= MAXSTATES))
    {
        printf("%4d\n", int(states));
        fprintf(outfile, "%4d\n", int(states));
        right = 0;
    }
}

```

```

    }
    for(state = 1; state <= states; ++state)
    {
        right = 1;
        while (right)
        {
            cout <<"How many modes for state "<<state;
            cout <<" (MAX = 4)\n";
            cin >>modes;
            if ((modes >0) && (modes <= MAXMODES))
            {
                printf("%4d\n",int(modes));
                fprintf(outfile,"%4d\n",int(modes));
                right = 0;
            }
        }
        right = 1;
        while (right)
        {
            cout <<"Origin for state "<<state;
            cout <<" (Ev)\n";
            cin >>origin;
            if (origin > 0)
            {
                printf("%15.3f\n",origin);
                fprintf(outfile,"%15.3f\n",origin);
                right = 0;
            }
        }
        right =1;
        while (right)
        {
            cout <<"Temperatur for the fit (K) for state "<<state<<" \n";
            cin >>temp;
            if (temp >0)
            {
                printf("%15.5f\n",temp );
                fprintf(outfile,"%15.5f\n",temp);
                right = 0;
            }
        }
    }
    for (mode = 1; mode <= modes; ++mode)
    {
        right =1;
        while (right)
        {
            cout <<"Frequencies for the Anion and Neutral";
            cout <<" for mode "<<mode<<" (cm-1)\n";
            cin >>wea>>wen;
            if ((wea > 0) && (wen > 0))
            {
                printf("%15.5f%15.5f\n",wea,wen );
                fprintf(outfile,"%15.5f%15.5f\n",wea,wen);
                right = 0;
            }
        }
    }

```

```

    }
    right =1;
    while (right)
    {
        cout <<"Anharmonicities for the Anion and Neutral";
        cout <<" for mode "<<mode<<"\n";
        cin >>xewea>>xewen;
        if ((xewea >= 0) && (xewen >= 0))
        {
            printf("%15.5f%15.5f\n",xewea,xewen );
            fprintf(outfile,"%15.5f%15.5f\n",xewea,xewen);
            right = 0;
        }
    }
    right =1;
    while (right)
    {
        cout <<"# of vibrational levels for the Anion and Neutral";
        cout <<" for mode "<<mode<<"\n";
        cin >>na>>nn;
        if ((na >= 0) && (nn > 0))
        {
            printf("%6d%6d\n",int(na),int(nn));
            fprintf(outfile,"%6d%6d\n",int(na),int(nn));
            right = 0;
        }
    }
    right =1;
    while (right)
    {
        cout <<"Atomic distances for the Anion and Neutral";
        cout <<" for mode "<<mode<<" (A)\n";
        cin >>ra>>rn;
        if (((ra >= 0) && (rn >= 0)) && ((ra <= MAXALEV) && (rn <=
MAXNLEV)))
        {
            printf("%15.5f%15.5f\n",ra,rn);
            fprintf(outfile,"%15.5f%15.5f\n",ra,rn);
            right = 0;
        }
    }

} //End of mode loop

right =1;
while (right)
{
    cout <<"Scale Factor for state "<<state<<" (0.01 - 1.0)\n";
    cin >>scale;
    if ((scale >0) && (scale <=1.0))
    {
        printf("%15.5f\n",scale );
        fprintf(outfile,"%15.5f\n",scale);
        right = 0;
    }
}

```

```

    } //End of state loop
    right = 1;
    while (right)
    {
        printf("Energy Resolution for the fit ?");
        cout << " (meV) (.1 - 200 meV)\n";
        cin >> res;
        if ((res >= .1) && (res <= 200))
        {
            printf("%15.5f\n", res);
            fprintf(outfile, "%15.5f\n", res);
            right = 0;
        }
    }
    cout << "File created \t\t: " << writefile << "\n";
    cout << "Run using \"pesn -i\" << writefile << "\n\n";

    fclose(outfile);

return(0);
}

```